Macquarie University

Department of Physics and Astronomy

Star Formation and the Hall Effect

Catherine Ruth Braiding

Doctor of Philosophy (Physics)

June 2011

Supervisor: Prof. Mark Wardle
Associate Supervisor: Dr. Alan Vaughan

Abstract

Magnetic fields play an important role in star formation by regulating the removal of angular momentum from collapsing molecular cloud cores. Hall diffusion is known to be important to the magnetic field behaviour at many of the intermediate densities and field strengths encountered during the gravitational collapse of molecular cloud cores into protostars, and yet its role in the star formation process is not well-studied. This thesis describes a semianalytic self-similar model of the collapse of rotating isothermal molecular cloud cores with both Hall and ambipolar diffusion, presenting similarity solutions that demonstrate that the Hall effect has a profound influence on the dynamics of collapse.

Two asymptotic power law similarity solutions to the collapse equations on the inner boundary are derived. The first of these represents a Keplerian disc in which accretion is regulated by the magnetic diffusion; with an appropriate value of the Hall diffusion parameter a stable rotationally-supported disc forms, but when the Hall parameter has the opposite sign disc formation is suppressed by the strong diffusion. The second solution describes the infall when the magnetic braking is so efficient at removing angular momentum from the core that no disc forms and the matter free falls onto the protostar.

The full similarity solutions show that the size and sign of the Hall parameter can change the size of the protostellar disc by up to an order of magnitude and the accretion rate onto the protostar by 1.5×10^{-6} $\mathrm{M}_{\odot}$ yr^{-1} when the ratio of the Hall to ambipolar diffusion parameters moves between the extremes of $-0.5 \leq \tilde{\eta}_H/\tilde{\eta}_A \leq 0.2$. These variations (and their dependence upon the orientation of the magnetic field with respect to the axis of rotation) create a preferred handedness to the solutions that could be observed in protostellar cores using next-generation instruments such as ALMA.

Hall diffusion also determines the strength of the magnetic diffusion and centrifugal shocks that bound the pseudo and rotationally-supported discs, and can introduce subshocks that further slow accretion onto the protostar. In cores that are not initially rotating Hall diffusion can even induce rotation, which could give rise to disc formation and resolve the magnetic braking catastrophe. The Hall effect clearly influences the dynamics of gravitational collapse and its role in controlling the magnetic braking and radial diffusion of the field would be worth exploring in future numerical simulations of star formation.

Statement of Candidate

I certify that the work in this thesis, entitled "Star Formation and the Hall Effect", has not previously been submitted for a degree nor has it been submitted as part of requirements for a degree to any other university or institution other than Macquarie University.

I also certify that this thesis is an original piece of research and that it has been written by myself. Any help and assistance that I have received in my research work and the preparation of the thesis itself have been appropriately acknowledged.

In addition, I certify that all information sources and literature used are indicated in the thesis.

Catherine Braiding (30615399) 15 / 7 / 2011

Acknowledgements

Writing this thesis has been the hardest thing I have ever done; over the course of the last few years my self-esteem and sense of self-worth have plummeted, and I could not have finished without the support of a great number of people. To all of them I give my heartfelt thanks, but in particular I would like to acknowledge:

- my supervisor, Mark Wardle, who is brilliant and funny and has always supported me, even when he was overburdened with too many PhD students to supervise and theses to read. You inspire me, and if I continue on this path it will be thanks to you.
- Gemma and James, for all the hugs, tears and unconditional love, as well as the gifts of backup drives. You make me a better person; when times were rocky you were there for me and I love you both.
- Korinne, Sarah and Anna, the best PhD buddies and officemates anyone could ask for. Thanks for the songs, the cupcakes, the hugs, and making it through to the end with me — I'm proud of all of us.
- Korinne again, because she proofread this beast twice. Thanks, crazy lady.
- my family, for everything. I promise I'll get a real job soon.
- the department of physics and astronomy and others, particularly Alan, Judith and Carol, for the moral and occasional monetary support.
- Raquel, Pandey, and the participants of the *DDP* and *CC2YSO* workshops in 2009 and 2010, for the engaging and stimulating discussions.
- finally, my closest friends: Brendan, Heidi, Tony, Nilanka, Roberto and Drew; the West Ryde knitters; and all the other friends, online and off, who have listened to my rants and offered sympathy as needed. May all of you continue to be awesome.

Thank you all,
Catherine

Contents

List of Figures

List of Tables

"It seems to me, that if the matter of our sun and planets, and all the matter of the universe, were evenly scattered throughout all the heavens, and every particle had an innate gravity towards all the rest, and the whole space throughout which this matter was scattered, was finite, the matter on the outside of this space would by its gravity tend towards the matter on the inside, and by consequence fall down into the middle of the whole space, and there compose one great spherical mass. But if the matter were evenly disposed throughout an infinite space, it could never convene into one mass; but some of it would convene into one mass and some into another, so as to make an infinite number of great masses, scattered great distances from one to another throughout all that infinite space. And thus might the sun and fixed stars be formed, supposing the matter were of a lucid nature."

- Newton to Bentley (December 10, 1692), quoted by Jeans (1928)

Chapter 1

Star Formation

In the seventeenth century Sir Isaac Newton pondered gravity's influence on the formation of stars and planets and the consequences of such star formation on an unbounded interstellar medium (Newton to Bentley, December 10, 1692; as quoted by Jeans, 1928). His assertion that the gradual growth of inhomogeneities in the material that forms stars could lead to runaway gravitational collapse remains at the heart of star formation theory today, and it is from this basic description that our modern understanding of star formation by the gravitational condensation of diffuse matter in space under the influence of rotational and magnetic effects has evolved.

Understanding star formation is critical to our understanding of the universe, as stars are the fundamental objects of astronomy. Star formation determines the structure, evolution and luminosity of galaxies (e.g. Freeman and Bland-Hawthorn, 2002); planet formation and evolution occurs in protoplanetary discs as a result of the star formation process (Safronov, 1967) and most of the elements that are not hydrogen are made in stars (Hoyle, 1946) — so it is no surprise that the intricacies of star formation are the focus of many studies in astronomy. The questions surrounding how molecular clouds are formed and supported against gravity (e.g. Tasker and Tan, 2009); what triggers their collapse (e.g. Chandrasekhar and Fermi, 1953; Field, 1978; Norman and Silk, 1980); the detailed dynamics of the collapse throughout the different stages of the star formation process (e.g. Larson, 1969; Penston, 1969; Shu, 1977; Terebey et al., 1984; Shu et al., 1987; Stahler and Palla, 2004; McKee and Ostriker, 2007) and the importance of the magnetic field and the angular momentum of the initial cloud in determining the final properties of the protostar and its protostellar disc (e.g. Mestel and Spitzer, 1956; Strittmatter, 1966; Basu, 1998; Dapp and Basu, 2010) are of vital importance to our understanding of the universe.

In the last fifty years the increasing availability of computers and numerical techniques enabled astronomers to simulate gravitational collapse and star formation with

increasing resolution and complexity (Klessen et al., 2011; Machida, 2011), while observations at infrared and radio wavelengths have started to unveil the physical processes at work in the molecular cloud cores from which stars form and determine the characteristics that distinguish the youngest stars from their host clouds (e.g. di Francesco et al., 2007; Ward-Thompson et al., 2007). Both theoretical and observational studies of star formation have gradually converged on the consensus theories that low-mass stars form as a result of the gravitational collapse of dense molecular cloud cores, while higher mass stars form under the influence of more complicated processes, such as the fragmentation of molecular cloud clumps, the merger of smaller stars, and turbulent motions within the molecular clouds (e.g. Basu and Ciolek, 2004; Mac Low and Klessen, 2004; Ballesteros-Paredes et al., 2007).

In the "standard model" of star formation proposed by Shu et al. (1987) it is assumed that magnetic fields and thermal pressure initially provide pressure support against gravity in these molecular cloud cores and carry away excess angular momentum; however, as the gas is weakly ionised it is not in a strictly-steady state and gradually contracts. The neutral molecules are pulled inwards by gravity and drift inward through the magnetic field (which is supported by ions) in the process of ambipolar diffusion (Spitzer, 1978). Once the density is high enough that the magnetic field is no longer able to support the core, it dynamically collapses to form a protostar, usually (although not always) surrounded by a protostellar disc from which it accretes further mass. The protostar quickly comes to gravitationally dominate a progressively larger region of the molecular cloud in which it has formed (Shu et al., 1987).

This introductory chapter outlines the previous research and current theories of primarily low-mass star formation, to motivate the research into the influence of Hall diffusion on the dynamics of gravitational collapse and accretion disc physics that is described within the rest of this thesis. The properties of molecular clouds and the star forming cores within them are described first, to provide an overview of the initial conditions of collapse, followed by a brief description of Hall magnetohydrodynamics, emphasising the importance of magnetic field diffusion on the dynamics of weakly ionised gases such as those found in molecular clouds.

The current state of gravitational collapse studies is then explored across several stages of the star formation process, with particular focus on the effects of rotation and the magnetic field on the collapsing core. The current major problem of star formation simulations — the "magnetic braking catastrophe", in which all of the angular momentum is removed from the collapsing core by magnetic braking — is outlined, along with recent approaches towards solving this problem and predictions for how Hall magnetohydrodynamics shall affect the magnetic braking behaviour in the flow. Finally, an overview of the thesis, its aims and primary results shall be presented with

reference to existing theories of star formation. Should readers wish for more detailed information on the current state of star formation research than is presented in this chapter, they are directed to the thorough reviews by McKee and Ostriker (2007) and Machida (2011), and the references cited therein.

1.1 Molecular Clouds

Stars form in molecular clouds, generally dark regions of the interstellar medium in which the density and temperature of the gas permit the formation of molecules. The gas is primarily composed of molecular hydrogen, which is difficult to detect observationally, and so the gas is traced and the mass inferred from its luminosity in the $J = 1 - 0$ line of ^{12}CO or ^{13}CO, which are the dominant carbon-bearing species (Langer et al., 2000).

Giant molecular clouds make up most of the mass of the interstellar medium; they have masses 10^4–10^6 $M_\odot$, diameters $\sim$ 30–50 pc and volume-averaged number densities of $n_H \sim 10^2$–10^4 cm^{-3} (André et al., 2000; Williams et al., 2000; di Francesco et al., 2007, and the references within these). They are in general not gravitationally bound (Dobbs et al., 2011), and are surrounded by a layer of less dense atomic gas which shields the molecules from the interstellar UV radiation field that is capable of dissociating molecules and leads to a low rate of heating by external radiation (Elmegreen, 1993). Giant molecular clouds may contain several sites of star formation, and while smaller molecular clouds with masses $\lesssim 10^2$ $M_\odot$ may also form stars, their contribution to the total star formation rate in the Galaxy is negligible (Magnani et al., 1995).

Molecular clouds have a hierarchical structure and the terminology used to describe the differently-scaled features varies across papers; the conventions outlined in McKee and Ostriker (2007) are followed here. Overdense coherent regions in *l*-*b*-*v* (galactic longitude, galactic latitude and radial velocity) space identified from spectral line maps of molecular emission within molecular clouds are referred to as *clumps*. *Cluster-forming clumps* are the massive clumps out of which stellar clusters form; they are gravitationally bound or bound by the pressure of the interclump medium even though most clusters are unbound (Williams et al., 1995). Molecular cloud *cores* are the particularly dense self-gravitating regions out of which single stars (or small multiple systems such as binaries) form. Not all of the material that goes into forming a star must come from the core — some may be accreted from the surrounding clump or cloud as the protostar moves through it (Bonnell et al., 1997). The physical properties of molecular clouds, clumps and cores are summarised in Table 1.1 (from Klessen et al., 2011).

	molecular clouds	cluster-forming clumps	protostellar cores
Size (pc)	2–50	0.1–2	$\lesssim 0.1$
Density ($n_{\rm H}$ cm^{-3})	10^2–10^4	10^3–10^5	$> 10^5$
Mass (M$_\odot$)	10^2–10^6	10–10^3	0.1–10
Temperature (K)	10–30	10–20	7–12
Line width (km s^{-1})	1–10	0.3–3	0.2–0.5
Column density (g cm^{-2})	0.03	0.03–1.0	0.3–3
Column density (M$_\odot$ pc^{-2})	∼144	144–5000	1500–15000
Crossing time (Myr)	2–10	$\lesssim 1$	0.1–0.5
Free fall time (Myr)	0.3–3	0.1–1	$\lesssim 0.1$
Examples	Taurus, Ophiuchus	L1641, L1709	B68, L1544

Table 1.1: Physical properties of molecular clouds, cluster-forming clumps and isolated protostellar cores from Klessen et al. (2011).

Molecular cloud cores that form single or binary low-mass stars (as opposed to clumps that form clusters and very massive stars) such as those in the Taurus, Orion and Ophiuchus molecular clouds have typical diameters $\lesssim 0.1$ pc, number densities $n_{\rm H} \gtrsim 3 \times 10^4$ cm^{-3} and masses ranging from a fraction of a solar mass to 10 M$_\odot$, although the masses can be uncertain by a factor of ~ 3 due to uncertainties in the measured distance, dust opacity, molecular abundances and calibration (di Francesco et al., 2007). The core morphologies depend on the intensity level chosen to mark the boundary between the core and the host cloud, as well as the wavelength range and angular resolution of the observations. In general, cores that are round (in projection against the sky) are interpreted as being spherical in shape, while cores that are elongated (again, in projection) are typically interpreted as being either oblate or prolate spheroids; statistical analyses have shown that most isolated cores are oblate rather than prolate (Jones et al., 2001; Jones and Basu, 2002, in contrast with the results of Ryden (1996) who assumed axisymmetry in their analysis); and that starless cores have more extreme axial ratios than protostellar cores (cores in which a protostar has formed; Goodwin et al., 2002).

Mappings of molecular cloud cores show that they often display nonzero initial infall velocities before they contain infrared sources (protostars). Lee et al. (2001) mapped 53 targets and identified 19 candidate collapsing cores that demonstrated infall based upon the shape of the CS lines and analysis of both the thick CS and the thin N_2H^+ peak velocities. They derived one-dimensional infall speeds for these starless cores to obtain typical values of 0.05–0.09 km s^{-1}, corresponding to mass infall rates of about 10^{-6}–10^{-5} M$_\odot$ yr^{-1}. These observations were consistent with both of the dominant models for the removal of support against gravity causing the contraction of molecular

cloud cores: ambipolar diffusion and dissipation of turbulence theories (Fatuzzo et al., 2004, these theories shall be explored in detail in Section 1.3).

Approximately 1% of the mass of a molecular cloud is in the form of dust particles or grains, on which hydrogen molecules form by condensation (Spitzer, 1978). The rate at which this process occurs increases with density, so that the abundance of molecules within the gas depends also upon density (Larson, 2003). The opacity of the dust shields the gas from the UV radiation that would normally dissociate the molecules; the continued existence of molecules requires that the host cloud possess a column density of at least 20 $M_\odot$ pc^{-2} (Elmegreen, 1993). Typical molecular clouds are quite opaque and have column densities in excess of 100 $M_\odot$ pc^{-2} (see Table 1.1).

About half of the known interstellar molecular species have been detected in the single core TMC-1 (Taurus Molecular Cloud-1; Ohishi and Kaifu, 1998). Surveys of isolated molecular cloud cores show that they are chemically differentiated with NH_3 and N_2H^+ dominant in the denser inner regions, and C_2S, CS and other carbon-rich molecules more abundant in the diffuse outer regions (Kuiper et al., 1996; Lada et al., 2003); the ratio of C_2S to N_2H^+ abundances has been proposed as an indicator of the time since the gas was atomic carbon-rich (Bergin and Langer, 1997; Langer et al., 2000). In regions of massive star and cluster formation hot cores are produced (in which the temperature is > 50 K); these may contain more complex organic molecules such as CH_3OH, CH_3CH_2OH and $HCOOCH_3$ and typically have a large deuterium fraction (Kuiper et al., 1996; Irvine, 1999). The chemical differences observed between regions of isolated and clustered star formation, such as the presence of complex organic molecules, may (if retained in comets) provide a way of tracing the formation conditions of the solar system (Irvine, 1999).

Molecular clouds are generally cold, with constant temperatures of around $T \simeq 10$ K across a wide range of densities (e.g. Hayashi and Nakano, 1965; Larson, 1985; Masunaga and Inutsuka, 2000). In regions of cluster formation compressional heating and radiative heating from new stars can cause the temperature of individual cores to rise to 100 K or higher, and when the density is particularly high the collapsing gas becomes thermally-coupled to the dust; despite this the temperature of cores typically remains constant so long as the density remains below $\sim 10^{10}$ cm^{-3}, above which radiative trapping occurs and the temperature increases (e.g. Winkler and Newman, 1980; Wardle and Königl, 1993; Ciolek and Königl, 1998). This corresponds to the formation of the "first" (opaque) core, which is followed later by dynamic collapse to the "second" core (the protostar) once molecular hydrogen dissociates (e.g. Larson, 1969). The rate at which molecular clouds are cooled by collisionally-excited atomic and molecular emission processes is high — this emission primarily takes the form of far-infrared radiation from molecules such as CO, which is the dominant coolant in

molecular clouds (McKee et al., 1982; Gilden, 1984).

The near-constant low temperature across molecular clouds is an important feature of the star formation process because of its influence on the Jeans mass, and it is what makes possible the collapse of prestellar cloud cores with masses as small as one solar mass (Larson, 2003). The Jeans mass is the critical mass at which a cloud becomes unstable and starts to collapse, as it possesses insufficient pressure support to balance the force of gravity. It is given by the equation

$$M_J = \left(\frac{\pi k T}{\mu m_{\rm H} G}\right)^{3/2} \rho^{-1/2} = 18 {\rm M}_\odot \left(\frac{T}{10 \text{ K}}\right)^{3/2} \left(\frac{n_{\rm H}}{50 \text{ cm}^{-3}}\right)^{-1/2} \tag{1.1}$$

where ρ is the density and μ is the mean atomic mass per particle, which is usually taken to be 2.29 in a fully molecular cloud that is 25% Helium by mass and 10% by number (Jeans, 1928). In the absence of pressure or other support, gravitational collapse of such a cloud will occur in a free fall time,

$$t_{ff} = \left(\frac{3\pi}{32 G \rho}\right)^{3/2} = 3.4 \times 10^7 \left(\frac{n_{\rm H}}{50 \text{ cm}^{-3}}\right)^{-1/2} \text{ years} \tag{1.2}$$

(Spitzer, 1978). For a cloud with typical temperature $T = 10$ K and density $n_{\rm H} \geq 50$ cm^{-3}, the Jeans mass is $M_J \leq 80$ M$_\odot$ and the free fall time is calculated to be $t_{ff} \leq 5 \times 10^6$ years. This suggests that molecular clouds are highly unstable; if thermal pressure support was the only mechanism holding up molecular clouds then free fall collapse would lead to a galactic star formation rate of $\dot{M}_\star \geq 200$ M$_\odot$ yr^{-1}, which is far in excess of the observed galactic average of ~ 3 M$_\odot$ yr^{-1}.

Molecular clouds appear to have lifetimes of about $\sim 10^6$–10^7 years; longer lifetimes would imply that they cannot all be collapsing at free fall speeds (as this would give a much higher observed star formation rate) — in general, they must be supported by another mechanism (Zuckerman and Palmer, 1974; Evans, 1999; André et al., 2000; Ward-Thompson et al., 2007). Various alternatives to thermal pressure support of molecular clouds have been theorised: magnetic fields (e.g. Chandrasekhar and Fermi, 1953; Basu and Mouschovias, 1994; Adams and Shu, 2007), rotation (e.g. Field, 1978; Evans, 1999) and turbulence (e.g. Norman and Silk, 1980; Mac Low and Klessen, 2004; Ballesteros-Paredes et al., 2007). All of these likely contribute in some measure, with magnetic fields the most important — without magnetic fields it would be difficult to explain the generation of observed levels of rotation and turbulence in molecular clouds.

The interstellar medium is strongly magnetised, and magnetic fields are important to the dynamics and evolution of molecular clouds (McKee et al., 1993). The most useful measure of the magnetic field is the Zeeman effect, which measures the line-of-sight component of the field, as opposed to the Chandrasekhar-Fermi method which

measures the component of the field in the plane of the sky. The morphology of the field is measured from dust polarisation and the linear polarisation of spectral lines. The largest compilation of Zeeman measurements of the magnetic field strengths in molecular clouds was performed by Crutcher (1999), who found that the median value of the Alfvén Mach number across 27 clouds of varying mass was $\mathcal{M}_A \simeq 1$ (although the observations also found a median temperature of 40 K, which is much higher than the average temperature typically measured in molecular clouds). From this the median value of the magnetic field was calculated to be

$$B_{\rm med} \simeq 30 \left(\frac{n_{\rm H}}{10^3 \text{ cm}^{-3}} \right)^{1/2} \left(\frac{\sigma_{\rm nt}}{1 \text{ km s}^{-1}} \right) \mu\text{G} \tag{1.3}$$

where $n_{\rm H} \gtrsim 2 \times 10^3$ cm^{-3} and $\sigma_{\rm nt}$ is the non-thermal velocity dispersion of the cloud. $\sigma_{\rm nt}$ is used as a measure of the amount of turbulence in a volume, and is typically observed to be $\propto r^q$ on large scales, where $q \simeq 1/2$ (Goodman et al., 1998).

Crutcher (1999) also found that the observed molecular cloud clumps and cores were in approximate virial equilibrium, that is, that the kinetic and magnetic energies were in approximate equipartition; this implies that the gas motions must provide a significant component of the support of molecular clouds against gravity. The gas velocities, calculated by examining the Doppler-broadening of spectral linewidths, were found to be supersonic (by about a factor of five) and approximately equal to the Alfvén velocity, which suggests that the internal motions in the gas were likely the result of magnetohydrodynamic (MHD) waves.

The average ratio of thermal to magnetic pressures across the 15 cores for which such measurements were possible was found to be $\beta_{\rm mag} \approx 0.04$, where $\beta_{\rm mag} < 1$ implies that magnetic effects dominate thermal effects, showing that magnetic fields are therefore very important to the physics of molecular clouds (Crutcher, 1999). These observations (as well as the later ones by Crutcher and Troland, 2007; Crutcher et al., 2009) fit the relation $B \propto n_{\rm H}^{0.47}$, which is consistent with simulations of molecular clouds supported by the magnetic field, in particular ambipolar diffusion of the field (where the flux is frozen into the ions, which scale as $n_i \propto n_{\rm H}^{0.5}$; this process is described in more detail in Section 1.2). However, this scaling is also expected from simulations of turbulent motions that are constrained so that they are comparable to the Alfvén velocity (Bertoldi and McKee, 1992; Fiedler and Mouschovias, 1993; Evans, 1999).

MHD star formation theory holds that a self-gravitating cloud can be supported by a purely static field with no associated waves (see e.g. Stahler and Palla, 2004). Flux freezing within molecular clouds signifies both that the magnetic field is tied to the motion of the fluid and that the gas itself is constrained by the field configuration; magnetic field lines in cores have been indirectly observed to possess bent or hour-glass

shapes (Cortes and Crutcher, 2006). Many giant molecular cloud complexes possess a stratified appearance that could well indicate alignment along the large-scale ambient field, as could the prolate shapes of dense cores (Goodwin et al., 2002; McKee and Ostriker, 2007).

Rotation is a stabilising influence that raises the Jeans mass for a fixed temperature and background radiation rate, and it flattens numerical models of molecular clouds and cores if the rotational kinetic energy is an appreciable fraction of the gravitational potential energy. Molecular line observations such as those of Goodman et al. (1993), Kane and Clemens (1997) and Pirogov et al. (2003) have shown that a majority of dense molecular cloud cores present evidence of rotation. Lada et al. (2003) in particular found evidence for differential rotation in the B68 core, observing velocity gradients of 3.4 km s^{-1} pc^{-1} from $C^{18}O$ and 4.8 km s^{-1} pc^{-1} from N_2H^+ emission, which, as mentioned previously, trace the outer and inner regions of the core respectively.

The typical angular momentum of cores is small and characterised by the ratio of the rotational kinetic energy to the gravitational binding energy, which is given by

$$\beta_{\rm rot} = \frac{1}{3}\left(\frac{V_\phi^2}{GM/R}\right) \tag{1.4}$$

for a uniformly rotating sphere of constant density (Goodman et al., 1993). If $\beta_{\rm rot}$ is large the core is stable against gravitational instability and collapse, however, if $\beta_{\rm rot}$ is very small the core will never have enough rotational energy to support it against collapse and it cannot develop any instabilities that are driven by rotation, such as fragmentation. Goodman et al. (1993) found that the cores they studied all had $\beta_{\rm rot} \leq 0.18$, with a typical value of $\beta_{\rm rot} \sim 0.02$ on scales of 0.1 pc, confirming that rotation was not rapid enough to support the cores on its own. This low value of $\beta_{\rm rot}$ could inhibit binary formation mechanisms such as that caused by the rotation-induced fragmentation of molecular cloud cores, however as all rotating cores are expected to form centrifugal discs and discs may fragment to form a binary system this value is not regarded as problematic.

The role of turbulence in supporting molecular cloud cores against collapse is an increasing source of contention within the star formation community, as the supersonic motions observed in cores by Goodman et al. (1998), Crutcher (1999) and others could be formed by magnetohydrodynamical turbulence that is in rough equipartition with self-gravity in the core. MHD turbulence may be more important than ambipolar diffusion in triggering the formation and collapse of molecular cloud cores, as turbulent support decays quickly and speeds star formation, while stronger turbulence could cause cores to fragment and form multiple star systems. This scenario would suggest that star-forming clouds are transient and that star formation is a rapid process,

in direct contrast with the quasistatic slow process that is star formation driven by ambipolar diffusion (Mac Low and Klessen, 2004; Elmegreen, 2007; Ward-Thompson et al., 2007; Ballesteros-Paredes et al., 2007, and the references within these reviews; see also Section 1.3). Recent observations by Crutcher et al. (2009) were unable to prove which of these mechanisms of core support and collapse is truly dominant in molecular clouds; studies of the magnetic field strength and orientations in cores with better resolution and higher signal-to-noise ratios are required to determine between them (Mouschovias and Tassis, 2009).

Depending on the local environment of a molecular cloud, different model scenarios for the support and structure of clumps and cores may be relevant in different regions of the cloud. The effect of local density, pressure, temperature and magnetic field variations, as well as the presence or absence of other nearby stars and protostars, likely all contribute to determining which forces dominate the formation and evolution of dense molecular cloud cores (Ward-Thompson et al., 2007).

1.2 Magnetic Diffusion

Simulations of star formation have typically approximated the magnetic field behaviour by ideal magnetohydrodynamics (IMHD), where the mass-to-flux ratio is held constant and the magnetic field is regarded as being frozen into the neutral medium (e.g. Galli et al., 2006; Mellon and Li, 2008; Machida et al., 2008b). In this situation the magnetic field and the particles move together in the collapsing flow, however, this simplification only truly applies in the outermost regions of gravitational collapse where the density is low. If IMHD were to hold true throughout the collapse then the magnetic flux in the star would be 10^3–10^5 times larger than that observed in young stars (this is the "magnetic flux problem", described in more detail in Chandrasekhar and Fermi, 1953, and Section 1.5). A mechanism for allowing the field to move against the inward flow of the neutral particles is required to reduce the field in the protostar to observed values; at densities higher than those encountered at the edge of molecular cloud cores flux freezing breaks down, so that the magnetic field diffusion depends upon the coupling of the field to the charged particles and the drift of these against the neutral gas.

The diffusion of a magnetic field through a molecular cloud core is determined by the drift of charged particles through the dominant neutral component in response to the electric field in the neutral rest frame. When the gas is weakly ionised, the charged particle species develop a drift velocity with respect to the neutral fluid velocity. The Lorentz force (which only acts on the charged particles) is transmitted to the neutral gas through the drag forces caused by collisions between the neutral and charged particles (e.g. Königl and Salmeron, 2011). These collisions determine the efficiency of

the angular momentum transport by the field in weakly ionised gas, and the outwards diffusion of the magnetic field in a molecular cloud core, which erodes the magnetic support until the core becomes gravitationally unstable and undergoes collapse (Mestel and Spitzer, 1956).

The degree of coupling between charged species and the neutral gas is measured by the Hall parameter, β_j, the ratio of the gyrofrequency to the frequency of collisions between charged species j and the neutrals (where j are typically ions or electrons, denoted by i and e respectively). The Hall parameter measures the relative importance of the Lorentz and drag forces in balancing the electric force, and is defined by

$$\beta_j = \frac{|Z_j|eB}{m_j c}\frac{1}{\gamma_j \rho} \tag{1.5}$$

for a particle of mass m_j, charge $Z_j e$ and collision frequency $\gamma_j \rho$, where

$$\gamma_j \equiv \frac{<\sigma\nu>_j}{(m + m_j)}; \tag{1.6}$$

$<\sigma\nu>_j$ is the rate coefficient for collisional momentum transfer between the charged particles and neutrals of mass m.

The relative drifts of different charged species with respect to the neutral particles delineate three different magnetic diffusivity regimes (aside from IMHD):

- the *Ohmic (resistive) diffusion* limit, which dominates in high density regions where the ionisation fraction is low. The ions and the electrons frequently collide with the neutrals over the electron gyration period, and the magnetic field is decoupled from all charged particles. In this limit $\beta_i \ll \beta_e \ll 1$ and the ion and electron drifts are not affected by the presence of the magnetic field. Ohmic diffusion is thought to be important in the innermost regions of the protostellar

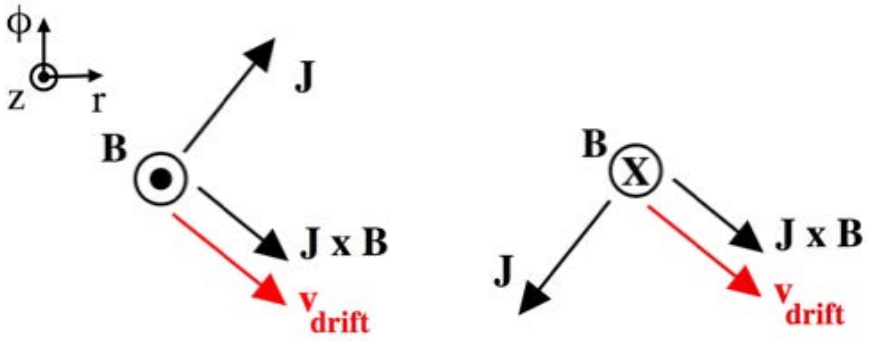

Figure 1.1: Vector diagram for ambipolar and Ohmic diffusion. When the orientation of the magnetic field is reversed, as in the second panel, the current **J** changes direction; however, $\mathbf{J} \times \mathbf{B}$, and the drift of the ions, electrons and the magnetic field through the neutral particles retain the same direction (from Wardle, 2009).

disc where the density and collisional rates are high (e.g. Shu et al., 2006; Machida et al., 2008a).

- the *ambipolar diffusion* limit, which dominates in regions of relatively low density where the fractional ionisation is high. In this limit $1 \ll \beta_i \ll \beta_e$ and the magnetic field is tied to the charged particles by electromagnetic stresses. The ionised component drifts with the field through the neutrals, redistributing the matter in the flux tubes. Ambipolar diffusion is dominant in molecular clouds (Wardle, 2007), in protostellar discs at radial distances beyond ~ 10 AU and close to the surface of these discs nearer to the protostar (Salmeron, 2009). It is the type of diffusion most commonly included in simulations of star formation that go beyond ideal MHD (e.g. Ciolek and Königl, 1998; Krasnopolsky and Königl, 2002; Adams and Shu, 2007; Mellon and Li, 2009, see also Section 1.3). In both the Ohmic and ambipolar diffusion limits, when the magnetic field is globally reversed the magnetic response of the disc is unchanged, as demonstrated in Figure 1.1.

- the *Hall diffusion* limit, which dominates in the intermediate regimes between ambipolar and Ohmic diffusion. In this limit $\beta_i \ll 1 \ll \beta_e$ and the charged species have a varied degree of coupling to the magnetic field, typically with the electrons tied to the magnetic field. The more massive particles such as ions and charged dust grains are decoupled from the magnetic field and are instead collisionally-coupled to the neutral gas. In the Hall regime, the magnetic response of the disc is no longer invariant under a global reversal of the magnetic field, as shown in Figure 1.2, and plane-polarised damped Alfvén waves do not exist (Wardle and Ng, 1999). Hall diffusion is expected to dominate in many regions of molecular clouds as they undergo gravitational collapse (Wardle, 2004a), and

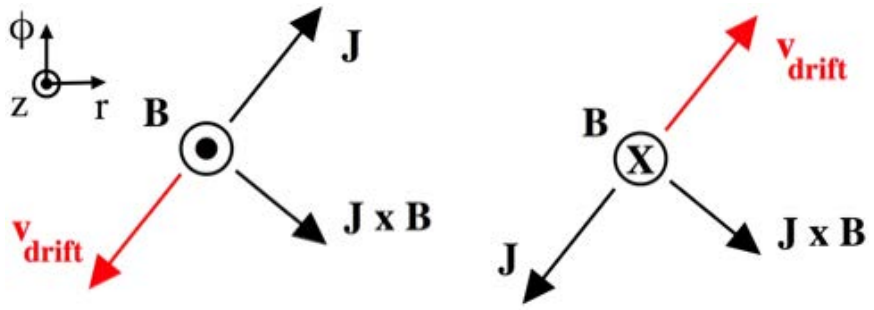

Figure 1.2: Vector diagram showing drift caused by Hall diffusion. Unlike in the ambipolar and Ohmic diffusion cases shown in Figure 1.1, when the field is reversed in the second panel, the direction of the drift of electrons and the magnetic field through the neutral particles and ions is also reversed. From Wardle (2009).

in protostellar discs (Sano and Stone, 2002a,b).

The degree of coupling between the magnetic field and the charged particles depends upon the fractional ionisation of the gas and the momentum transfer cross sections for collisions between the charged particles and the neutrals. In a weakly ionised gas, such as that encountered in molecular clouds, the abundances of charged species are so low that their inertia and thermal pressure are negligible. Typically in molecular clouds, molecular ionisation by cosmic rays is balanced by the rapid dissociative recombination of molecular ions with the metal ions that are the dominant positive charge carriers (Umebayashi and Nakano, 1990; Wardle and Ng, 1999).

For grains of radius $a = 0.1$ μm at a temperature of 10 K in a cloud with cosmic ray ionisation rate $\xi = 10^{-17}$ s^{-1}, the ion density is usually taken to scale as $\rho_i \propto \rho_n^{1/2}$ when $10^4 \lesssim n_{\rm H} \lesssim 10^7$ cm^{-3} (Elmegreen, 1979; Kamaya and Nishi, 2000). This behaviour is an oversimplification, as Ciolek and Mouschovias (1998) showed that for typical cloud and grain parameters the proportionality of the ion density cannot be parameterised by a single power law exponent k, as $k > 1/2$ for densities $n_{\rm H} \lesssim 10^5$ cm^{-3} and $k \ll 1/2$ for densities $n_{\rm H} \gg 10^5$ cm^{-3}, but it is still a reasonable and widely-adopted approximation to the ion density in collapsing cores on scales $\gtrsim 10^3$ AU (see e.g. Shu et al., 1987; Galli and Shu, 1993a; Ciolek and Königl, 1998; Contopoulos et al., 1998; Krasnopolsky and Königl, 2002). This shall be discussed further in Chapter 2.

Outside of the central ~ 0.1 AU of a protostellar system the ionisation of the gas is driven by stellar X-ray and UV radiation, as well as interstellar cosmic rays (Hayashi, 1981; Glassgold et al., 2005). At the higher densities found here and more generally in the inner regions of the collapsing core, grains are typically the dominant carriers of both positive and negative charge and their densities scale as $n_{\rm H}^{1/2}$ (Nishi et al., 1991; Tielens, 2005). In these innermost regions of protostellar systems, the fractional ionisation is low, as the high density leads to a very rapid recombination rate and the disc column density shields the gas from cosmic rays and X-rays.

The degree of the coupling between the material and the magnetic field depends also upon the abundance and size distribution of grains in the gas. As dust grains have large cross sections they typically become decoupled from the field at lower densities than other ions, reducing the diffusivity of the gas. If grains are important and decoupled from the field then Ohmic diffusion dominates, however if the grains have settled or aggregated then Hall diffusion is important. In molecular clouds that are not overdense, the ions and electrons are tied to the field while large grains are not, so that ambipolar diffusion dominates the magnetic field behaviour (Wardle, 2007).

The regions of parameter space in which each of the three types of coupling are dominant in a weakly ionised three-component plasma are shown on a simplified log B-

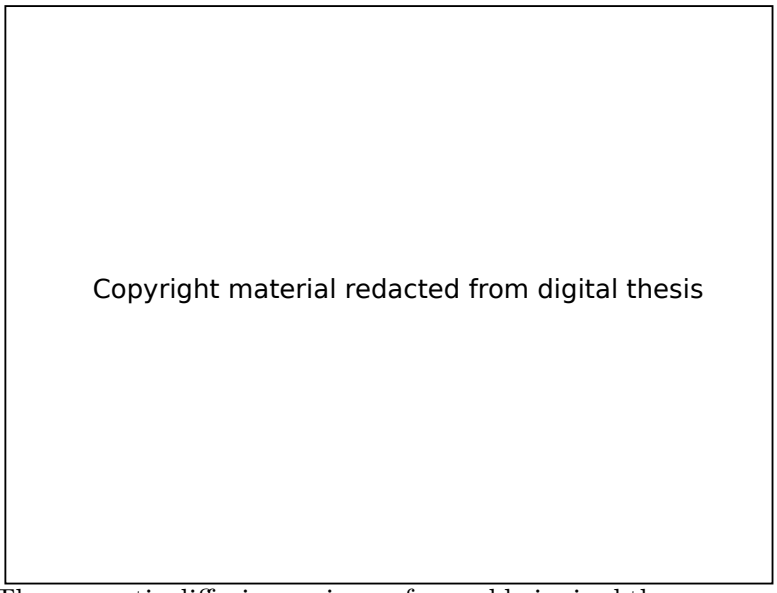

Figure 1.3: The magnetic diffusion regimes of a weakly ionised three-component plasma are determined by the ion and electron Hall parameters β_i and β_e, which are proportional to $B/n_{\rm H}$, with β_e/β_i typically ~ 1000 (from Wardle, 2007).

$\log n_{\rm H}$ plane in Figure 1.3 (from Wardle, 2007). It is clear from the figure that Ohmic diffusion dominates at high densities with weak fields, while the opposite is true for ambipolar diffusion. The intermediate region of parameter space between these two limits is dominated by Hall diffusion. In particular, the Hall term is significant for molecular gas densities in the range $\sim 10^8$–10^{11} cm^{-3} (when B scales as $B \propto n_{\rm H}^{1/4}$), although the presence and particular distribution of grains complicates the calculation of the diffusivities (Wardle and Ng, 1999).

The nature of the coupling (ambipolar, Hall, Ohmic) determines the magnetic field direction as the field lines emerge from the surface of the protostellar disc. This in turn controls the amount of material that is able to slide along the field lines and be flung outwards from the surface instead of being accreted in disc-driven wind models (Wardle and Königl, 1993; Wardle, 2004b).

It was noted by Norman and Heyvaerts (1985) that the Hall component of the conductivity tensor could be important in cloud regions where the neutral density and the temperature are weakly variable. They dismissed the effects of the Hall term in their discussion of the resistivity of molecular clouds, arguing that the Hall current leads to a charge separation that generates an electrostatic field which modifies the direction of the total field until the Hall current vanishes.

However, this logic does not hold in situations where the boundaries are not idealised, and Wardle and Ng (1999) countered this argument using the specific example of the quasistatic collapse of an axisymmetric cloud core through a poloidal magnetic

field. In their example the current is toroidal and the electric field in the neutral fluid frame is poloidal so that if the Hall and ambipolar diffusion components of the conductivity are of the same order then the toroidal components of the velocity and magnetic field will both contribute to the gravitational support of the core. For this simple model, the boundaries on which Norman and Heyvaerts (1985) presumed that the charge would build up would be surfaces of constant azimuth, which cannot exist under axisymmetry.

More generally, it is not possible in MHD to build up charged surfaces such as those proposed by Norman and Heyvaerts (1985), as typically $E \sim \frac{V}{c}B$. As the gas velocities in molecular clouds are very low compared to the speed of light (typically around 0.1–10 km s^{-1}; see Section 1.1 and Crutcher, 1999; Lee et al., 2001) then $E \ll B$ and the effects of charge separation are negligible compared to the magnetic field effects. As the current $\mathbf{J} \propto \nabla \times \mathbf{B}$ in MHD then $\nabla \cdot \mathbf{J} = 0$, and the Hall current cannot cause a build up of charge that would generate an electrostatic field. The argument that electrostatic fields would negate the Hall current cannot then be used to dismiss the Hall effect in collapse calculations, and it will be shown to be important to the infall dynamics.

The magnitude and type of coupling that occurs between the fluid and magnetic fields in molecular clouds and protostellar discs is uncertain due to the difficulty in obtaining detailed observations in these regions, particularly of the magnetic field. Calculations of the ionisation equilibrium and resistivity by Wardle (2004a) suggested that the Hall diffusion term is important and may dominate the magnetic field diffusion at many of the densities and field strengths encountered in molecular clouds and protostellar discs, and presumably also during the collapse stages between these two evolutionary phases. Further calculations of the resistivity in protoplanetary discs by Wardle (2007) showed that Hall diffusion dominates in the innermost regions of protoplanetary discs. The Hall effect also imparts an implicit handedness to the fluid dynamics (as illustrated in Figure 1.2) that is sensitive to a global reversal of the magnetic field direction and could be important in calculations of gravitational collapse and protostellar disc formation (Wardle, 2007).

As will be discussed in the following sections, in those simulations of star formation that take a more sophisticated approach to the magnetic field diffusion than adopting the IMHD approximation, the breakdown of flux freezing in molecular clouds and protostellar discs is usually approximated by either ambipolar diffusion in simulations of the early stages of collapse where the density is low or Ohmic diffusion in the higher density late stages of protostellar disc evolution. In most numerical or semianalytic simulations of star formation the Hall diffusion term is dismissed as insignificant, using the same arguments as Norman and Heyvaerts (1985); however, the consequences of

including Hall diffusion in calculations of star formation by quasistatic gravitational collapse and of the subsequent evolution of protostellar discs are likely to be profound, in a similar manner to that found for the magnetorotational instability (the MRI; Wardle, 1999; Sano and Stone, 2002a,b).

The coupling between the field and the charged particles determines the dynamics of the collapse and can help resolve the angular momentum and magnetic flux problems of star formation, in which young stars have rotation rates and field strengths much smaller than their equivalent mass in a molecular cloud (Chandrasekhar and Fermi, 1953; Mestel and Spitzer, 1956; Spitzer, 1978). These problems are discussed in more detail in Sections 1.4 and 1.5; while the relevance of Hall diffusion in simulations of gravitational collapse, and its ability to enhance or mitigate the magnetic braking catastrophe (which prevents disc formation), are explored further in Section 1.6.

1.3 Gravitational Collapse

Low-mass star formation by the gravitational collapse of molecular clouds takes place in stages over many orders of magnitude in size and density as illustrated in Figure 1.4 (adapted from figure 7 of Shu et al., 1987 and figure 2 of Greene, 2001). Firstly, cores form within the cloud as a result of turbulent fluctuations, and they gradually contract as ambipolar diffusion erodes the magnetic support (Figure 1.4 a, b; Tasker and Tan, 2009; Federrath et al., 2010). Turbulence may also support the core against collapse, and its decay can aid the magnetic diffusion in triggering star formation (Mac Low and Klessen, 2004; Ballesteros-Paredes et al., 2007).

The core becomes gravitationally unstable and collapses dynamically into what is termed a "pseudodisc" (Galli and Shu, 1993a,b), which has a flattened shape due to the material falling in preferentially along the magnetic field lines that support it against collapse in the radial direction. A protostar arises at the centre of the pseudodisc, which may be surrounded by a centrifugally-supported protostellar disc (Terebey et al., 1984; Shu et al., 1987). Material collapsing from the envelope onto the protostar must pass through the pseudodisc and protostellar disc, building up material and flux at the boundaries of these that take the form of shock fronts as the dynamically-infalling gas collides with the slower-moving disc material. A disc wind or jet may form, launched from the inner regions of the collapse (Figure 1.4 c; Wardle and Königl, 1993; Tomisaka, 2002; Allen et al., 2003a).

When the density becomes larger than $\simeq 10^{10}$ cm^{-3} the gas becomes optically thick and the thermal structure of the collapsing core is nearly adiabatic, forming a thermally supported inner core (the "first" or "opaque" core; e.g. Larson, 1969; Machida et al., 2007) which collapses dynamically into the protostar (the "second

core"; Larson, 1969; Machida et al., 2006). Eventually the remainders of the collapsing envelope and pseudodisc are accreted or dissipated by the wind, and the protostar becomes visible at optical wavelengths as a T Tauri star with associated protoplanetary disc and outflow (Figure 1.4 d; Norman and Silk, 1980; Kitamura et al., 2002; Andrews and Williams, 2007; Dullemond and Monnier, 2010). The system continues to contract, and planets may accrete from or fragment the disc around the pre-main sequence star. Gaps begin to appear in the protoplanetary disc as the planets sweep up the gas, and the system is visible as a protostar with debris disc (Figure 1.4 e; Blum and Wurm, 2008; Wyatt, 2008). Finally, the star joins the main sequence and the stellar wind dissipates the remainder of the protoplanetary disc, leaving behind a young stellar system (Figure 1.4 f; Terebey et al., 1984; Ward-Thompson, 2002).

It is impossible to cover all of the work that has been done both observationally and in theoretical simulations of star formation in the space available here. Instead, this section shall focus primarily on the isothermal collapse of a molecular cloud core to an adiabatic protostar, potentially surrounded by a centrifugally-supported disc (Figure 1.4 b–c) for low-mass molecular cloud cores. For further information on the other stages of star formation, the evolution and dynamics of protostellar discs, or the processes involved in the formation of higher-mass stars such as fragmentation and turbulence, the reader is directed to the review of Stahler and Palla (2004) for a basic overview and the more detailed reviews by Larson (2003), McKee and Ostriker (2007) and Machida (2011) for a more complete description.

1.3.1 Core formation and support

Molecular clouds are transient objects, with irregular structures and internal motions that suggest they are dynamic and rapidly changing (di Francesco et al., 2007). They are likely formed by compressive motions of gravitational or turbulent origin (or some combination of the two). Giant molecular clouds are believed to be formed by gravitational instability (Tasker and Tan, 2009), or the agglomeration of smaller clouds (Dobbs, 2008); and they are concentrated towards the spiral arms of galaxies (Stark and Lee, 2006). Smaller molecular clouds can be formed by ram pressure from supersonic flows such as those driven by supernova blast waves and the MRI in galaxies (Norman and Silk, 1980; Ballesteros-Paredes et al., 2007, and the references therein).

Molecular cloud cores are the gravitationally-bound regions of higher density within molecular clouds that are the progenitors of protostars. There are currently two competing models for the formation of molecular cloud cores which are most likely extremes on the continuum of collapse models. The first is a slow, quasistatic core formation in which a dense region of the molecular cloud becomes centrally-condensed by an

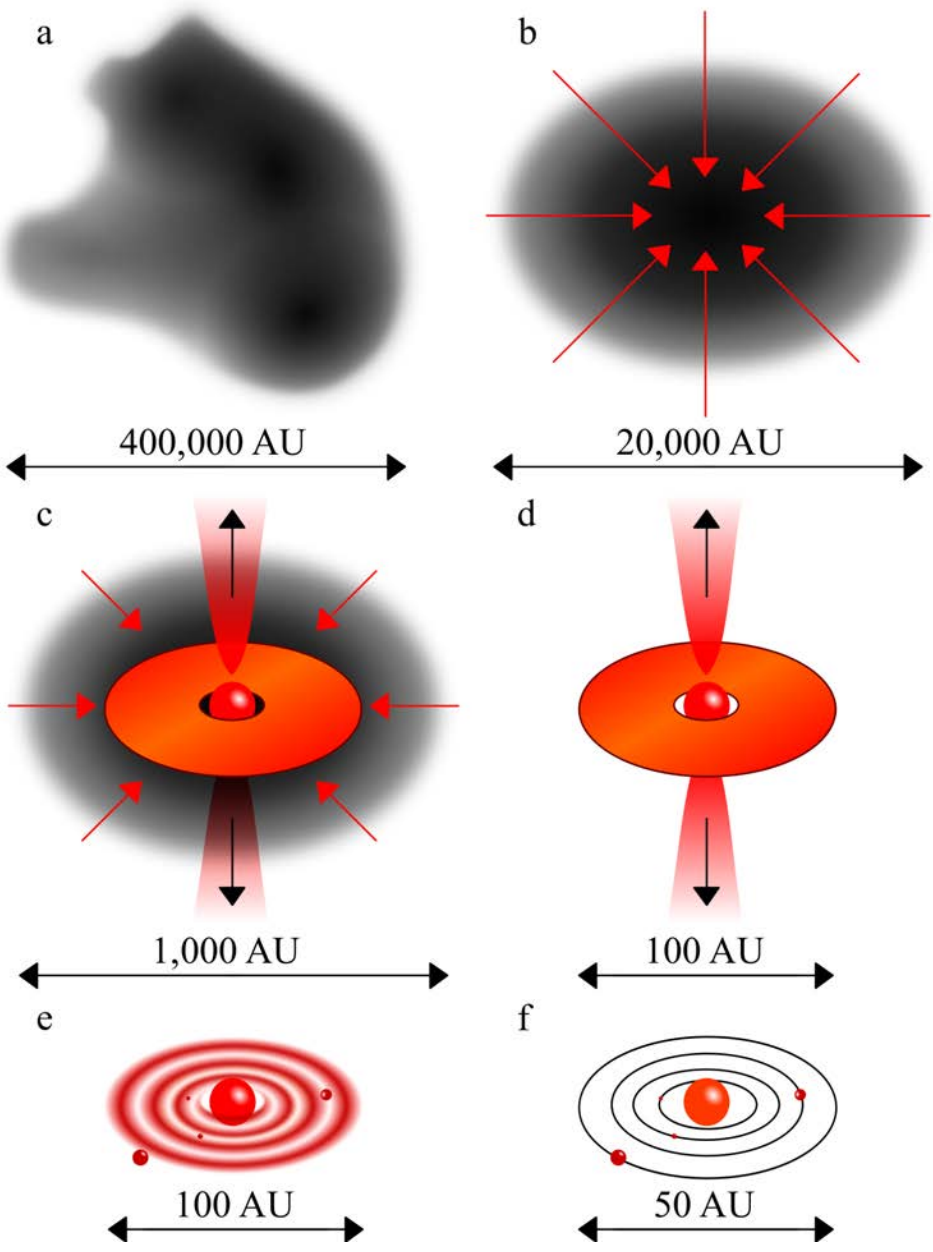

Figure 1.4: Developmental stages and scales of low-mass star formation (adapted from figure 7 of Shu et al., 1987 and figure 2 of Greene, 2001). (a) Star formation begins when cores form as magnetic and turbulent support in molecular clouds is lost through ambipolar diffusion. (b) A core becomes unstable and collapses dynamically into a pseudodisc. (c) As centrifugal forces balance gravitational forces, a protostar and disc form from the collapsing envelope, and a disc wind or jet may start. (d) The envelope dissipates or is accreted and the protostar becomes visible at optical wavelengths as a T Tauri star, with associated outflow and protoplanetary disc. (e) The protoplanetary disc starts to form planets and may be visible as a debris disc, while the pre-main sequence star continues to contract. (f) Nuclear fusion begins and the star joins the main sequence, and stellar winds blow away the remainders of the disc.

ambipolar diffusion-driven phase of collapse (e.g. Shu et al., 1987; Basu and Ciolek, 2004) or by the gradual dissipation of low-level turbulent fields (e.g. Myers, 1999). At the other extreme is a more dynamic formation process in which highly turbulent flows create large scale fluctuations and inhomogeneities in the gas of the molecular cloud, some of which become gravitationally unstable and collapse to form stars, with MHD waves carrying away any excess turbulent energy. This behaviour has yet to be seen in simulations of nonmagnetic molecular clouds, however the models of Tasker and Tan (2009) and Federrath et al. (2010) both demonstrated gravitational instabilities in nonmagnetic clouds, and gravitational instabilities have been observed in simulations of large isolated cores and small clouds with a few magnetic cores (e.g. Basu and Ciolek, 2004; Price and Bate, 2007).

Observations of isolated cores show that mild turbulence and magnetic fields play an approximately equal role in the evolution of molecular cloud cores (Crutcher, 1999), while observations of protoclusters and molecular cloud clumps show supersonic infall velocities that require strong external compression and are inconsistent with self-initiated forms of collapse (di Francesco et al., 2001; Ward-Thompson et al., 2007, and the references therein). These suggest that each of the core formation models may be valid under differing circumstances, with the turbulence-driven model applying to cluster-forming clumps and the ambipolar diffusion model to isolated low-mass star forming cores.

Assuming that the ionisation rate in a core scales with density as

$$\rho_i = C_i \rho_n^{1/2}, \tag{1.7}$$

where C_i is the numerical coefficient of the ionisation with typical value $C_i = 3 \times 10^{-16}$ $\mathrm{cm}^{-3/2}$ $\mathrm{g}^{1/2}$ (Elmegreen, 1979), the ratio of the ambipolar diffusion time scale to the time scale for dynamical collapse is approximately given by

$$\frac{t_{AD}}{t_{dyn}} \sim \frac{\gamma_i C_i}{2\sqrt{2\pi G}}. \tag{1.8}$$

For a typical value of the ion-neutral drag coefficient $\gamma_i = 3.5 \times 10^{13}$ cm^3 g^{-1} s^{-1} (Draine et al., 1983), this ratio is evaluated as $t_{AD}/t_{dyn} \approx 8$, demonstrating that ambipolar diffusion takes place at a relatively slow rate until the density is sufficiently high that the ionisation fraction begins to depart from the relationship described in Equation 1.7 (Ciolek and Mouschovias, 1998). As ambipolar diffusion is a slow process, once the magnetic support of the core has been eroded, the core will undergo rapid dynamic collapse and form a protostar before the more gradual contraction under ambipolar diffusion could cause a protostar to appear at the origin.

Star formation is an inefficient process (Evans, 1999) and the ratio of the ambipolar diffusion to dynamical time scales in Equation 1.8 provides an explanation for this,

as a slow rate of contraction caused by ambipolar diffusion could see many cores dissipating before they have the chance to form stars (Shu et al., 1987). On the other hand, numerical simulations by Clark and Bonnell (2004) showed that clouds with large turbulent motions also result in low star formation efficiencies as the bulk of the cloud escapes due to the initial supersonic motion. Both of the dominant theoretical mechanisms for star formation (ambipolar diffusion and turbulence) could then be responsible for the observed low rate of star formation.

Molecular cloud cores are supported against gravitational collapse by the magnetic field as long as the core is thermally and magnetically "subcritical", that is, the mass-to-flux ratio is less than the critical value,

$$\left(\frac{M}{\Phi}\right)_{crit} = \frac{C_\Phi}{G^{1/2}} \tag{1.9}$$

where Φ is the magnetic flux threading the cloud and C_Φ is a dimensionless (in cgs units) numerical coefficient that depends upon the internal distribution of the magnetic field and density (McKee et al., 1993). Discs with only thermal support along the field lines have $C_\Phi \approx 0.126$ (Mouschovias and Spitzer, 1976); an infinite cold sheet has $C_\Phi = 1/2\pi \simeq 0.16$ (Nakano and Nakamura, 1978), and simulations of cold clouds with different distributions of a poloidal field require $C_\Phi \simeq 0.17$–0.18 for the central flux tube to be critical (Tomisaka et al., 1988b).

Taking a value of $C_\Phi = 0.12$, Crutcher (1999) found that the mass-to-flux ratio in their observed molecular cloud cores was typically twice the critical value, suggesting that static magnetic fields are insufficient to support molecular cloud cores against gravity on their own. They also found that cores were in near-virial balance, which was used as evidence to suggest that the cores were supported by turbulence and that it is the decay of such turbulence that triggers collapse (Myers, 1999). Simulations have shown that for cores that are close to the critical value the dynamical and ambipolar diffusion time scales are comparable (Li and Nakamura, 2004; Klessen et al., 2011). It is likely to be the case that both the decay of turbulence and the loss of magnetic support in cores are important in initiating dynamic collapse, although only magnetic support is considered in this work.

Magnetic braking, by which the torque exerted on the rotating gas by the twisting of magnetic field lines transports angular momentum from the collapsing core to the molecular cloud, is very effective during this phase of molecular cloud core contraction. This process reduces the angular momentum of cores to the low values observed (Contopoulos et al., 1998), helping to resolve the traditional angular momentum problem of star formation in which young stars have less angular momentum than the initial core from which they formed during this early, isothermal phase of collapse (see Sections 1.4 and 1.5 and the references therein).

1.3.2 Dynamic collapse

Once ambipolar diffusion has caused enough of the neutral material to move inwards with respect to the magnetic field, the mass-to-flux ratio exceeds the critical value defined in Equation 1.9. The core is then said to be "supercritical" and the central density of the molecular cloud core formally tries to achieve infinite values. It contracts dynamically to form a protostar surrounded by a slowly-rotating pseudodisc, while the envelope remains magnetically subcritical. The ambipolar diffusion time scale remains relevant to the evolution of the core envelope so long as it is subcritical.

During this contraction, the field is effectively frozen into the cloud as IMHD holds true, and the infalling material is deflected by the field lines towards the equatorial plane, creating a pseudodisc that is not rotationally-supported. The pseudodisc contracts dynamically in the radial direction, dragging the field lines into a split monopole configuration (Galli and Shu, 1993a,b). The resulting build up in magnetic pressure acts as an impediment to further collapse, however, the magnetic tension in the envelope never suffices to suspend the envelope against the gravity of the growing protostar (Allen et al., 2003b,a).

Disregarding the effects of rotation and the magnetic field on the core for the moment, a slowly contracting molecular cloud core that is not artificially separated from its surroundings will tend to acquire the density distribution of a singular isothermal sphere,

$$\rho = \frac{c_s^2}{2\pi G r^2}\,, \tag{1.10}$$

where c_s is the isothermal sound speed (Larson, 1969; Shu et al., 1987). There are two limiting cases to the gravitational collapse of a singular isothermal sphere. The first is that presented in the solutions of Larson (1969) and Penston (1969), in which the collapse begins near the outer radius of a marginally unstable core and the r^{-2} density gradient is created as the wave of collapse propagates inward, leaving every scale marginally unstable as the collapse accelerates. At the time when the protostar first forms the collapse is highly dynamic with an infall speed of $3.3c_s$, and the accretion rate onto the star is high.

The second case is that of Shu (1977), in which the evolution of the core is much slower and the infall velocity at the moment of protostar formation is negligible. The collapse is initiated in the centre of the core, and the "expansion wave", the point at which gas begins to fall inward, propagates outward at the sound speed. This process is referred to as "inside-out collapse" and inside of this rarefaction wave the gas accelerates until it is nearly free falling onto the protostar.

These solutions are referred to as examples of "self-similar" or scale-invariant collapse, as the properties of the collapsing core are similar (in the mathematical sense)

to those properties at an earlier period of time at smaller radii (self-similarity is a typical property of fractals). The self-similar collapse models represent a semianalytic method of exploring collapse at higher resolution than is possible in numerical calculations, which are limited by either the number of particles or the scaling of the box in which the collapse takes place. Although they require many assumptions and simplifications to the gas dynamics (see Chapter 2 for more information on the formulation of a self-similar model), the calculation of similarity solutions is a useful analytic technique for studying star formation. Self-similar behaviour is often observed in numerical simulations of collapse (e.g. Masunaga and Inutsuka, 2000; Tomisaka, 2002; Mellon and Li, 2009; Dapp and Basu, 2010, and others); yet similarity solutions can follow the collapse to regions of high density close to the protostar, including inside the boundary of the sink cells that are often used to represent the inner point mass in numerical calculations.

The evolution of star-forming molecular clouds has been studied through numerical simulations, primarily of the ambipolar diffusion-initiated formation of supercritical cores and the early stages of dynamical collapse (e.g. Machida et al., 2008a; Kunz and Mouschovias, 2009, 2010). These numerical simulations of collapse tend towards the similarity solutions during the dynamical collapse stage despite being started with different initial conditions in the core (e.g. Tomisaka, 2002; Mellon and Li, 2008, 2009; Federrath et al., 2010), even though collapsing flows may never actually approach the similarity solutions in reality.

The Larson–Penston and Shu similarity solutions represent extreme cases of the continuum of nonmagnetic, nonrotating solutions ("fast" and "slow" collapse), and their applicability is determined by the initial conditions chosen to describe the core. The more general family of nonmagnetic, nonrotating self-similar gravitational collapse solutions were explored by Whitworth and Summers (1985); the outer density profile in this type of solution is $\propto r^{-2}$ whereas in the innermost regions near the central singularity the density is $\propto r^{-3/2}$.

The similarity solutions have been duplicated by numerical simulations: for example, Federrath et al. (2010) were able to reproduce the density gradients and mass accretion rates of the isothermal sphere modelled by Shu (1977) in their calculations of cluster formation. This was achieved using sink particles in their hydrodynamic simulations to represent the central point masses which are notoriously difficult to model otherwise due to their high concentration of mass in a small region of the calculation grid. The simulations of Tomisaka (2002) and Mellon and Li (2008, 2009) also demonstrated self-similarity in their collapsing flows for single cores; this behaviour is regarded as an important test of the models.

These early similarity solutions did not include the effects of rotation and magnetic

fields on the core, nor did they include turbulence, which becomes more important as the core mass increases. It is the addition of a magnetic field that leads to the formation of a pseudodisc (Galli and Shu, 1993a,b), while rotation may lead to the formation and growth of a rotationally-supported disc at the centre of the pseudodisc (Terebey et al., 1984).

In rotating collapse simulations the conservation of angular momentum during the near-free fall dynamical collapse results in a progressive increase in the centrifugal force that eventually becomes important and creates a centrifugal barrier to collapse, forming a rotationally-supported disc around the central protostar. If the centrifugal force becomes strong enough it may trigger the fragmentation of the contracting core and cause the formation of a binary or multiple star system (e.g. the solutions of Ward-Thompson, 2002; Clark and Bonnell, 2006; Kudoh et al., 2007; Price and Bate, 2007; Machida et al., 2008b; Klessen et al., 2011; André et al., 2009).

Early similarity solutions that included rotation showed that it causes a centrally-condensed disc to form around the protostar, disrupting the near-spherical dynamic collapse. For the singular isothermal sphere, most of the collapsing envelope settles into a centrifugally-supported disc around the protostar (Terebey et al., 1984; Shu et al., 1987). Numerical simulations by Matsumoto et al. (1997) showed that the behaviour of collapsing cores with rotation approached that of analytic self-similar models of a singular isothermal disc (e.g. Hayashi et al., 1982; Toomre, 1982), or a rotationally-flattened (due to the conservation of angular momentum) fast isothermal collapse (Saigo and Hanawa, 1998). This same self-similar behaviour is seen in numerical simulations with rotation and magnetic fields (e.g. Machida et al., 2008a; Mellon and Li, 2009, and the references in Section 1.5).

When a magnetic field (aligned with the axis of rotation) is present during the dynamic collapse phase, the protostar develops in a nearly self-similar way. The collapse propagates as a fast MHD wave, travelling faster in the direction perpendicular to the field, creating a prolate shape immediately inside the head of the expansion wave. Further inside the collapsing core, the tangential component of the Lorentz force produced by the curvature of the magnetic field lines deflects the gas towards the equatorial plane, forming an oblate pseudodisc of flattened infalling material (Galli and Shu, 1993a,b). The magnetic field of the core takes on a characteristic hourglass shape in which the field lines flare above and below the pseudodisc (also called a split monopole) that is consistent with observations (Cortes and Crutcher, 2006; Girart et al., 2006; Gonçalves et al., 2008; Attard et al., 2009).

Calculations of magnetic collapse that continued through to the stage of accretion by a central point mass, such as those by Ciolek and Mouschovias (1993, 1994, 1995), Ciolek and Königl (1998), and Mellon and Li (2009), showed that ambipolar diffusion,

which is unimportant during the dynamic collapse phase, is revitalised once a protostar starts to grow in the centre of the core. This leads to a decoupling of the magnetic flux from the inflowing gas, which takes place within an outwardly-propagating magnetohydrodynamic shock, the existence of which was first proposed by Li and McKee (1996). This MHD shock (referred to as the magnetic diffusion shock in the results presented in this work) takes the form of a continuous transition in the calculations of Desch and Mouschovias (2001) and Krasnopolsky and Königl (2002) because the shock structure depends upon ambipolar diffusion, which is explicitly determined in their equations. Inwards of the shock the magnetic braking reduces the angular momentum, and ambipolar diffusion reduces the magnetic flux as the neutral material continues to fall inward at a near-free fall speed. The centrifugal force starts to become important, gradually triggering the formation of a hydrodynamic shock that strongly decelerates the infalling matter and allows a Keplerian disc to form.

Accretion through the pseudodisc to the free fall region and inner disc may occur in bursts, as mass piled up at the magnetic barriers opposes rapid accretion. As the split monopole field inside of the pseudodisc grows, mass builds at the boundary of the disc until it becomes too heavy to be supported. The excess mass rushes inside towards the origin, dragging in more flux to be assimilated by the split monopole; the magnetic barrier grows and mass must then build up over a longer time interval before overcoming the barrier and becoming part of the protostar. These oscillations first appeared in the numerical simulations of Allen et al. (2003a,b) as a result of instabilities that were caused by the simplified physics in their simulations, however they were later reproduced in the "magnetic wall" that inhibits collapse in the calculations of Tassis and Mouschovias (2005a,b), and in the magnetogyrosphere of Mellon and Li (2008, 2009). Allen et al. (2003b) suggested that this magnetic behaviour may be responsible for observed FU Orionis outbursts that are not well-explained at present.

1.3.3 Late stages of collapse

Once the central density reaches $n_{\rm H} \gtrsim 10^{10}$ cm^{-3} the assumption of isothermality breaks down as the gas becomes optically thick against the thermal radiation from dust grains. The gas becomes adiabatic, and once it is hot enough to dissociate molecular hydrogen, the protostar undergoes a second dynamic collapse (Tomisaka, 2002; Machida et al., 2007, 2008a). At $n_{\rm H} \gtrsim 10^{12}$ cm^{-3} the magnetic field is effectively decoupled from the gas and Ohmic diffusion becomes dominant (Nakano et al., 2002). This expected behaviour was not seen in the numerical simulations of Desch and Mouschovias (2001) where the gas decoupled from the field before the breakdown of isothermality. During the decoupling stage in their simulations the electrons were

very well attached to the magnetic field instead of the expected ions; the ions had detached from the field at lower densities. Desch and Mouschovias (2001) found that Ohmic dissipation was unimportant during the decoupling stage because of the high electron mobility and the small $e-H_2$ cross section, although it does become important in the innermost regions of the adiabatic core and protostellar disc where the density is particularly high (e.g. Dapp and Basu, 2010; Machida, 2011).

Accretion onto the adiabatic core and protostar may be stopped by hydrodynamic, magnetohydrodynamic and photoevaporative processes. Because of the ubiquity of bipolar outflows in star forming regions, Terebey et al. (1984) implicated young stellar object (YSO) winds and jets as the dominant practical mechanisms by which forming stars define their own masses, particularly in isolated regions of low-mass star formation. It is believed that YSO outflows arise because of a fundamental interaction between the rapid rotation in a Keplerian disc and a strongly magnetised object such as a protostar (e.g. Ghosh and Lamb, 1979a; Blandford and Payne, 1982; Wardle and Königl, 1993).

The collapsing pseudodisc, protostellar disc and adiabatic core can lose angular momentum and collapse further when the magnetic field threading the collapsing material is able to generate an outflow. Many numerical simulations have now demonstrated that both fast and slow jets and winds can be generated from the thin disc both before and after the formation of the adiabatic core (for example, the simulations of Tomisaka, 2002; Allen et al., 2003a; Machida et al., 2007, 2008a,b; Mellon and Li, 2008, 2009; Bate, 2010; Ciardi and Hennebelle, 2010). The weakly ionised gas in the rotating collapsing flow induces a toroidal field that is able to accelerate the gas and form an outflow, the intensity of which depends upon the rotation rate and field strength. Krasnopolsky and Königl (2002) were able to demonstrate how a disc wind could be included into their semianalytic solutions by including a mass loss term in their asymptotic inner disc solutions (which satisfy the conditions necessary for wind launching), however at present this work has yet to be performed (see Wardle and Königl, 1993, and Section 6.3 for further details).

Studies of three-dimensional radiation hydrodynamical calculations have shown that the formation of the stellar core drives a shock wave through the disc, and dramatically decreases the accretion rate onto the stellar core (Bate, 2010) — this behaviour was also present in earlier one-dimensional simulations of radiative, hydrodynamical collapse of molecular cloud cores (e.g. Masunaga and Inutsuka, 2000). Radiation produced in the first stars in a molecular cloud reduces the ability of cores to fragment, which can suppress formation of low mass objects by increasing the temperature in the high density material (Krumholz and McKee, 2008; Price and Bate, 2009; Krumholz, 2011; Kunz and Mouschovias, 2009, 2010). Numerical simulations of molecular clouds

Object	J/M (cm^2 s^{-1})
Molecular cloud (scale 1 pc)	10^{23}
Molecular cloud core (scale 0.1 pc)	10^{21}
Binary (10^4 yr period)	4×10^{20}–10^{21}
Binary (10 yr period)	4×10^{19}–10^{20}
Binary (3 day period)	4×10^{18}–10^{19}
100 AU disc (1 $M_\odot$ central star)	4.5×10^{20}
Jupiter (orbit)	10^{20}
T Tauri star (spin)	5×10^{17}
Present Sun	10^{15}

Table 1.2: Characteristic values of the specific angular momentum for molecular clouds, cores, binaries, discs, and stars, indicating the many orders of magnitude difference between the initial cloud and the present day Sun (Bodenheimer, 1995).

with strong (though supercritical) magnetic fields and radiative feedback demonstrate an inefficient star formation process with a star formation rate that approaches the observed rate in molecular clouds (Price and Bate, 2009).

1.4 Rotation and the Angular Momentum Problem

One of the classic problems of star formation is the requirement that nearly all of the initial angular momentum of the molecular cloud core must be removed or redistributed during the formation process. Stars typically have far less angular momentum than the equivalent mass in the interstellar medium; even molecular cloud cores rotate much more slowly than would be expected if they had condensed from the diffuse interstellar medium with no loss of angular momentum (e.g. Goodman et al., 1993). Table 1.2 lists characteristic values of the angular momentum for many of the stages of star formation and evolution to illustrate this point.

The basic angular momentum problem is well illustrated by the example presented in Spitzer (1978): as an extreme case, consider a filamentary interstellar cloud in the form of a cylinder with length 10 pc and a radius 0.2 pc, rotating around its long axis at the galactic value of angular velocity $\Omega = 10^{-15}$ s^{-1}. This cloud will have a mass of about 1 $M_\odot$ when the number density is $n_{\rm H} = 20$ cm^{-3}. The rotational effects will not impede collapse parallel to the long axis, but in order to form a star of solar density the radius must decrease by a factor of about 10^{-7}, while the conservation of angular momentum requires that Ω must increase by 10^{14}. The resulting rotation period would then be roughly a minute, with the rotational velocity of the star becoming 20% of the speed of light, and the centrifugal force exceeds gravity at the equator by four orders of magnitude.

While this is a simplified example, the argument demonstrates the problem well. In Table 1.2 the discrepancy between the specific angular momentum of a T Tauri star (10^{17} cm^2 s^{-1}) and that of a molecular cloud core on the scale of 0.1 pc (10^{21} cm^2 s^{-1}) is shown to be around four orders of magnitude. The angular momentum problem is also highlighted by observations that show many young stars are rotating slowly in comparison to molecular clouds (e.g. Goodman et al., 1993; di Francesco et al., 2001; Lada et al., 2003; di Francesco et al., 2007). It is possible that young stars could be braked after formation by such mechanisms as stellar winds or interactions between the magnetic field of the star and the protoplanetary disc (e.g. Ghosh and Lamb, 1979a; Königl, 1991; Matt and Pudritz, 2008), but some braking must occur earlier to allow the protostar and disc to form.

Magnetic forces, gravitational forces and pressure forces may all play a role in transporting angular momentum in star forming clouds. As outlined in Section 1.1, the magnetic forces can exceed thermal forces in molecular clouds and cores, and magnetic braking can remove much of the initial angular momentum from a large scale cloud and determine the amount of angular momentum remaining in the dense core (Basu and Mouschovias, 1994, 1995a,b). The basic process of magnetic braking is that the torque exerted on the rotating fluid by the twisting of magnetic field lines causes the vertical propagation of Alfvén waves. These waves carry angular momentum from the cloud to material external to the cloud, in a manner first described by Mestel and Spitzer (1956) and numerically calculated by Mouschovias and Paleologou (1979, 1980). This braking of the rotational motions by the magnetic field is believed to be the dominant mechanism for reducing the angular momentum in collapsing flows to the low values observed in YSOs (McKee et al., 1993; McKee and Ostriker, 2007), and shall be explained more fully in Chapter 2.

There are three major episodes of angular momentum transfer during the formation and evolution of a young star. The first is the formation of molecular cloud cores from the host cloud, where the usual solution to the angular momentum problem is magnetic braking and the transfer of angular momentum by Alfvén waves from the centre to the outer regions (Mouschovias, 1991). This tends to produce centrally-condensed uniformly-rotating cloud cores that are stable against fragmentation (Basu and Mouschovias, 1994). This solution has been considered somewhat problematic as it is difficult to form binaries from such stable cores and young binary stars are very common, however, stable cores form centrifugal discs that may fragment and form binary systems (Bodenheimer, 1995).

More recent research has shown that the formation of cores may also be triggered by fragmentation that is regulated by magnetic fields and ambipolar diffusion, and that the rate of core growth is dependant upon the magnetic field strength in the core

(Kudoh et al., 2007). Boss (2009) showed further that the shape of molecular cloud cores is important to the angular momentum transport and fragmentation. Their radiative hydrodynamical code, which included prescriptions for the magnetic braking and ambipolar diffusion, showed that oblate cores collapse to form rings that are susceptible to fragmentation; and that the fragmentation of prolate cores depends upon the density profile in the core — cores that possess shallow density profiles being more likely to fragment than those with steep profiles.

As is expected, angular momentum is approximately conserved during the dynamic near-free fall collapse of a core into a flattened pseudodisc and so this phase of star formation does not add to the angular momentum problem (Galli and Shu, 1993a,b). However inside the pseudodisc at the centre of the dynamic collapse the magnetic field has built up to the point where it is possible for magnetic braking to be the dominant force reducing the angular momentum in the collapsing fluid.

Fragmentation into a wide binary is likely during the phase of isothermal pseudodisc evolution if the initial angular momentum is high; the spin angular momentum of the cloud is converted into the orbital angular momentum of the binary (Mestel and Spitzer, 1956; Larson, 1985; Bodenheimer, 1995). The occurrence of fragmentation during collapse depends on the initial ratio of thermal to gravitational energy (Tsuribe and Inutsuka, 1999a,b) and in a wide range of cases the final outcome of gravitational collapse is the formation of a binary or multiple system via the formation and fragmentation of a ring or bar structure in the fluid instead of, or as well as, the expected disc configuration (Matsumoto and Hanawa, 2003).

If the initial angular momentum of the core is low then the flattened pseudodisc will be unable to fragment and will instead form a central protostellar core surrounded by an optically thick disc where the angular momentum must be removed by magnetic fields, turbulent viscosity or the formation of a massive planet that may interact with the disc to allow material to accrete onto the star.

The ideal MHD simulations of Mellon and Li (2008) showed that their strongly-braked disc was surrounded by a vertically-extended structure, referred to as a magnetogyrosphere, where the angular momentum was parked; this was supported by a combination of the (toroidal) magnetic field and rotation. The collapsing fluid was channelled by the magnetic wall surrounding the magnetogyrosphere into the equatorial region, and the infalling material was braked as it crossed a series of centrifugal barriers. It is possible that such a magnetogyrosphere has been observed in the Class 0 source IRAM 04191 (see the references and interpretation within Mellon and Li, 2008); however higher resolution observations are needed to confirm this.

The magnetorotational instability (MRI) has been shown to generate turbulence that can remove angular momentum from the infalling gas in the pseudodisc and later

Keplerian disc (Balbus and Hawley, 1998). The MRI acts by converting the free energy of differential rotation into turbulent motions that transfer angular momentum radially outward via the Maxwell stress of small scale, disordered magnetic fields. Its properties have been studied in both the linear and nonlinear stages and it has been shown to be very efficient at removing angular momentum from discs (e.g. Sano and Stone, 2002a,b; Salmeron and Wardle, 2003, 2004, 2005). Salmeron et al. (2007a,b) showed that radial angular momentum transport by the MRI operates where $2\eta\alpha^2 < 1$, where η is the ratio of the Keplerian rotation time to the neutral-ion momentum exchange time and α is the midplane ratio of the Alfvén speed to the sound speed. They also found that radial and vertical angular momentum transport operate in different regions of the disc, with the MRI dominant when $\alpha \ll 1$.

The semianalytic self-similar collapse solutions of Krasnopolsky and Königl (2002) produced rotationally-supported discs that were magnetorotationally stable, however, their calculations were limited to one dimension and contained only ambipolar diffusion in their approximation to the magnetic field diffusion, so they may have oversimplified the calculations to the point where the disc could not be magnetorotationally unstable. The MRI has been shown to be important in protostellar and protoplanetary discs (Sano and Stone, 2002a,b) and may be important at other points in the star formation process.

Another possible way to remove angular momentum from lower-mass flattened pseudodiscs is to form a massive planet or companion star in the disc. The torques exerted on the disc by a planet can transport angular momentum from the inner regions to the outer parts of the disc, and can also drive inflow towards the central protostar. This behaviour has been observed in numerical simulations of gravitational collapse such as those by Bate and Bonnell (2005), Machida et al. (2008b) and others.

The final evolutionary stage in which the angular momentum problem is evident is the necessary removal of angular momentum from the fluid that is accreting from the innermost rotationally-supported disc, as it typically carries enough angular momentum that it will spin up the star in a relatively short period of time (Bodenheimer, 1995). In this regime the problem is likely solved by the formation of a disc wind or stellar winds, as the protostellar wind blows away the majority of the remaining non-accreted envelope of the core independent of the magnetic braking (Shu et al., 1987). It has been shown that a rotating disc wind can remove angular momentum as well as mass from the innermost partially-ionised region of the disc very efficiently (Machida et al., 2007, 2008a); the simulations of Tomisaka (2002) showed that 99% of the total angular momentum of their protostellar systems was transferred from the system by outflows during the adiabatic second phase of collapse.

Stellar dynamo activity may also contribute to the formation of a magnetospheric

region around the protostar that can generate a bipolar jet; this could remove further angular momentum in order to resolve the angular momentum problem (Larson, 2003). Alternatively, the interaction of the stellar dipole magnetic field with the accretion disc could also remove angular momentum from the protostar (or spin it up, if the initial rotation rate is low). Such accretion would take place in a steady state along the stellar magnetic field lines, where the spin-up torque on the star is balanced by a spin-down torque transmitted by field lines that thread the disc beyond the corotation radius (Ghosh and Lamb, 1979a,b; Königl, 1991).

During the later stages of pre-main sequence contraction, when the interaction between the star and disc is no longer important, the YSO evolves with near-conservation of angular momentum, and the angular velocity of the pre-main sequence protostar decouples from that of the envelope (Bodenheimer, 1995).

The angular momentum problem has in recent years been so well solved by simulations that include the transport of angular momentum by magnetic braking that it has given rise to the magnetic braking catastrophe in which all of the angular momentum has been removed from the collapsing material so that it free falls with no rotation onto the protostar. This behaviour has been observed in many simulations with different coupling between the field and the matter; generally it occurs in simulations that adopt IMHD (e.g. Allen et al., 2003b,a; Mellon and Li, 2008) or non-ideal MHD in the form of ambipolar diffusion (e.g. Krasnopolsky and Königl, 2002; Mellon and Li, 2009). This catastrophe has also been seen in simulations in which the magnetic field and the rotational axis of the core are not initially aligned (Price and Bate, 2007; Hennebelle and Ciardi, 2009; Ciardi and Hennebelle, 2010).

1.5 Magnetic Fields and the Magnetic Flux Problem

In a similar puzzle to the angular momentum problem, there is a several orders of magnitude discrepancy between the observed values and upper limits on the magnetic flux of T Tauri stars and the flux associated with the corresponding mass in the pre-collapse molecular cloud (Chandrasekhar and Fermi, 1953; Mestel and Spitzer, 1956). The mass-to-flux ratio in stars is very large, with $\mu \sim 10^4$–10^5 in magnetic stars and $\mu \sim 10^8$ in the Sun, whereas the mass-to-flux ratio in molecular clouds is typically $\mu \sim 1$ (Nakano, 1983; Crutcher, 1999). The magnetic flux problem of protostellar collapse is a complex puzzle that has not yet been completely solved.

The problem is illustrated using Spitzer's example of a cylinder-shaped cloud containing 1 $M_\odot$ of constant density gas from Section 1.4 once more. Assuming conservation of flux, the magnetic field in the collapsed protostar exceeds that in the original cloud by 10^{14}, the same factor as Ω, so that if B were 3 μG in the original cloud,

the formed star of solar type would possess a magnetic field that is equal to 3×10^8 G. The magnetic energy in the star exceeds the gravitational energy by several times, but the difference between the field in the model star and that in a real young stellar object ($\sim 10^3$–10^5 times) is not as large a discrepancy as that which defines the angular momentum problem (Spitzer, 1978, see also the previous section).

In order to reduce the magnetic flux in the collapsing cloud, there are several processes that can be invoked: the first is local reconnection of field lines. This process occurs when two lines of force intersect at a point of zero magnetic field strength or where two oppositely-directed lines of magnetic force are pushed together by gravitational or hydromagnetic forces (Spitzer, 1978). This alters the topology of the field, and reconnection can displace the region in which the flux crosses the forming or accreting disc. Galli and Shu (1993b) observed reconnection as a numerical artefact in their calculations, arguing that the pinched configuration of the magnetic field in the equatorial plane of their pseudodisc could be subject to several instabilities that would cause reconnection. Numerical reconnection has been observed in the collapse calculations of Galli et al. (2006, 2009) and Krasnopolsky et al. (2010); this is not true reconnection and can lead to anomalous effects in their solutions (such as the large resistivity required to form centrifugal discs in Krasnopolsky et al., 2010).

The second and more commonly discussed mechanism for solving the magnetic flux problem is ambipolar diffusion (see e.g. Mestel and Spitzer, 1956; Mouschovias, 1991; Fiedler and Mouschovias, 1993; Basu and Mouschovias, 1994; Shu and Li, 1997, and many others). Simulations have shown that ambipolar diffusion is important during the phase of collapse pre-point mass formation, when the mass-to-flux ratio is still subcritical and the contraction is slow (see Section 1.3); however, the flux contained in a 1 $M_\odot$ region of a molecular cloud core at point mass formation is still 10^3–10^5 times larger than that of a typical 1 $M_\odot$ protostar (Ciolek and Mouschovias, 1994, 1995).

Further dissipation must then occur after the cloud becomes supercritical and enters into the dynamic, near-free fall phase of collapse, prior to or during the formation of a circumstellar disc. Ambipolar diffusion allows the magnetic field to decouple from the rapidly collapsing neutral particles at small radii, reducing the amount of magnetic flux dragged into the origin (Li and McKee, 1996; Li, 1998); in the numerical simulations of Desch and Mouschovias (2001) this was demonstrated to such a degree that they concluded that the magnetic flux problem could be solved by ambipolar diffusion alone. The earlier numerical simulation of Ciolek and Königl (1998) had shown that the rate of ambipolar diffusion is strongly increased during dynamical collapse and causes a decrease in the magnetic field of over two orders of magnitude (relative to the flux associated with the same mass of pre-collapse gas) in their central object. The semianalytic solutions of Li (1998) demonstrated that it was possible to

find similarity solutions for which there was no central flux when certain constraints upon the coupling parameters, the degree of magnetisation and the initial conditions of the core held true.

By considering the timescales for ambipolar and Ohmic diffusion at high densities Nakano and Umebayashi (1986a,b), building on the calculations of Pneuman and Mitchell (1965), suggested that significant flux loss could only occur during the dynamical phase of core collapse by Ohmic dissipation, which is important once densities of $\sim 10^{11}$ cm^{-3} are achieved in the core. The ratio of the ambipolar diffusion to Ohmic diffusion timescales depends upon the inverse square of the magnetic field, so that as the field is weakened, Ohmic dissipation will come to dominate over ambipolar diffusion at the later stages when the density is high and the magnetic field has decoupled from the gas (see Figure 1.3).

The Ohmic dissipation process has been shown to be more important than vertical collapse (in which the gas infalls along the magnetic field lines) in resolving the magnetic flux problem both analytically (Nakano et al., 2002) and numerically (Machida et al., 2007). Shu et al. (2006) showed that for their semianalytic solution with a large spatially-uniform Ohmic diffusion coefficient and numerical reconnection the magnetic flux problem was resolved, and Tassis and Mouschovias (2007a,b,c) found that their numerical simulations of collapse with ambipolar and Ohmic diffusion produced a magnetic field in the central region ($r \lesssim 10$ AU) of about 0.1 G when the central protostar has a mass ~ 0.01 M$_\odot$, which is approaching that observed in strongly-magnetic stars; their simulations were, however, unable to follow the growth of the protostar to actual stellar masses.

Santos-Lima et al. (2010) performed numerical simulations comparing the relative importance of ambipolar diffusion and "reconnection diffusion": the removal of flux from gravitating clouds by turbulent reconnection (as outlined by Lazarian, 2005). They showed that while cores with low turbulence will be dominated by ambipolar diffusion, cores that are more active will be subject to reconnection diffusion at many densities, and that this will speed the quasistatic contraction of the cloud core before dynamic collapse occurs. They also showed that turbulent diffusivity behaved in a similar manner to enhanced Ohmic diffusivity in non-turbulent simulations, aiding the removal of magnetic flux from the collapsing fluid.

It seems likely that star formation requires all of these processes to a greater or lesser degree. While individual solutions may demonstrate a solved magnetic flux problem for particular controlled parameters, there has been no complete solution that includes both ambipolar and Ohmic diffusion, which are crucial to the magnetic field behaviour. Similarly, these studies have disregarded the potential of Hall diffusion changing the dynamics of collapse and aiding the resolution of the magnetic flux problem at those

intermediate densities between the ambipolar and Ohmic diffusion regimes where Hall diffusion dominates (Wardle and Ng, 1999).

It will be shown in Chapter 3 that no rotationally-supported disc can form in certain Hall similarity solutions when the magnetic braking is particularly strong. This "magnetic braking catastrophe" in which all of the angular momentum of the collapsing material is removed so that there is no rotational support and no inner Keplerian disc forms has been observed in many numerical simulations (e.g. Krasnopolsky and Königl, 2002; Mellon and Li, 2009) and shall be discussed in more detail in Section 6.2. It may be resolved by the inclusion of Ohmic dissipation, which reduces the amount of magnetic braking in the inner high density regions of collapse, allowing rotationally-supported discs to form (Dapp and Basu, 2010; Machida et al., 2011). It will also be demonstrated in Chapter 6 that it is possible to form larger Keplerian discs in the Hall similarity solutions when the magnetic field is reversed (with respect to the axis of rotation); in this situation the magnetic field diffusion can increase the angular momentum of the collapsing gas, spinning it up and changing the dynamics of the angular momentum problem in molecular cloud cores that have low initial rotation rates.

1.6 The Hall Effect in Star Formation

Figure 1.3 showed the magnetic diffusion regimes of a weakly ionised plasma, and indicated that Hall diffusion is important at intermediate densities and field strengths such as those encountered in molecular cloud cores. Wardle (2007) showed that in molecular clouds ions and electrons were coupled to the field while the largest grains are not. As the density increases the smaller grains and the ions also decouple from the field, suggesting that Hall diffusion would become important after molecular cloud cores start to collapse.

Within a fluid in which the Hall diffusion is dominant the ions (and grains) are strongly tied to the neutral particles by collisions, which also are responsible for transmitting the electromagnetic stresses to the neutral particles. The current is dominated by the electrons, which drift perpendicular to the magnetic and electric fields so that the net Lorentz force is zero. Collisions with the neutrals and oppositely-charged grains have negligible effect on the electron motion (Wardle and Ng, 1999).

The drift velocity of the magnetic field in a weakly ionised medium is given by

$$\mathbf{V}_B = \frac{c}{4\pi B}\left[(\eta_\parallel + \eta_A)\mathbf{J}_\perp \times \mathbf{B} - \eta_H \mathbf{J}_\perp\right] \tag{1.11}$$

where $\mathbf{J}$ is the current density, defined by

$$\mathbf{J} = \frac{4\pi}{c}(\nabla \times \mathbf{B}), \tag{1.12}$$

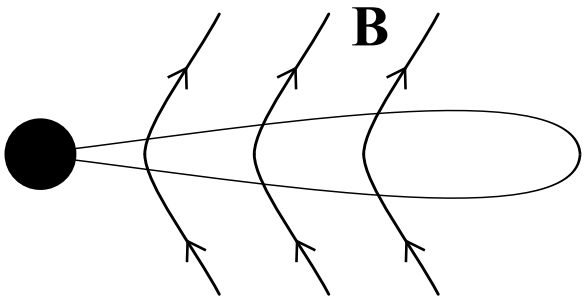

Figure 1.5: Cartoon of a thin disc with a protostar at the centre. The disc has a pinched magnetic field **B** with an azimuthal component that is out of the page. The magnetic field is strictly vertical at the midplane of the disc, and the current at the equator is toroidal.

and $\mathbf{J}_\perp$ is the component of $\mathbf{J}$ that is perpendicular to the magnetic field. The diffusivities $\eta_{\parallel,A,H}$ are those for Ohmic, ambipolar and Hall diffusion respectively — these determine the coupling between the gas and the field, and shall be discussed in more detail in Chapter 2. Clearly, this can be divided into two velocities, that caused by Hall diffusion of the field,

$$\mathbf{V}_H \approx \eta_H \mathbf{J}, \tag{1.13}$$

and that of ambipolar and Ohmic diffusion,

$$\mathbf{V}_{AO} \approx (\eta_A + \eta_\parallel)(\mathbf{J} \times \mathbf{B}). \tag{1.14}$$

For a thin disc such as that illustrated in Figure 1.5, the magnetic field has been pulled into a pinched configuration by the initial collapse under IMHD; this field shape is expected from simulations of gravitational collapse under a variety of conditions (e.g. Galli and Shu, 1993a,b) and observations (e.g. Cortes and Crutcher, 2006; Gonçalves et al., 2008). It is only once the density has built up that ambipolar and Hall diffusion start to become important (e.g. Desch and Mouschovias, 2001; Wardle, 2004a). This pinching produces a strong toroidal current as indicated by Equation 1.12, which causes Hall diffusion in the azimuthal direction (Equation 1.13).

Hall diffusion twists up the field and in turn changes the angular momentum of the neutral fluid, which in a rotationally-supported disc causes the gas to fall inwards if it loses angular momentum, or outwards if it gains it. The direction in which the field diffuses is determined by the initial orientation of the field with respect to the axis of rotation, and the field drifts in the opposite direction if the initial direction of the field is reversed. Ambipolar and Ohmic diffusion, however, always cause the field to move in the radial direction against the flow of the neutrals — reversing the direction of the field does not affect the direction of the field diffusion.

Under Hall diffusion any radial field drift causes an increase in the azimuthal field and correspondingly the angular momentum, tying together the angular momentum and magnetic flux problems outlined in previous sections. It provides a mechanism for resolving both of these problems in simulations of star formation, yet because of the numerical difficulties it incurs and the previous assumption that it would not be important, Hall diffusion is only just starting to be included in simulations of collapsing molecular cloud cores (e.g. Krasnopolsky et al., 2011). The inclusion of Hall diffusion in the semianalytic collapse model will provide a better understanding of the collapse and disc dynamics in observed cores, and shall show that the Hall effect can help resolve the magnetic braking catastrophe, as will be discussed further in Section 6.2.

1.7 Project Outline

This project aims to find similarity solutions for the gravitational collapse of rotating, isothermal, magnetic molecular cloud cores that are similar to those of Krasnopolsky and Königl (2002) but with Hall diffusion included in the conductivity tensor. Krasnopolsky and Königl (2002) adopted a conductivity that contained only ambipolar diffusion, but it has been shown that the Hall diffusion term is important at many of the intermediate densities found during gravitational collapse (Wardle, 2004a). Hall diffusion also significantly alters the vector evolution of the magnetic field (see Figure 1.2), and it is Hall diffusion that is of particular interest here, especially in contrast with the ambipolar and Ohmic diffusion terms.

In Chapter 2 the problem of gravitational collapse is properly set out and the self-similar MHD equations are derived under the assumptions of isothermality, axisymmetry, that the forming pseudodisc is thin and others describing the magnetic field behaviour. These assumptions are discussed in detail and the outer boundary conditions (corresponding also to the initial conditions of the core, due to the self-similar nature of the problem) are derived with values chosen to be compatible with both observations and three-dimensional numerical collapse simulations.

Chapter 3 derives the inner asymptotic solutions, which function as the second set of boundary conditions for the collapse problem (at the inner edge and infinite time). These inner similarity solutions are power law descriptions of a Keplerian accretion disc which is supported by the influence of both Hall and ambipolar diffusion, and a rapidly infalling solution in which the material falls directly onto the central star without forming a disc. These similarity solutions demonstrate the restrictions that must be placed upon the Hall and ambipolar diffusion parameters in order to find the true solutions, as the handedness of the magnetic response (shown in Figure 1.2) can lead to unphysical solutions if the adopted nondimensional Hall diffusion parameter is

too large with respect to the ambipolar diffusion parameter and the orientation of the magnetic field.

Chapter 4 describes the construction of the self-similar model in stages of increasing complexity, duplicating the results of Krasnopolsky and Königl (2002) and comparing these with numerical simulations. The iterative code that numerically integrates the self-similar equations and solves the boundary condition problem is outlined, as well as the approximations used to estimate the positions of the magnetic diffusion and centrifugal shocks. The similarity solutions to collapse models that have no magnetic field, ideal magnetohydrodynamics or only ambipolar diffusion are then presented and analysed; these are used to demonstrate that the size of the rotationally-supported disc and the accretion rate onto the protostar depend upon the initial rotation rate and the amount of magnetic braking in the core.

The main results of the project are presented in Chapter 5, where the similarity solutions for the expanded model with the full conductivity tensor are explored. Further details of the modelling process are described, including simplifications adopted to calculate initial values of the variables at a matching point (to increase the likelihood of convergence onto the true solutions) and modifications to the equation set that are necessary near the inner boundary. The importance of Hall diffusion to the collapse process is compared with the ambipolar term that was previously expected to dominate the magnetic field behaviour in the earlier stages of collapse. In particular, Hall diffusion is shown to introduce additional shock fronts interior to the magnetic diffusion and centrifugal shocks that alter the dynamics of the collapse.

The primary results of this thesis are summarised and discussed in more detail in Chapter 6, where the limitations of the model and the assumptions supporting it are considered in the context of the results. The difference in the behaviour and size of the protostar and Keplerian disc are examined with respect to the boundary conditions of the core and the diffusion coefficients. Depending upon the orientation of the magnetic field with respect to the axis of rotation, Hall diffusion is shown to change the size of the Keplerian disc by an order of magnitude, and can increase the accretion rate onto the protostar. Hall diffusion is also shown to have a clear impact on the magnetic braking catastrophe — enhancing it by further decreasing the angular momentum of the collapsing flow so that no disc forms, or changing the magnetic braking behaviour to the point where Hall diffusion can *induce* rotation in initially nonrotating flows, again depending upon the orientation of the field. Observational tests of this model are proposed and suggestions for future work expanding the model by better calculating the vertical angular momentum transport and adopting a different scaling in self-similar space for the nondimensional Hall diffusion parameter are presented. Finally, the conclusions of this work and its implications will be summarised, emphasising that

the Hall effect is indeed important in studies of star formation.

Chapter 2

Self-Similar Gravitational Collapse

Simulations of gravitational collapse are some of the most important tools available for studying star formation. Numerical simulations, while increasingly able to model complex physics across a wide range of densities, are limited in resolution. Due to the computational costs of these, only the most typical regions of parameter space are able to be explored; novel or otherwise interesting solutions may be overlooked as typical values of the model parameters are adopted.

Semianalytic simulations are instead able to model solutions with very high resolution rapidly, so that it is possible to explore larger regions of parameter space. This is achieved by reducing the dimensionality of the problem and sacrificing some of the featured physics. A semianalytic model then is the optimal choice for studying a simplified collapse problem with Hall diffusion, so that the parameter space can be quickly explored and the prospects for future research in numerical simulations identified.

The goal of this work is to construct a semianalytic model of gravitational collapse similar to that of Krasnopolsky and Königl (2002) but including terms for Hall diffusion in the equations for the magnetic field diffusion and braking. This will allow the calculation of similarity solutions that show the importance of Hall diffusion in molecular cloud cores and collapsing flows, as well as comparisons between the influence of the Hall and ambipolar diffusion terms. These solutions will then be used to motivate the inclusion of Hall diffusion in numerical models of star formation and protostellar discs.

This chapter describes the derivation of the self-similar equations, and the set of initial (outer) boundary conditions that describe a molecular cloud core which is magnetically supercritical and in the process of contracting slowly in the radial direction. The MHD equations are presented in cylindrical coordinates and the assumptions that

must be adopted to ensure that self-similarity holds are outlined. These assumptions include isothermality, which guarantees that the sound speed in the core is constant, and axisymmetry, which is adopted to reduce the dimensionality of the problem, The core is then assumed to be a thin disc, so that the equations may be averaged over the scale height of the collapsing flow — this further reduces the dimensionality of the problem so that the MHD variables then depend only on the radius and time. The prescriptions for the radial and azimuthal field components are derived, and the azimuthal term is shown to control the magnetic braking of angular momentum, which slows the rotation of the inner regions of the core by transporting angular momentum to the external envelope.

Finally, the equations are self-similarised by choosing a similarity variable that is a function of r and t and adopting nondimensional scalings of the fluid variables so that they become functions of the similarity variable. The MHD equations can then be written in terms of the nondimensional variables, and once the outer boundary conditions are modified to reflect this self-similarity, it is then possible to integrate the one-dimension equations and find similarity solutions that shall provide new insight into the star formation process.

2.1 Basic Equations

The methods of Krasnopolsky and Königl (2002) are used to simplify and rearrange the MHD equations into the self-similar form in which the equations depend only upon the nondimensional similarity variable, $x = r/c_s t$, and are one-dimensional ordinary differential equations. The principal difference between this work and theirs is the inclusion of the full conductivity tensor in the induction equation, rather than just the ambipolar diffusion term. The vertical angular momentum transport is also modified by the inclusion of a Hall diffusion term.

The magnetohydrodynamics equations are:

$$\frac{\partial \rho}{\partial t} + \nabla \cdot (\rho \mathbf{V}) = 0, \tag{2.1}$$

$$\rho \frac{\partial \mathbf{V}}{\partial t} + \rho(\mathbf{V} \cdot \nabla)\mathbf{V} + \nabla P = \rho \mathbf{g} + \frac{\mathbf{J} \times \mathbf{B}}{c}, \tag{2.2}$$

$$\nabla^2 \Phi = 4\pi G \rho, \tag{2.3}$$

$$\nabla \cdot \mathbf{B} = 0 \tag{2.4}$$

$$\text{and } \frac{\partial \mathbf{B}}{\partial t} = \nabla \times (\mathbf{V} \times \mathbf{B}) - \nabla \times \left[\eta_{\parallel} (\nabla \times \mathbf{B}) + \eta_H (\nabla \times \mathbf{B}) \times \hat{\mathbf{B}} + \eta_A (\nabla \times \mathbf{B})_{\perp} \right] \tag{2.5}$$

where ρ is the gas density, $\mathbf{V}$ the velocity field, P the pressure, $\mathbf{g}$ the gravitational field, Φ the gravitational potential, c the speed of light, $\mathbf{J}$ the current, $\mathbf{B}$ the magnetic

field, $\hat{\mathbf{B}}$ is the unit vector in the direction of $\mathbf{B}$, and $\eta_{\parallel,H,A}$ are the respective diffusion coefficients for the Ohmic, Hall and ambipolar terms in the induction equation.

To simplify the calculations of the collapsing cloud core, the axis of rotation is aligned with the background magnetic field. The external cloud medium is characterised by constant low density, thermal pressure and angular velocity.

Using cylindrical coordinates, under the assumptions of isothermality (that $P = \rho c_s^2$) and axisymmetry (that the derivatives with respect to ϕ are equal to zero), the mass, radial momentum, and angular momentum conservation relations, as well as the hydrostatic equilibrium equation and the induction equation are given by:

$$\frac{\partial \rho}{\partial t} + \frac{1}{r}\frac{\partial}{\partial r}(r\rho V_r) = -\frac{\partial}{\partial z}(\rho V_z), \tag{2.6}$$

$$\begin{aligned}\rho\frac{\partial V_r}{\partial t} + \rho V_r\frac{\partial V_r}{\partial r} = \rho g_r - c_s^2\frac{\partial \rho}{\partial r} + \rho\frac{V_\phi^2}{r} + \frac{B_z}{4\pi}\frac{\partial B_r}{\partial z} \\ - \frac{\partial}{\partial r}\left(\frac{B_z^2}{8\pi}\right) - \frac{1}{8\pi r^2}\frac{\partial}{\partial r}(rB_\phi)^2 - \rho V_z\frac{\partial V_r}{\partial z},\end{aligned} \tag{2.7}$$

$$\frac{\rho}{r}\frac{\partial}{\partial t}(rV_\phi) + \frac{\rho V_r}{r}\frac{\partial}{\partial r}(rV_\phi) = \frac{B_z}{4\pi}\frac{\partial B_\phi}{\partial z} + \frac{B_r}{4\pi r}\frac{\partial}{\partial r}(rB_\phi) - \rho V_z\frac{\partial}{\partial z}(rV_\phi), \tag{2.8}$$

$$\rho\frac{\partial V_z}{\partial t} + \rho V_r\frac{\partial V_z}{\partial r} + \rho V_z\frac{\partial V_z}{\partial z} + c_s^2\frac{\partial \rho}{\partial z} = \rho g_z - \frac{\partial}{\partial z}\left(\frac{B_\phi^2}{8\pi} + \frac{B_r^2}{8\pi}\right) + \frac{B_r}{4\pi}\frac{\partial B_z}{\partial r} \tag{2.9}$$

and

$$\frac{\partial \mathbf{B}}{\partial t} = \nabla \times (\mathbf{V} \times \mathbf{B}) - \nabla \times \left[\eta_\parallel (\nabla \times \mathbf{B}) + \eta_H (\nabla \times \mathbf{B}) \times \hat{\mathbf{B}} + \eta_A (\nabla \times \mathbf{B})_\perp\right], \tag{2.10}$$

where g_r and g_z are the radial and vertical components of the gravitational field, and c_s is the isothermal sound speed given by $c_s = (k_B T/m_n)^{1/2} \approx 0.19$ km s^{-1} (with k_B the Boltzmann constant, T the gas temperature, typically taken to be 10 K, and m_n the mean mass of a gas particle). For the sake of comparison, the sound speed is denoted C in many papers (including Krasnopolsky and Königl, 2002, and others such as Ciolek and Mouschovias, 1993; Kunz and Mouschovias, 2010, etc), and a in others (e.g. Shu et al., 1987; Galli et al., 2006; Mellon and Li, 2009, etc). The notation adopted here matches that of Norman and Heyvaerts (1985), Wardle and Ng (1999) and Pandey and Wardle (2008), which was originally chosen in order to differentiate the sound speed from the speed of light (c, no subscript).

2.2 Assumptions

A number of assumptions must be made to simplify the equations to the point that they are ordinary differential equations that can be solved semianalytically. These assumptions are justified below.

The cloud, pseudodisc and inner disc are all rotating slowly, and because of this it is possible to assume that axisymmetry (that the partial derivatives with respect to the azimuthal angle are equal to zero) holds true; this is not expected to introduce significant errors to the simulations. This assumption makes it impossible to include direct calculations of nonaxisymmetric effects such as fragmentation or turbulence, which are important in studies of high-mass star formation (e.g. Mac Low and Klessen, 2004; Ballesteros-Paredes et al., 2007) but are less relevant to the collapse of smaller isolated cores into low-mass stars such as those studied in this work.

The nonaxisymmetric core collapse calculations of Basu and Ciolek (2004) found that the cores formed were near-oblate or triaxial rather than prolate, however, the timescales, infall speeds and mass-to-flux ratios in their cores were compatible with those from axisymmetric calculations. The three-dimensional non-ideal MHD calculations of Machida et al. (2007) showed that in their rapidly-rotating collapses the thin disc is occasionally transformed into a bar by nonaxisymmetric effects, and that this bar may fragment at later stages of the collapse, however, they too were able to form discs with behaviour that did not vary with azimuth. The assumption of axisymmetry in this model is required in order to reduce the dimensionality of the problem to a one-dimensional self-similar equation set, and as near-axisymmetric collapse occurs in three-dimensional models this assumption is considered generally to be appropriate everywhere, except potentially in the inner disc regions.

The magnetic field and the axis of rotation are assumed to be aligned, which is not necessarily supported by observations of molecular cloud cores, although it is a common and accepted simplification of the problem in theoretical studies. Theoretical simulations have shown that the combination of aligned rotation axis and magnetic field leads to the formation of molecular cloud cores that have oblate shapes that match observations (Ciolek and Mouschovias, 1993; Goodwin et al., 2002). Observations of the magnetic field orientation and the rotation of cores (e.g. Vink et al., 2005) have yet to provide a decisive answer on this matter, but the observations of the binary protostellar system NGC 1333 IRAS 4A by Girart et al. (2006) showed that the axis normal to the envelope surrounding the binary lay between the outflow and the magnetic field axes, which suggests that the spin and magnetic field axes were not in alignment when collapse was initiated. These analyses were supported by further observations by Attard et al. (2009) and modelling by Gonçalves et al. (2008), which showed that the field in this core possesses the classic hourglass shape, even though it is not aligned with the outflow from the binary star.

The simulations of Price and Bate (2007), Hennebelle and Ciardi (2009) and Ciardi and Hennebelle (2010) have shown that the angle between the rotation axis and the magnetic field influences the dynamics of collapse, and could prevent the formation of

a rotationally-supported disc. Disc formation in calculations with high initial magnetic flux occurred most often when the magnetic field and axis of rotation were orthogonal due to the reduced magnetic braking caused by the field. Given these results, it would appear that a better choice for the initial shape of the magnetic field would see it lie at an angle to the rotational axis, however by definition this would violate axisymmetry, which, as stated previously, is necessary for one-dimensional self-similarity.

The assumption that the pseudodisc is thin is based upon the results of Fiedler and Mouschovias (1992, 1993) and the many other simulations of Mouschovias and coworkers, which have shown that an initially uniform, self-gravitating, magnetised molecular cloud core that is spherically or cylindrically-symmetric rapidly flattens along magnetic field lines. This assumption allows for a further reduction in the dimensionality of the problem, although again it implies that effects that depend on variation in the density or magnetic field with height within the disc cannot be included in the collapse calculation. Such processes may include turbulence and interactions between active and dead zones in the disc that are caused by the differential (with respect to r and z) ionisation of the disc by external sources (Pudritz et al., 2007). They are not expected to have a large effect on the overall dynamics of early collapse, but they may again become important in the innermost regions of protostellar discs in the later stages of collapse once the adiabatic core and protostar have formed.

Isothermality is required for self-similarity, as the similarity variable x is defined in terms of the isothermal sound speed, c_s. This assumption breaks down due to radiative trapping when the central density reaches values $\sim 10^{10}$ cm^{-3} (Gaustad, 1963). For a typical simulation of the collapse of a nonrotating molecular cloud core this occurs on scales $r \lesssim 5$ AU, which is several orders of magnitude smaller than the size of the average core, and so nonmagnetic or nonrotating simulations (e.g. Ciolek and Königl, 1998) and numerical simulations (e.g. Tassis and Mouschovias, 2005a,b) often treat the inner region as point-like.

By treating the forming protostar and the region around it as a central sink cell into which the infalling matter disappears, it is possible to avoid having to deal with complications such as the breakdown of isothermality and the difficulty of tracking regions of high density in grid-based calculations. The breakdown of isothermality is usually treated by adopting an adiabatic equation of state once a critical density is exceeded in the inner region of the collapse, as a way of avoiding the computational expense of performing radiative transfer calculations (e.g. Machida et al., 2007, 2008a; Tassis and Mouschovias, 2007a,b,c). It is now possible to perform some full radiative transfer simulations, but usually at the expense of magnetic field behaviour or grid resolution (e.g. Krumholz and McKee, 2008; Kunz and Mouschovias, 2009, 2010; Price and Bate, 2009).

Isothermality breaks down in the inner disc region of the self-similar collapse calculations of Krasnopolsky and Königl (2002), as the surface density in their quasistatic Keplerian disc is much higher than that in the preceding near-free fall stage. They estimated that radiative trapping occurs on scales $\lesssim 10^2$ AU, although irradiation by the central protostar would mitigate this to maintain vertical isothermality in the outer regions of the disc. However, this same irradiation establishes a $T \propto r^{-1/2}$ variation in temperature in the innermost regions of the disc (D'Alessio et al., 1998). While this obviously means that self-similarity could break down in the innermost regions of this disc, thermal stresses do not play a significant role in the larger-scale core collapse dynamics and the assumption of isothermality is not expected to introduce significant inaccuracies into the overall results.

The pressure support that could be provided by internal turbulence is neglected, as it cannot be directly calculated due to the dimensional simplifications adopted and any parameterisation possible within the self-similar framework would be so simplistic as to render it useless as a measure of the influence of turbulence on collapse simulations. As with all the other assumptions on the collapsing material, this is unlikely to introduce large errors into the calculations.

2.3 Vertical Averaging

In order to simplify the calculations and reduce the problem to one that depends only on r and t, the pseudodisc is assumed to be geometrically thin with a half-thickness $H(r) \ll r$, and Equations 2.6–2.10 are vertically averaged by integrating over z.

The density, radial velocity, azimuthal velocity and radial gravity are taken to be constant with height, and the surface density of the pseudodisc is defined as

$$\Sigma = \int_{-\infty}^{\infty} \rho dz = 2H\rho, \tag{2.11}$$

while the specific angular momentum is given by the equation

$$J = rV_\phi. \tag{2.12}$$

It is assumed that the thin disc is threaded by an open magnetic field configuration possessing an even symmetry:

$$B_r(r,-z) = -B_r(r,z), \tag{2.13}$$

$$B_\phi(r,-z) = -B_\phi(r,z), \tag{2.14}$$

$$\text{and } B_z(r,-z) = B_z(r,z); \tag{2.15}$$

clearly $B_r = B_\phi = 0$ at the midplane of the disc. Where they are not held constant with height the other physical variables are assumed to be reflection-symmetric about the midplane.

The solenoidal condition on the magnetic field (derived from Gauss' law for magnetic fields, Equation 2.4, under the assumption of axisymmetry) is given by

$$\frac{\partial B_z}{\partial z} = -\frac{1}{r}\frac{\partial}{\partial r}(rB_r). \tag{2.16}$$

This implies that

$$\frac{\Delta B_r}{r} \approx \frac{\Delta B_z}{H}; \tag{2.17}$$

and the variation of B_z from $z = 0$ to $z = H$ is then

$$\Delta B_z \approx \frac{H}{r} B_{r,s} \tag{2.18}$$

where $B_{r,s}$ is the value of B_r at the surface of the disc. Assuming that B_z is the dominant field component (that $B_{r,s} \lesssim B_z$, which is not always true although the terms are always of the same order of magnitude), and that $H \ll r$, then

$$\Delta B_z \ll B_z, \tag{2.19}$$

so the variation of B_z within the disc is small (Lovelace et al., 1994). It is then possible to treat B_z in the thin disc as being constant with height during the vertical averaging; the solenoidal condition is used to average any terms in which $\partial B_z/\partial z$ appears.

The other field components are assumed to scale as

$$B_r(r, z) = B_{r,s}(r)\frac{z}{H(r)} \tag{2.20}$$

and

$$B_\phi(r, z) = B_{\phi,s}(r)\frac{z}{H(r)} \tag{2.21}$$

where $B_{\phi,s}$ is the surface value of the azimuthal field component, B_ϕ; these scalings are motivated by the field configuration of a rotationally-supported thin disc in which the field is comparatively well-coupled to the gas (Wardle and Königl, 1993). While this holds true in the outer regions of the collapse, this approximation is no longer adequate to describe the field behaviour in the inner regions of the disc where the field is only weakly-coupled to the fluid (Li, 1996; Wardle, 1997). However, as none of the dominant terms in the equation set depend upon the particulars of the vertical variation of the field within the disc, it is reasonable to adopt these scalings across the domain of the self-similar collapse (Krasnopolsky and Königl, 2002). A better method of handing the field variation with height in the disc should be explored in future research.

The radial component of gravity, g_r, is taken from the monopole expression

$$g_r = -\frac{GM(r)}{r^2}, \tag{2.22}$$

where the enclosed mass $M(r) \approx M_c$ when the central mass dominates. This was found by Contopoulos et al. (1998) to be near enough to the value given for the radial gravitational force by an iterative calculation method that it could be used without correction terms in their self-similar model. Following their work, the monopole expression for gravity is similarly adopted here (as in Krasnopolsky and Königl, 2002), with little expectation that it will introduce significant errors into the calculation.

In the interest of keeping this text readable, each of the MHD equations is treated separately below.

2.3.1 Conservation of mass

Using Equation 2.11, the equation of continuity (Equation 2.6) integrates to

$$\frac{\partial \Sigma}{\partial t} + \frac{1}{r}\frac{\partial}{\partial r}(r\Sigma V_r) = -\frac{1}{2\pi r}\frac{\partial \dot{M}_w}{\partial r}, \tag{2.23}$$

where the term on the right hand side represents the mass flux in a disc wind with total outflow rate $\dot{M}_w(r)$ within a radius r, defined by the relation

$$\frac{\partial \dot{M}_w}{\partial r} = 2\pi r \Sigma V_z. \tag{2.24}$$

The calculations presented here do not include a disc wind, so this term is now set to zero. A discussion of how a nonzero outflow mass flux could be incorporated into the work in future is included in Chapter 6 (see also appendix C of Krasnopolsky and Königl, 2002).

2.3.2 Conservation of radial momentum

With the approximation that V_r is constant with height, the final term in the radial momentum conservation equation (Equation 2.7), $\rho V_z \frac{\partial V_r}{\partial z}$, vanishes. Applying the approximations outlined above and integrating the rest of the radial momentum conservation equation over z gives

$$\begin{aligned}\Sigma\frac{\partial V_r}{\partial t} + \Sigma V_r\frac{\partial V_r}{\partial r} = \Sigma g_r - c_s^2\frac{\partial \Sigma}{\partial r} + \Sigma\frac{V_\phi^2}{r} \\ + \frac{1}{8\pi}\int_\infty^\infty \left[2B_z\frac{\partial B_r}{\partial r} - \frac{\partial (B_z^2)}{\partial r} - \frac{1}{r^2}\frac{\partial}{\partial r}(rB_\phi)^2\right] dz,\end{aligned} \tag{2.25}$$

where the final integral cannot be integrated as easily as the terms on the first line of the equation.

The first term in the integral is integrated by rewriting the inner derivative as

$$\int_{-\infty}^{\infty} \frac{B_z}{4\pi}\frac{\partial B_r}{\partial z}dz = \frac{1}{4\pi}\int_{-\infty}^{\infty}\left[\frac{\partial}{\partial z}(B_z B_r) - B_r\frac{\partial B_z}{\partial z}\right]dz; \tag{2.26}$$

the scaling of B_r given in Equation 2.20 and the solenoidal condition (Equation 2.16) are then applied so that

$$\int_{-\infty}^{\infty} \frac{B_z}{4\pi}\frac{\partial B_r}{\partial z}dz = \frac{1}{4\pi}\int_{-\infty}^{\infty}\left[\frac{\partial}{\partial z}\left(\frac{B_z B_{r,s} z}{H}\right) + \frac{B_r}{r}\frac{\partial}{\partial r}(rB_r)\right]dz, \tag{2.27}$$

and finally the first term in this equation can be integrated over the disc scale height and the second term simplified to give

$$\int_{-\infty}^{\infty} \frac{B_z}{4\pi}\frac{\partial B_r}{\partial z}dz = \frac{B_z B_{r,s}}{2\pi} + \frac{1}{8\pi r^2}\int_{-\infty}^{\infty}\frac{\partial}{\partial r}(rB_r)^2 dz. \tag{2.28}$$

The second term in the integral in 2.25 is then integrated using the assumption that B_z is constant with height:

$$\int_{-\infty}^{\infty}\frac{\partial}{\partial r}\left(\frac{B_z^2}{8\pi}\right)dz = \frac{H}{4\pi}\frac{\partial}{\partial r}(B_z^2); \tag{2.29}$$

and this and Equation 2.28 are then substituted into Equation 2.25:

$$\begin{aligned}\Sigma\frac{\partial V_r}{\partial t} + \Sigma V_r\frac{\partial V_r}{\partial r} = \Sigma g_r - c_s^2\frac{\partial \Sigma}{\partial r} + \Sigma\frac{V_\phi^2}{r} + \frac{B_z B_{r,s}}{2\pi} - \frac{H}{4\pi}\frac{\partial B_z^2}{\partial r} \\ + \frac{1}{8\pi r^2}\int_{-\infty}^{\infty}\frac{\partial}{\partial r}[r^2(B_r^2 - B_\phi^2)]dz.\end{aligned} \tag{2.30}$$

The last term of Equation 2.30 is evaluated over the finite interval of the disc height, $[-H(r), +H(r)]$, as the mass is distributed only between the boundaries of the disc. This integral is then solved by parts:

$$\int_{-\infty}^{\infty}\frac{\partial}{\partial r}[r^2(B_r^2 - B_\phi^2)]dz = \frac{\partial}{\partial r}\left[r^2\int_{-H}^{H}(B_r^2 - B_\phi^2)dz\right] - 2r^2(B_{r,s}^2 - B_{\phi,s}^2)\left(\frac{dH}{dr}\right) \tag{2.31}$$

(Lovelace et al., 1994). The vertical scalings for the field components (2.20–2.21) are substituted into this, and the integral on the right hand side of Equation 2.31 then becomes

$$\int_{-H}^{H}\frac{\partial}{\partial r}[r^2(B_r^2 - B_\phi^2)]dz = \frac{2}{3}\frac{\partial}{\partial r}[r^2 H(B_{r,s}^2 - B_{\phi,s}^2)] - 2r^2(B_{r,s}^2 - B_{\phi,s}^2)\left(\frac{dH}{dr}\right); \tag{2.32}$$

the derivative on the left of this equation is then expanded out so that the integral becomes

$$\int_{-H}^{H}\frac{\partial}{\partial r}[r^2(B_r^2 - B_\phi^2)]dz = \frac{2H}{3}\frac{\partial}{\partial r}[r^2(B_{r,s}^2 - B_{\phi,s}^2)] - \frac{4r^2}{3}(B_{r,s}^2 - B_{\phi,s}^2)\left(\frac{dH}{dr}\right). \tag{2.33}$$

All of the above terms are collected together so that the radial momentum conservation equation is thus

$$\Sigma\frac{\partial V_r}{\partial t}+\Sigma V_r\frac{\partial V_r}{\partial r}=\Sigma g_r-c_s^2\frac{\partial\Sigma}{\partial r}+\Sigma\frac{V_\phi^2}{r}+\frac{B_zB_{r,s}}{2\pi}-\frac{H}{4\pi}\frac{\partial B_z^2}{\partial r}$$
$$+\frac{H}{12\pi r^2}\frac{\partial}{\partial r}[r^2(B_{r,s}^2-B_{\phi,s}^2)]-\frac{1}{6\pi}(B_{r,s}^2-B_{\phi,s}^2)\left(\frac{dH}{dr}\right). \quad (2.34)$$

Rearranging this and substituting in the monopole approximation for g_r (given in Equation 2.22) gives the full vertically-averaged radial momentum conservation equation:

$$\frac{\partial V_r}{\partial t}+V_r\frac{\partial V_r}{\partial r}=-\frac{GM}{r^2}-\frac{c_s^2}{\Sigma}\frac{\partial\Sigma}{\partial r}+\frac{J^2}{r^3}+\frac{B_zB_{r,s}}{2\pi\Sigma}-\frac{HB_z}{2\pi\Sigma}\frac{\partial B_z}{\partial r}$$
$$+\frac{H}{12\pi\Sigma r^2}\frac{\partial}{\partial r}[r^2(B_{r,s}^2-B_{\phi,s}^2)]-\frac{1}{6\pi\Sigma}\left(\frac{dH}{dr}\right)(B_{r,s}^2-B_{\phi,s}^2). \quad (2.35)$$

2.3.3 Conservation of angular momentum

As in the case of the radial momentum, the final term in the angular momentum conservation equation (Equation 2.8), $\rho V_z\frac{\partial}{\partial z}(rV_\phi)$, vanishes as V_ϕ is constant with respect to z. By rearranging the equation and applying the solenoidal condition to the partial derivatives of B_z with respect to z, the angular momentum equation becomes:

$$\frac{\rho}{r}\frac{\partial}{\partial t}(rV_\phi)+\frac{\rho V_r}{r}\frac{\partial}{\partial r}(rV_\phi)=\frac{1}{4\pi}\frac{\partial}{\partial z}(B_zB_\phi)+\frac{B_r}{4\pi r}\frac{\partial}{\partial r}(rB_\phi)+\frac{B_\phi}{4\pi r}\frac{\partial}{\partial r}(rB_r); \quad (2.36)$$

this equation is integrated over z to give

$$\frac{\Sigma}{r}\frac{\partial}{\partial t}(rV_\phi)+\frac{\Sigma V_r}{r}\frac{\partial}{\partial r}(rV_\phi)=\frac{B_zB_{\phi,s}}{4\pi}+\int_{-\infty}^{\infty}\left[\frac{B_r}{4\pi r}\frac{\partial}{\partial r}(rB_\phi)+\frac{B_\phi}{4\pi r}\frac{\partial}{\partial r}(rB_r)\right]dz. \quad (2.37)$$

Using the same methods as for the radial momentum conservation equation, the integral on the right hand side of Equation 2.37 becomes

$$\int_{-\infty}^{\infty}\left[\frac{B_r}{4\pi r}\frac{\partial}{\partial r}(rB_\phi)+\frac{B_\phi}{4\pi r}\frac{\partial}{\partial r}(rB_r)\right]dz=\frac{1}{6\pi r^2}\frac{\partial}{\partial r}(r^2B_{r,s}B_{\phi,s})-\frac{B_{r,s}B_{\phi,s}}{3\pi}\frac{dH}{dr}. \quad (2.38)$$

Substituting this and Equation 2.12 for the specific angular momentum into Equation 2.37, and rearranging the terms once more gives the final version of the vertically-averaged angular momentum conservation equation:

$$\frac{\partial J}{\partial t}+V_r\frac{\partial J}{\partial r}=\frac{rB_zB_{\phi,s}}{2\pi\Sigma}+\frac{H}{6\pi r\Sigma}\frac{\partial}{\partial r}(r^2B_{r,s}B_{\phi,s})-\frac{rB_{r,s}B_{\phi,s}}{3\pi\Sigma}\left(\frac{dH}{dr}\right). \quad (2.39)$$

2.3.4 Vertical hydrostatic balance

The gas pressure is assumed to vanish at the disc surface. The pressure at the midplane of the disc is approximated by

$$p_c \approx \frac{\Sigma c_s^2}{2H}. \tag{2.40}$$

Because the disc is thin, it is assumed that all accretion onto it in the vertical direction has already taken place, so that $V_z = 0$ and all of the terms in Equation 2.9 that feature it vanish. The vertical hydrostatic balance equation, when integrated, becomes

$$p_c = \Sigma g_z - \frac{B_{r,s}^2 + B_{\phi,s}^2}{8\pi} - \frac{H B_{r,s}}{8\pi}\frac{\partial B_z}{\partial r}. \tag{2.41}$$

The vertical component of gravity, g_z, is approximated by

$$g_z = \frac{\pi}{2} G\Sigma^2 + \frac{G M_c \Sigma H}{4r^3}, \tag{2.42}$$

where the first term is the local disc self-gravity, and the other is the tidal squeezing by the central point mass. This is then substituted into Equation 2.41, which is rearranged to give

$$\left(\frac{G M_c \Sigma}{4r^3} - \frac{B_{r,s}}{8\pi}\frac{\partial B_z}{\partial r}\right) H^2 + \left(\frac{B_{r,s}^2 + B_{\phi,s}^2}{8\pi} + \frac{\pi}{2} G\Sigma^2\right) H - \frac{\Sigma c_s^2}{2} = 0, \tag{2.43}$$

the final form of the vertical hydrostatic equilibrium equation.

2.3.5 z-component of the induction equation

The preceding four derivations produce the same equations as their counterparts in Krasnopolsky and Königl (2002). As the focus of this work is to adopt a more complete induction equation than has been modelled previously, which contains terms for the ambipolar, Hall and Ohmic diffusion of the magnetic field, the simplifications that affect the induction equation must be closely examined. This will ensure that the similarity solutions obtained properly explore how Hall diffusion of the field affects star formation.

The z-component of the induction equation (Equation 2.10) is

$$\frac{\partial B_z}{\partial t} = \Big[\nabla \times (\mathbf{V} \times \mathbf{B})\Big]_z - \Big[\nabla \times \Big(\eta_\parallel (\nabla \times \mathbf{B}) + \eta_H (\nabla \times \mathbf{B}) \times \hat{\mathbf{B}} + \eta_A (\nabla \times \mathbf{B})_\perp\Big)\Big]_z \tag{2.44}$$

which is expanded into the form

$$\begin{aligned}\frac{\partial B_z}{\partial t} = {} & \frac{1}{r}\frac{\partial}{\partial r}\Big[r(V_z B_r - V_r B_z)\Big] \\ & - \left[\nabla \times \left(\eta_\parallel (\nabla \times \mathbf{B}) + \eta_H (\nabla \times \mathbf{B}) \times \hat{\mathbf{B}} - \eta_A \left((\nabla \times \mathbf{B}) \times \hat{\mathbf{B}}\right) \times \hat{\mathbf{B}}\right)\right]_z\end{aligned} \tag{2.45}$$

where $\hat{\mathbf{B}} = \mathbf{B}/B$ and $B = \sqrt{B_r^2 + B_\phi^2 + B_z^2}$. As before, it is assumed that the solutions are axisymmetric, so that all partial derivatives with respect to ϕ are zero. The vertical mass flux was defined to be equal to zero, so the vertical component of the gas velocity is $V_z = 0$. Applying these assumptions and expanding out the right hand side further gives

$$\frac{\partial B_z}{\partial t} = -\frac{1}{r}\frac{\partial}{\partial r}\left[r\left(V_r B_z + \left[\eta_\parallel(\nabla\times\mathbf{B}) + \frac{\eta_H}{B}(\nabla\times\mathbf{B})\times\mathbf{B} - \frac{\eta_A}{B^2}\left((\nabla\times\mathbf{B})\times\mathbf{B}\right)\times\mathbf{B}\right]_\phi\right)\right] \tag{2.46}$$

which becomes

$$\begin{aligned}\frac{\partial B_z}{\partial t} = &-\frac{1}{r}\frac{\partial}{\partial r}\left[r\left(V_r B_z + \eta_\parallel\left(\frac{\partial B_r}{\partial z} - \frac{\partial B_z}{\partial r}\right) + \frac{\eta_H}{B}\left(B_z\frac{\partial B_\phi}{\partial z} + \frac{B_r}{r}\frac{\partial}{\partial r}(rB_\phi)\right)\right.\right.\\ &\left.\left. - \frac{\eta_A}{B^2}\left((B_z^2 + B_r^2)\left(\frac{\partial B_z}{\partial r} - \frac{\partial B_r}{\partial z}\right) - B_r B_\phi\frac{\partial B_\phi}{\partial z} + \frac{B_z B_\phi}{r}\frac{\partial}{\partial r}(rB_\phi)\right)\right)\right].\end{aligned} \tag{2.47}$$

The magnetic flux enclosed within a radius r is given by

$$\Psi(r) = \Psi_c + 2\pi\int_0^r B_z(r')r'dr', \tag{2.48}$$

where Ψ_c is the flux within the central point mass. This equation is then rewritten in differential form as

$$B_z = \frac{1}{2\pi r}\frac{\partial\Psi}{\partial r}, \tag{2.49}$$

and its derivative with respect to time is

$$\frac{\partial B_z}{\partial t} = \frac{1}{2\pi r}\frac{\partial}{\partial r}\left(\frac{\partial\Psi}{\partial t}\right). \tag{2.50}$$

This is substituted into Equation 2.47 and the partial derivative with respect to r and the factor of r^{-1} are cancelled to obtain

$$\begin{aligned}\frac{1}{2\pi}\frac{\partial\Psi}{\partial t} = &-r\left[V_r B_z + \eta_\parallel\left(\frac{\partial B_r}{\partial z} - \frac{\partial B_z}{\partial r}\right) + \frac{\eta_H}{B}\left(B_z\frac{\partial B_\phi}{\partial z} + \frac{B_r}{r}\frac{\partial}{\partial r}(rB_\phi)\right)\right.\\ &\left. - \frac{\eta_A}{B^2}\left((B_z^2 + B_r^2)\left(\frac{\partial B_z}{\partial r} - \frac{\partial B_r}{\partial z}\right) - B_r B_\phi\frac{\partial B_\phi}{\partial z} + \frac{B_z B_\phi}{r}\frac{\partial}{\partial r}(rB_\phi)\right)\right].\end{aligned} \tag{2.51}$$

In dealing with the partial derivatives with respect to z, such as the $B_z\frac{\partial B_\phi}{\partial z}$ term above, care must be taken to ensure that the vertical scaling of all of the variables is properly accounted for. As such, the integration is presented with more intermediate steps than in the previous calculations.

The $\eta_{\parallel,H,A}$ terms depend on $B^{0,1,2}$ respectively, so the leading fractions of the diffusive terms may be ignored as the integration over z is performed.

The flux, magnetic force and Ohmic diffusion terms are integrated over z to give:

$$\int_{-\infty}^{+\infty} \frac{1}{2\pi}\frac{\partial \Psi}{\partial t} dz = \left[\frac{1}{2\pi}\frac{\partial \Psi}{\partial t} z\right]_{-H}^{+H} = \frac{2H}{2\pi}\frac{\partial \Psi}{\partial t}; \tag{2.52}$$

$$\int_{-\infty}^{+\infty} V_r B_z dz = \Big[V_r B_z z\Big]_{-H}^{+H} = 2H V_r B_z; \tag{2.53}$$

and

$$\begin{aligned}\int_{-\infty}^{+\infty} \left(\frac{\partial B_r}{\partial z} - \frac{\partial B_z}{\partial r}\right) dz &= \int_{-\infty}^{+\infty} \frac{\partial}{\partial z}\left(\frac{B_{r,s} z}{H}\right) - \frac{\partial B_z}{\partial r} dz \\ &= \left[\frac{B_{r,s} z}{H} - \frac{\partial B_z}{\partial r} z\right]_{-H}^{+H} \\ &= 2\left(B_{r,s} - H\frac{\partial B_z}{\partial r}\right).\end{aligned} \tag{2.54}$$

The Hall diffusion terms are rearranged into the form

$$B_z \frac{\partial B_\phi}{\partial z} + \frac{B_r}{r}\frac{\partial}{\partial r}(r B_\phi) = \frac{\partial}{\partial z}(B_z B_\phi) - B_\phi \frac{\partial B_z}{\partial z} + \frac{B_r}{r}\frac{\partial}{\partial r}(r B_\phi); \tag{2.55}$$

and the vertical scaling of the azimuthal field component is substituted into the first term and the solenoidal condition (Equation 2.16) is applied to the second:

$$B_z \frac{\partial B_\phi}{\partial z} + \frac{B_r}{r}\frac{\partial}{\partial r}(r B_\phi) = \frac{\partial}{\partial z}\left(\frac{B_z B_{\phi,s} z}{H}\right) + \frac{B_\phi}{r}\frac{\partial}{\partial r}(r B_r) + \frac{B_r}{r}\frac{\partial}{\partial r}(r B_\phi). \tag{2.56}$$

The integral of the Hall terms may then by written as

$$\int_{-\infty}^{+\infty} \left[B_z \frac{\partial B_\phi}{\partial z} + \frac{B_r}{r}\frac{\partial}{\partial r}(r B_\phi)\right] dz = \int_{-\infty}^{+\infty} \left[\frac{\partial}{\partial z}\left(\frac{B_z B_{\phi,s} z}{H}\right) + \frac{1}{r^2}\frac{\partial}{\partial r}(r^2 B_r B_\phi)\right] dz, \tag{2.57}$$

which, after the vertical scalings of B_r and B_ϕ are substituted into it, is evaluated to give:

$$\begin{aligned}\int_{-\infty}^{+\infty} \left[B_z \frac{\partial B_\phi}{\partial z} + \frac{B_r}{r}\frac{\partial}{\partial r}(r B_\phi)\right] dz &= \left[\frac{B_z B_{\phi,s} z}{H} + \frac{z^3}{3r^2}\frac{\partial}{\partial r}\left(\frac{r^2 B_{r,s} B_{\phi,s}}{H^2}\right)\right]_{-H}^{+H} \\ &= 2 B_z B_{\phi,s} + \frac{2H^3}{3r^2}\frac{\partial}{\partial r}\left(\frac{r^2 B_{r,s} B_{\phi,s}}{H^2}\right).\end{aligned} \tag{2.58}$$

Finally, the ambipolar diffusion terms are expanded out and integrated. The first of these terms is straightforward, as B_z is regarded as constant with height unless specifically differentiated with respect to z and may be taken outside of the integral,

which is solved to obtain

$$\begin{aligned}\int_{-\infty}^{+\infty}(B_r^2+B_z^2)\frac{\partial B_z}{\partial r}dz &= \frac{\partial B_z}{\partial r}\int_{-\infty}^{+\infty}\left(\frac{B_{r,s}^2z^2}{H^2}+B_z^2\right)dz \\ &= \frac{\partial B_z}{\partial r}\left[\frac{B_{r,s}^2z^2}{3H^2}+zB_z^2\right]_{-H}^{+H} \\ &= 2H\frac{\partial B_z}{\partial r}\left(\frac{B_{r,s}^2}{3}+B_z^2\right). \end{aligned} \tag{2.59}$$

The second of the ambipolar diffusion terms is rearranged into the form

$$(B_r^2+B_z^2)\frac{\partial B_r}{\partial z} = B_r^2\frac{\partial B_r}{\partial z}+B_z\frac{\partial}{\partial z}(B_rB_z)-B_rB_z\frac{\partial B_z}{\partial z} \tag{2.60}$$

to which the solenoidal condition (Equation 2.16) and the scalings for the other field components are applied. The integral of this term is then

$$\begin{aligned}&\int_{-\infty}^{+\infty}(B_r^2+B_z^2)\frac{\partial B_r}{\partial z}dz \\ &\quad=\int_{-\infty}^{+\infty}\frac{B_{r,s}^2z^2}{H^2}\frac{\partial}{\partial z}\left(\frac{B_{r,s}z}{H}\right)+B_z\frac{\partial}{\partial z}\left(\frac{B_{r,s}B_zz}{H}\right)+\frac{B_{r,s}B_zz^2}{Hr}\frac{\partial}{\partial r}\left(\frac{rB_{r,s}}{H}\right)dz; \end{aligned} \tag{2.61}$$

this is evaluated over the height of the disc to give

$$\begin{aligned}\int_{-\infty}^{+\infty}(B_r^2+B_z^2)\frac{\partial B_r}{\partial z}dz &= \left[\frac{B_{r,s}^3z^3}{3H^3}+\frac{B_z^2B_{r,s}z}{H}+\frac{B_{r,s}B_zz^3}{3rH}\frac{\partial}{\partial r}\left(\frac{rB_{r,s}}{H}\right)\right]_{-H}^{+H} \\ &= \frac{2}{3}B_{r,s}^3+2B_z^2B_{r,s}+\frac{2}{3}H^2B_{r,s}^2B_z\left[\frac{d}{dr}[\ln(rB_{r,s})]-\frac{d}{dr}[\ln H]\right]. \end{aligned} \tag{2.62}$$

The third of the ambipolar diffusion terms is again straightforward; it is vertically-averaged by applying the vertical scalings to the radial and azimuthal components to the field and then performing the integral over z to find

$$\begin{aligned}\int_{-\infty}^{+\infty}B_rB_\phi\frac{\partial B_\phi}{\partial z}dz &= \int_{-\infty}^{+\infty}\frac{B_{r,s}B_{\phi,s}z^2}{H^2}\frac{\partial}{\partial z}\left(\frac{B_{\phi,s}z}{H}\right)dz \\ &= \frac{B_{r,s}B_{\phi,s}^2}{H^3}\int_{-H}^{+H}z^2dz \\ &= \frac{2}{3}B_{r,s}B_{\phi,s}^2. \end{aligned} \tag{2.63}$$

Finally, the last of the ambipolar diffusion terms in Equation 2.51 is averaged by substituting in the vertical scalings of the field components and then performing the

integral:

$$\begin{aligned}\int_{-\infty}^{+\infty}\frac{B_\phi B_z}{r}\frac{\partial}{\partial r}(rB_\phi)dz &= \int_{-\infty}^{+\infty}\frac{B_{\phi,s}B_z z}{rH}\frac{\partial}{\partial r}\left(\frac{rB_{\phi,s}z}{H}\right)dz \\ &= \frac{B_{\phi,s}B_z}{rH}\frac{\partial}{\partial r}\left(\frac{rB_{\phi,s}}{H}\right)\int_{-\infty}^{+\infty}z^2dz \\ &= \frac{2}{3}B_z B_{\phi,s}^2 H\left[\frac{d}{dr}[\ln(rB_{\phi,s})]-\frac{d}{dr}[\ln H]\right]. \end{aligned} \tag{2.64}$$

Collecting all of these integrated terms into the same order as in Equation 2.51 then gives the full vertically-averaged induction equation:

$$\begin{aligned}\frac{H}{2\pi}\frac{\partial\Psi}{\partial t} = -r\Bigg[&HV_rB_z+\eta_\parallel\left(B_{r,s}-H\frac{\partial B_z}{\partial r}\right)+\frac{\eta_H}{B}\left(B_zB_{\phi,s}+\frac{H^3}{3r^2}\frac{\partial}{\partial r}\left(\frac{r^2B_{r,s}B_{\phi,s}}{H^2}\right)\right)\\ &-\frac{\eta_A}{B^2}\Bigg[-\left(B_{r,s}-H\frac{\partial B_z}{\partial r}\right)\left(B_z^2+\frac{1}{3}B_{r,s}^2\right)-\frac{1}{3}B_{\phi,s}^2B_{r,s}\\ &+\frac{1}{3}HB_zB_{\phi,s}^2\left(\frac{d}{dr}[\ln(rB_{\phi,s})]-\frac{d}{dr}[\ln H]\right)-\frac{1}{3}HB_zB_{r,s}^2\left(\frac{d}{dr}[\ln(rB_{r,s})]-\frac{d}{dr}[\ln H]\right)\Bigg]\Bigg].\end{aligned} \tag{2.65}$$

It is clear from this equation that the azimuthal field is pivotal in causing Hall drift in the radial direction; $B_{\phi,s}$ should not be neglected, even in axisymmetric models.

2.3.6 Radial field component, $B_{r,s}$

Contopoulos et al. (1998) found that, as with the radial component of gravity, one could calculate $B_{r,s}$ iteratively for more accurate similarity solutions, however the behaviour of the disc at $t \geq 0$ was sufficiently well described by the monopole expression that they did not need to adopt a more complete method of calculating the radial field component. Following their example the monopole approximation to $B_{r,s}$ is also adopted here to simplify the calculation of the field:

$$B_{r,s} = \frac{\Psi(r,t)}{2\pi r^2}. \tag{2.66}$$

This simplification, which was also used by Krasnopolsky and Königl (2002), is not expected to introduce any significant errors to the calculations.

2.4 Vertical Angular Momentum Transport

The vertical angular momentum transport above and within the pseudodisc is achieved by magnetic braking, especially during the dynamic collapse phase inwards of the magnetic diffusion shock. It is assumed that magnetic braking remains the dominant angular momentum transport mechanism during the subsequent evolution of the core,

although it is likely that a centrifugally-driven disc wind may dominate in the innermost rotationally-supported disc. The approach to modelling the magnetic braking adopted here is adapted from that of Basu and Mouschovias (1994) for the pre-point mass formation collapse phase. This formulation is not well-defined in the innermost rotationally-supported regions of the disc, where the calculated magnetic braking becomes stronger than is expected and the angular momentum transport is expected to be dominated by a disc wind (this is discussed in more detail in Chapter 6). A cap is then placed upon the azimuthal magnetic field component in order to ensure that it does not greatly exceed the vertical component; because of this the magnetic braking prescription is not expected to introduce significant errors into the inner regions of the calculations.

The geometry of the magnetic field is illustrated in Figure 2.1; the magnetic field is frozen into the low-density, constant-pressure external medium, which has density ρ_{ext} and angular velocity Ω_b. Within the external medium the magnetic field assumes the value $\mathbf{B} = B_{ref}\hat{z}$, and the exterior flux tubes corotate with the core. Because the transition region has a low moment of inertia relative to the core, and the crossing time for Alfvén waves is always much smaller than the evolutionary time of the core, the transition region can relax to a steady state during all stages of contraction (Basu and Mouschovias, 1994).

The induction equation under IMHD implies that

$$(B_p \cdot \nabla)\Omega = 0, \tag{2.67}$$

where B_p is the poloidal field, so that the angular velocity Ω is constant on a magnetic surface. The force equation is similarly reduced to

$$(B_p \cdot \nabla) r B_\phi = 0, \tag{2.68}$$

which further implies that rB_ϕ does not change along the field lines. The neutral particles carry the torque and angular momentum is carried upwards by torsional Alfvén waves generated by the rotation of the disc.

Over a period of time dt an amount of material equal to $2\pi\rho\, r_{ref} dr_{ref}$ moves from the undisturbed position $r_{ref}dr_{ref}$ in the external medium along a flux tube with angular velocity Ω to a radius rdr at the disc surface. The angular momentum of the gas goes as

$$dJ = -[2\pi\rho_{ext} r_{ref} dr_{ref}](V_{A,ext}dt) r_{ref}^2(\Omega - \Omega_b), \tag{2.69}$$

where $V_{A,ext}$, the external Alfvén speed, is given by

$$V_{A,ext} = \frac{B_{ref}}{\sqrt{4\pi\rho_{ext}}}. \tag{2.70}$$

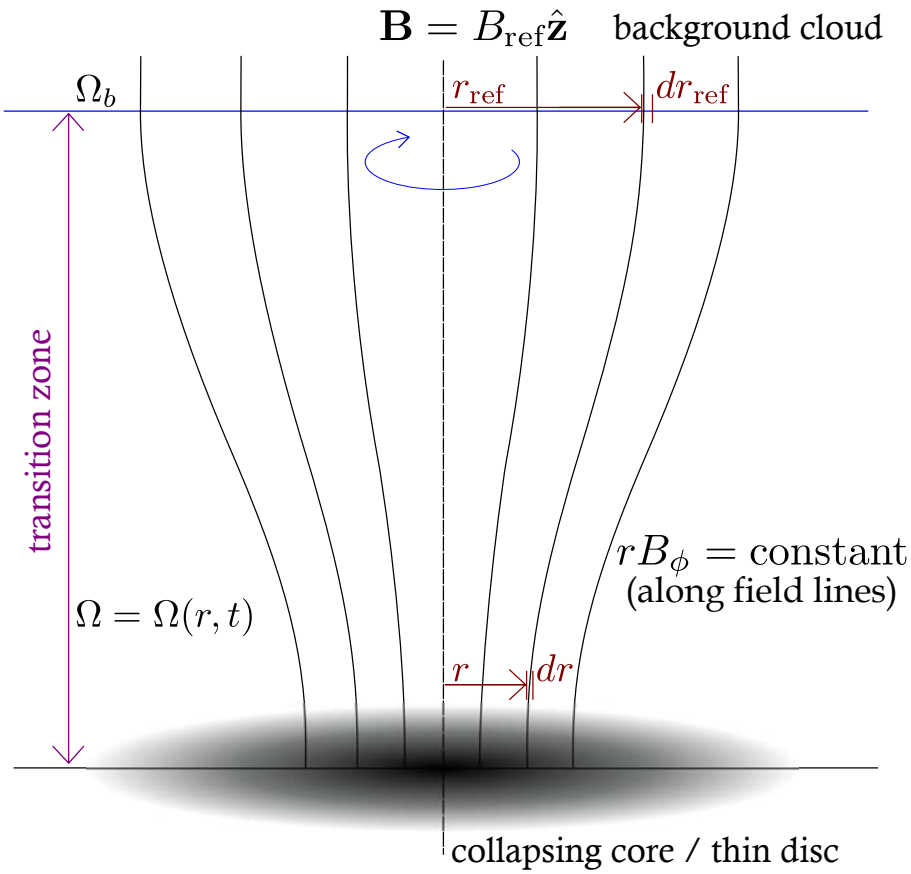

Figure 2.1: The geometry of the thin (pseudo) disc, background cloud and magnetic field lines, illustrating the terms used to derive the angular momentum transport in the disc. The field is assumed to be vertical at the disc midplane and in the background cloud.

For purely azimuthal motions in the external medium, the total angular momentum in each flux tube is conserved. This angular momentum must be removed from the disc at a rate equal to

$$\frac{dJ}{dt} = -2\pi r_{ref}^2 v_{A,ext}\rho_{ext}(\Omega - \Omega_b)r_{ref}dr_{ref}, \tag{2.71}$$

which gives a torque on the disc equal to

$$N = -\frac{2\pi r_{ref}^2 (V_{A,ext}\rho_{ext})(\Omega - \Omega_b)r_{ref}dr_{ref}}{\pi r dr}. \tag{2.72}$$

The amount of flux remains constant along flux tubes, so that the flux through the disc inside of a radius r is equal to the amount of flux through the cylindrical external cloud inside of the radius r_{ref}:

$$\Psi = \int_0^r 2\pi r' B_{z,eq}(r')dr' = \pi r_{ref}^2 B_{ref}, \tag{2.73}$$

where $B_{z,eq}$ is the value of B_z at the midplane of the disc. Thus

$$d\Psi = 2\pi r B_{z,eq} dr = 2\pi r_{ref} B_{ref} dr_{ref} \tag{2.74}$$

and

$$\frac{r_{ref} dr_{ref}}{r dr} = \frac{B_{z,eq}}{B_{ref}}, \tag{2.75}$$

so that the torque in Equation 2.72 becomes

$$\begin{aligned} N &= -\frac{2r_{ref}^2(\Omega - \Omega_b)B_{z,eq}}{B_{ref}} \left(\frac{B_{ref}\rho_{ext}}{\sqrt{4\pi\rho_{ext}}} \right), \\ &= -\frac{(\Omega - \Omega_b)B_{z,eq}(\Psi/2\pi)}{\pi V_{A,ext}}. \end{aligned} \tag{2.76}$$

The torque per unit area on the disc is given by

$$N = \frac{r B_{z,eq} B_{\phi,s}}{2\pi}, \tag{2.77}$$

and combining Equations 2.76 and 2.77 gives the steady state azimuthal component of the magnetic field at the surface of the disc:

$$B_{\phi,s} = -\frac{\Psi}{\pi r^2} \frac{(r\Omega - r\Omega_b)}{V_{A,ext}}. \tag{2.78}$$

It is clear that the properties of the external medium determine the conditions at the disc surface. This steady state approximation requires that the ratio of the Alfvén travel time in the external medium to the initial radius of the cloud be less than the evolutionary timescale, which scales with r as $\sim r/|V_r|$. For the rotationally-supported discs presented in this work $|V_r| \lesssim c_s$ (and $|V_r| \to 0$ as $r \to 0$), which is much smaller than $V_{A,ext} \approx 5c_s$, the Alfvén speed for the adopted temperature in the gas of 10K; this implies that the assumption of rapid braking of the core should not introduce large errors into the solutions.

The angular velocity Ω is given by the equation

$$\Omega = \frac{1}{r}(V_\phi + V_{B\phi}), \tag{2.79}$$

where, using $\eta_P = \eta_A + \eta_\parallel$,

$$V_{B\phi} = -\frac{1}{B}\left[\eta_H (\nabla \times \mathbf{B})_\perp - \eta_P (\nabla \times \mathbf{B})_\perp \times \hat{\mathbf{B}}\right]_\phi. \tag{2.80}$$

This equation is then expanded out to become

$$\begin{aligned} V_{B\phi} = -\frac{1}{B^2}\Bigg[&\frac{\eta_H}{B}\left((B_z^2 + B_r^2)\left(\frac{\partial B_z}{\partial r} - \frac{\partial B_z}{\partial z} \right) + B_\phi B_z \frac{1}{r}\frac{\partial}{\partial r}(rB_\phi) - B_\phi B_r \frac{\partial B_\phi}{\partial z} \right) \\ &- \frac{\eta_P}{B^2}(B_r^2 + B_\phi^2 + B_z^2)\left(\frac{B_r}{r}\frac{\partial}{\partial r}(rB_\phi) + B_z \frac{\partial B_\phi}{\partial z} \right) \Bigg], \end{aligned} \tag{2.81}$$

which is then vertically-integrated over the thin disc as in subsection 2.3.5 to obtain

$$\begin{aligned} HV_{B\phi}\left(\frac{1}{3}B_{r,s}^2+\frac{1}{3}B_{\phi,s}^2+B_z^2\right) &= \frac{\eta_P}{B^2}\Bigg[B_zB_{\phi,s}\left(\frac{1}{3}B_{r,s}^2+\frac{1}{3}B_{\phi,s}^2+B_z^2\right) \\ &\quad + HB_{r,s}B_{\phi,s}\left(\frac{B_{r,s}^2}{5}+\frac{B_{\phi,s}^2}{5}+\frac{B_z^2}{3}\right)\left(\frac{d}{dr}[\ln(rB_{\phi,s})]+\frac{d}{dr}[\ln(rB_{r,s})]-2\frac{d}{dr}[\ln H]\right)\Bigg] \\ &\quad - \frac{\eta_H}{B}\Bigg[\left(\frac{B_{r,s}^2}{3}+B_z^2\right)\left(B_{r,s}-H\frac{\partial B_z}{\partial r}\right)+\frac{1}{3}HB_zB_{r,s}^2\left(\frac{d}{dr}[\ln(rB_{r,s})]-\frac{d}{dr}[\ln H]\right) \\ &\quad + \frac{1}{3}B_{r,s}B_{\phi,s}^2-\frac{1}{3}HB_zB_{\phi,s}^2\left(\frac{d}{dr}[\ln(rB_{\phi,s})]-\frac{d}{dr}[\ln H]\right)\Bigg]. \end{aligned} \tag{2.82}$$

Most of the terms in Equation 2.81 have direct analogies in Equation 2.51, and the individual steps of the integration are not reproduced here.

This equation is simplified by omitting any terms of order $\mathcal{O}(H/r)$ save for the $[B_{r,s}-H(\partial B_z/\partial r)]$ term, which is important in refining the structure of the magnetic diffusion shock. This simplification is explained in more detail and justified below in Section 2.5; and the final form of $V_{B\phi}$ is then:

$$V_{B\phi}=-\frac{1}{H}\left[\frac{\eta_H}{B}\left(B_{r,s}-H\frac{\partial B_z}{\partial r}\right)-\frac{\eta_P}{B^2}B_zB_{\phi,s}\right]; \tag{2.83}$$

this equation is equivalent to the ion-neutral drift velocity adopted by Krasnopolsky and Königl (2002, equation 9), with the inclusion of terms describing the effect of Hall diffusion.

The Ω_b term is then dropped from Equation 2.78 as the molecular cloud rotation rate is slow compared with that of the collapsing material. Rotation is dynamically important in the inner regions of the solutions presented in this thesis, while it is not important in most molecular clouds (see Section 1.1 and the references therein), so it is reasonable to declare that $\Omega \gg \Omega_b$ and dismiss Ω_b as small.

The external Alfvén speed, $V_{A,ext}$, is treated as a constant with respect to the isothermal sound speed in these calculations, and is parameterised by the formula

$$\alpha=\frac{c_s}{V_{A,ext}}, \tag{2.84}$$

where α is a constant, typically of order 0.1 in the solutions. This scaling of $V_{A,ext}$ is also a reasonable assumption, as the observations by Crutcher (1999) indicated that $V_A \approx 1$ km s^{-1} over at least four orders of magnitude in density ($\sim 10^3$–10^7 cm^{-3}) in their observed molecular clouds.

Equations 2.83 and 2.84 are substituted into 2.78 to find that

$$B_{\phi,s}=-\frac{\Psi\alpha}{\pi r^2c_s}\left[\frac{J}{r}-\frac{\eta_H}{B}\left(B_{r,s}-H\frac{\partial B_z}{\partial r}\right)\right]\left[1+\frac{\Psi\alpha}{\pi r^2c_s}\frac{\eta_P}{B^2}\frac{B_z}{H}\right]^{-1}. \tag{2.85}$$

Note that $B = \sqrt{B_{r,s}^2 + B_{\phi,s}^2 + B_z^2}$, so that the terms featuring $\eta_{H,P}/B^{1,2}$ have an implied $B_{\phi,s}$ dependence. This is typically solved for numerically when calculating the azimuthal field component.

For the inner solutions, Ω increases with decreasing r (proportional to $r^{-3/2}$ in the Keplerian disc solution and r^{-1} in the free fall solution); this would make $B_{\phi,s}$ the dominant field component at the surface near to the central point mass. Such behaviour is not expected in a real disc, where internal kinks of the field and magnetohydrodynamical instabilities (for example, the magnetorotational instability) should reduce the value of B_ϕ at the surface. An artificial limit on $B_{\phi,s}$ is imposed so that

$$|B_{\phi,s}| \leq \delta B_z, \tag{2.86}$$

where δ is a parameter of the model usually chosen to be $\delta = 1$ in order to ensure that the azimuthal field component does not exceed the vertical component. Krasnopolsky and Königl (2002) point out that this value quite conveniently corresponds to that expected for a rotationally-supported ambipolar diffusive disc where the vertical angular momentum transport is dominated by a centrifugally-driven wind.

Applying this cap to Equation 2.85 then gives the final equation for $B_{\phi,s}$:

$$B_{\phi,s} = -\min\left[\frac{\Psi\alpha}{\pi r^2 c_s}\left[\frac{J}{r} - \frac{\eta_H}{B}\left(B_{r,s} - H\frac{\partial B_z}{\partial r}\right)\right]\left[1 + \frac{\Psi\alpha}{\pi r^2 c_s}\frac{\eta_P}{B^2}\frac{B_z}{H}\right]^{-1}; \delta B_z\right]. \tag{2.87}$$

2.5 Further Simplifications

The disc equations are further simplified by recognising that the thin disc approximation adopted earlier states that $H \ll r$, this in turn means that terms of order $\mathcal{O}(H/r)$ are small in comparison with other terms and can then be dropped from the equations.

The only term of order $\mathcal{O}(H/r)$ that was found to influence the solutions of Krasnopolsky and Königl (2002) was the $[B_{r,s} - H(\partial B_z/\partial r)]$ term in the radial momentum equation, which was necessary to refine the structure of the magnetic diffusion shock. A similar result is obtained in these solutions, and the term is retained in all of the equations in which it appears, including Equation 2.83 where it is the dominant component of the Hall diffusion term in $V_{B\phi}$.

It is expected that B_z will generally be the dominant field component within the disc, although due to the cap placed upon $B_{\phi,s}$ and the monopole approximation adopted for $B_{r,s}$ it may not be the dominant term at the disc surface. In order to reproduce the results and equations of Krasnopolsky and Königl (2002), the B_z^2 terms are kept preferentially over those of the other field components of the same order in the induction and azimuthal field drift equations.

Taking all of these into account gives the simplified set of equations:

$$\frac{\partial \Sigma}{\partial t} + \frac{1}{r}\frac{\partial}{\partial r}(rV_r\Sigma) = 0, \tag{2.88}$$

$$\frac{\partial V_r}{\partial r} + V_r\frac{\partial V_r}{\partial t} = g_r - \frac{c_s^2}{\Sigma}\frac{\partial \Sigma}{\partial r} + \frac{B_z}{2\pi\Sigma}\left(B_{r,s} - H\frac{\partial B_z}{\partial r}\right) + \frac{J^2}{r^3}, \tag{2.89}$$

$$\frac{\partial J}{\partial t} + V_r\frac{\partial J}{\partial r} = \frac{rB_zB_{\phi,s}}{2\pi\Sigma}, \tag{2.90}$$

$$\frac{\Sigma c_s^2}{2H} = \frac{\pi}{2}G\Sigma^2 + \frac{GM_c\rho H^2}{2r^3} + \frac{1}{8\pi}\left(B_{r,s}^2 + B_{\phi,s}^2 - B_{r,s}H\frac{\partial B_z}{\partial r}\right), \tag{2.91}$$

and

$$\frac{H}{2\pi}\frac{\partial \Psi}{\partial t} = -rHV_rB_z - r\eta_\parallel\left[B_{r,s} - H\frac{\partial B_z}{\partial r}\right] - \frac{r\eta_H}{B}B_zB_{\phi,s} - \frac{r\eta_A}{B^2}\left[B_{r,s} - H\frac{\partial B_z}{\partial r}\right]B_z^2. \tag{2.92}$$

2.6 Self-Similar Form of the Equations

With the assumption that the disc is axisymmetric and thin, the collapse behaviour resembles the shape of the inside-out collapse models described in Chapter 1, where at any instant in time the solution looks like a stretched version of itself at previous times; this fractal-like behaviour is referred to as self-similarity. The pseudodisc forms as a collapse wave (referred to as the magnetic diffusion shock) propagates outwards at the speed of sound, and similarly the outer boundary of the inner rotationally-supported disc or free fall collapse region moves outwards at the sound speed.

Gravitational collapse occurs over many orders of magnitude in radius and density, so that the point mass has negligible dimensions in comparison with the accretion flow. The self-similarity of the waves of infall arises because of the lack of characteristic time and length scales in the flow. The only dimensional quantities that effect the flow are the magnetic field $\mathbf{B}$, the diffusion coefficients $\eta_{\parallel,H,A}$, the gravitational constant G, the isothermal sound speed c_s, the local radius r and the instantaneous time t; this means that, except for scaling factors, all of the flow variables may be written as functions of a similarity variable x, which is defined as

$$x = \frac{r}{c_s t}. \tag{2.93}$$

At a temperature of $T = 10$ K in a molecular cloud core of typical composition, $c_s = 0.19$ km s^{-1}; Krasnopolsky and Königl (2002) noted that for this value of the sound speed $x = 1$ corresponds to a distance of $r \approx 6\times10^{15}$ cm (400 AU) when $t = 10^4$ yr (which is the characteristic age of a Class 0 YSO) and to a distance of $r \approx 6\times10^{16}$ cm (4,000 AU) when $t = 10^5$ yr (the age of a Class 1 YSO). The Class 0 YSO IRAM 04191 has a dense inner disc-like structure that resembles a tilted ring with an average

radius of $r_0 \sim 1400$ AU (Lee et al., 2005) — this is of the same order of magnitude as the centrifugal shock radius in the disc-forming solutions at the same age.

The physical quantities are then expressed as the product of a nondimensional flow variable that depends only upon x and a dimensional part constructed from c_s, G and t. These are:

$$\Sigma(r,t) = \left(\frac{c_s}{2\pi G t}\right)\sigma(x), \qquad g_r(r,t) = \left(\frac{c_s}{t}\right)g(x), \tag{2.94}$$

$$V_r(r,t) = c_s u(x), \qquad H(r,t) = c_s t h(x), \tag{2.95}$$

$$V_\phi(r,t) = c_s v(x), \qquad J(r,t) = c_s^2 t j(x), \tag{2.96}$$

$$M(r,t) = \left(\frac{c_s^3 t}{G}\right)m(x), \qquad \dot{M}(r,t) = \left(\frac{c_s^3}{G}\right)\dot{m}(x), \tag{2.97}$$

$$\mathbf{B}(r,t) = \left(\frac{c_s}{G^{1/2}t}\right)\mathbf{b}(x), \qquad \Psi(r,t) = \left(\frac{2\pi c_s^3 t}{G^{1/2}}\right)\psi(x), \tag{2.98}$$

$$\text{and } \eta_{\parallel,H,A} = c_s^2 t \eta'_{\parallel,H,A}. \tag{2.99}$$

These equations take the same form and notation as those in Krasnopolsky and Königl (2002), with the addition of extra diffusion coefficients to model the magnetic field diffusion more completely.

The Ohmic and ambipolar diffusion terms scale together, to a zeroth-order approximation, as they possess a similar dependence upon B and appear in the induction equation and the azimuthal field component equation multiplied with the same magnetic field terms. Because the field within the thin disc is effectively vertical, both ambipolar and Ohmic diffusion influence the field drift in the same manner (see Figure 1.1). While one type of diffusion may dominate over the other at any individual point in the disc (in general, ambipolar diffusion dominates in the outer regions where the density is low and Ohmic diffusion dominates in the innermost regions where the density is high), only one term is needed in order to study the change in the disc behaviour introduced by the Hall diffusion term that is of most interest in this work. The Ohmic and ambipolar diffusion terms are then combined into a single term parameterised by the dimensionless constant $\tilde{\eta}_A$, that for simplifying the discussion is referred to as the ambipolar diffusion parameter.

The ambipolar diffusion coefficient in a molecular cloud core without grains is given (in cgs units) by the equation

$$\eta_A = \frac{B^2}{4\pi\gamma\rho_i\rho}, \tag{2.100}$$

where $1/\gamma\rho_i = \tau_{ni}$ is the neutral-ion momentum exchange timescale, parameterised as

$$\tau_{ni} = \frac{\tilde{\eta}_A}{\sqrt{4\pi G\rho}}; \tag{2.101}$$

the nondimensional ambipolar diffusion parameter $\tilde{\eta}_A$ is a constant of the model (simply denoted η in the solutions of Krasnopolsky and Königl, 2002). η_A/B^2 is then self-similarised using the scalings above to give

$$\frac{\eta'_A}{b^2} = \tilde{\eta}_A \frac{h^{3/2}}{\sigma^{3/2}}; \tag{2.102}$$

it is important to note that the self-similarity of the solution depends upon the relationship $\rho_i \propto \rho^{1/2}$ as discussed in Section 1.2 (and Elmegreen, 1979).

As a matter of pragmatism, a similar scaling with respect to the density and scale height is adopted for the Hall diffusion parameter, η_H. By stating that the self-similar Hall diffusion coefficient scales as

$$\frac{\eta'_H}{b} = \tilde{\eta}_H b \frac{h^{3/2}}{\sigma^{3/2}}, \tag{2.103}$$

where $\tilde{\eta}_H$ is the constant nondimensional Hall diffusion parameter used to characterise the solutions, the ratio of the nondimensional ambipolar and Hall diffusion parameters becomes the most important factor in determining the magnetic behaviour of the similarity solutions. In truth, the Hall diffusion coefficient could be scaled with respect to the density and field strength by multiplying the nondimensional Hall parameter by any function of the similarity variable x and the fluid variables. This topic is discussed in more detail in Section 6.3, where an alternate scaling is proposed for future work on the self-similar collapse model. The scaling of η'_H given in Equation 2.103 is appropriate for a molecular cloud core with grains acting as the dominant positive charge carriers.

For convenience the variable $w \equiv x - u$ is used to simplify the equation set. The similarity variables are then used to rewrite Equations 2.49 and 2.88–2.92 in self-similar form:

$$\frac{d\psi}{dx} = x b_z, \tag{2.104}$$

$$\frac{dm}{dx} = x\sigma, \tag{2.105}$$

$$(1-w^2)\frac{1}{\sigma}\frac{d\sigma}{dx} = g + \frac{b_z}{\sigma}\left(b_{r,s} - h\frac{db_z}{dz}\right) + \frac{j^2}{x^3} + \frac{w^2}{x}, \tag{2.106}$$

$$\frac{dj}{dx} = \frac{1}{w}\left(j - \frac{x b_z b_{\phi,s}}{\sigma}\right), \tag{2.107}$$

$$\left(\frac{\sigma m_c}{x^3} - b_{r,s}\frac{db_z}{dx}\right)h^2 + \left(b_{r,s}^2 + b_{\phi,s}^2 + \sigma^2\right)h - 2\sigma = 0, \tag{2.108}$$

and

$$\psi - x w b_z + \tilde{\eta}_H x b_{\phi,s} b_z b h^{1/2}\sigma^{-3/2} + \tilde{\eta}_A x b_z^2 h^{1/2}\sigma^{-3/2}\left(b_{r,s} - h\frac{db_z}{dx}\right) = 0. \tag{2.109}$$

These equations are augmented by the self-similar definitions

$$m = xw\sigma, \tag{2.110}$$

$$\dot{m} = -xu\sigma \tag{2.111}$$

$$\text{and } g = -\frac{m}{x^2}, \tag{2.112}$$

while the other field components are given by

$$b_{r,s} = \frac{\psi}{x^2} \tag{2.113}$$

and

$$b_{\phi,s} = -\min\left[\frac{2\alpha\psi}{x^2}\left[\frac{j}{x} - \frac{\tilde{\eta}_H h^{1/2} b}{\sigma^{3/2}}\left(b_{r,s} - h\frac{db_z}{dx}\right)\right]\left[1 + \frac{2\alpha\tilde{\eta}_A h^{1/2}\psi b_z}{x^2\sigma^{3/2}}\right]^{-1}; \delta b_z\right]. \tag{2.114}$$

These equations completely describe the collapse of the core into a pseudodisc and the accretion onto the central point mass (potentially through a rotationally-supported disc). The equations are the same as equations 20–32 of Krasnopolsky and Königl (2002), save for the induction and azimuthal field equations which contain new terms describing the effect of Hall diffusion. In the ambipolar diffusion limit, $\tilde{\eta}_H = 0$, Equations 2.104–2.114 reduce to those of Krasnopolsky and Königl (2002), allowing direct comparisons to be made between the similarity solutions from both models.

In order to solve the collapse equations a good understanding of the asymptotic boundary conditions of the collapse (which take the form of power law relations in x) is necessary to ensure that the solutions match onto observations of collapsing cores and protostellar discs. While the innermost boundary conditions are derived explicitly in the following chapter, the outer boundary conditions describing a supercritical molecular cloud core at the moment of point mass formation are discussed below.

2.7 The Outer Solution

The outer boundary of the self-similar collapse is chosen to match the density and magnetic profile of a molecular cloud core contracting quasistatically under ambipolar diffusion until it has just become supercritical and a point mass forms at the centre (e.g. Shu, 1977; Shu et al., 1987). Such a description is chosen because while the similarity variable $x = r/c_s t$ is undefined at $t = 0$, $x \to \infty$ also corresponds to $r \to \infty$ and so the initial conditions of the collapse may also be regarded as the outer boundary conditions of a core that is just starting to collapse. Such cores are described by the equations for singular isothermal spheres, which have a density profile $\rho \propto r^{-2}$ (Larson, 1969;

Penston, 1969; Shu, 1977; Whitworth and Summers, 1985; McKee and Ostriker, 2007). The surface density is then given by

$$\Sigma(t=0) = \frac{Ac_s^2}{2\pi G r} \tag{2.115}$$

where A is a constant parameter of the core. This density profile matches observations of cores (e.g. André et al., 2000; Ward-Thompson et al., 2007, and the references within) and simulations of cores produced by turbulent compression (Ballesteros-Paredes et al., 2007) or contracting under ambipolar diffusion (Basu and Mouschovias, 1994). This is then self-similarised using Equation 2.94 into the outer boundary condition

$$\sigma(x \to \infty) = A\, x^{-1}; \tag{2.116}$$

the value of A is determined from the initial accretion rate of the core, which is discussed further below.

Magnetically supercritical cores that are contracting slowly have typical observed radial infall speeds of around 0.05–0.10 km s^{-1} (Lee et al., 2001). The initial state of the model core is taken to have a spatially-constant radial inflow velocity

$$V_r(t=0) = u_0\, c_s, \tag{2.117}$$

where u_0 is the constant nondimensional velocity, which has the self-similar form:

$$u(x \to \infty) = u_0 \tag{2.118}$$

(using Equation 2.95). For an isothermal molecular cloud core at $T = 10$ K, the sound speed is given by $c_s = 0.19$ km s^{-1}, so u_0 must be of order unity to match observed values of core inflow. The similarity solutions presented in this work use values of $u_0 \in -[0.1, 1.5]$ as the outer boundary condition, which are within the range of values observed in molecular cloud cores by Lee et al. (2001).

Because the infall velocity is constant, so too is the accretion rate, which is determined by the equation

$$\dot{M}_0 = -\frac{Au_0c_s^3}{G}\,. \tag{2.119}$$

A constant accretion rate may not be strictly realistic, as accretion onto stars and cores are thought to be time-variable, however it is required to preserve the self-similarity of the collapse solutions. Equation 2.119 may be expressed in self-similar form using Equation 2.97 in the limit of large x to give the dimensionless enclosed mass

$$m(x \to \infty) = Ax. \tag{2.120}$$

Equation 2.105 shows that this is equivalent to the boundary condition in Equation 2.116; because they are not unique only one of these relations may be used to find the

similarity solutions. In the numerical solutions of Ciolek and Königl (1998) for the collapse of a nonrotating magnetic core with ambipolar diffusion the mass accretion rate at point mass formation was found to be $\dot{M} \simeq 5$ $M_\odot$ Myr^{-1}. This corresponds to a nondimensional parameter $A \simeq 3$, which is the value used in the self-similar calculations of Contopoulos et al. (1998) and Krasnopolsky and Königl (2002). A typical accretion rate for such cores is $A = 3$, as observations show that $\dot{M} \in [1, 10]$ $M_\odot$ Myr^{-1} across many cores (these rates correspond to values of $A \in [0.6, 6.1]$; Lee et al., 2001); and this value of this parameter is held constant throughout this work in order to match the solutions of Krasnopolsky and Königl (2002).

In the outermost regions of the core where the density is low the magnetic field behaviour is described best by ideal MHD; this means that the mass-to-flux ratio is a constant, given by

$$\frac{M}{\Psi} = \frac{\mu_0}{2\pi\sqrt{G}}, \tag{2.121}$$

where μ_0 is a constant parameter of the core. In particular, μ_0 is the dimensionless mass-to-flux ratio in the outer core, and is defined by

$$\mu_0 = \frac{M/\Psi}{(M/\Psi)_{crit}}; \tag{2.122}$$

that is, μ_0 is the ratio of the mass-to-flux ratio in the outermost regions of the core to the critical value for support against gravity derived in Equation 1.9 (Nakano and Nakamura, 1978). Again, to match Krasnopolsky and Königl (2002), the value of $\mu_0 = 2.9$ is adopted for all of the similarity solutions in this work; this particular value was taken from the numerical simulations of Ciolek and Königl (1998). It also matches the observations of Crutcher (1999), which showed that most cores possess mass-to-flux ratios that are more than twice critical. From Equations 2.116 and 2.120 it is then possible to derive the magnetic boundary conditions for a supercritical core under ideal MHD:

$$b_z(x \to \infty) = \frac{\sigma}{\mu_0} \tag{2.123}$$

$$\text{and } \psi(x \to \infty) = \frac{m}{\mu_0}; \tag{2.124}$$

again, these are equivalent and only one may be used to calculate the similarity solutions.

The initial value of the rotational velocity in the outer regions of the molecular cloud core is also spatially-uniform and given by

$$V_\phi = v_0\, c_s, \tag{2.125}$$

which is written in nondimensional form as

$$v(x \to \infty) = v_0. \tag{2.126}$$

The constant v_0 is the initial dimensionless rotational velocity, determined by the expression

$$v_0 \approx \frac{A\Omega_b c_s}{\sqrt{G}B_{ref}} \tag{2.127}$$

(which was derived using the r^{-1} dependance of the core surface density and magnetic field in Basu, 1997). As outlined in Chapter 1, a typical value of the uniform background angular velocity of a molecular cloud core is $\Omega_b = 2 \times 10^{-14}$ rad s^{-1} (Goodman et al., 1993; Kane and Clemens, 1997, and the other references in Section 1.1) and the background magnetic field may be taken to be $B_{ref} = 30$ μG (Crutcher, 1999). Substituting these and the values of A and c_s given above into Equation 2.127 gives the value of the initial rotational velocity to be $v_0 = 0.15$. This is a factor of 10 larger than that found in Basu (1997), however, the range of observed core velocities is $v_0 \in [0.01, 1.0]$, and the dependence of the similarity solutions on the initial core rotational velocity is explored in Chapter 4, where it is shown that the rotational velocity directly influence the size of the inner Keplerian disc. The Hall similarity solutions presented in Chapter 5 possess a constant value of $v_0 = 0.73$ for the rotational velocity in order to facilitate comparison with the fiducial ambipolar diffusion solution of Krasnopolsky and Königl (2002).

To summarise, the outer boundary conditions of the collapse, which also serve as initial conditions at point mass formation, are described by the set of unique self-similar asymptotic equations:

$$\sigma \rightarrow \frac{A}{x}, \tag{2.128}$$

$$b_z \rightarrow \frac{\sigma}{\mu_0}, \tag{2.129}$$

$$u \rightarrow u_0 \tag{2.130}$$

$$\text{and } v \rightarrow v_0, \tag{2.131}$$

where A, μ_0, u_0 and v_0 are the parameters that describe the outer collapse. In the similarity solutions presented in this work, these constants take on the values listed in Table 2.1 unless explicitly stated. These conditions match those of Krasnopolsky and Königl (2002), as neither Hall nor ambipolar diffusion are expected to be important in the low density outer regions where ideal MHD is dominant.

The boundary conditions that describe the collapse behaviour in the innermost regions of self-similar space (corresponding to $r \rightarrow 0$ or $t \rightarrow \infty$) are less straightforward than those on the outer boundary. These are influenced by both ambipolar and Hall diffusion, which determine the surface density and the accretion rate onto the central mass, and by the strength of the magnetic braking within the core, which slows the rotation of the gas and may prevent the formation of a rotationally-supported disc

boundary condition	value
A	3
μ_0	2.9
u_0	-1
v_0	0.15

Table 2.1: Outer boundary conditions describing a molecular cloud core that is supercritical at point mass formation. The fiducial value of v_0 listed in this table (derived above using Equation 2.127) is lower than that used as a boundary condition for calculating the Hall similarity solutions ($v_0 = 0.73$), but both are within the large range of observed core rotational velocities, $v_0 \in [0.01, 1.0]$ (Goodman et al., 1993).

around the protostar. Two sets of inner boundary conditions satisfy the collapse equations as $x \to 0$: these are similarity solutions both with and without an inner Keplerian disc. The derivation of these asymptotic power law solutions, and their individual applicability and dependence upon the magnetic parameters of the core are the focus of the following chapter.

Chapter 3

The Inner Asymptotic Solutions

Whether or not a rotationally-supported disc forms as a result of the initial collapse of a molecular cloud core is a point of contention in current simulations of star formation. The previously-accepted model for innermost regions of the collapsing flow says that the conservation of angular momentum during collapse results in the progressive increase of the centrifugal force, which eventually halts the infalling gas and leads to the development of a central mass surrounded by a flattened rotationally-supported disc. This has recently been called into question by both numerical simulations and observations of young stars.

In particular, Mellon and Li (2009) have shown that no discs could form around the protostars in their numerical MHD simulations unless the calculations were started with very dense cores or unreasonably low ionisation rates. Hennebelle and Ciardi (2009) and Ciardi and Hennebelle (2010) examined the influence of the orientation of the field with respect to the axis of rotation in the core, and found that disc formation was suppressed for cores with an initial nondimensional mass-to-flux ratio of $\mu_0 \simeq 3$ when the magnetic field and rotational axes are perpendicular and for $\mu_0 \lesssim 5 - 10$ when the field was aligned with the axis of rotation. However, the observations of Crutcher (1999) showed that molecular cloud cores typically possess mass-to-flux ratios that are $\mu_0 < 5$, which would preclude disc formation based upon the results of Hennebelle and Ciardi (2009). Price and Bate (2007) compared hydrodynamical and magnetohydrodynamical simulations and found that protostar formation was delayed in calculations with a magnetic field; they also found that magnetic pressure support causes the suppression of fragmentation within a forming disc. These results present a complicated picture in which Keplerian disc formation is not a certain consequence of the star formation process.

Observations have also cast doubt on the star-and-disc formation model. Stassun et al. (2001, following up on the observations of Stassun et al. (1999)) found in their

observations a population of fifteen slowly-rotating ($P_{rot} > 4$ days) pre-main-sequence stars that show no evidence of circumstellar discs. This result was unexpected, as it had previously been believed that such slowing of the angular momentum of young stars could only occur so early in the collapse process through interactions between the protostar and a protostellar disc (e.g. Königl, 1991; Ghosh and Lamb, 1979a,b).

The semianalytic solutions of Krasnopolsky and Königl (2002, as well as the similarity solutions presented in Chapter 5) demonstrated disc formation for cores with $\mu_0 < 5$, however they were also able to show that no disc would form if the magnetic braking is particularly strong or the initial cloud rotation rate too slow. Shu et al. (2006) describe the problem of forming discs as a further manifestation of the magnetic flux problem outlined in Chapter 1 (while others and this work refer to it as the magnetic braking catastrophe); they also showed that the addition of non-ideal MHD processes make it possible to dissipate the flux and form a thin disc (in their particular calculations with numerical reconnection they chose to include Ohmic resistivity).

For the self-similar collapse equations developed in the preceding chapter there are two distinct power law similarity solutions for the innermost region: one in which a rotationally-supported disc forms and the fluid accretes slowly onto the central object, and a second in which the material supersonically falls onto the central protostar in a magnetically-diluted free fall. This chapter presents these similarity solutions, the dominant physics in each and the initial conditions in the molecular cloud core that determine whether or not a disc may form during collapse. The implications of these solutions on the dichotomy of results that form the magnetic braking catastrophe are also discussed.

3.1 Derivation

In the innermost regions of the gravitational collapse of a molecular cloud core, the self-similar collapse equations derived in Chapter 2 are satisfied by similarity solutions in which the variables take the form of power laws with respect to the similarity variable, $x = r/c_s t$. These solutions are found by taking the limit of the equations as $x \to 0$; this limit can also be thought of as either of the dimensional limits $r \to 0$ or $t \to \infty$, which are the innermost region and the late stages of collapse respectively.

The similarity solutions to the full collapse process that are presented in Chapters 4 and 5 tend asymptotically towards these power law solutions which are then imposed as boundary conditions on the inner boundary of the collapse calculations. While there may be other mathematically valid similarity solutions to the disc equations in the central regions of the collapse, these are unphysical (typically with negative values of the scale height or surface density) and therefore are not within the scope of this

work.

The two similarity solutions presented here are found by assuming that the collapse variables take the form of a set of power law relations defined by

$$\sigma = \sigma_1 \, x^{-p}, \tag{3.1}$$

$$b_z = b_{z1} \, x^{-q}, \tag{3.2}$$

$$\text{and } j = j_1 \, x^{-r}, \tag{3.3}$$

where the exponents p, q and r are real numbers, and the coefficients σ_1, b_{z1} and j_1 are constants that are found by solving the collapse equations once the exponents have been derived. The other variables are calculated by substituting these equations into the MHD equations and taking the limit as $x \to 0$ to find and equate the dominant terms.

As the differential equation for m depends only on σ and x, Equation 3.1 can be substituted into Equation 2.105 and integrated to give

$$m = m_c + \frac{\sigma_1}{2-p} \, x^{2-p}. \tag{3.4}$$

This equation cannot be simplified further until the value of p is known, or until limits are placed upon p such that one term or the other is dominant. Clearly, the term with the lower exponent of x will be larger when $x \ll 1$, so that for the case when $p < 2$, $x^0 \gg x^{2-p}$, so that the enclosed mass $m \to m_c$; and conversely when $p > 2$, $m \to \sigma_1 x^{2-p}/(2-p)$ as $x \to 0$.

Similarly, the differential equation for the enclosed flux depends only on b_z and x, so that Equation 2.104, when integrated, becomes

$$\psi = \psi_c + \frac{b_{z1}}{2-q} \, x^{2-q}. \tag{3.5}$$

The vertical magnetic field is expected to scale with x in the same manner as the magnetic dominant field component, if it is not itself the dominant component. When $q < 2$ then $\psi = \psi_c$ and $b_{r,s}$ scales as $x^{-2} > x^{-q}$, so that it becomes the dominant scaling term in the magnetic field. In order to maintain the dominance of b_z, the central flux is set to $\psi_c = 0$. This is supported in the literature, as Krasnopolsky and Königl (2002) also drop this term in their description of the inner disc.

Having accepted this rationale for the behaviour of the flux, the radial field component is then defined by the monopole approximation (Equation 2.112) as

$$b_{r,s} = \frac{b_{z1}}{(2-q)} \, x^{-q}, \tag{3.6}$$

which clearly scales with the vertical field component.

The exact scaling of the azimuthal field component cannot be so easily determined, due to the artificial cap that keeps $|b_{\phi,s}| \leq \delta b_z$. This cap implies that $b_{\phi,s}$ can be regarded as scaling with $b_z \sim x^{-q}$ as a first approximation, especially as $b_{\phi,s}$ typically appears in the disc equations summed with another component of the magnetic field, with the precise value of $b_{\phi,s}$ to be determined once the other scalings are known.

The scale height is written as the solution to the quadratic equation for the vertical hydrostatic equilibrium (2.108):

$$h = \frac{\hat{\sigma} x^3}{2\hat{m}_c} \left[-1 + \sqrt{1 + \frac{8\hat{m}_c}{\hat{\sigma}^2 x^3}} \right], \tag{3.7}$$

where

$$\hat{m}_c = m_c - x^3 b_{r,s} \frac{db_z}{dx} \tag{3.8}$$

and

$$\hat{\sigma} = \sigma + \frac{b_{r,s}^2 + b_{\phi,s}^2}{\sigma}\,. \tag{3.9}$$

Applying Equations 3.1–3.6 to $\hat{\sigma}$ and $\hat{m}_c$, these terms become

$$\begin{aligned} \hat{m}_c &= m_c - \frac{b_{z1} x^{3-q}}{(2-q)\sigma_1 x^{-p}} \left(-q b_{z1} x^{-q-1}\right) \\ &= m_c + \frac{q b_{z1}^2}{(2-q)\sigma_1}\, x^{2-2q+p} \end{aligned} \tag{3.10}$$

and

$$\hat{\sigma} = \sigma_1 x^{-p} + \frac{x^p}{\sigma_1} \left[\frac{b_{z1}^2}{(2-q)^2} x^{-2q} + b_{\phi 1}^2 (\sim x^{-2q}) \right]; \tag{3.11}$$

so that for any combination of p and q the behaviour of h can be determined. There are two terms that can be dominant for each of $\hat{\sigma}$ and $\hat{m}_c$, and each applies when the following conditions on p and q are satisfied:

A. $\hat{m}_c = m_c$ $(p > 2q - 2)$ (3.12)

B. $\hat{m}_c = -\frac{x^3 b_{r,s}}{\sigma} \left(\frac{db_z}{dx} \right)$ $(p < 2q - 2)$ (3.13)

C. $\hat{\sigma} = \sigma$ $(p > q)$ (3.14)

D. $\hat{\sigma} = \frac{(b_{r,s}^2 + b_{\phi,s}^2)}{\sigma}$ $(p < q)$ (3.15)

The different regions of pq-space that are delineated by these inequalities are shown in Figure 3.1, where the combinations of A/B and C/D describe particular regions of behaviour for h.

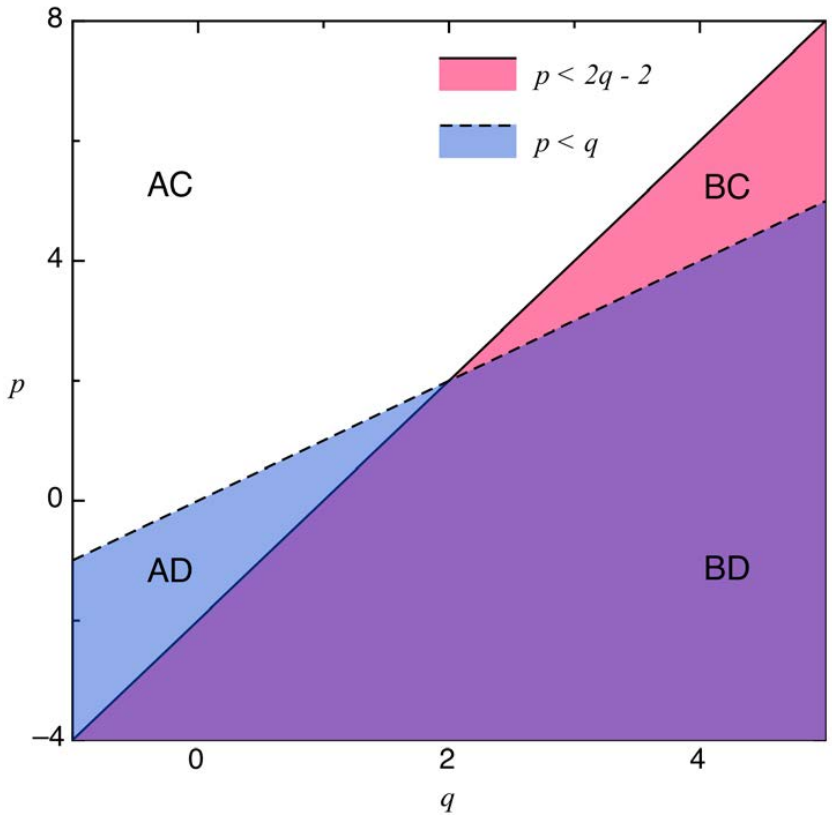

Figure 3.1: The pq-plane used to describe the different regions of pq-space that dictate how the components of h behave. The different regions have been colour coded, for example, the white area in the upper left of the plot represents the region AC where $p > 2q - 2$ and $p > q$.

The scaling of h, with respect to $\hat{m}_c$ and $\hat{\sigma}$, can have one of two different values, depending upon the scalings of the terms within the square root in Equation 3.7; clearly the larger of $8\hat{m}_c/\hat{\sigma}^2 x^3$ and 1 will dominate and determine the behaviour of h. Again, there are two possible cases:

$$\text{a.} \qquad \frac{8\hat{m}_c}{\hat{\sigma}^2 x^3} \ll 1 \qquad h \sim \frac{\hat{\sigma} x^3}{2\hat{m}_c}\left[-1 + \sqrt{1^+}\right] \to 0^+, \tag{3.16}$$

$$\text{and b.} \qquad \frac{8\hat{m}_c}{\hat{\sigma}^2 x^3} \gg 1 \qquad h \sim \sqrt{\frac{2x^3}{\hat{m}_c}}\,. \tag{3.17}$$

Case a, regardless of the region of pq-space in which it is calculated, represents the trivial solution of h and will not be examined further in this work, as any solution that satisfies this condition, while mathematically valid, would represent a state that is intrinsically unphysical. Case b, and the boundary case where $8\hat{m}_c/\hat{\sigma}^2 x^3$ scales as x^0, must be examined in each of the four regions of the pq-plane in order to determine all of the possible similarity solutions of interest for the innermost regions of the gravitational

collapse.

This exploration of pq-space, and the derivation of the two physical similarity solutions to the fluid equations, is presented in Appendix A for the interested reader who wishes to study the solutions in more depth. The first of these is a slowly-accreting Keplerian disc, which is discussed in the following section, while the second is a magnetically-diluted free fall flow onto the central protostar, which is discussed in detail in Section 3.3.

3.2 Keplerian Disc Solution

The first solution (derived in Section A.2 and belonging to the region AC of the pq-plane) is a Keplerian disc, where the material is supported against gravity by its angular momentum, and only slowly accretes onto the central mass. The scale height of the disc and the surface density are both dependent upon the Hall and ambipolar diffusion coefficients, represented here by the nondimensional constants $\tilde{\eta}_H$ and $\tilde{\eta}_A$.

The similarity solution in nondimensional form is given by the set of relations:

$$m = m_c, \tag{3.18}$$

$$\dot{m} = m_c, \tag{3.19}$$

$$\sigma = \sigma_1 \, x^{-3/2}, \tag{3.20}$$

$$h = h_1 \, x^{3/2}, \tag{3.21}$$

$$u = -\frac{m_c}{\sigma_1} \, x^{1/2}, \tag{3.22}$$

$$v = \sqrt{\frac{m_c}{x}}, \tag{3.23}$$

$$j = \sqrt{m_c x}, \tag{3.24}$$

$$\psi = \frac{4}{3} \, b_z x^2, \tag{3.25}$$

$$b_z = \frac{m_c^{3/4}}{\sqrt{2\delta}} \, x^{-5/4}, \tag{3.26}$$

$$b_{r,s} = \frac{4}{3} \, b_z, \tag{3.27}$$

$$\text{and } b_{\phi,s} = -\delta b_z; \tag{3.28}$$

the constant m_c is the nondimensional infall rate onto the central star and δ is the constant parameterising the artificial cap placed upon $b_{\phi,s}$ to prevent it from becoming the dominant field component in the innermost regions of the disc. The coefficients h_1 and σ_1 are constants, determined by the expressions

$$h_1 = \left(\frac{2}{m_c[1 + (f/2\delta)^2]} \right)^{1/2} \tag{3.29}$$

and

$$\sigma_1 = \frac{\sqrt{2m_c}f}{2\delta\sqrt{(2\delta/f)^2+1}}\,, \tag{3.30}$$

where f is a function of the magnetic diffusion parameters, given by the equation

$$f = \frac{4}{3}\tilde{\eta}_A - \delta\tilde{\eta}_H\sqrt{\frac{25}{9}+\delta^2}. \tag{3.31}$$

Rather than continuing to study this solution in the nondimensional form, it is more illuminating to convert these power law relations to dimensional form using Equations 2.94–2.99, so that the Keplerian disc variables are

$$M = \frac{c_s^3 m_c}{G}\,t, \tag{3.32}$$

$$\dot{M} = \frac{c_s^3 m_c}{G}, \tag{3.33}$$

$$\Sigma = \frac{\sigma_1 c_s^{5/2}}{2\pi G}\,\frac{t^{1/2}}{r^{3/2}}, \tag{3.34}$$

$$H = h_1\,\frac{r^{3/2}}{\sqrt{c_s t}}, \tag{3.35}$$

$$V_r = -\frac{m_c}{\sigma_1}\sqrt{\frac{rc_s}{t}}, \tag{3.36}$$

$$V_\phi = \sqrt{\frac{m_c c_s^3 t}{r}}, \tag{3.37}$$

$$J = \sqrt{m_c c_s^3 r t}, \tag{3.38}$$

$$\Psi = \frac{8\pi {c_s}^{9/4} m_c^{3/4}}{3\sqrt{2\delta G}}\,r^{3/4}t^{1/4}, \tag{3.39}$$

$$B_z = \frac{m_c^{3/4} c_s^{9/4}}{\sqrt{2\delta G}}\,\frac{t^{1/4}}{r^{5/4}}, \tag{3.40}$$

$$B_{r,s} = \frac{4}{3}B_z, \tag{3.41}$$

$$\text{and } B_{\phi,s} = -\delta B_z; \tag{3.42}$$

the coefficients σ_1 and h_1 remain those in Equations 3.29–3.31, c_s is the isothermal sound speed and G is the gravitational constant. The disc matter is in Keplerian orbit, with V_ϕ given by the canonical value ($V_\phi = \sqrt{GM/r}$; Newton, 1760). The radial scaling of the surface density ($\Sigma \propto r^{-3/2}$) is that expected from the minimum mass solar nebula (Weidenschilling, 1977) and other simulations of protostellar discs (e.g. Cameron and Pine, 1973); and the magnetic field scaling also matches that from theory, particularly of discs that support disc winds ($B_z \propto r^{-5/4}$; Blandford and Payne, 1982). It is interesting to note that the coefficient of the vertical magnetic field, B_z, does not

depend upon the magnetic diffusion parameters, but rather the nondimensional mass infall rate and the cap placed upon $B_{\phi,s}$.

The azimuthal magnetic field component blows up with respect to the other field components in this small x limit because the azimuthal magnetic field drift speed is slow compared with the Keplerian speed. The model adopted for the vertical angular momentum transport is unable to properly account for the effects of magnetic braking in the small x limit, so $B_{\phi,s}$ takes on the value of the cap placed upon it. If a different scaling for η_H were adopted then Hall diffusion could act to limit $B_{\phi,s}$ in such a way that the cap becomes unnecessary; however, within the context of this disc solution other scalings of η_H lead either to a breakdown of self-similarity, or to a solution in which the diffusion is so strong that the fluid falls rapidly onto the protostar and no rotationally-supported disc may form, in a similar manner to the second similarity solution presented in Section 3.3.

These power laws are the solutions to the following simplified equations:

$$g_r + \frac{J^2}{r^3} = 0, \tag{3.43}$$

$$V_r \frac{\partial J}{\partial r} = \frac{r B_z B_{\phi,s}}{2\pi\Sigma}, \tag{3.44}$$

$$HV_r + \frac{\eta_H}{B} B_{\phi,s} + \frac{\eta_A}{B^2} B_{r,s} B_z = 0, \tag{3.45}$$

$$\frac{GM}{2r^3} H^2 + \pi G \Sigma H - c_s^2 = 0, \tag{3.46}$$

$$\dot{M} = \text{constant}, \tag{3.47}$$

$$J = r V_\phi, \tag{3.48}$$

$$B_{r,s} = \frac{4}{3} B_z, \tag{3.49}$$

$$B_{\phi,s} = -\delta B_z, \tag{3.50}$$

$$\text{and } \Psi = \frac{8}{3} \pi r^2 B_z. \tag{3.51}$$

The induction equation (3.45) can be written quite simply as $V_r + V_{Br} = 0$, that is, the inward radial velocity of the fluid is balanced by the drift of the magnetic field with respect to the gas. Any accretion through the centrifugally-supported disc is regulated by the outward diffusion of the magnetic field against the flow.

The size of the magnetic diffusion parameters determine the build up of fluid relative to the magnetic field in the disc, and the sign of the Hall diffusion term places limits on its size. Should the Hall parameter become too large, and possess the wrong sign, relative to the other diffusion term, then f becomes negative and the surface density with it, which is clearly unphysical. In order to ensure that the induction equation is satisfied and a rotationally-supported disc forms, the diffusion parameters

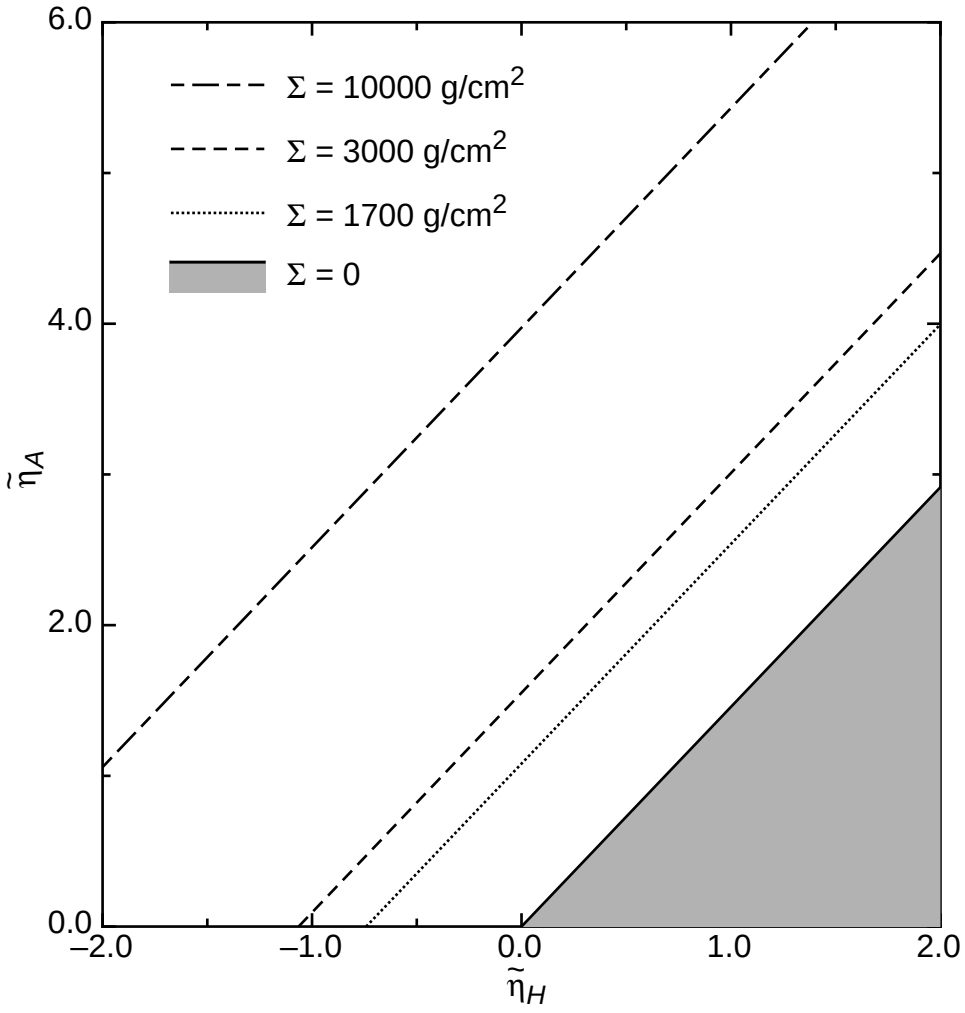

Figure 3.2: Exploration of the relationship between $\tilde{\eta}_H$ and $\tilde{\eta}_A$ in the Keplerian disc solution, for various different values of Σ at $r = 1$ AU and $t = 10,000$ yr, when $\delta = 1$, $c_s = 0.19$ km s^{-1} and $\dot{M} = 10^{-5}$ M$_\odot$ yr^{-1} (which corresponds to $B_z = 1.15$ G). The solid black line corresponds to $\Sigma = 0$, and the shaded region beneath it is unphysical; no centrifugally-supported disc may form in this region of parameter space. The dashed lines above this correspond to $\Sigma = 1700$, 3000 and 10000 g cm^{-2} respectively.

must satisfy the inequality $f \geq 0$, which becomes

$$\tilde{\eta}_A \geq \tilde{\eta}_H \sqrt{\frac{17}{8}} \tag{3.52}$$

for the typical value of $\delta = 1$. The forbidden region of parameter space in which no disc may form is the shaded area in Figure 3.2, with the solid boundary line corresponding to $f = \Sigma = 0$.

As is clear from Figure 3.2, there can be no solution for the core with purely Hall diffusion where the Hall diffusion parameter is positive, as the positive Hall parameter acts to restrain the effects of ambipolar and Ohmic diffusion. However, when the Hall diffusion parameter is negative (corresponding to a reversal of the magnetic field) it acts in the same radial direction as the ambipolar diffusion term, enhancing the diffusion of the magnetic field through the disc. In the case of pure ambipolar diffusion the field moves inward slower than the neutral particles and the solution reduces to that depicted in the inner asymptotic region of the fiducial solution of Krasnopolsky and Königl (2002, equations 51–57).

The plot in Figure 3.2 shows the two-dimensional area of magnetic diffusion parameter space that gives feasible values of the surface density Σ at $r = 1$ AU when $t = 10,000$ years, $c_s = 0.19$ km s^{-1} and $\delta = 1$ for solutions with an accretion rate of $\dot{M}_c = 10^{-5}$ M$_\odot$ yr^{-1} (which corresponds to $B_z = 1.15$ G). The dotted line represents a surface density at 1 AU of $\Sigma = 1700$ g/cm^2, which is the value from the minimum mass solar nebula model (Weidenschilling, 1977) in which the surface density of the solar nebula is estimated by adding sufficient hydrogen and helium to the solid bodies in the solar system to recover standard interstellar abundances, and spreading this material smoothly into a disc. The dashed lines in Figure 3.2 correspond to higher surface densities that are more like those realistically expected to occur in protostellar discs.

As $\tilde{\eta}_H$ decreases in comparison to a constant $\tilde{\eta}_A$ the surface density becomes large due to the changed amount of field line drift as the radial field diffusion slows the rate of infall. The ambipolar diffusion-only fiducial solution of Krasnopolsky and Königl (2002), which shall be discussed in detail in Section 4.3, has an accretion rate of $\dot{M}_c = 7.66 \times 10^{-6}$ M$_\odot$ yr^{-1}, and the surface density at 1 AU in their solution is 1310 g/cm^2. Adding a positive value of $\tilde{\eta}_H$ to this similarity solution causes the surface density to decrease, which is problematic if one expects to form large planets from their disc, however, if the Hall parameter is negative then its presence raises the surface density to something more realistic.

As an experiment, the equations are solved to obtain a set of variables that are functions of B_z, r, t, and the core parameters to get the relationships modelled in

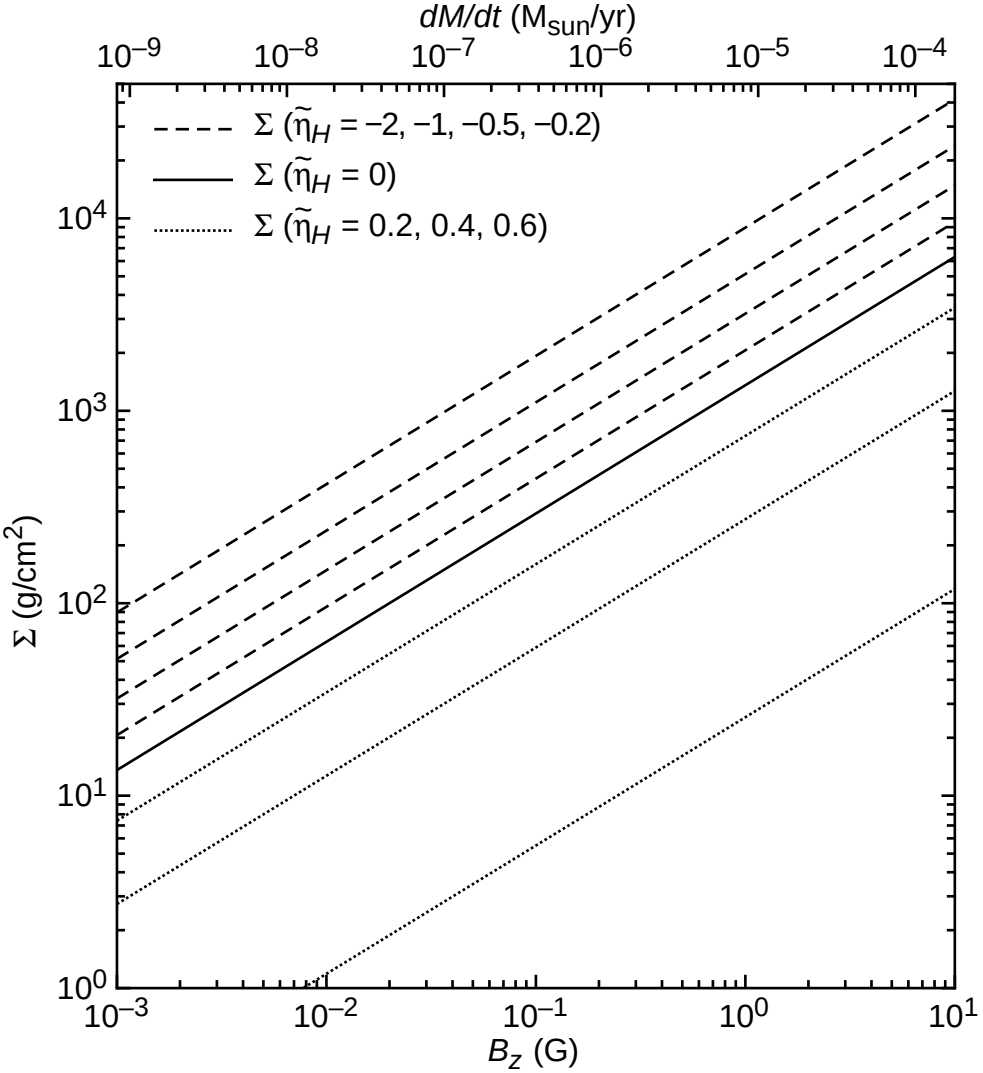

Figure 3.3: Plot of Σ against B_z and $\dot{M}$ for different values of $\tilde{\eta}_H$ in the Keplerian disc solution, where $\tilde{\eta}_A = \delta = 1.0$ and $c = 0.19$ km s^{-1}, at $r = 1$ AU and $t = 10000$ yr. The solid line presents the behaviour of Σ in the case that $\tilde{\eta}_H = 0$; the dashed lines above this are the cases where $\tilde{\eta}_H = -0.2, -0.5, -1.0$ and -2 respectively; and the dotted lower lines are $\tilde{\eta}_H = 0.2, 0.4$ and 0.6.

Figure 3.3. These functions are outlined below:

$$\dot{M} = B_z^{4/3} r^{5/3} (2\delta)^{2/3} (Gt)^{-1/3}, \tag{3.53}$$

$$M = B_z^{4/3} r^{5/3} (2\delta t)^{2/3} G^{-1/3}, \tag{3.54}$$

$$\Sigma = \frac{c_s f \sqrt{M}}{2\delta\pi\sqrt{2Gr^3[(2\delta/f)^2+1]}}, \tag{3.55}$$

$$H = \frac{\sqrt{2} r^{3/2} c_s}{\sqrt{GM[1+(f/2\delta)^2]}}, \tag{3.56}$$

$$J = (2\delta G B_z^2 r^4 t)^{1/3}, \tag{3.57}$$

$$V_\phi = (2\delta G B_z^2 r t)^{1/3} \tag{3.58}$$

$$\text{and } V_r = -\frac{\delta B_z^2 r}{\pi V_\phi \Sigma}; \tag{3.59}$$

the other field components were defined as being of order B_z in Equations 3.49–3.51. This model emphasizes the build up of the central mass through accretion, and Figure 3.3 shows the effect of Hall diffusion and the magnetic field strength on the surface density at $r = 1$ AU for a system with $\tilde{\eta}_A = \delta = 1$.

Alternatively, the disc variables can be thought of as functions of M and $\dot{M}$, treating t as the ratio between M and $\dot{M}$ rather than the actual age of the system. This makes it possible to regard the system as a steady state disc, where the other variables are defined by

$$B_z = \left(\frac{GM\dot{M}^2}{r^5(2\delta)^2}\right)^{1/4}, \tag{3.60}$$

$$J = \sqrt{GMr}, \tag{3.61}$$

$$V_\phi = V_K = \sqrt{\frac{GM}{r}} \tag{3.62}$$

$$\text{and } V_r = -\frac{\dot{M}}{2\pi r\Sigma}; \tag{3.63}$$

Σ and H are unchanged from Equations 3.55 and 3.56, as are the field components from Equation 3.49–3.51. The relationship between B_z and $\dot{M}$ is shown on the horizontal axes of Figure 3.3.

Figure 3.3 shows the influence of Hall diffusion on the surface density, plotted against B_z and $\dot{M}$ for constant $\tilde{\eta}_A = \delta = 1$. When the Hall diffusion term is negative, the surface density increases, creating a larger and heavier disc, while a positive Hall term, corresponding to a reversal of the field with respect to the axis of rotation, causes a decrease in Σ which drops off dramatically as the Hall term approaches the lower limit implied by the inequality $f \geq 0$.

The Keplerian disc solution says nothing about the angular momentum problem of star formation described in Section 1.4, as the accretion through the disc is slow and the model for the angular momentum transport by magnetic braking is oversimplified by the cap that is placed on the azimuthal field component. Magnetic diffusion is key to the magnetic flux problem outlined in Section 1.5 and the addition of Hall diffusion to the self-similar collapse model has been shown to assist in solving this, or to complicate it further, depending upon the orientation of the field.

3.3 Free Fall Solution

The second similarity solution, derived in Section A.2 and located in the blue lower left region AD of the pq-plane (Figure 3.1), describes the behaviour of the infall when the magnetic braking is very efficient at removing angular momentum from the flow. In this case there is very little angular momentum remaining and the reduced centrifugal support inhibits disc formation, so that the collapsing flow becomes a supersonic magnetically-diluted free fall onto the central protostellar mass. This solution is representative of the magnetic braking catastrophe that affects many numerical simulations of gravitational collapse.

The nondimensional form of this similarity solution is given by the complete set of fluid variables:

$$m = m_c, \tag{3.64}$$

$$\sigma = \sqrt{\frac{m_c}{2x}}, \tag{3.65}$$

$$h = h_{1,2}\, x^{3/2}, \tag{3.66}$$

$$u = -\sqrt{\frac{2m_c}{x}}, \tag{3.67}$$

$$v = j_{1,2}, \tag{3.68}$$

$$j = j_{1,2}\, x, \tag{3.69}$$

$$\psi = b_{z1,2}\, x, \tag{3.70}$$

$$b_z = b_{z1,2}\, x^{-1}, \tag{3.71}$$

$$b_{r,s} = b_z, \tag{3.72}$$

$$\text{and } b_{\phi,s} = -\min\left[\frac{|\tilde{\eta}_H|}{\tilde{\eta}_A}\, b\,;\, \delta b_z\right]. \tag{3.73}$$

In the limit where there is only ambipolar diffusion, this similarity solution reduces to the asymptotic inner solution to the "strong braking" collapse, which was presented without explicit derivation by Krasnopolsky and Königl (2002, equations 66–71). In

their solutions the angular momentum and the azimuthal field component are reduced to a small plateau value as the strong magnetic braking has removed almost all of the angular momentum early in the collapse (see Figure 6.4 and Section 6.2, where this is discussed in more detail). Their similarity solutions tended towards this behaviour when the magnetic braking parameter, α, was large, even though it does not appear in Equations 3.64–3.73.

Given that there are two possible values for $b_{\phi,s}$, depending upon the chosen values of the parameters $\tilde{\eta}_{H,A}$ and δ, there are two possible sets of coefficients for h, j and b_z. These are derived in Section A.3 in region AD of the pq-plane (see Figure 3.1), and are referenced by the subscripts 1 and 2 depending on which term in Equation 3.73 is the minimum that defines $b_{\phi,s}$.

The first set of coefficients occur when

$$\sqrt{\frac{2\tilde{\eta}_H^2}{\tilde{\eta}_A^2 - \tilde{\eta}_H^2}} < \delta, \tag{3.74}$$

corresponding to the left hand side of the minimum choice for $b_{\phi,s}$ in Equation 3.73. The coefficient b_{z1} is then the single real root of the polynomial

$$b_{z1}^8 - \frac{m_c^2}{2\tilde{\eta}_A^2 f_1}\, b_{z1}^6 - \frac{m_c^6}{4\tilde{\eta}_A^4 f_1^4} = 0, \tag{3.75}$$

where f_1 is a constant defined by the magnetic diffusion parameters:

$$f_1 = \frac{\tilde{\eta}_A^2 + \tilde{\eta}_H^2}{\tilde{\eta}_A^2 - \tilde{\eta}_H^2}. \tag{3.76}$$

The coefficients for j and h are given by

$$j_1 = -\frac{b_{z1}^2}{m_c}\, \frac{\sqrt{2}\,\tilde{\eta}_H}{\sqrt{\tilde{\eta}_A^2 - \tilde{\eta}_H^2}} \tag{3.77}$$

and

$$h_1 = \frac{f_1 b_{z1}^2}{\sqrt{2m_c^3}} \left[-1 + \sqrt{1 - \frac{4m_c^2}{f_1^2 b_{z1}^4}} \right]. \tag{3.78}$$

This solution is the asymptotic inner solution of Krasnopolsky and Königl (2002) for their strong braking similarity solutions. In their solution, $\tilde{\eta}_H = 0$, $f_1 = 1$, and the angular momentum coefficient $j = 0$, so the angular momentum tends towards zero as $x \to 0$.

The second set of coefficients are adopted when the inequality

$$\sqrt{\frac{2\tilde{\eta}_H^2}{\tilde{\eta}_A^2 - \tilde{\eta}_H^2}} > \delta \tag{3.79}$$

is satisfied, so that $b_{\phi,s}$ takes on the second value in 3.73, $b_{\phi,s} = -\delta b_z$. The coefficient b_{z2} is given by the single positive real root of the equation

$$b_{z2}^8 - \frac{m_c^2(1+\delta^2)}{2f_2^2}\, b_{z2}^6 - \frac{m_c^6}{4f_2^4} = 0 \tag{3.80}$$

where f_2 is given by

$$f_2 = \tilde{\eta}_A - \tilde{\eta}_H \delta \sqrt{2+\delta^2}. \tag{3.81}$$

This then gives the other coefficients as

$$j_2 = \frac{\delta b_{z2}^2}{m_c} \tag{3.82}$$

and

$$h_2 = \frac{(1+\delta^2) b_{z2}^2}{\sqrt{2m_c^3}} \left[-1 + \sqrt{1 + \frac{4m_c^2}{(1+\delta^2)^2 b_{z2}^4}} \right]. \tag{3.83}$$

This solution was not explored in Krasnopolsky and Königl (2002), as without the Hall term the left hand side of the minimum condition in Equation 3.73 is always zero and can never exceed the right hand side.

As in the Keplerian disc solution, this similarity solution can be converted to dimensional form using Equations 2.94–2.99, to better understand the physics behind the free fall collapse. In this case the solution becomes:

$$M = \frac{c_s^3 m_c}{G}\, t, \tag{3.84}$$

$$\dot{M} = \frac{c_s^2 m_c}{G}, \tag{3.85}$$

$$\Sigma = \frac{1}{\pi G} \sqrt{\frac{c_s^3 m_c}{2^3 r t}}, \tag{3.86}$$

$$H = h_{1,2}\, \frac{r^{3/2}}{\sqrt{c_s t}}, \tag{3.87}$$

$$V_r = -\sqrt{\frac{2 m_c c_s^3 t}{r}}, \tag{3.88}$$

$$V_\phi = j_{1,2}\, c_s, \tag{3.89}$$

$$J = j_{1,2}\, c_s r, \tag{3.90}$$

$$\Psi = \frac{2\pi c_s^2 b_{z1,2}}{G^{1/2}}\, r, \tag{3.91}$$

$$B_z = \frac{c_s^2 b_{z1,2}}{G^{1/2}}\, r^{-1}, \tag{3.92}$$

$$B_{r,s} = B_z, \tag{3.93}$$

$$\text{and } B_{\phi,s} = -\min\left[\frac{|\tilde{\eta}_H|}{\tilde{\eta}_A} B\,;\, \delta B_z \right]. \tag{3.94}$$

By taking the absolute value of $\tilde{\eta}_H$ the sign of $B_{\phi,s}$ is held constant. Were the sign of $B_{\phi,s}$ to change, then the signs of J and B_z would also change, resulting in a set of flow variables that are identical but for a reversed direction of $\hat{\mathbf{z}}$. The absolute value of the Hall diffusion coefficient is adopted merely to simplify the calculations.

The power laws are solutions to the simplified equations:

$$V_r \frac{\partial V_r}{\partial r} = g_r, \tag{3.95}$$

$$\frac{\partial J}{\partial r} = \frac{r B_{\phi,s} B_z}{2\pi \Sigma V_r}, \tag{3.96}$$

$$-V_r H = \frac{\eta_H}{B} B_{\phi,s} + \frac{\eta_A}{B^2} B_z^2, \tag{3.97}$$

$$\frac{GM_c}{2r^3} H^2 + \frac{(B_{\phi,s}^2 + B_{r,s}^2)}{4\pi\Sigma} H - c_s^2 = 0, \tag{3.98}$$

$$\dot{M} = \text{constant} \tag{3.99}$$

$$J = r V_\phi, \tag{3.100}$$

$$B_{r,s} = B_z \tag{3.101}$$

$$B_{\phi,s} = -\min\left[\frac{|\eta_H|}{\eta_A} B\,;\, \delta B_z\right] \tag{3.102}$$

$$\text{and } \Psi = 2\pi r^2 B_z; \tag{3.103}$$

as in the Keplerian disc solution the induction equation takes the simplified form $V_r + V_{Br} = 0$. In this similarity solution any remaining rotation of the flow is that induced by the magnetic "braking", which can cause rotation by Hall diffusion in the azimuthal direction of the field lines tied to the electrons, which creates a rotational torque on the neutrals and grains as they fall inward rapidly.

Equations 3.95–3.100 may be solved to give the disc variables as functions of the surface density and magnetic field:

$$V_r = -\sqrt{\frac{2GM}{r}}\,, \tag{3.104}$$

$$M = -2\pi r \Sigma V_r t \tag{3.105}$$

$$\dot{M} = -2\pi r \Sigma V_r \tag{3.106}$$

$$\text{and } J = \frac{B_{\phi,s} B_z}{2\pi \Sigma V_r}\, r^2, \tag{3.107}$$

where the field components are given by Equations 3.101–3.103 and the scale height of the disc is given by the equation

$$H_1 = \frac{f_1 B_z^2 r^{7/2} t}{\sqrt{2GM^3}} \left[-1 + \sqrt{1 - \frac{4c_s^2 M^2}{f_1^2 B_z^4 r^4 t^2}}\right] \tag{3.108}$$

$$\text{or } H_2 = \frac{(1+\delta^2)B_z^2 r^{7/2} t}{\sqrt{2GM^3}} \left[-1 + \sqrt{1 - \frac{4c_s^2 M^2}{(1+\delta^2)^2 B_z^4 r^4 t^2}} \right] \tag{3.109}$$

depending on which value of the azimuthal field component is adopted.

This similarity solution is an example of the magnetic braking catastrophe that occurs in numerical simulations of star formation when the magnetic braking of a collapsing core is so strong that all angular momentum is removed from the gas and it is impossible to form a rotationally-supported disc (e.g. Mellon and Li, 2008, 2009). It is clear from Equations 3.69, 3.73 and 3.77 that when there is no Hall diffusion the magnetic braking in this solution causes $B_{\phi,s} = J = 0$, which is indicative of the catastrophe and prevents disc formation. This behaviour was demonstrated in the "strong braking" solution of Krasnopolsky and Königl (2002) where $\delta = \alpha = 10$ and the fluid was able to fall onto the protostar with very little angular momentum remaining. This particular solution, and the magnetic braking catastrophe more generally, are discussed in more detail in Section 6.2.

The introduction of Hall diffusion to the similarity solution can cause additional twisting of the field lines and magnetic braking, or it can cause a reduction in these by twisting the magnetic field lines in the opposite direction, in effect spinning up the collapse. The direction of the Hall diffusion depends upon the orientation of the field with respect to the axis of rotation, and it is obvious that this directionality has an important effect on the magnetic braking catastrophe. The linear scaling of the angular momentum with radius (Equation 3.90) suggests that the point mass at the origin has no angular momentum, however, Hall diffusion will likely ensure that in the innermost regions of the collapse the angular momentum shall reach a plateau value similar to that in Figure 6.4 for the ambipolar diffusion-only collapse. No similarity solutions to the full collapse problem were found that matched onto the free fall inner asymptotic solution discussed in this section, however, work is underway to find similarity solutions with strong α and δ that demonstrate this asymptotic behaviour and illustrate how the Hall effect influences the magnetic braking catastrophe directly.

3.4 Summary

This chapter saw the derivation of two distinct power law similarity solutions to the fluid equations in the innermost regions of the collapse as $x \to 0$. The first of these was a rotationally-supported disc through which the gas is slowly accreted. The surface density and scale height of the disc are determined by the magnetic diffusion coefficients, with Hall diffusion either adding to or reducing the surface density. The magnetic field and surface density scale with radius in the same way as in previous

protostellar disc models and any accretion through the disc is regulated by the outward diffusion of the magnetic field against the flow.

The diffusion coefficients also placed limits upon the flow. In order to form a Keplerian disc as described by the first asymptotic solution, certain restrictions are placed upon the diffusion coefficients. Hall diffusion can counteract the ambipolar diffusion and prevent the gas from falling in; a disc may only form when the nondimensional Hall parameter $\tilde{\eta}_H$ is no larger than $\tilde{\eta}_A\sqrt{\frac{8}{17}}$ (for $\delta = 1$). There is no lower limit on the size of the Hall diffusion parameter, as when $\tilde{\eta}_H$ is negative it aids the outward diffusion of the field, reducing the amount of magnetic flux that is accreted onto the central protostar. The orientation of the field with respect to the axis of rotation determines the direction of the Hall diffusion and whether it resolves or furthers the magnetic flux problem outlined in Section 1.5.

Similarly, the Hall effect can increase or reduce the angular momentum problem in the second asymptotic solution, where the matter is free falling onto the central protostar and the only rotational velocity is that induced by Hall diffusion in the azimuthal direction. No disc may form in this solution, as the strong magnetic braking prevents the centrifugal force from becoming large enough to support the infalling gas against gravity. The amount of magnetic braking affecting the flow depends upon the Hall parameter as well as the values of the magnetic braking parameter, α (Equation 2.84), and the cap on $b_{\phi,s}$, δ (see Equation 2.114). This is expected to be the asymptotic inner solution for the collapse when the parameters α and δ are large, as in the "strong braking" similarity solution of Krasnopolsky and Königl (2002), which is discussed further in Section 6.2.

The two similarity solutions represent both sides of the disc formation problem that is referred to in the literature as the magnetic braking catastrophe. In the first, the magnetic braking is limited, and a rotationally-supported disc such as those in the simulations of Machida et al. (2011) forms, while in the second no disc forms as the catastrophic magnetic braking removes almost all of the angular momentum so that the matter is falling rapidly onto the central protostar as in the simulations of Mellon and Li (2009) and others. This problem has yet to be fully resolved, however the magnetic diffusion is clearly important in determining whether or not a disc forms and which of the two asymptotic solutions shall describe the inner region of any given collapsing molecular cloud core.

All of the similarity solutions presented in Chapters 4 and 5 form rotationally-supported discs, and those with Hall and ambipolar diffusion match specifically onto the Keplerian disc solution described here. The asymptotic similarity solution is used as the inner boundary condition for these models, enforcing disc formation to show how the Hall effect influences the properties of disc-forming similarity solutions. The

free fall solution is not studied further as part of the full collapse models, but it shall be discussed in Section 6.2 and it is expected that similarity solutions matching onto this asymptotic solution will be found in future.

Chapter 4

Collapse without the Hall Effect

The construction of the self-similar model for studying gravitational collapse with the Hall effect was a gradual affair, taking place in stages of increasing physical complexity. The reasons for this were twofold: firstly, a good initial guess of the variables was required in order to solve the equations with Hall diffusion — the calculation of similarity solutions without Hall diffusion would provide this guess. Secondly, by reproducing the results of previous self-similar collapse models it is possible to check the calculation code to ensure that it is both numerically robust and physically sound, and to be certain that the changes brought on by the introduction of Hall diffusion are properly contrasted with similarity solutions that contain less complex physics. The three models calculated in this chapter belong to different families of similarity solutions: those that are nonmagnetic, those with ideal magnetohydrodynamics, and those with non-ideal MHD and ambipolar diffusion.

This chapter is dedicated to outlining the construction, testing and physical behaviour of these models, and the derivation of the necessary inner asymptotic solutions and jump conditions that determine the collapse behaviour as $x \to 0$. These are then compared to models found in the literature, adopting their boundary conditions and reproduce their results. As may be expected, the primary targets of these comparisons are the results of Krasnopolsky and Königl (2002), although the work of Saigo and Hanawa (1998) shall also be discussed. The similarity solutions presented in this chapter provide a baseline for the discussion of the physics affecting the solutions presented in Chapter 5 once the Hall term is activated.

All of the similarity solutions presented in this chapter include the effects of rotation, and all of them form rotationally-supported discs. Although it was shown by Krasnopolsky and Königl (2002) that there exist similarity solutions for which the magnetic braking is so strong that no disc forms (the free fall asymptotic solution presented in Section 3.3 demonstrates the inner boundary conditions for such a solution

in the Hall regime), those solutions are not reproduced in this work. This modified angular momentum problem, in which the magnetic braking is so strong that it removes all of the angular momentum from the collapsing flow has been seen in many numerical simulations (e.g. Mellon and Li, 2008, 2009; Hennebelle and Ciardi, 2009), and has yet to be fully resolved. The inclusion of Ohmic diffusion (Dapp and Basu, 2010) and Hall diffusion (Krasnopolsky et al., 2011) has been shown to reduce the magnetic braking catastrophe, which is discussed further in Section 6.2.

Discs form in the collapse solutions presented in this chapter because the magnetic braking is artificially capped in a manner that could be a reasonable substitute for nonaxisymmetric effects, or a disc wind, that could change the transport of angular momentum above the pseudodisc. By studying those solutions with discs the importance of the magnetic field diffusion in driving and controlling gravitational collapse will be demonstrated.

This chapter outlines the construction and results of collapse models that are nonmagnetic (Section 4.1), that are magnetic under ideal MHD (Section 4.2), and that are magnetic with ambipolar diffusion in Section 4.3. For each of these collapse simulations the inner asymptotic solution must be derived, as well as the jump conditions at the centrifugal shock and an estimation of the shock position. The calculation procedure is then described and the results of each model examined. The impact of rotation and magnetic fields on the structural features of the similarity solutions, particularly the centrifugal shock and the size of the rotationally-supported disc, are analysed with reference to previous models of collapse in order to provide a solid foundation for discussing the influence of the Hall effect on the solutions in the following chapter.

4.1 Nonmagnetic Solutions

The simplest model constructed here is that of a nonmagnetic rotating collapse, which has been examined by Saigo and Hanawa (1998) and Krasnopolsky and Königl (2002). This model is characterised by the equations

$$\frac{\partial \Sigma}{\partial t} + \frac{1}{r}\frac{\partial}{\partial r}(r\Sigma V_r) = 0, \tag{4.1}$$

$$\frac{\partial V_r}{\partial t} + V_r\frac{\partial V_r}{\partial r} = g_r - \frac{c_s^2}{\Sigma}\frac{\partial \Sigma}{\partial r} + \frac{J^2}{r^3}, \tag{4.2}$$

$$\frac{\partial J}{\partial t} + V_r\frac{\partial J}{\partial r} = 0 \tag{4.3}$$

$$\text{and } \frac{c_s^2\Sigma}{2H} = \frac{\pi}{2}G\Sigma^2, \tag{4.4}$$

which are the nonmagnetic form of Equations 2.88–2.91. Because there is no mechanism for braking the angular momentum, no central mass forms and the only term left

to control the vertical squeezing of the pseudodisc is its self-gravity.

The nondimensional form of Equations 4.1, 4.2 and 4.4 is

$$\frac{dm}{dx} = x\sigma, \tag{4.5}$$

$$(1-w^2)\frac{1}{\sigma}\frac{d\sigma}{dx} = -\frac{m}{x^2} + \frac{j^2}{x^3} + \frac{w^2}{x}, \tag{4.6}$$

$$\text{and } h = \frac{2}{\sigma}; \tag{4.7}$$

while the simplified self-similar angular momentum equation,

$$\frac{dj}{dx} = \frac{j}{w}, \tag{4.8}$$

is integrated to give

$$j = \Phi m \tag{4.9}$$

where Φ is a constant. Its value is the initial ($x \to \infty$) ratio of the angular momentum to the mass at the outer boundary, given by the expression

$$\Phi = \frac{v_0}{A}, \tag{4.10}$$

where the constants v_0 and A characterise the outer boundary conditions $j = v_0 x$ and $m = Ax$ (see Section 2.7). This ratio Φ is denoted ω by Saigo and Hanawa (1998); their outer boundary conditions are described by the same equations as in this work, however the values of the parameters characterising any given similarity solution are subtly different from those chosen in this work. Their $\omega = 0.3$ solution corresponds quite well to the fast rotation solution presented in subsection 4.1.3.

Equation 4.9, which takes the dimensional form

$$J = \frac{\Phi G M}{c_s}, \tag{4.11}$$

holds true in the outer (large x) regions of all of the solutions presented in this thesis, although it breaks down in the magnetic solutions at lower x as the flux builds up and magnetic braking starts to reduce the angular momentum. Matsumoto et al. (1997) showed that Equation 4.11 held true across many orders of magnitude in their non-magnetic two-dimensional numerical solutions of the collapse of a rotating cloud into a rotating disc. Clearly this relation holds when the rotational velocity and the density are uniform, and if the initial cloud has constant density and rotational velocity before it is centrally condensed Equation 4.11 will hold true for the nonmagnetic collapse so long as the collapse is axisymmetric.

From Equations 4.5–4.10 it is possible to derive the asymptotic similarity solution describing the behaviour of the flow inwards of the centrifugal shock, the jump conditions and the position of the shock itself.

4.1.1 Inner solution

As in Chapter 3 for the full model with Hall diffusion, the inner asymptotic solution is found by assuming that the surface density takes the form of a power law in x,

$$\sigma = \sigma_1 x^{-p}, \tag{4.12}$$

where σ_1 and p are both real constants. The conservation of mass equation (4.5),

$$\frac{dm}{dx} = \sigma_1 x^{1-p}, \tag{4.13}$$

is integrated to give

$$m = \frac{\sigma_1 x^{2-p}}{2-p}. \tag{4.14}$$

The requirement that the rotational velocity must not diverge as $x \to 0$ means that the angular momentum must vanish at the origin, and that no central point mass can form. Using Equation 4.9 the angular momentum of the fluid is then given by

$$j = \frac{\Phi \sigma_1 x^{2-p}}{2-p}. \tag{4.15}$$

Equations 4.12, 4.14 and 4.15 are then substituted into the conservation of radial momentum equation (4.6), so that it is then expressed in terms of x and the constants,

$$-p\left(1 - \frac{x^2}{(2-p)^2}\right) = -\frac{\sigma_1 x^{1-p}}{2-p} + \frac{\Phi^2 \sigma_1^2 x^{2-2p}}{(2-p)^2} + \frac{x^2}{(2-p)^2}. \tag{4.16}$$

Taking the limit as $x \to 0$, the $\mathcal{O}(x^2)$ terms are clearly much smaller than those terms of $\mathcal{O}(x^0)$, and so they may be dropped from the equation. This then becomes

$$\frac{\Phi^2 \sigma_1^2}{(2-p)^2} x^{2-2p} - \frac{\sigma_1}{2-p} x^{1-p} + p = 0, \tag{4.17}$$

and when each pair of exponents are equated it becomes obvious that the only solution is $p = 1$. Substituting this into Equation 4.17 reduces it to a quadratic in σ_1,

$$\Phi^2 \sigma_1^2 - \sigma_1 + 1 = 0. \tag{4.18}$$

The inner asymptotic solution is thus defined by the equations:

$$\sigma = \sigma_1 x^{-1} = \left(\frac{1 + \sqrt{1 - 4\Phi^2}}{2\Phi^2}\right) x^{-1}, \tag{4.19}$$

$$m = \sigma_1 x, \tag{4.20}$$

$$j = \Phi \sigma_1 x, \tag{4.21}$$

$$v_\phi = \Phi \sigma_1, \tag{4.22}$$

$$h = \frac{2}{\sigma_1} x, \tag{4.23}$$

$$u = 0 \tag{4.24}$$

$$\text{and } \dot{m} = 0. \tag{4.25}$$

These equations are identical to the inner solution that was presented without explicit derivation in §3.1 of Krasnopolsky and Königl (2002). This inner solution ceases to exist when $\Phi > 0.5$, as in this regime σ_1 becomes complex; and a second unstable solution exists when the coefficient of σ is the second root of Equation 4.18. Any increase in Φ corresponds to a reduction in the gravitational force, so that it is no longer able to balance the centrifugal and pressure forces in the disc. If the initial ratio of the centrifugal to gravitational forces is too high then no disc can form, as there is no mechanism for reducing the centrifugal forces to create a stable disc.

In order to better understand the behaviour of this disc, it is worthwhile to convert the asymptotic similarity solution back to dimensional form:

$$\Sigma = \frac{c_s^2 \sigma_1}{2\pi G}\, r^{-1}, \tag{4.26}$$

$$M = \frac{c_s^2 \sigma_1}{G}\, r, \tag{4.27}$$

$$J = \Phi c_s \sigma_1\, r, \tag{4.28}$$

$$V_\phi = \Phi c_s \sigma_1, \tag{4.29}$$

$$H = \frac{2}{\sigma_1}\, r, \tag{4.30}$$

$$V_r = 0 \tag{4.31}$$

$$\text{and } \dot{M} = 0, \tag{4.32}$$

where the constant σ_1 retains its definition from Equation 4.19. At any given radius the enclosed mass and surface density are constant with time, and the material orbits with a stable rotational velocity. These relations may also be written as a set of variables that are functions of Σ and M:

$$M = 2\pi r^2 \Sigma, \tag{4.33}$$

$$H = \frac{c_s^2}{\pi G \Sigma}, \tag{4.34}$$

$$J = \Phi c_s G M \tag{4.35}$$

$$\text{and } V_\phi = \frac{\Phi c_s G M}{r}. \tag{4.36}$$

These are all steady state equations, as the material joining the disc quickly loses its radial momentum and stops moving inward. The gas is unable to move inwards after this point as there is no way to change its angular momentum, and so the material remains in orbit, unable to fall to the origin to form a point mass.

These inner asymptotic solutions match quite well onto the inner regions of the similarity solutions close to the origin. The outer edge of this region is marked by

a steep shock, which separates the inner centrifugally-supported disc from the outer dynamic collapse. The properties of this shock are outlined in the following subsection.

4.1.2 Shock position and jump conditions

The transition between the outer supersonic collapse and the inner steady state disc takes the form of an abrupt change in both the surface density σ and the radial velocity u. Inward of this shock, the density increases dramatically, and the infall velocity is slowed to a very low value, which rapidly drops to zero in the post-shock region. In solutions where the matter is initially rapidly rotating, the radial velocity can change sign as the shock front overtakes it, creating a region of shocked backflow that follows behind the shock front until the radial velocity decreases enough that the gas settles into the asymptotic steady state disc.

Although the form of the inner asymptotic solution changes with the addition of magnetic fields and then magnetic diffusion, this shock is a common feature of all the similarity solutions presented in this work. Its position is estimated to occur at the *centrifugal radius*, the point where gravity and the centrifugal forces are first in approximate balance (which is near to the boundary of the rotationally-supported disc), and this radius will be shown to be a reasonable approximation to the shock position. It is calculated by equating the gravitational and centrifugal forces in the radial momentum equation (4.6):

$$\frac{m(x_c)}{x_c^2} = \frac{j(x_c)^2}{x_c^3} \tag{4.37}$$

and then solving for the centrifugal radius, x_c:

$$x_c = \frac{j(x_c)^2}{m(x_c)}. \tag{4.38}$$

This calculation requires a deep understanding of the behaviour of both the enclosed mass and the angular momentum in the region of the shock; these become more difficult to estimate with the increasing complexity of the models. However, in the nonmagnetic case this is clearly given by

$$x_c = \Phi^2 m(x_c); \tag{4.39}$$

where an approximation to the mass is still needed in order to determine the centrifugal radius.

The initial (outer) conditions have the gas infalling at a velocity $|u_0| \ll x$, however, as the mass of the inner disc grows more matter is pulled inwards faster, so that in the slower rotation cases, the gas close to the centrifugal shock is falling in at free

model	Φ	estimated x_c	actual x_c
$v_0 = 0.1$	$0.0\dot{3}$	$0.00\dot{6}$	0.0077
$v_0 = 1.0$	$0.\dot{3}$	$0.\dot{6}$	0.64

Table 4.1: Comparison between the estimated and actual values of the centrifugal shock position, x_c.

fall speeds. When the radial velocity becomes much larger than x, then $w \approx |u|$ and $m \approx \dot{m}$, and the continuity equation becomes

$$\frac{dm}{dx} = x\sigma = \frac{m}{w} \ll \frac{m}{x} \tag{4.40}$$

(using $m = xw\sigma$); this causes the value of the enclosed mass to drop to a plateau value that remains near-constant until the centrifugal shock position (as can be seen in the results in the following subsection). The outer edge of this plateau is estimated to occur at

$$x_{pl} \approx |u_0|, \tag{4.41}$$

which is something of an overestimate as $|u|$ is typically larger than $|u_0|$ when m reaches the plateau value. At this point the outer asymptotic solution is still a good approximation to σ, and so it and Equation 4.41 are substituted into $m = xw\sigma$ to give an approximation to the plateau mass:

$$m_{pl} \approx x_{pl}(x_{pl} - u_0)\sigma_{pl} = x_{pl}(|u_0| - u_0)\left(\frac{A}{x_{pl}}\right) = 2|u_0|A. \tag{4.42}$$

The value of the mass in the plateau changes very little between x_{pl} and x_c, and so this calculated value can be substituted into Equation 4.39 to give the approximate centrifugal shock position,

$$x_c \approx \frac{2|u_0|v_0^2}{A}. \tag{4.43}$$

This equation (derived in equations 34–35 of Krasnopolsky and Königl, 2002) only applies if $x_c \lesssim x_{pl}$, which is true whenever $v_0 \lesssim (A/2)^{1/2}$. Given the limit on Φ established in 4.1.1, this weak inequality is not violated in the similarity solutions explored in this thesis. There is no solution if the mass has yet to reach its plateau value.

For the models presented in the next subsection, the actual centrifugal shock position is close to the one calculated by Equation 4.43, and the values of these are presented for comparison in Table 4.1. As they are so close, Equation 4.43 is an acceptable initial guess to use when finding the shock position by the iterative process described in Section 5.2.2 for the Hall similarity solutions. While this process is used

with few modifications in all of the models presented in this work, its description is left to the following chapter for the reader interested only in the model with Hall diffusion.

Because the centrifugal shock manifests as a discontinuity in σ and u, the jump conditions must be calculated explicitly at the shock position. At the shock, the radial momentum equation (4.6) can be written as

$$(1 - w^2)\frac{d\sigma}{dx} = 0, \tag{4.44}$$

where the terms on the right hand side of Equation 4.6 are all small at the shock in comparison to the steep derivative term on the left. The shock occurs because of the singularity inherent to the equation, which occurs at the locus of points where $(1 - w^2) = 0$, that is, where

$$(x - u)^2 = 1. \tag{4.45}$$

In dimensional form the singularity takes the form of the sonic line,

$$\left(\frac{r}{t} - V_r\right)^2 = c_s^2. \tag{4.46}$$

The shock occurs when the curve describing the flow crosses the singular line in the xu-plane. The shock propagates outwards at the speed of sound, and occurs near the centrifugal radius defined above.

The jump conditions are found by solving the continuity and radial momentum equations at the position of the shock. At the shock, the derivatives of σ and u become large with respect to the other terms in the equations, which may then be disregarded. The equations are then integrated at x_c to define the jump conditions.

Starting by examining the conservation of mass across the shock, $m = xw\sigma$ is substituted into Equation 4.5 to give

$$\frac{dm}{dx} = w\sigma + x\frac{d(w\sigma)}{dx} = x\sigma, \tag{4.47}$$

which can be simplified to

$$\frac{d(w\sigma)}{dx} = \frac{u\sigma}{x}. \tag{4.48}$$

As mentioned above, the terms on the right hand side of this equation are small compared to the large derivatives on the left, and so they are dropped. The derivative is then integrated across the shock front to give the first of the jump conditions:

$$w\sigma = \text{constant}, \tag{4.49}$$

which ensures that the mass is conserved across the shock.

Similarly, the terms on the right hand side of the radial momentum equation can be dropped, and it is then rearranged into the form

$$\frac{d\sigma}{dx} = w^2 \frac{d\sigma}{dx}. \tag{4.50}$$

This term is integrated across the shock front to become

$$\sigma = w^2\sigma - \int\limits_{\substack{\text{shock}\\\text{front}}} \sigma \frac{d(w^2)}{dx}\, dx + \text{constant}; \tag{4.51}$$

taking advantage of Equation 4.49, a factor of $w\sigma$ can be removed from the integral in 4.51:

$$\sigma = w^2\sigma - 2w\sigma \int\limits_{\substack{\text{shock}\\\text{front}}} \frac{dw}{dx}\, dx + \text{constant}; \tag{4.52}$$

and the fully integrated radial momentum equation is rearranged into the form of the second jump condition:

$$\sigma(1 + w^2) = \text{constant}. \tag{4.53}$$

The jump conditions presented in Equations 4.49 and 4.53 are solved simultaneously by denoting the upstream and downstream sides of the shock by the subscripts u and d and rewriting them in the form

$$\sigma_u w_u = \sigma_d w_d \tag{4.54}$$

$$\text{and } \sigma_u(1 + w_u^2) = \sigma_d(1 + w_d^2). \tag{4.55}$$

The first of these is substituted into the second, and this is factorised to give the equation

$$\left(w_u - \frac{1}{w_d}\right)(w_u - w_d) = 0, \tag{4.56}$$

which has the non-trivial solution:

$$w_d = \frac{1}{w_u}, \tag{4.57}$$

$$\text{and } \sigma_d = \sigma_u w_u^2. \tag{4.58}$$

These jump conditions, presented with minimal derivation in appendix B1 of Krasnopolsky and Königl (2002), are applicable to all of the collapse calculations in which there is no mechanism by which the magnetic field can be changed by the passage of the shock front. Even in those solutions with magnetic diffusion, the magnetic pressure and tension terms are never large enough to influence the behaviour of the field in the centrifugal shock; the magnetic field is not affected directly by the shock,

although the field behaviour quickly changes in the post-shock region, and so these jump conditions are used in those solutions.

The only similarity solutions with different jump conditions are those for ideal MHD; these conditions are derived in subsection 4.2.2. Krasnopolsky and Königl (2002) also derived jump conditions for a shock in which the scale height h was unaffected by the change in the density at the shock because the thickness of the disc is determined by the gravity of the central point mass. These jump conditions are not required here, as the similarity solutions studied in this text occur in regions of parameter space where the gravity of the central mass does not yet control the vertical squeezing of the collapsing flow in the area of the centrifugal shock.

The jump conditions in Equations 4.57 and 4.58 make it possible to calculate the similarity solutions to the nonmagnetic rotational collapse equations.

4.1.3 Similarity solutions

The similarity solutions are found by integrating the fluid equations from the outer boundary to the inner one using the `stifbs` integrator routine for integrating stiff sets of equations from *Numerical Recipes in Fortran 77* (Press et al., 1992), and checked against the output from the fifth order Runge–Kutter integrator `rkqs` from the same source. Stiff equations are those for which the normal numerical methods used to integrate them are numerically unstable unless the step size is very small; the fluid equations describing gravitational collapse are often stiff, particularly in the innermost regions of the collapse. These routines (and their dependencies) were modified from their original form to use double precision floating point variables, and produce output that in general is identical to the seventh significant figure. While either routine may be used to calculate this model, the more complicated models following on from this are sometimes unable to be completed using the `stifbs` routine as it uses a finite differences method for calculating the Jacobian of the derivatives which operates poorly in those regions near to the shocks (it was too complicated to derive a set of analytic expressions for the Jacobian for the later collapse models). In those instances the `rkqs` routine is used; this change is not expected to introduce significant errors.

As the code integrates the variables inwards from the outer boundary towards the inner boundary, the jump conditions derived in the previous subsection are applied at the approximate position of the shock. The behaviour of the variables inwards of the shock allows for a better estimate of the shock position to be determined, and by a process of iteration the true value of the shock is found. This routine is described in full in Section 5.2 for the collapse with Hall diffusion; qualitatively, the same downstream behaviour is observed in each of the earlier collapse models. If the jump conditions are

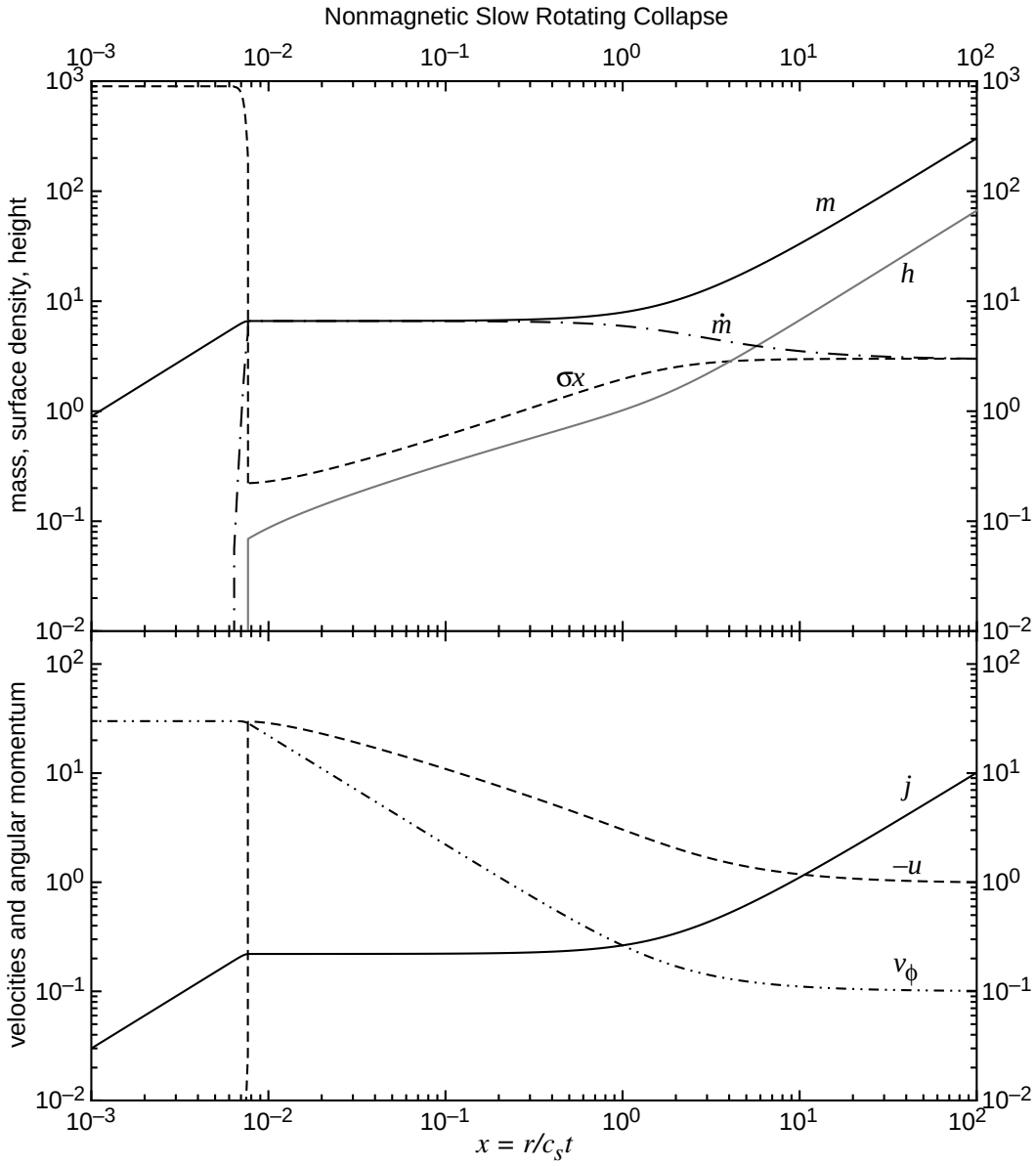

Figure 4.1: Similarity solution for the slowly rotating nonmagnetic collapse, with outer asymptotic boundary conditions $A = 3$, $u_0 = -1$, and $v_0 = 0.1$. The top panel shows the nondimensional enclosed mass m, accretion rate $\dot{m}$, surface density σ and scale height h, while the lower panel displays the nondimensional angular momentum j, radial infall speed $-u$ and angular velocity v_ϕ all as functions of the similarity variable x. Inwards of the centrifugal shock (located at $x_c = 7.7 \times 10^{-3}$) the radial velocity and accretion rate drop rapidly to zero, and no central mass forms. In this solution, as the initial rotation rate is slow, it takes longer for the centrifugal forces to build up and balance gravity, allowing the infall velocity to achieve free fall speeds.

applied at the true shock position, then as the variables are integrated inwards they tend asymptotically to the inner power law behaviour derived in subsection 4.1.1.

Two similarity solutions are presented in Figures 4.1 and 4.2, the first showing a slow rotation case where the initial rotational velocity is $V_\phi = 0.1c_s$, and the second a faster rotation case characterised by an initial $V_\phi = c_s$. These values were chosen to match the solutions in figures 1 and 2 of Krasnopolsky and Königl (2002), both to test the modelling code and to duplicate their results. The fast rotation similarity solution is also close to the $\omega = 0.3$ solution from Saigo and Hanawa (1998), however their initial (outer) boundary conditions are very slightly different, as the values $v_0 = 1.05$ and $A = 3.5$ (compared to $A = 3.0$ in these solutions) were chosen to match onto their solutions for runaway dynamic collapse. Despite these differences, as the inner solution depends only upon $\Phi = \omega$ their solution is identical to that in Figure 4.2 in the regions interior to the centrifugal shock. Similarly, their centrifugal shock position is close to the value for the fast solution of $x_c = 0.643$.

As outlined in Section 2.7, the outer region of the collapse corresponds to a collapsing core just before point mass formation. For the two solutions presented here, the outer collapse is similar, as the difference in the initial angular momentum between the two only really becomes important in the region close to the centrifugal shock. The material initially falls from the outer edge at the constant radial velocity $V_r = -c_s$, with the infall speed gradually increasing as the matter nears the disc, so that in the slow rotation solution the gas is falling onto the disc at free fall speeds. In the fast rotation similarity solution the centrifugal shock occurs before the mass plateau is fully established; because of this the fluid is infalling slowly when it hits the shock.

The mass plateau forms because the material is moving inward rapidly, with the radial pressure terms in the radial momentum equation becoming less important as gravity and the centrifugal forces start to dominate. The height of the collapsing flow continues to decrease as the surface density does; because all of the matter in this region is infalling rapidly, the pseudodisc self-gravity pulls what remains in the thin disc towards the equator.

The increase in the gravitational and centrifugal forces causes the formation of a centrifugal barrier occurring at approximately the position predicted by the estimation in the previous subsection, as was shown in Table 4.1. The centrifugal shock moves outwards in physical space at a velocity equal to the sound speed multiplied by the nondimensional shock position, so that it is propagating slowly outwards in the slow rotation case where it is located close to the origin in self-similar space, and rapidly outwards for the fast rotation solution. If the material is initially rotating rapidly, it may be so shocked that it is pulled along after the shock in a backflow, before losing its outward momentum and settling to become part of the disc. Using the jump condition

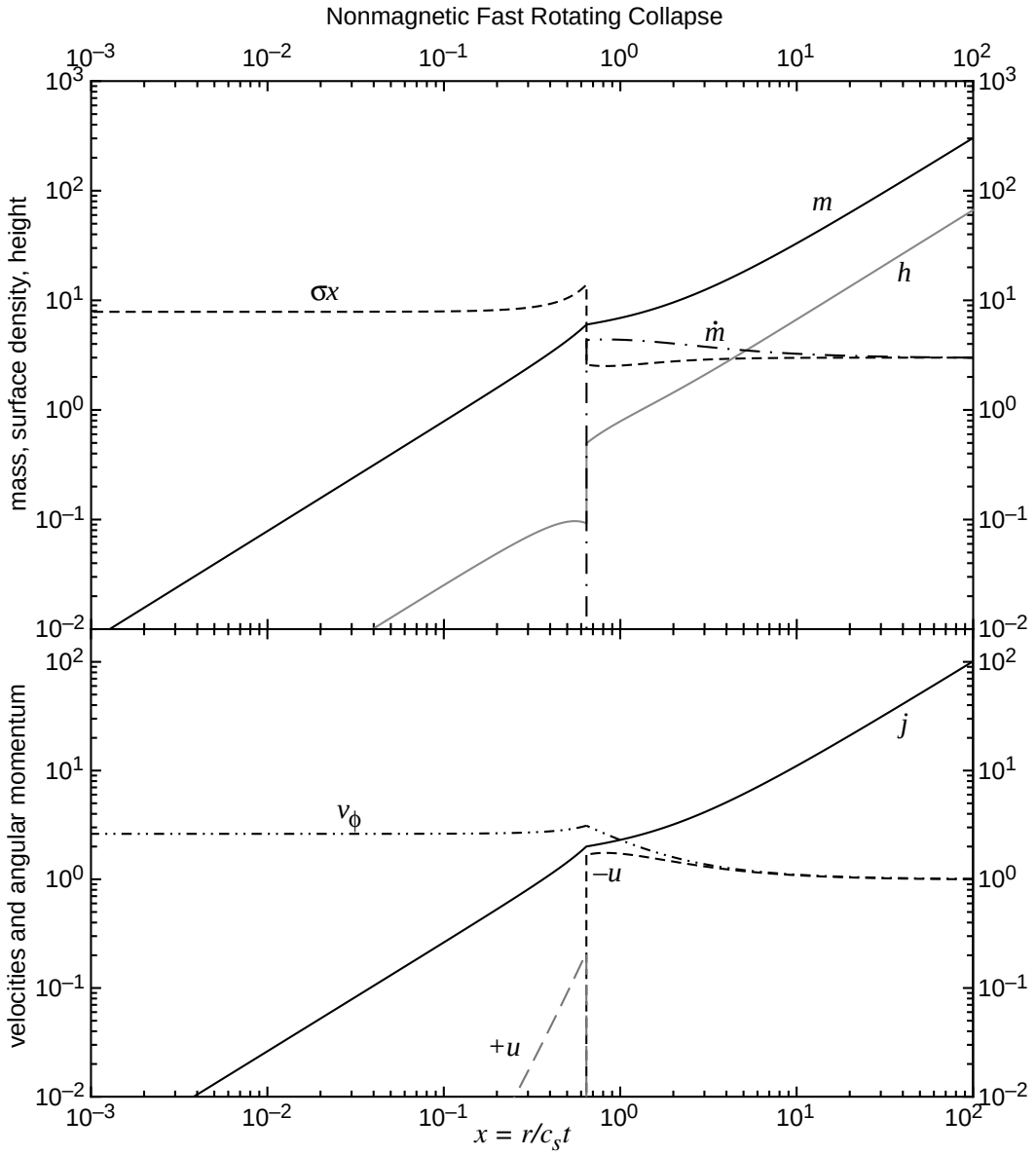

Figure 4.2: Similarity solution for the rapidly rotating nonmagnetic collapse. The outer asymptotic boundary conditions are as in Figure 4.1, however the initial (outer) rotational velocity is increased to $v_0 = 1.0$. The faster initial rotation causes the centrifugal force to balance gravity earlier in the collapse, so that the centrifugal shock occurs at $x_c = 0.64$. Although the radial velocity is much lower in this case than in the slow rotation calculation, the shock is intense enough to change the sign of the radial velocity immediately after the shock (indicated by the long-dash curve, $+u$), creating a region of shocked backflow that moves outwards in physical space.

4.57, it is possible to show that a backflow will occur when

$$w_u > \frac{1}{x_c}, \tag{4.59}$$

that is, when the upstream radial velocity satisfies the inequality

$$u_u < x_c - \frac{1}{x_c}. \tag{4.60}$$

The region of backflow is usually thin, and the material is quickly decelerated by the shocked increase in density to a value near to zero.

The passage of the centrifugal shock causes the material to be abruptly slowed, creating a large increase in the surface density and a flattening of the centrifugally-supported disc that forms interior to the shock. The variables quickly settle to their asymptotic values, taking the form of a rotationally-supported disc of material orbiting around the origin without ever falling in, as there is no way to brake its angular momentum. The enclosed mass in the disc decreases linearly, as does the angular momentum. It is clear that introducing a mechanism for braking the angular momentum will allow the material to move inwards through the Keplerian disc and fall onto a central point mass, resulting in the formation of a protostar at the centre of the disc. The most obvious way to achieve this is by the introduction of magnetic braking, which will be explored in the following section.

4.2 Ideal Magnetohydrodynamics Solutions

The most elementary form that the magnetic field behaviour can take is that dictated by ideal magnetohydrodynamics (IMHD), where there is no magnetic diffusion and the gas and magnetic field are tied by the insistence that the mass-to-flux ratio is constant. The field is frozen into the gas and moves with it throughout the collapse, with the constant nondimensional mass-to-flux ratio given by its initial value $\mu = \mu_0$. In this situation the collapse is described by the equations:

$$\frac{\partial \Sigma}{\partial t} + \frac{1}{r}\frac{\partial}{\partial r}(r\Sigma V_r) = 0, \tag{4.61}$$

$$\frac{\partial V_r}{\partial t} + V_r\frac{\partial V_r}{\partial r} = g_r - \frac{c_s^2}{\Sigma}\frac{\partial \Sigma}{\partial r} + \frac{B_z}{2\pi\Sigma}\left(B_{r,s} - H\frac{\partial B_z}{\partial r}\right) + \frac{J^2}{r^3}, \tag{4.62}$$

$$\frac{\partial J}{\partial t} + V_r\frac{\partial J}{\partial r} = \frac{rB_zB_{\phi,s}}{2\pi\Sigma} \tag{4.63}$$

$$\text{and } \frac{\Sigma c_s^2}{2H} = \frac{\pi}{2}G\Sigma^2 + \frac{GM_c\rho H^2}{2r^3} + \frac{1}{8\pi}\left(B_{r,s}^2 + B_{\phi,s}^2 - B_{r,s}H\frac{\partial B_z}{\partial r}\right); \tag{4.64}$$

where the flux and field are tied to the matter and defined by the relations

$$\Psi = \frac{2\pi G^{1/2} M}{\mu_0}, \tag{4.65}$$

$$B_z = \frac{2\pi G^{1/2} \Sigma}{\mu_0}, \tag{4.66}$$

$$B_{r,s} = \frac{\Psi}{2\pi r^2} \tag{4.67}$$

$$\text{and } B_{\phi,s} = -\min\left[\frac{\Psi}{2\pi r}\frac{V_\phi}{V_{A,ext}}; \delta B_z\right]. \tag{4.68}$$

In this model, the presence of a magnetic braking term in the angular momentum equation allows for the transfer of angular momentum from the pseudodisc to the envelope, so the gas may accrete onto a central mass (with mass M_c). The equation set is essentially the full set from Chapter 2 with $\tilde{\eta}_H = \tilde{\eta}_A = 0$, save for the induction and flux conservation equations, which have been reduced to the flux freezing descriptions in Equations 4.65 and 4.66.

The dimensionless form of these equations is

$$\frac{dm}{dx} = x\sigma, \tag{4.69}$$

$$(1-w^2)\frac{1}{\sigma}\frac{d\sigma}{dx} = -\frac{m}{x^2} + \frac{b_z}{\sigma}\left(b_{r,s} - h\frac{db_z}{dx}\right) + \frac{j^2}{x^3} + \frac{w^2}{x}, \tag{4.70}$$

$$\frac{dj}{dx} = \frac{1}{w}\left(j - \frac{x b_z b_{\phi,s}}{\sigma}\right) \tag{4.71}$$

$$\text{and } \left(\frac{\sigma m_c}{x^3} - b_{r,s}\frac{db_z}{dx}\right)h^2 + \left(b_{r,s}^2 + b_{\phi,s}^2 + \sigma^2\right)h - 2\sigma = 0; \tag{4.72}$$

with the magnetic field terms given by

$$\psi = \frac{m}{\mu_0} \tag{4.73}$$

$$b_z = \frac{\sigma}{\mu_0} \tag{4.74}$$

$$b_{r,s} = \frac{\psi}{x^2} \tag{4.75}$$

$$\text{and } b_{\phi,s} = -\min\left[\frac{2\alpha\psi j}{x^3}; \delta b_z\right]. \tag{4.76}$$

In order to calculate the solutions to these equations, a set of inner boundary conditions must be derived, as the formation of a protostellar mass at the origin changes the dynamics of the inner accretion disc. The jump conditions for the centrifugal shock that separates the dynamic outer collapse from the inner slowly-accreting Keplerian disc must also be derived anew, as the requirements of flux freezing demand that the centrifugal shock force a change in the strength of the magnetic field as well as the

density at the boundary of the inner disc. The derivations of the conditions describing each of these phenomena are presented in the following subsections; once their behaviour is understood it is then possible to calculate the similarity solutions presented in subsection 4.2.3. The similarity solutions show how the addition of a magnetic field changes the collapse behaviour, particularly in the innermost regions around the newly-formed protostar.

4.2.1 Inner solution

The addition of a magnetic field changes the form of the inner asymptotic solution, allowing for the formation of a semi-Keplerian, magnetically-diluted disc around a central point mass. It is not possible to obtain this solution by setting the diffusion terms in the asymptotic similarity solution derived in Chapter 3 to zero — doing this causes the density to vanish — so the derivation of a new inner similarity solution is performed here, using the same methodology as in the nonmagnetic and diffusive cases.

As before, the inner asymptotic solution is assumed to take the form of a series of power laws in x:

$$\sigma = \sigma_1 x^{-p} \tag{4.77}$$

$$\text{and } j = j_1 x^{-r}. \tag{4.78}$$

In this work, only those solutions in which a central mass forms are sought, and so the domain of p is limited such that $p < 2$. There exists a solution in which all of the angular momentum is removed from the collapse and no central mass may form, however no such collapse calculations are presented in this work. For further information about this "strong braking" solution the reader is directed to §3.2.3 of Krasnopolsky and Königl (2002).

Adopting this limit on p, the continuity equation then integrates to

$$m = m_c \tag{4.79}$$

(as in Sections A.1, A.2 and A.4). This is substituted into Equations 4.73 and 4.75:

$$\psi = \frac{m_c}{\mu_0} \tag{4.80}$$

$$\text{and } b_{r,s} = \frac{m_c}{\mu_0}\, x^{-2}. \tag{4.81}$$

These scalings for m and σ are then used to define

$$w = \frac{m_c}{\sigma_1}\, x^{p-1}, \tag{4.82}$$

$$\text{and } b_z = \frac{\sigma_1}{\mu_0}\, x^{-p}. \tag{4.83}$$

The behaviour of the azimuthal component of the magnetic field is examined by substituting the above scalings into Equation 4.76 to obtain

$$b_{\phi,s} = -\min\left[\frac{2\alpha j_1 m_c}{\mu_0}\, x^{-r-3}; \frac{\delta\sigma_1}{\mu_0}\, x^{-p}\right]; \tag{4.84}$$

of the two terms inside the brackets the term with the higher exponent is sought, in order to satisfy the requirements of the cap on the magnetic braking (for it is the smaller term as $x \to 0$). There are then two possible values of $b_{\phi,s}$:

$$b_{\phi,s} = -\frac{2\alpha j_1 m_c}{\mu_0}\, x^{-r-3} \tag{4.85}$$

which implies that $-r-3 > -p$ (this, together with $p < 2$, further requires that $r < -1$); or

$$b_{\phi,s} = -\frac{\delta\sigma_1}{\mu_0}\, x^{-p} \tag{4.86}$$

in the case that $r \geq -1$. Using the knowledge that a rotationally-supported disc is sought, the second of these values is chosen (the first leads to a solution in which the surface density σ is constant with respect to x, and the angular momentum of the fluid is too low to support it against gravity, preventing the formation of a rotationally-supported disc). This implies that the magnetic braking is strong enough in the disc that the artificial cap on $b_{\phi,s}$ must be invoked in order to prevent the removal of all angular momentum from the gas. While the cap is a simplistic way of limiting the transferral of angular momentum, it is not an unreasonable assumption, as it is expected that other effects such as a disc wind or the MRI will prevent the field lines from twisting too much and removing all chance of disc formation (Krasnopolsky and Königl, 2002).

The scalings for all of the terms are then substituted into the angular momentum equation (4.71), which becomes

$$-r j_1 x^{-r-1} = \frac{j_1\sigma_1}{m_c} x^{1-r-p} + \frac{\delta\sigma_1^2}{\mu_0^2 m_c} x^{2-2p}; \tag{4.87}$$

the exponent of the left hand term is then compared to the exponent of each of the terms on the right hand side in order to determine which is the dominant term. There are two possible solutions:

$$-r-1 = 1-r-p \qquad \text{or} \qquad -r-1 = 2-2p, \tag{4.88}$$

which are simplified to give

$$p = 2 \qquad \text{or} \qquad r = 2p-3. \tag{4.89}$$

As the domain of p has been limited to that where $p < 2$, the relevant solution is clearly $r = 2p - 3$, so that in this inner limit the angular momentum evolution is dominated by the magnetic braking. Furthermore, the condition $r \geq -1$ may be used to find a lower limit on p so that $1 \leq p < 2$. Having discarded the smaller term on the right hand side of Equation 4.87, the constant terms in the angular momentum equation are then rearranged to give the constant coefficient j_1 in terms of σ_1:

$$j_1 = \frac{\delta\sigma_1^2}{(3-2p)\mu_0^2 m_c}. \tag{4.90}$$

The vertical momentum equation (4.72), upon substitution of the above power laws, becomes

$$\left(\sigma_1 m_c x^{-3-p} + \frac{p m_c \sigma_1}{\mu_0^2} x^{-3-p}\right) h^2 + \left(\frac{m_c^2}{\mu_0^2} x^{-4} + \frac{\delta^2\sigma_1^2}{\mu_0^2} x^{-2p} + \sigma_1^2 x^{-2p}\right) h - 2\sigma_1 x^{-p} = 0. \tag{4.91}$$

Once more, using the restriction that $p < 2$ it is easy to show that $-4 < -2p$, so that the second and third term in the second set of brackets are small and may be dropped:

$$\left(\sigma_1 m_c + \frac{p m_c \sigma_1}{\mu_0^2}\right) h^2 x^{-3-p} + \left(\frac{m_c^2}{\mu_0^2} x^{-4}\right) h - 2\sigma_1 x^{-p} = 0; \tag{4.92}$$

this equation is then rearranged into the neater form

$$\left(1 + \frac{p}{\mu_0^2}\right) h^2 + \frac{m_c}{\sigma_1\mu_0^2} x^{p-1} h - \frac{2}{m_c} x^3 = 0. \tag{4.93}$$

The positive solution to this quadratic is

$$h = \frac{1}{2}\left(1 + \frac{p}{\mu_0^2}\right)^{-1} \left[-\frac{m_c}{\sigma_1\mu_0^2} x^{p-1} + \sqrt{\frac{m_c^2}{\sigma_1^2\mu_0^4} x^{2p-2} + \frac{8}{m_c}\left(1 + \frac{p}{\mu_0^2}\right) x^3}\right]; \tag{4.94}$$

clearly as $2p - 2 < 2$, then the second term in the square root is small and should be disregarded, however, if this is the case then the solution to Equation 4.94 is $h = 0$, which is unrealistic. Equation 4.94 can be rewritten as

$$h = 4\sigma_1 x^{-p} \left[\frac{m_c}{\sigma_1\mu_0^2} x^{p-1} + \sqrt{\frac{m_c^2}{\sigma_1^2\mu_0^4} x^{2p-2} + \frac{8}{m_c}\left(1 + \frac{p}{\mu_0^2}\right) x^3}\right]^{-1}, \tag{4.95}$$

which becomes

$$h = \frac{2\sigma_1\mu_0^2}{m_c^2} x^{4-p} \tag{4.96}$$

when the second term in the square root is small. The vertical pressure in the disc is therefore dominated by magnetic squeezing from the radial field term in the IMHD limit, rather than the gravitational field of the central mass. This result is to be

expected from the flux freezing condition — as the density of the disc increases in the innermost region the flux is increased proportionately so that it quickly comes to be the dominant force in determining the scale height of the disc.

All of the above power law scalings for the variables are then directly substituted into the radial momentum equation (4.70) so that it becomes

$$\left(1-\frac{m_c^2}{\sigma_1^2}x^{2p-2}\right)\frac{1}{\sigma_1 x^{-p}}\frac{d}{dx}(\sigma_1 x^{-p}) = -\frac{m_c}{x^2}+\frac{1}{\mu_0}\left(\frac{m_c}{\mu_0 x^2}-\frac{2\sigma_1\mu_0}{m_c^2}x^{4-p}\frac{d}{dx}(\sigma_1 x^{-p})\right) + \left(\frac{\delta\sigma_1^2}{(3-2p)\mu_0^2 m_c}\right)^2 x^{3-4p}+\frac{m_c^2}{\sigma_1^2}x^{2p-3}, \quad (4.97)$$

which is rearranged and simplified into

$$-\left(1-\frac{m_c^2}{\sigma_1^2}x^{2p-2}\right)\frac{p}{x} = -\frac{m_c}{x^2}\left(1-\frac{1}{\mu_0^2}\right)+\frac{2p\sigma_1^2}{m_c^2}x^{3-2p} + \left(\frac{\delta\sigma_1^2}{(3-2p)\mu_0^2 m_c}\right)^2 x^{3-4p}+\frac{m_c^2}{\sigma_1^2}x^{2p-3}. \quad (4.98)$$

As $p \geq 1$, then $2p-2 \geq 0$ and the second term in the first set of brackets is smaller than its predecessor and can be disregarded. The first term in those brackets scales as $\sim x^{-1}$ and as such becomes smaller than the gravitational term as $x \to 0$, so that the entire left hand side of Equation 4.98 is effectively zero. Because $3-2p > -1$ the $h(db_z/dx)$ term may also be dropped, and as $r = 2p-3 \geq -1$ the final term is also smaller than the gravitational force and becomes negligible as $x \to 0$. Thus the radial momentum equation may be simplified into the form

$$m_c\left(1-\frac{1}{\mu_0^2}\right)x^{-2} = \left(\frac{\delta\sigma_1^2}{(3-2p)\mu_0^2 m_c}\right)^2 x^{3-4p}, \quad (4.99)$$

which can be solved to give the exponents of the density and angular momentum:

$$p = \frac{5}{4} \quad (4.100)$$

$$\text{and } r = -\frac{1}{2}. \quad (4.101)$$

The coefficients in Equation 4.99 are then solved for the constant σ_1:

$$\sigma_1 = \frac{\mu_0 m_c^{3/4}}{\sqrt{2\delta}}\left(1-\frac{1}{\mu_0^2}\right)^{\frac{1}{4}}, \quad (4.102)$$

and this is substituted into Equations 4.90 and 4.96 to calculate the other coefficients:

$$j_1 = \sqrt{m_c\left(1-\frac{1}{\mu_0^2}\right)} \quad (4.103)$$

$$\text{and } h_1 = \sqrt{\frac{2}{\delta}}\frac{\mu_0^3}{m_c^{5/4}}\left(1-\frac{1}{\mu_0^2}\right)^{\frac{1}{4}}. \quad (4.104)$$

The full inner asymptotic solution is then given by the set of power law relations:

$$\sigma = \sigma_1 x^{-5/4} = \frac{\mu_0 m_c^{3/4}}{\sqrt{2\delta}}(1-\mu_0^{-2})^{1/4}\, x^{-5/4}, \tag{4.105}$$

$$m = m_c, \tag{4.106}$$

$$v = \sqrt{m_c(1-\mu_0^{-2})}\, x^{-1/2}, \tag{4.107}$$

$$j = \sqrt{m_c(1-\mu_0^{-2})}\, x^{1/2}, \tag{4.108}$$

$$u = -\frac{m_c}{\sigma_1}\, x^{1/4}, \tag{4.109}$$

$$h = \frac{2\mu_0^2\sigma_1}{m_c^2}\, x^{11/4}, \tag{4.110}$$

$$\psi = \frac{m_c}{\mu_0}, \tag{4.111}$$

$$b_z = \frac{\sigma_1}{\mu_0}\, x^{-5/4}, \tag{4.112}$$

$$b_{r,s} = \frac{m_c}{\mu_0}\, x^{-2}, \tag{4.113}$$

$$b_{\phi,s} = -\frac{\delta\sigma_1}{\mu_0}\, x^{-5/4} \tag{4.114}$$

$$\text{and } \dot{m} = m_c; \tag{4.115}$$

these are the same as those presented without explicit derivation in §3.2 of Krasnopolsky and Königl (2002). In dimensional form the similarity solution becomes:

$$\Sigma = \frac{c_s^{9/4}\sigma_1}{2\pi G}\,\frac{t^{1/4}}{r^{5/4}}, \tag{4.116}$$

$$M = \frac{c_s^3 m_c}{G}\, t, \tag{4.117}$$

$$V_\phi = \sqrt{c_s^3 m_c(1-\mu_0^{-2})\frac{t}{r}} = \sqrt{\frac{GM}{r}(1-\mu_0^{-2})} \tag{4.118}$$

$$J = \sqrt{c_s^3 m_c(1-\mu_0^{-2})rt} = \sqrt{GMr(1-\mu_0^{-2})}, \tag{4.119}$$

$$V_r = -\frac{c_s^{3/4} m_c}{\sigma_1}\left(\frac{r}{t}\right)^{1/4}, \tag{4.120}$$

$$H = \frac{2\mu_0^2\sigma_1}{m_c^2}\,\frac{r^{11/4}}{(c_s t)^{7/4}}, \tag{4.121}$$

$$\Psi = \frac{2\pi c_s^3 m_c t}{\mu_0 G^{1/2}} = \frac{2\pi\sqrt{G}}{\mu_0}\, M, \tag{4.122}$$

$$B_z = \frac{\sigma_1 c_s^{9/4} t^{1/4}}{\mu_0 G^{1/2} r^{5/4}} = \frac{2\pi\sqrt{G}}{\mu_0}\,\Sigma, \tag{4.123}$$

$$B_{r,s} = \frac{\Psi}{2\pi r^2} = \frac{\sqrt{G}}{\mu_0 r^2}\, M, \tag{4.124}$$

$$B_{\phi,s} = -\delta B_z = -\frac{2\pi\sqrt{G}\delta}{\mu_0}\,\Sigma \tag{4.125}$$

$$\text{and } \dot{M} = \frac{c_s^3 m_c}{G} = -2\pi r V_r \Sigma. \tag{4.126}$$

The disc is in near-Keplerian rotation, with the deviation from Keplerian determined by the magnetic "dilution" factor $(1-\mu_0^{-2})^{1/2}$. The larger the mass-to-flux ratio μ_0 (i.e. the less flux there is in the initial molecular cloud) the closer the rotational speed is to that of the nonmagnetic Keplerian disc solution in the preceding section. It is the magnetic braking that causes this effect, as it transports the angular momentum of the disc material to the envelope, allowing the fluid to spiral inwards towards the central mass. For the similarity solutions presented in subsection 4.2.3 this magnetic dilution factor is close to one (0.939), so the discs are in near-Keplerian rotation.

Equation 4.105 shows that the magnetic dilution factor also reduces the surface density, however the presence of the mass-to-flux ratio in the definition of the coefficient σ_1 typically has more of an effect on the density of the inner disc, enhancing it while also reducing the equivalent constant in the radial velocity power law relation (Equation 4.109). The magnetic forces determine the radial dependence of these terms and the scale height, which becomes very small in the disc as expected. The low infall speed ensures that the disc remains in a near-exact dynamical equilibrium.

The magnetic field takes on a split monopole form, with the field lines strongly inclined due to the domination of the radial component over the vertical and azimuthal components (see Equations 4.112 and 4.113). The strong magnetic field changes the dynamics of the disc from being strictly Keplerian, and its increasing strength in the innermost regions demonstrates the magnetic flux problem that occurs in simulations of star formation (Li, 1998, also Section 1.5). As the angle between the field and the disc surface is $< 60°$ ($B_{r,s}/B_z > 1/\sqrt{3}$) the disc is able to drive a centrifugal wind from its surface, which would reduce the amount of matter that reaches the origin and carry away excess flux (Blandford and Payne, 1982). Although this is not explored further in this work, it has been shown that the presence of a disc wind could assist in solving the magnetic flux problem (Krasnopolsky and Königl, 2002, appendix C).

As in the nonmagnetic case, the transition between the collapsing flow and the near-Keplerian inner disc is marked by a sharp transition in the radial velocity and surface density. The constraint of flux freezing means that the magnetic field must also change in the shock transition to ensure continuity. These new jump conditions are derived in the following subsection.

4.2.2 Shock position and jump conditions

Similarly to the nonmagnetic case, the position of the centrifugal shock is found iteratively, using the behaviour of the downstream variables to refine the shock position, x_c, until a convergence is reached. Because the ratio j/m does not change greatly from its initial value before it encounters the centrifugal shock, the initial guess used to find the position of x_c is that defined by Equation 4.43 from the nonmagnetic case. Table 4.2, which lists both the estimated and true shock positions for the similarity solutions calculated in the following subsection, shows that this is still an acceptable approximation to the shock position; the difference between the estimated and actual shock positions is typically $\lesssim 10\%$.

There are two different sets of jump conditions used in the ideal magnetohydrodynamics models, and the choice of which of these to use is determined by the dominant vertical forces in the disc in the region of the shock. For both solutions the continuity equation gives the first jump condition to be

$$w\sigma = \text{constant} \tag{4.127}$$

as in the nonmagnetic case. Flux freezing, which takes the form of $b_z = \sigma/\mu_0$ from the induction equation, allows for the vertical field jump condition to be given by the similar equation

$$wb_z = \text{constant}. \tag{4.128}$$

As before, the radial momentum equation takes the form

$$(1 - w^2)\frac{d\sigma}{dx} = -b_z h \frac{db_z}{dx} \tag{4.129}$$

where the other terms in Equation 4.70 are small at the shock position compared to the derivatives of the rapidly changing surface density and magnetic field. The flux freezing condition is substituted into the right hand side of this equation so that it becomes

$$(1 - w^2)\frac{d\sigma}{dx} = -\frac{h\sigma}{\mu_0^2}\frac{d\sigma}{dx}; \tag{4.130}$$

and a good understanding of how the disc scale height behaves in the shock region is required in order to calculate the integral of the right hand side of this equation.

If magnetic squeezing due to the radial field component dominates the scale height (as in the asymptotic inner solution) then $h \approx 2\sigma/b_{r,s}^2$ and the right hand side of Equation 4.130 becomes

$$-\frac{h\sigma}{\mu_0^2}\frac{d\sigma}{dx} = -\frac{2\sigma^2}{\mu_0^2 b_{r,s}^2}\frac{d\sigma}{dx} = -\frac{2}{3\mu_0 b_{r,s}^2}\frac{d(\sigma^3)}{dx}. \tag{4.131}$$

model	estimated x_c	actual x_c
$v_0 = 0.1$, $\alpha = 0.1$	$0.00\dot{6}$	0.0049
$v_0 = 1.5$, $\alpha = 0.1$	1.5	1.48
$v_0 = 1.5$, $\alpha = 0.01$	1.5	1.59

Table 4.2: Comparison between the estimated and actual values of the centrifugal shock position, x_c, for the models calculated in the following subsection. The estimated values are typically larger than the true shock position, save for when the magnetic braking parameter α is particularly weak, however they are close enough that they provide a reasonable first approximation for the iterative routine.

As $b_{r,s} = m/\mu_0 x^2$ is constant across the shock due to the conservation of mass, the integral of Equation 4.130 is then the final jump condition

$$\sigma(1+w^2) = -\frac{2\sigma^3}{3\mu_0 b_{r,s}^2} + \text{constant} \tag{4.132}$$

using the result from Section 4.1.2 for the left hand side. Denoting the upstream and downstream variables by the subscripts u and d as in the nonmagnetic case, it can be shown that these jump conditions have one real solution that is given by

$$\sigma_d = -\frac{\sigma_u}{3} + q_+ + q_-, \tag{4.133}$$

where

$$q_\pm = \left(-q/2 \pm D^{1/2}\right)^{1/3}, \tag{4.134}$$

$$q = -\frac{3}{2}\mu_0^2 b_{r,s}^2 \sigma_u w_u^2 - \frac{\sigma_u}{3}\left(\sigma_u^2 + \frac{3}{2}\mu_0^2 b_{r,s}^2\right), \tag{4.135}$$

$$D = (p/3)^3 + (q/2)^2 \tag{4.136}$$

$$\text{and } p = \frac{2}{3}\sigma_u^2 + \frac{3}{2}\mu_0^2 b_{r,s}^2. \tag{4.137}$$

The greater details of this derivation are provided in appendix B3 of Krasnopolsky and Königl (2002), as this set of jump conditions is the same as those for their "magnetically squeezed shock". These jump conditions are used in the slowly rotating collapse solution shown in Figure 4.3 where the radial field component is already large in the region of the shock.

The second set of possible jump conditions are those that apply when the shock occurs in the region where the disc self-gravity still dominates the vertical forces in the disc, so that $h \approx 2/\sigma$. In this case the right hand side of the radial momentum equation at the shock (4.130) is then

$$-b_z h \frac{db_z}{dx} = -\frac{2}{\mu_0^2}\frac{d\sigma}{dx}; \tag{4.138}$$

this is integrated at the shock position to give the jump condition

$$\sigma(1+w^2) = -\frac{2\sigma}{\mu_0^2} + \text{constant}. \tag{4.139}$$

Combining this with the other jump conditions in Equations 4.127 and 4.128 gives the nontrivial solution to the jump conditions:

$$w_d = \left(1+\frac{2}{\mu_0^2}\right)\frac{1}{w_u}, \tag{4.140}$$

$$\sigma_d = \sigma_u w_u^2 \left(1+\frac{2}{\mu_0^2}\right)^{-1} \tag{4.141}$$

$$\text{and } b_{zd} = b_{zu} w_u^2 \left(1+\frac{2}{\mu_0^2}\right)^{-1}, \tag{4.142}$$

which is the solution for the nonmagnetic case with the additional magnetic factor $(1+2/\mu_0^2)$. These jump conditions are used in the rapidly rotating solutions shown in Figures 4.4 and 4.5, in which the shock occurs much earlier in the collapse process before the radial field has built up enough to dominate the vertical squeezing.

4.2.3 Similarity solutions

The IMHD similarity solutions are calculated in a similar manner to those for the non-magnetic model, by integrating the equations (in this case Equations 4.69–4.71) from the outer boundary to the centrifugal shock position, performing the jump calculations and then continuing the integration to the inner boundary. The exact location of the shock is found iteratively by performing the integration using an estimated shock position (starting at the value of x_c derived in subsection 4.1.2) and using the post-shock behaviour to refine the estimate of the shock position until the integrated variables at the inner boundary match onto the asymptotic inner solution as expected. The full details of this routine are described in Section 5.2 for the Hall similarity solutions.

The addition of magnetic braking to the calculations causes the formation of a central point mass, parameterised by the nondimensional mass and accretion rate m_c. The value of m_c is initially unknown, although it is first approximated by the value of the plateau mass m_{pl} given by Equation 4.42. The true value of the central mass is determined by iteration and is typically easier to find than the shock position, as the gravity of the central mass becomes important to the collapse dynamics only in the innermost regions of the collapsing pseudodisc. While small changes to the assumed value of m_c may greatly change the integrated values of m and the surface density at the inner boundary, the outer and mid-regions are only superficially altered.

The full calculation, including the convergence on the true values of x_c and m_c, typically takes under a minute on a current generation desktop computer, provided

that the influence of an incorrect shock position on the post-shock variables is well-understood. A discussion of the types of post-shock behaviour observed while trying to calculate the shock position is provided in Chapter 5 for the Hall MHD solutions.

The three similarity solutions presented here show a slow collapse with initial conditions matching those in the nonmagnetic slow collapse and a faster collapse with two different values of the magnetic braking parameter α (the ratio of the sound speed to the Alfvén speed in the external envelope) defined in Equation 2.84. As before, the parameters were chosen to match those used in the solutions in §3.2 of Krasnopolsky and Königl (2002) as a mechanism for testing the model calculations. The mass-to-flux ratio is held constant at $\mu_0 = 2.9$; and the other initial parameters match those in the nonmagnetic solutions, with mass parameter $A = 3$ and infall velocity $u_0 = -1$. The azimuthal field cap is fixed at $\delta = 1$, as the azimuthal field component is unlikely to exceed the vertical one dramatically in a real collapsing flow. These values were chosen to match onto both the numerical calculations of Ciolek and Königl (1998) and observations such as those by Crutcher (1999); all are within the range of physical parameters believed to be encountered in collapsing molecular cloud cores.

All three solutions look similar to the nonmagnetic solutions from Section 4.1 in the outer regions of the collapse, where the ratio of the enclosed mass to the specific angular momentum is constant and the mass scales with x. However, the nonmagnetic and IMHD similarity solutions diverge as the magnetic field builds up and the magnetic braking begins transporting the angular momentum to the envelope, increasing this ratio and breaking the resemblance. The behaviour of the solutions interior to this outer collapse is determined by the initial rotation speed v_0 and the value of the magnetic braking parameter α.

The slow rotation solution presented in Figure 4.3 is characterised by the parameters $V_0 = 0.1c_s$ and $\alpha = 0.1$, corresponding to moderate rotation and magnetic braking rates. As in the slowly rotating nonmagnetic solution in Figure 4.1, the mass and angular momentum plateau as the radial velocity of the collapsing matter increases. The addition of magnetic braking to the calculations causes a slight reduction of the angular momentum in the plateau region from $j_{pl} \sim 2.5$ to ~ 1.8, which in turn reduces the centrifugal force so that the shock position drops from $x_c = 7.7 \times 10^{-3}$ in the nonmagnetic similarity solution to $x_c = 4.9 \times 10^{-3}$ in the IMHD solution.

The magnetic field builds up in the plateau region until the magnetic squeezing comes to dominate the vertical compression of the disc, so that it is much thinner than its nonmagnetic counterpart in Figure 4.1 (note that in Figure 4.3 and the other IMHD similarity solutions the scale height is plotted as $100h/x$, while for the nonmagnetic similarity solutions in Figures 4.1 and 4.2 h is plotted directly). The scale height is therefore approximated by $h \approx 2\sigma/b_{r,s}$ and the jump conditions used at the centrifugal

shock are the first set derived in subsection 4.2.2 (Equations 4.127, 4.128 and 4.133).

As in the nonmagnetic case, the matter is falling in at near-free fall speeds as the centrifugal force builds up until it is able to counter the influence of the central mass gravity and the centrifugal shock is formed. The fluid is rapidly decelerated by the encounter with the ring of increased density that is the shock front. The spike that occurs in the surface density corresponds to an equivalent increase in the magnetic field strength; this in turn produces a rapid drop in the angular momentum caused by increased magnetic braking.

The post-shock region of the slowly rotating similarity solution is very narrow, with no backflow region as may occur in rapidly rotating solutions. After a thin transition region the flow merges into the asymptotic magnetically-diluted Keplerian disc solution outlined in subsection 4.2.1. Accretion through this disc is slow and driven by the magnetic braking, which gives j its characteristic near-Keplerian profile (which scales with $x^{1/2}$), so that the disc is in almost perfect dynamical equilibrium. The disc mass is $\sim 3\%$ that of the central mass, and the accretion rate from the disc onto the point mass is given by $\dot{m} = m_c = 6.0$; this corresponds to a dimensional value of $\dot{M}_c \approx 10^{-5}$ $\mathrm{M}_\odot$ yr^{-1}, which is at the high end of the range of expected accretion rates for protostellar cores (Lee et al., 2001).

Figure 4.4 shows the similarity solution for a rapidly rotating IMHD collapse, with the same initial conditions and parameters as those in the slowly rotating solution in Figure 4.3 save for the initial rotational velocity which has been increased to $V_0 = 1.5c_s$. This is higher than the value in the corresponding nonmagnetic similarity solution presented in Figure 4.2 ($v_0 = 1.0$), however, the two solutions are qualitatively similar. The increase in the initial angular momentum implies that the centrifugal force comes to balance gravity earlier in the collapse, resulting in a much higher value of the shock position $x_c = 1.48$. In this region of the flow the enclosed mass is still much higher than m_c, the infall rate is slow and the disc scale height is still dominated by the disc self-gravity; the jump conditions applied at this shock are the generalised isothermal shock conditions given by Equations 4.140–4.142.

Similarly to the fast nonmagnetic similarity solution, the centrifugal shock in Figure 4.4 is so strong that it creates a region of shocked backflow in the post-shock annulus. This region has a finite width in x, during which the outflowing gas is first slowed and then begins to inflow once more as the surface density decreases from its shocked value. The disc of accreting material is still larger than in the slowly rotating solution, and contains approximately four times as much mass as the central protostar. It is only in the inner regions of this disc that the variables attain their asymptotic magnetically-diluted Keplerian disc values, after an extended region in which the disc is self-gravitating.

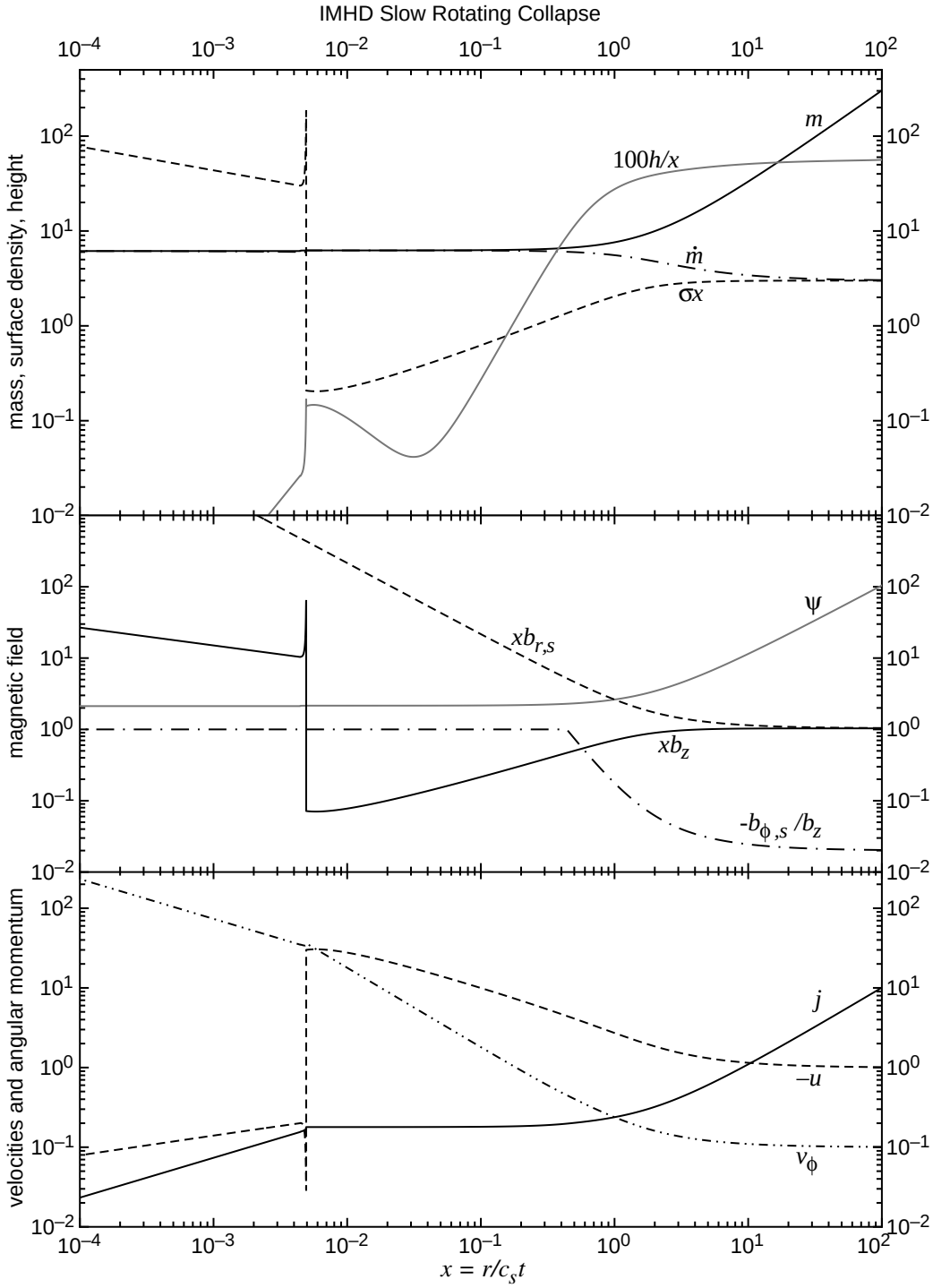

Figure 4.3: Similarity solution for the slowly rotating IMHD collapse, with outer asymptotic boundary conditions $A = 3$, $u_0 = -1$, $\mu_0 = 2.9$ and $v_0 = 0.1$, matching those in Figure 4.1 and figure 3 of Krasnopolsky and Königl (2002). The top and lower panels display the same variables as in Figure 4.1, while the central panel displays the nondimensional magnetic field components $b_{r,s}$, $b_{\phi,s}$ and b_z, as well as the magnetic flux ψ, as functions of the similarity variable x. A magnetically-diluted Keplerian disc forms inside a centrifugal shock (located at $x_c = 4.93 \times 10^{-3}$).

The angular momentum remains high throughout the extended disc that forms behind the shock as the low field density implies that magnetic braking has little effect and the outer disc regions are strongly non-Keplerian. Because the braking is so inefficient, very little mass accumulates at the origin compared with the slow rotation case; the central mass is $m_c = 0.57$, which corresponds to a reduced accretion rate of $\dot{M}_c \approx 9 \times 10^{-7}$ $\mathrm{M}_\odot$ yr^{-1}. It is clear that increasing the angular momentum in the initial cloud creates an angular momentum problem similar to that encountered in the nonmagnetic case, in which the inefficiency of magnetic braking transportation of the angular momentum inhibits the star formation process, creating a smaller central mass surrounded by an extended disc that very slowly falls inward.

The final plot, Figure 4.5, shows a second rapidly rotating similarity solution that has the same initial values as Figure 4.4, save that the magnetic braking parameter α is reduced from 0.1 to 0.01. This solution has even less efficient braking than Figure 4.4, which causes the centrifugal shock to occur even sooner at $x_c = 1.59$ and extends the region of backflow so that it occurs over an order of magnitude in self-similar space. The backflow fuels the shock, but eventually the matter slows enough that it is able to start infalling once more.

Even once the fluid is inflowing again, it takes much longer to join the asymptotic inner solution (see the turning point in σx at around $x = 0.004$) as the low rate of infall prevents the magnetic field from building up and compressing the disc. It is only once the magnetic field is strong enough that the azimuthal field parameter attains its capped value that the collapse starts to behave in a manner similar to the asymptotic solution. As the region of inflow is reduced so too is the central mass, with $m_c = 0.05$ corresponding to a very low accretion rate of $\dot{M}_c \approx 8 \times 10^{-8}$ $\mathrm{M}_\odot$ yr^{-1}. Again, the mass of the rotationally-supported and self-gravitating disc is about four times that at the origin.

In all of the similarity solutions the magnetic braking acts to transfer the angular momentum to the external medium, and the reduction of α or an increase in the initial angular momentum of the cloud leads to a reduction in the amount of matter that can fall onto the central point mass, resulting in an enhanced angular momentum problem. As the angular momentum inside of the centrifugal shock is increased, the inner similarity solutions tend towards a near-nonmagnetic solution similar to that in Figure 4.2 in which no central mass is able to form.

The azimuthal field component reaches its capped value in all of the solutions presented here, which limits the amount of magnetic braking that is possible in the inner regions of the collapse. If this cap were lifted then further braking could reduce the disc mass and size while increasing accretion onto the central point mass that forms, perhaps even to the point where no disc is able to form around the star, as in

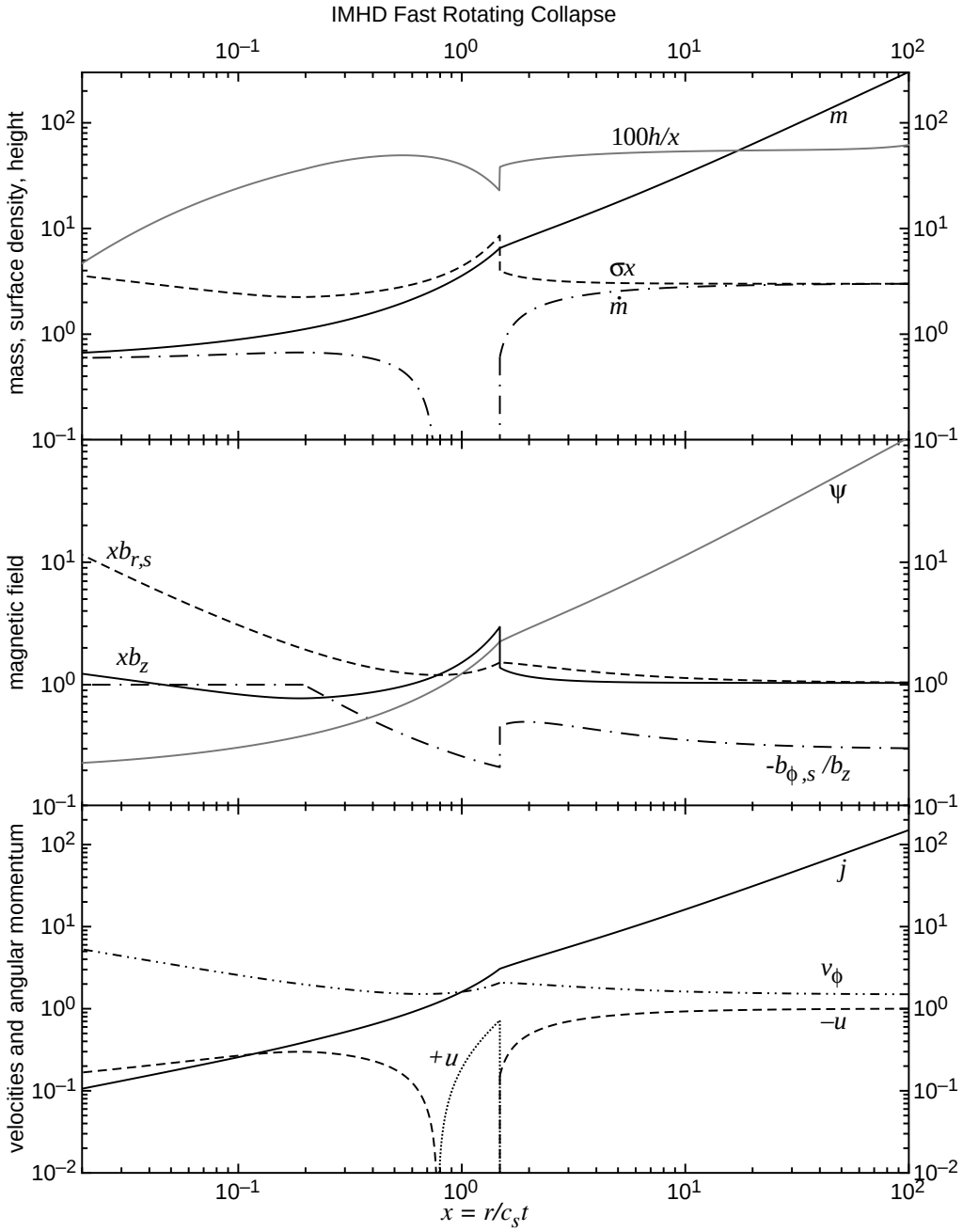

Figure 4.4: Similarity solution for the rapidly rotating IMHD collapse, with outer asymptotic boundary conditions matching those in Figure 4.3, save for the initial rotational velocity, $v_0 = 1.5$, which is higher than the equivalent nonmagnetic case in Figure 4.2 but matches figure 4 of Krasnopolsky and Königl (2002). Note that the horizontal scale is different to that in Figure 4.2, as the variables attain their asymptotic forms much earlier in this solution. In this case the centrifugal shock occurs sooner at $x_c = 1.48$, and as in the nonmagnetic case the infall velocity changes sign at the shock, creating a region of backflow. The variables gradually settle to their asymptotic values once the gas starts collapsing again and the azimuthal field reaches its capped value; however, the forming central mass is very small ($m_c = 0.57$) compared to that in the slow rotation solution.

the numerical solutions of Mellon and Li (2008). It is clear that limiting the magnetic braking is a solution to the problem of disc formation, yet this needs to be better studied, either by increasing the resolution of the numerical models so that those mechanisms which could decrease the magnetic braking (such as nonaxisymmetric turbulence in the thin inner disc) can be explored, or by adopting a better prescription for the azimuthal field component in the similarity solutions.

The other major problem in star formation is introduced here in the IMHD models: the magnetic flux problem (Spitzer, 1978, also Section 1.5), in which too much magnetic flux is dragged into the central protostar and disc. This is obvious from the way that $b_{r,s}$, which scales with x^{-2} (and the other magnetic field components to a lesser extent), increase dramatically in the innermost regions of disc. This problem is exemplified by the restrictions of IMHD, as the matter is tied to the field lines and any gas accreted through the disc will bring flux with it, leading to a high concentration of the magnetic field in the inner disc regions of high density and the central point mass.

The angular momentum and magnetic flux problems are mitigated by breaking the assumption of flux freezing in the collapsing gas, which changes the dynamics of both the angular momentum and magnetic field transport in the pseudodisc. The first step in achieving this is to introduce ambipolar diffusion, which causes the decoupling of the field from the neutral particles at the densities encountered around the beginning of the mass plateau and enhances the magnetic braking in the forming disc. The influence of ambipolar diffusion on the collapse process is explored in detail in the following section.

4.3 Ambipolar Diffusion Solutions

The last of the preliminary models used to test the code is the non-ideal MHD calculation with ambipolar diffusion. In this model, the field is no longer strictly tied to the neutral material, for as the density increases the field is decoupled from the neutral particles and is instead tied to the ions via the nondimensional ambipolar diffusion parameter $\tilde{\eta}_A$. The magnetic field is then able to be advected against the flow, reducing the magnitude of the magnetic flux problem that occurs in the central region of the IMHD solutions. The ambipolar diffusion term in the induction equation becomes dominant near the origin; this changes the structure of the inner Keplerian disc, increasing the density and reducing the angular momentum and flux carried inwards by the gas.

The ambipolar diffusion model is described by Equations 2.88–2.92 in the limit that $\tilde{\eta}_H = 0$. For brevity these shall not be duplicated here, however the corresponding set of nondimensional equations (originally stated in Equations 2.104–2.114) are reproduced

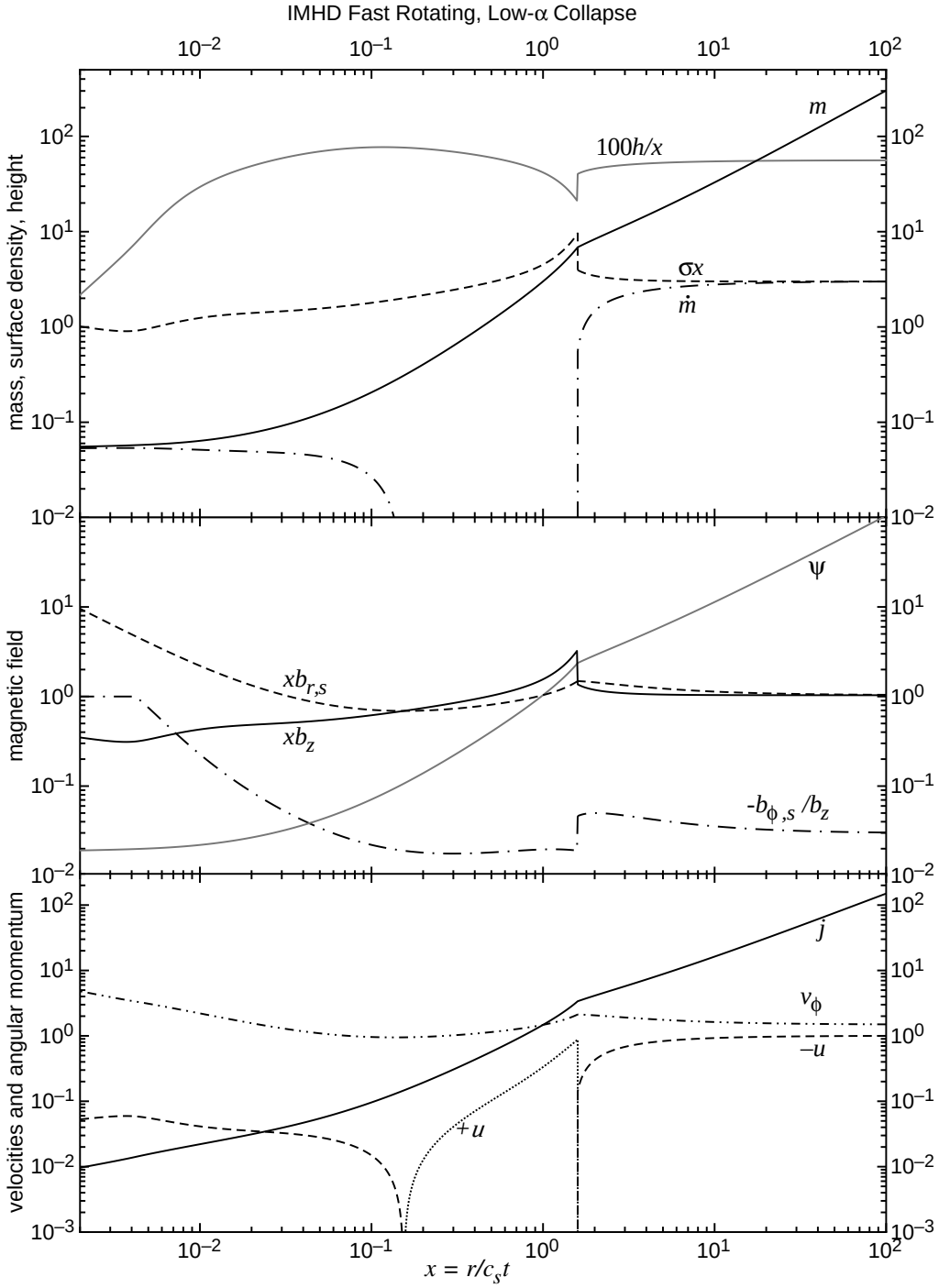

Figure 4.5: Similarity solution for the rapidly rotating IMHD collapse with reduced magnetic braking parameter $\alpha = 0.01$. The boundary conditions otherwise match those in Figure 4.4 and figure 5 of Krasnopolsky and Königl (2002); the horizontal scale is again changed to show the inner regions of the collapse. The reduced magnetic braking parameter causes there to be a wider backflow region inwards of the centrifugal shock at $x_c = 1.59$, which reduces the size of the extended accretion disc. The near-Keplerian disc region is much smaller, beginning around $x \approx 0.004$, and the central mass is reduced to $m_c = 0.054$.

in the interests of clarity, as the important terms in these equations shall be discussed in the following subsections. These are

$$\frac{dm}{dx} = x\sigma, \tag{4.143}$$

$$(1-w^2)\frac{1}{\sigma}\frac{d\sigma}{dx} = -\frac{m}{x^2} + \frac{b_z}{\sigma}\left(b_{r,s} - h\frac{db_z}{dz}\right) + \frac{j^2}{x^3} + \frac{w^2}{x}, \tag{4.144}$$

$$\frac{dj}{dx} = \frac{1}{w}\left(j - \frac{xb_z b_{\phi,s}}{\sigma}\right), \tag{4.145}$$

$$\left(\frac{\sigma m_c}{x^3} - b_{r,s}\frac{db_z}{dx}\right)h^2 + \left(b_{r,s}^2 + b_{\phi,s}^2 + \sigma^2\right)h - 2\sigma = 0, \tag{4.146}$$

$$\frac{d\psi}{dx} = xb_z, \tag{4.147}$$

$$\text{and } \psi - xwb_z + \tilde{\eta}_A x b_z^2 h^{1/2}\sigma^{-3/2}\left(b_{r,s} - h\frac{db_z}{dx}\right) = 0; \tag{4.148}$$

while the accretion rate and other field components are given by

$$\dot{m} = -xu\sigma, \tag{4.149}$$

$$b_{r,s} = \frac{\psi}{x^2}, \tag{4.150}$$

$$\text{and } b_{\phi,s} = -\min\left[\frac{2\alpha\psi j}{x^3}\left(1 + \frac{2\alpha\tilde{\eta}_A h^{1/2}\psi b_z}{x^2\sigma^{3/2}}\right)^{-1}; \delta b_z\right]. \tag{4.151}$$

The ambipolar diffusion calculations were the most advanced of those performed by Krasnopolsky and Königl (2002) and their solutions shall be examined in detail in this section. In addition to the centrifugal shock that separates the region of dynamic inflow and the slow-infall Keplerian disc, ambipolar diffusion drives a continuous shock outwards as it decouples the field from the neutral fluid. The position and behaviour of these shocks, and the dynamics of the asymptotic inner disc solution must both be discussed before the similarity solutions to the full set of MHD equations with ambipolar diffusion can be presented and analysed.

4.3.1 Inner solution

As was mentioned in Section 3.2, the inner asymptotic solution for the full model with both ambipolar and Hall diffusion reduces to the solution for a model with just ambipolar diffusion in the limit that the Hall diffusion parameter $\tilde{\eta}_H = 0$. This solution was presented without explicit derivation in §3.3 of Krasnopolsky and Königl (2002), and it is reproduced here for the purpose of discussion.

The derivation of the nondimensional inner similarity solution directly follows that in Section 3.1 so that the asymptotic power law relations take the form:

$$m = m_c, \tag{4.152}$$

$$\dot{m} = m_c, \tag{4.153}$$

$$\sigma = \sigma_1 x^{-3/2} = \frac{2\tilde{\eta}_A\sqrt{2m_c}}{3\delta\sqrt{(3\delta/2\tilde{\eta}_A)^2+1}}\, x^{-3/2}, \tag{4.154}$$

$$h = h_1 x^{3/2} = \sqrt{\frac{2}{m_c[1+(2\tilde{\eta}_A/3\delta)^2]}}\, x^{3/2}, \tag{4.155}$$

$$u = -\frac{m_c}{\sigma_1}\, x^{1/2}, \tag{4.156}$$

$$v = \sqrt{\frac{m_c}{x}}, \tag{4.157}$$

$$j = \sqrt{m_c x}, \tag{4.158}$$

$$\psi = \frac{4}{3} b_z x^2, \tag{4.159}$$

$$b_z = \frac{m_c^{3/4}}{\sqrt{2\delta}}\, x^{-5/4}, \tag{4.160}$$

$$b_{r,s} = \frac{4}{3}\, b_z, \tag{4.161}$$

$$\text{and } b_{\phi,s} = -\delta\, b_z; \tag{4.162}$$

m_c is the constant nondimensional mass infall rate. The dimensional form of these variables are given by substituting the above definitions of the constants σ_1 and h_1 into Equations 3.32–3.42; the other coefficients and the dimensional scaling of the variables are unchanged from the inner asymptotic solution with both ambipolar and Hall diffusion.

The inner solution represents a disc in Keplerian rotation; it is supported against gravity by the angular momentum and has a low accretion rate onto the central protostar (which has mass $M_c = m_c c_s^3 t/G$, where c_s is the thermal sound speed and G the gravitational constant). As in the full Keplerian disc solution discussed in Section 3.2, the scale height and the surface density of the centrifugally-supported disc depend upon the ambipolar diffusion coefficient, while the magnetic field strength in the disc depends only on the nondimensional mass infall rate and the cap on the azimuthal component of the magnetic field.

The dimensional value of the surface density Σ similarly depends on the ambipolar diffusion parameter $\tilde{\eta}_A$. For the position $r = 1$ AU at a time $t = 10,000$ yr in a disc with sound speed $c_s = 0.19$ km s^{-1}, azimuthal field cap $\delta = 1$ and accretion rate $\dot{M}_c = 10^{-5}$ M$_\odot$ yr^{-1} (which corresponds to a vertical magnetic field component

$B_z = 1.15$ G), the surface density is given by

$$\Sigma \simeq \frac{2690\,\tilde{\eta}_A}{\sqrt{1 + 2.25\tilde{\eta}_A^{-2}}} \text{ g cm}^{-3}. \tag{4.163}$$

The size of the ambipolar diffusion parameter $\tilde{\eta}_A$ determines the build-up of material relative to the magnetic field, which moves inward slower than the neutral particles in the disc. The disc is kept in Keplerian rotation by the ambipolar diffusion, which holds up the gas and balances its inward radial velocity with the drift of the field lines against the flow.

As the only real difference between this solution and the full ambipolar and Hall diffusion solution is the change in the values of Σ and H, which depend upon the ratio of the diffusion parameters, it will not be discussed further here. The reader is directed to Section 3.2 and Chapter 5 for further analysis and discussion of the Keplerian disc behaviour in the diffusive regime.

4.3.2 Shock positions and jump conditions

Ambipolar diffusion causes the magnetic field and charged particles to accrete onto the central point mass more slowly than the neutral particles, and collisions between the neutrals and ions slow the primarily neutral fluid so that it accretes even more slowly than in the IMHD solution. Its importance to the dynamics of the flow depends upon the density, and so in the outermost regions of the collapsing cloud it has little effect on the infall rate of the field, which is ruled by IMHD as in the previous model. However, at lower x, as the magnetic field and the density build up, ambipolar diffusion becomes important and the field is decoupled from the neutral matter, though it remains attached to the charged particles. The decoupling causes the field to build up rapidly, and the magnetic forces may become stronger than gravity as the field lines are forced to diffuse outwards against the accreting neutrals at a speed almost as high as the accretion speed. The compressed field lines take the form of an extended shock front that slows the accretion and compresses the disc in the vertical direction.

This magnetic diffusion shock was first predicted to occur by Li and McKee (1996), and appeared in the numerical and analytic solutions of Ciolek and Königl (1998), Contopoulos et al. (1998) and Krasnopolsky and Königl (2002), where it was referred to as the "ambipolar diffusion shock". In the model of Li and McKee (1996) the shock was driven by the decoupling of the field from the gas by Ohmic dissipation, however ambipolar diffusion is known to become important at lower densities than Ohmic diffusion (see Section 1.2 for an overview) and so it causes the development of the shock at this early stage of collapse before Ohmic dissipation is able to decouple the field from the gas. Ohmic dissipation does become important in the innermost

and later stages of collapse (Shu et al., 2006), when the density is high and the field becomes entirely decoupled from the gas.

The magnetic diffusion shock is of C-type (Draine and McKee, 1993) and can be resolved as a continuous transition in the flow variables, so that no explicit jump conditions need to be imposed. Li and McKee (1996) showed that their shock creates a region of downstream turbulent inflow that may be subject to interchange instabilities (Spruit et al., 1995) and the Wardle instability (Wardle, 1990); it is not possible to observe such instabilities in this model, as the turbulent region is smoothed by the various approximations adopted, in particular the assumption of axisymmetry. Inwards of the shock Contopoulos et al. (1998) observed that the gas establishes a laminar free fall collapse, as their simulations were nonrotating; it is the presence of rotation that causes the formation of the Keplerian disc in this solution, while the size of the disc is determined by the amount of magnetic diffusion and braking.

The position of the magnetic diffusion shock, x_d, can be estimated by examining the induction equation (4.148). The inequality $b_{r,s} \ll h db_z/dx$ holds true everywhere except during the shocks, and as this term is otherwise smaller than any others it can be disregarded in order to simplify and solve the induction equation. This can then be written as a quadratic equation in b_z:

$$x h^{1/2} \sigma^{-3/2} \tilde{\eta}_A b_{r,s} b_z^2 - x w b_z + \psi = 0. \tag{4.164}$$

The two regimes of flux behaviour, described by ideal MHD in the outer asymptotic solution and ambipolar diffusion in the inner, can be approximated by the two roots of this equation, which are usually well-separated.

In the large x limit, the quadratic term in Equation 4.164 becomes small and IMHD is dominant. The smaller of the two roots is then a good approximation to the vertical field component, and is given by

$$b_{z,low} \approx \frac{\psi}{xw} = \frac{\psi\sigma}{m}. \tag{4.165}$$

As this holds true during the initial dynamic collapse when the mass-to-flux ratio is constant and given by the initial value $\mu = \mu_0$, Equation 4.165 can be simplified into

$$b_{z,low} \approx \frac{\sigma}{\mu_0} \tag{4.166}$$

which is the initial (outer) boundary condition for the field derived in Section 2.7.

The larger root of Equation 4.164 gives the vertical field component in the ambipolar diffusion regime, where it is approximated by dropping the now-small constant (with respect to b_z) term in the quadratic (Equation 4.164). In this case the equation is solved to give

$$b_{z,high} \approx \frac{xm}{\tilde{\eta}_A \psi} \left(\frac{\sigma}{h}\right)^{1/2}, \tag{4.167}$$

model	estimated x_d	actual x_d
$v_0 = 0.73$, $\tilde{\eta}_A = 1.0$	0.49	0.41
$v_0 = 0.18$, $\tilde{\eta}_A = 1.0$	0.49	0.46
$v_0 = 0.18$, $\tilde{\eta}_A = 0.7$	0.34	0.33

Table 4.3: Comparison between the estimated and actual values of the magnetic diffusion shock position, x_d, for the similarity solutions in subsection 4.3.4. The estimated position of the shock is typically accurate to 10%.

which is equation 50 of Krasnopolsky and Königl (2002) — the smaller root is their equation 49. Following their derivation further, inwards of the diffusive shock position, the vertical compression of the disc is controlled by the magnetic squeezing induced by $b_{r,s}$ (as $b_{\phi,s}$ is still small). The scale height is then given by

$$h \approx \frac{2\sigma x^4}{\psi^2}; \tag{4.168}$$

and this is then substituted into the approximation to the vertical field component so that

$$b_{z,high} \approx \frac{xm}{\tilde{\eta}_A \psi} \left(\frac{\psi^2}{2x^4} \right)^{1/2} = \frac{m}{\sqrt{2}\tilde{\eta}_A x}. \tag{4.169}$$

The magnetic diffusion shock is smooth, even though the db_z/dx term is large in the shock itself, and its position may be approximated by recognising that just inwards of the shock the radial field component may be approximated by $b_{r,s} \approx b_z \approx b_{z,high}$. This then gives the relation

$$\frac{\psi}{x_d^2} \approx \frac{m}{\sqrt{2}\tilde{\eta}_A x_d}, \tag{4.170}$$

and as flux freezing is still approximately valid in this region, then $\psi = m/\mu_0$ and Equation 4.170 may be solved for the position of the magnetic diffusion shock:

$$x_d \approx \frac{\sqrt{2}\tilde{\eta}_A}{\mu_0} \tag{4.171}$$

(equation 58 of Krasnopolsky and Königl, 2002), which depends only on the initial conditions of the collapsing molecular cloud. This expression is generally a good approximation to the shock position for all of the similarity solutions explored in this section, with the estimated and actual positions of the magnetic diffusion shocks for each solution listed in Table 4.3 for the purpose of comparison. Typically, Equation 4.171 gives the position of x_d to $\sim 10\%$, although it is much closer for those solutions in which the initial rotation rate is slow, as the centrifugal force is not yet significant, and this affects the amount of magnetic braking and the behaviour of the scale height in this approximation.

Inwards of the magnetic diffusion shock and its associated turbulent post-shock region, the slowed gas is accelerated inwards by the gravity of the central point mass until it is falling inwards at near-free fall speeds. As in the previous solutions, the centrifugal force builds up as the matter falls in and triggers the formation of the centrifugal shock. In order to estimate the position of the centrifugal shock the behaviour of the angular momentum and magnetic braking in the free fall region must be well understood.

During the free fall collapse region, the angular momentum is reduced by the magnetic braking in an exponential manner, and if the region is wide enough then the angular momentum may be reduced to an essentially constant value $j = j_{pl2}$ (which is much smaller than the first angular momentum plateau value j_{pl} that is attained at the inner edge of the IMHD region). The amplification of the magnetic field in the magnetic diffusion shock causes an increase in the amount of magnetic braking that is strongly dependent on $\tilde{\eta}_A$, and so the value of the secondary angular momentum plateau can not be easily approximated from the initial conditions of the collapse.

Angular momentum is transported from the disc to the envelope by the twisting of the field lines in the azimuthal direction, and so it is the azimuthal field component that must be examined in order to determine the degree of magnetic braking affecting the disc. As mentioned above, inwards of the magnetic diffusion shock ambipolar diffusion dominates the behaviour of the vertical field in the collapse region. Therefore, substituting $b_{r,s} \approx b_z \approx b_{z,high}$ (given by Equation 4.169) into Equation 4.151 for $b_{\phi,s}$ gives an approximation to the azimuthal field in this region,

$$b_{\phi,s} \approx -\frac{2\alpha\psi j}{x^3}(1 + 2\alpha w)^{-1}; \tag{4.172}$$

this does not strictly hold true, as $b_{\phi,s} = -\delta b_z$ in the innermost area of the free fall collapse region. Equation 4.172 is then an overestimate of the azimuthal field near the centrifugal shock, but is an acceptable approximation for the purpose of estimating j_{pl2} and the position of the centrifugal shock. In this region the angular momentum equation (4.145) can be simplified into

$$\frac{dj}{dx} \approx -\frac{x^2}{m} b_z b_{\phi,s}. \tag{4.173}$$

Substituting Equations 4.169 for b_z and 4.172 into this equation yields

$$\frac{dj}{dx} \approx \frac{\alpha m}{\tilde{\eta}_A^2 x} j(1 + 2\alpha w)^{-1}. \tag{4.174}$$

In this free fall region the mass is well approximated by its plateau value $m = m_{pl}$ (see Section 4.1.2), which is also a good first approximation to the central mass m_c.

Similarly, as the matter is falling in under gravity, $w \approx \sqrt{2m/x}$, and this and $m \approx m_c$ are substituted into Equation 4.174 to give

$$\frac{dj}{dx} \approx \frac{\alpha m_c}{\tilde{\eta}_A^2 x}\, j \left(1 + \alpha\sqrt{\frac{8m_c}{x}}\right)^{-1}. \tag{4.175}$$

As x is small, then $2\alpha w \gg 1$ and the angular momentum equation may then be simplified as

$$\frac{dj}{dx} \approx \frac{j}{\tilde{\eta}_A^2}\sqrt{\frac{m_c}{8x}}. \tag{4.176}$$

This ordinary differential equation is separable and is integrated to give

$$j \approx j_1 \exp\left[\frac{1}{\tilde{\eta}_A^2}\sqrt{\frac{m_c x}{2}}\right], \tag{4.177}$$

where j_1 is a constant. This exponential is a good approximation to j between the two shocks, and may be used to estimate the position of the centrifugal shock once the boundary condition is solved. The constant, j_1, is the value of the second plateau in the angular momentum, j_{pl2}, which is used to approximate the position of the centrifugal shock. It is calculated by evaluating Equation 4.177 at x_d where the angular momentum is given by the first plateau value

$$j_{pl} \approx \frac{v_0}{A}\, m_{pl} \approx \frac{v_0}{A}\, m_c, \tag{4.178}$$

assuming that there is little magnetic braking before the formation of the magnetic diffusion shock (so that the ratio of the mass to the angular momentum is equal to its initial value), and that the value of the mass plateau is approximately equal to that of the central mass. The second plateau value of the angular momentum is then given by

$$j_{pl2} \approx \frac{v_0}{A}\, m_c \exp\left[-\sqrt{\frac{m_c}{\mu_0 2^{1/2}\tilde{\eta}_A^3}}\right] \tag{4.179}$$

(equation 64 of Krasnopolsky and Königl, 2002); and using Equation 4.38, which defines the centrifugal radius, the centrifugal shock position is approximately:

$$x_c \approx \frac{v_0^2}{A^2} m_c \exp\left[-\sqrt{\frac{2^{3/2} m_c}{\mu_0 \tilde{\eta}_A^3}}\right] \tag{4.180}$$

(equation 65 of Krasnopolsky and Königl, 2002).

This estimate of the shock position is only valid if the centrifugal radius occurs once the angular momentum has attained its secondary plateau value, which makes it a poor estimate for the moderately rotating similarity solution calculated in subsection 4.3.4. It is, however, a good fit to the position of the shock for the other solutions

model	j_{pl2}	j_{x_c}	estimated x_c	actual x_c
$v_0 = 0.73$, $\tilde{\eta}_A = 1.0$	0.39	0.20	3.3×10^{-2}	1.32×10^{-2}
$v_0 = 0.18$, $\tilde{\eta}_A = 1.0$	0.11	~ 0.1	1.9×10^{-3}	1.7×10^{-3}
$v_0 = 0.18$, $\tilde{\eta}_A = 0.7$	0.05	~ 0.04	3.5×10^{-4}	2.6×10^{-4}
$v_0 = 1.50$, $\tilde{\eta}_A = 1.0^*$			1.5	1.5

Table 4.4: Comparison between the estimated and actual values of the angular momentum j at the centrifugal shock and the shock position x_c for the similarity solutions in subsection 4.3.4. The first similarity solution has poor matches between estimated and actual values, as the poor approximation of the magnetic diffusion shock position carries through to give a poor estimate of the angular momentum plateau and the centrifugal shock position.

*Note: The $v_0 = 1.50$, $\tilde{\eta}_A = 1.0$ model (which also has $\alpha = 0.1$ instead of 0.08) is a rapidly rotating similarity solution in which the angular momentum does not form a plateau before the centrifugal shock. In this instance the centrifugal shock position is estimated using Equation 4.43 as in the nonmagnetic and IMHD solutions.

of Krasnopolsky and Königl (2002), which are reproduced in this work for discussion purposes. The estimated value of the angular momentum plateau, the actual value of j at x_c and the estimated and converged centrifugal shock positions of each of the similarity solutions in subsection 4.3.4 are presented in Table 4.4 for the purpose of comparison. The two estimations are intimately tied; when the angular momentum plateau is approximated to a value close to the actual value of j at the shock, the position of the centrifugal shock is also estimated to a high precision. The discrepancy in the calculations for the first similarity solution is likely due to the overestimate of the diffusion shock position (see Table 4.3), which affects both the value of j_{pl2} and the centrifugal shock position in turn.

The centrifugal shock is again treated as a discontinuity in the radial velocity and surface density in which the flow changes from being in near-free fall collapse to a subsonic accretion disc in Keplerian orbit. The shock is calculated explicitly using the jump conditions derived for the nonmagnetic model in subsection 4.1.2 (Equations 4.57 and 4.58), as the magnetic field is decoupled from the neutrals in this region and so does not change across the shock. The shock is followed by a thin numerically resolvable post-shock layer in which b_z increases, and the flow then settles into its asymptotic disc solution, as will be shown in the following subsections.

4.3.3 Model construction

The addition of two further equations to the set to be integrated complicates the numerical routine so that it is no longer possible to integrate inwards from the outer boundary, as small numerical errors in the calculation of the derivatives can compound

and cause the integration to veer unphysically from the expected asymptotic collapse solution (see the inner region of Figure 4.6 for an example of this behaviour). Similarly, it is not possible to integrate out from the inner boundary, as the calculation rapidly breaks down in the outward direction as well.

The solution to this problem is to treat the integration as a two-point boundary value problem in which the values of the variables m, σ, j, ψ and b_z and the constant boundary condition m_c are known at the inner and outer boundary, but unknown at an intermediate value of x (the "matching point", denoted x_m). The values of the variables at this matching point are treated as free parameters that are initially "guessed" and refined by iteration. The integration of the equations is performed in both directions from the matching point, with the shock position and conditions calculated on the inwards path, until they reach the boundaries. Here the discrepancies between the integrated variables and the boundary conditions are evaluated — these are initially nonzero. The integration process can then be treated as a multidimensional root-finding problem, which can be solved using a globally convergent Newton-Raphson procedure (`newt` and its dependencies from *Numerical Recipes*; Press et al., 1992). As the differential equations are nonlinear, zeroing the discrepancies between the integrated variables and the boundary conditions by varying the variables at x_m is a time-consuming process requiring many iterations of the integration. This technique for solving two-point boundary value problems is known as the "shooting method", and is discussed in more detail in chapter 17 of Press et al. (1992).

The shooting method for solving the boundary condition problem requires a good initial estimate of the variables at the matching point, which is chosen such that it lies between the centrifugal and magnetic diffusion shocks (i.e. $x_c < x_m < x_d$). This estimate is found by calculating a simplified model of the collapse with ambipolar diffusion in which the derivative of the vertical magnetic field component with respect to x is assumed to be small everywhere and may be disregarded. As explained in Section 2.5, this is generally valid because hdb_z/dx is small everywhere (except in the magnetic diffusion shock) due to the thin disc approximation which requires that $h \ll x$. The induction equation is then replaced by the approximations to b_z that were used in estimating the shock positions: $b_z = b_{z,low}$ (Equation 4.166) when $x > x_d$, and $b_z = b_{z,high}$ (Equation 4.169) when $x < x_d$; the position of the magnetic diffusion shock is assumed to be that given by Equation 4.171. The other variables (m, σ, j, and ψ) are integrated from the upper boundary to the matching point, creating a solution that is close enough to the expected full solution that the values of the variables at the matching point may be used as an initial guess for the shooting routine.

Figure 4.6 shows such a simple calculation for the same parameters as the full solution in Figure 4.9 (the matching point for that solution is chosen to be $x_m = 0.3$).

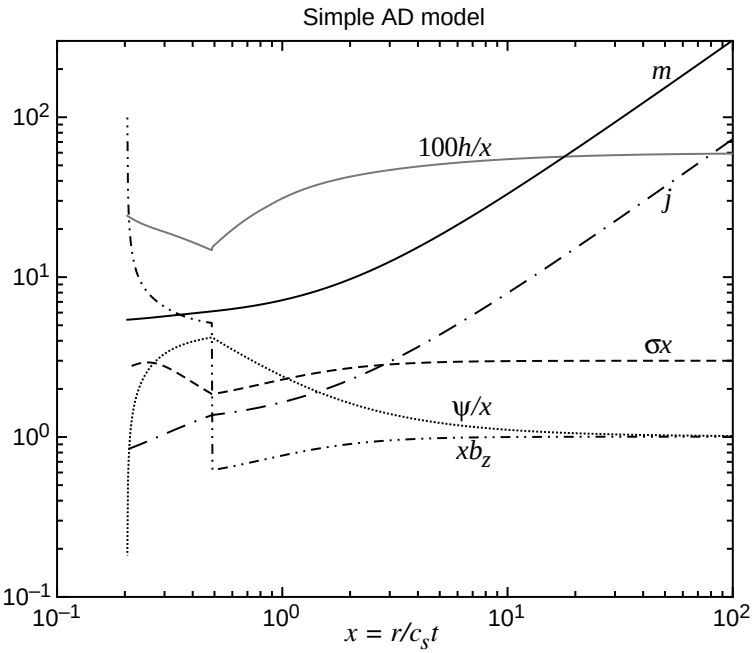

Figure 4.6: Simple model for the ambipolar diffusion collapse, with $x_d = 0.487$ (the estimated value calculated in Table 4.3) and outer asymptotic boundary conditions matching those in Figure 4.9. Note that h, ψ and b_z are unstable and veer away from a singularity in the inner regions, so the matching point is chosen to be $x_m = 0.3$, before the solution has been much affected by these instabilities.

This similarity solution is qualitatively similar to the IMHD similarity solutions in the outer region of the collapse where IMHD is dominant, however inwards of the magnetic diffusion shock the vertical field component and the flux diverge from their expected behaviour: the field becomes infinitely large as the enclosed flux decreases rapidly, causing the integrator to fail. The percentage error between the variables in the full solution and their values in this simple model is shown in Figure 4.7 — the biggest discrepancy between the two solutions is in the position of the magnetic diffusion shock, which is located at $x_d = 0.406$ in the full similarity solution and at $x_d = 0.487$ in the simple model. This incorrect shock position fuels the divergence of the simple solution; if a more accurate estimate of the shock location were adopted then the simple model would be able to produce variables at the matching point that are closer to the true values.

Divergences from the expected behaviour such as those undergone by ψ/x and xb_z in Figure 4.6 can be so strong that using such values at the matching point (even after choosing x_m as close to x_d as possible) may cause the full integration to fail. Typically, adopting an initial guess that is too far from the true values causes the integration to either encounter a spontaneous singularity and diverge (as in Figure 4.6) or to score so badly against the boundary conditions that the routine will never converge on the

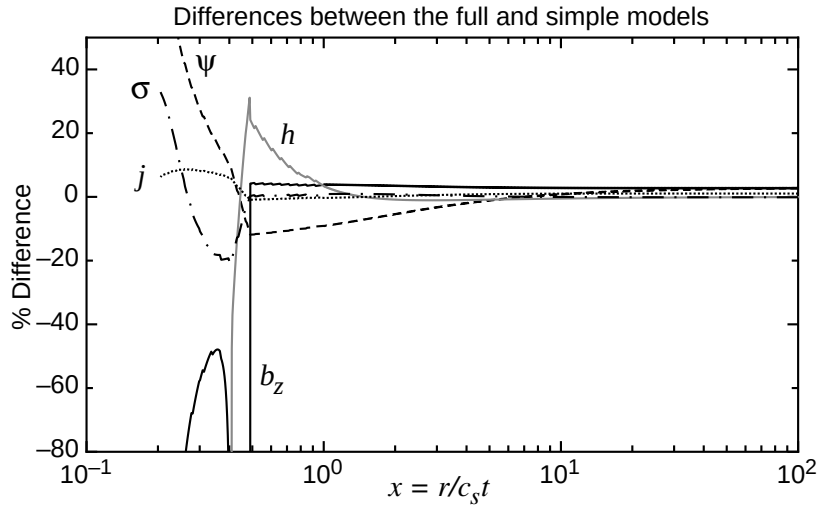

Figure 4.7: The difference between the values of σ, j, ψ, b_z and h in the simple model from Figure 4.6 and the full similarity solution in Figure 4.9 as percentages of the true value. In the outer regions the variables match very well save for some minor constant discrepancies, however, near the magnetic diffusion shock the magnetic flux and the scale height drift from their expected values. The biggest discrepancy between the two solutions is the position of the diffusion shock (see Table 4.3), which causes the large drop in b_z at the simple shock position (to -5x that of the full model) and then the peak downstream at the true shock. It is possible that this discrepancy causes the singularity inwards of the shock shown in Figure 4.6.

true solution. In these cases it is prudent to adjust ψ and b_z at the matching point by hand until the code is able to integrate to both boundaries while matching the boundary conditions to $\lesssim 10\%$. Such tweaking is not always needed, however it can be a significant additional source of overhead in an already much-slowed process.

One other simplification is required in order to integrate inwards to the inner boundary. Even though the position of x_c can be calculated to the maximum possible precision, a spontaneous singularity may occur at some point $0 < x < x_c$ after the solution has seemingly matched onto the inner asymptotic solution. An example of this behaviour is shown graphically in Figure 4.8, in which the asymptotic solutions are shown as dotted lines that run parallel to the similarity solution for some length of similarity space before diverging (note that this solution has yet to converge on the true value of m_c). Rather than choosing a point just outwards of this singularity to be the inner boundary, it is more productive to switch the integration to a simpler set of equations while the variables are still close to their asymptotic values.

The inner singularity occurs because the derivatives for the surface density and the vertical field component become large in the inner regions, and in calculating these (as is required to numerically integrate the ordinary differential equations) numerical errors compound and cause the code to fail. In order to counteract this effect a simplified

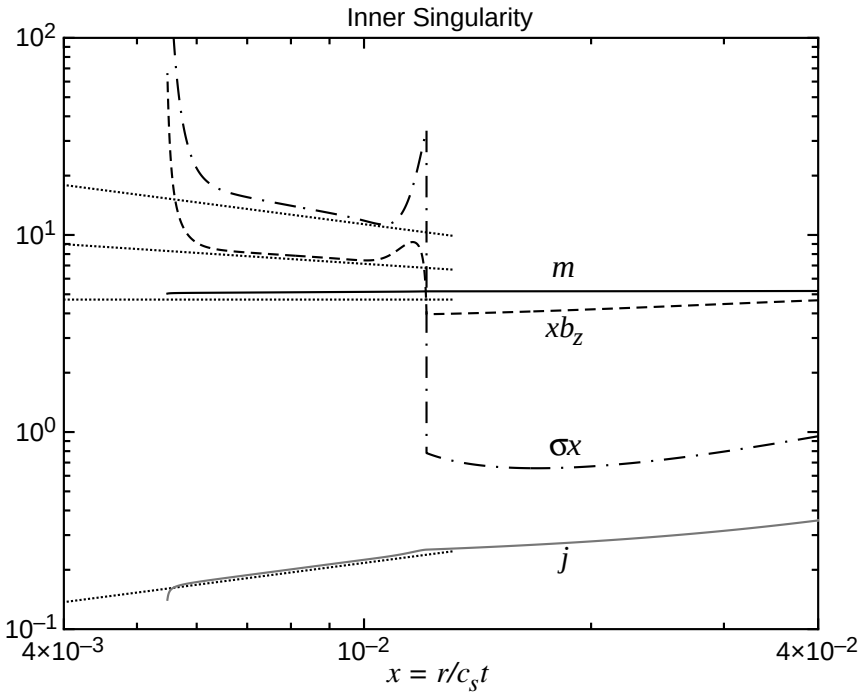

Figure 4.8: Close-up on the centrifugal shock region for a collapse calculation with the same boundary conditions and parameters as Figure 4.9. Inwards of the centrifugal shock at $x_c = 1.32 \times 10^{-2}$ the variables tend towards the asymptotic solutions (the dotted lines), before encountering a singularity at $\sim 5.5 \times 10^{-3}$ and veering away. Note that this particular simulation has yet to converge on the true value of m_c.

model is used to perform the innermost integration; in this model the problematic derivatives are given by the values from the inner asymptotic solution in subsection 4.3.1:

$$\frac{d\sigma}{dx} = -\frac{3}{2}\,\sigma_1\, x^{-5/2} \tag{4.181}$$

$$\text{and } \frac{db_z}{dx} = -\frac{5 m_c^{3/4}}{4\sqrt{2\delta}}\, x^{-9/4}, \tag{4.182}$$

where σ_1 is the constant coefficient defined in Equation 4.154. These values are substituted into the simplified equation set:

$$\frac{\sigma m_c}{x^3}\, h^2 + \left(b_{r,s}^2 + b_{\phi,s}^2 + \sigma^2\right) h - 2\sigma = 0, \tag{4.183}$$

$$g + \frac{b_z b_{r,s}}{\sigma} + \frac{j^2}{x^3} - \frac{1}{\sigma}\frac{d\sigma}{dx} - \frac{b_z h}{\sigma}\,\frac{db_z}{dx} = 0 \tag{4.184}$$

$$\text{and } -xwb_z + \tilde{\eta}_A x b_z^2 b_{r,s} h^{1/2} \sigma^{-3/2} = 0, \tag{4.185}$$

which is then solved for h, σ and b_z. The other variables are determined by integrating

the remaining differential equations

$$\frac{dm}{dx} = x\sigma, \tag{4.186}$$

$$\frac{d\psi}{dx} = xb_z \tag{4.187}$$

$$\text{and } \frac{dj}{dx} = \frac{j}{w} - \frac{x^2 b_z b_{\phi,s}}{m} \tag{4.188}$$

to the inner boundary, whereupon the discrepancy between the boundary condition $m = m_c$ and the integrated value of m is passed back to the shooting routine for refinement.

The simplified model is able to integrate to the inner boundary because of the assumption that $d\sigma/dx$ and db_z/dx are given by their asymptotic expressions, which reduces the numerical error of the calculation, and makes it possible to solve the resulting reduced set of fluid equations. The validity of this assumption is demonstrated in Figure 4.8, which shows that downstream of the centrifugal shock the variables settle quickly to their asymptotic forms and the derivatives of σ and b_z calculated using the full set of equations are close to the asymptotic values. Because of this, adopting the simple model is not expected to introduce any significant errors to the calculations, provided that it matches well to the full solution.

The transition between the full and simplified models occurs when both the derivatives of σ and b_z match their asymptotic values in Equations 4.181 and 4.182 to an appropriate degree. In most of the solutions calculated in the following subsection and the Hall diffusion solutions in Chapter 5, matching the derivatives to 1% is considered acceptable for switching between the two models, although a finer match may be required if the solution is otherwise unable to converge. The transition is usually seamless, however if not all of the values of the variables (particularly m_c) at the matching point have converged, or if the criteria for changing between the models is not vigorous enough, the point of transition may be visible in the plots, as occurs to ψ/x in Figure 4.12 just inwards of the expanded shock region. If the variables (including m_c) at x_m are particularly poorly chosen then the simple model may also encounter spontaneous singularities as it integrates inwards.

Even with a good estimate of the variables at the matching point as input to the root-finding routine, and the simplified model for calculating the innermost integrals, the calculation of the true solution with its minimized scores (typically of order 10^{-5}%) may take up to a day to compute. The initial step of finding a set of variables at x_m that would integrate to both boundaries was not fully automatable, as poor guesses would cause the code to crash in ways that could not always be predicted or accounted for. Multiple iterations of this procedure were often necessary to ensure convergence on the value of the central mass.

Solution	Figure	$\tilde{\eta}_A$	v_0	α
moderate rotation	4.9	1.0	0.73	0.08
slow rotation	4.11	1.0	0.18	0.08
slow rotation, reduced $\tilde{\eta}_A$	4.12	0.7	0.18	0.08
fast rotation	4.13	1.0	1.50	0.10

Table 4.5: Ambipolar diffusion, initial rotational velocity and magnetic braking parameters for the ambipolar diffusion similarity solutions. All of the other parameters are identical and given by $A = 3$, $u_0 = -1.0$, $\mu_0 = 2.9$ and $\delta = 1$.

4.3.4 Similarity solutions

The ambipolar diffusion similarity solutions are calculated using the method outlined above, however only the first of the ambipolar diffusion solutions from Krasnopolsky and Königl (2002) was calculated as a test of the computation code; this similarity solution is shown in Figure 4.9. Their other ambipolar diffusion solutions are reproduced in Figures 4.11–4.13 in order to properly examine and discuss the role of ambipolar diffusion in the star formation process. The initial conditions and parameters of all of the similarity solutions presented in this section are given in Table 4.5.

The similarity solutions presented in this section have much in common with the IMHD solutions, as the basic interplay between the magnetic, gravitational and centrifugal forces remains the same. However, altering the coupling between the gas and the magnetic field allows the field lines to be transported from the innermost regions of the collapse to the outer ones, reducing the magnetic flux problem so there is less of a magnetic field excess near the origin. Similarly, the magnetic braking is reduced by the presence of ambipolar diffusion, so that the magnetic braking catastrophe may be resolved completely.

The amount of ambipolar diffusion present in the solutions is determined by the nondimensional parameter $\tilde{\eta}_A$, which is a constant of order ~ 1. The justification for this is that in the outer regions of collapsing cores at radii $\gtrsim 10^3$ AU, the grains have a typical radius $a = 0.1\mu$m, the temperature is 10 K and the cosmic ray ionisation rate is given by $\xi = 10^{-17}\xi_{-17}$ s^{-1} (where $\xi_{-17} \approx 1$; Ciolek and Mouschovias, 1998; Kamaya and Nishi, 2000). The ambipolar diffusion parameter is given by $\tilde{\eta}_A \approx 0.2\xi_{-17}^{-1/2}$ when the scaling of the ion density is proportional to the square root of the neutral density (see Section 1.2) and the molecular ionisation by cosmic rays is balanced by rapid dissociative recombination of the molecular ions.

Further inward, at radii $\lesssim 10$ AU where the density is higher, the temperature in the collapsing core is around $T = 10^2 T_2$ K (where $T_2 \approx 1$). The ambipolar diffusion parameter is then given by $\tilde{\eta}_A \approx 0.07\xi_{-17}^{-1/2} T_2^{-1/4} (a/5\ \text{Å})^{-1/4}$ (see Krasnopolsky and

Königl, 2002, for the justification of this approximation), where a is the average grain size, assumed in this region to be small singly-charged particles that are PAH-like (Neufeld and Hollenbach, 1994). This relationship breaks down during the intermediate regions where Hall diffusion is expected to be important, however, given that the value of $\tilde{\eta}_A$ only changes by an order of magnitude over 8 orders of magnitude in density, choosing a constant $\tilde{\eta}_A$ of order 1 is an acceptable parameterisation for the ambipolar diffusivity. The value of the diffusion parameter is varied in the solutions presented in this section in order to properly explore the role played by ambipolar diffusion in self-similar collapse, and its variation is discussed further in Section 6.2.

Figure 4.9 shows the only ambipolar diffusion similarity solution calculated in this work, which was performed in order to test the code for solving the collapse problem with both Hall and ambipolar diffusion and confirm the results of Krasnopolsky and Königl (2002). It has the same initial (outer) conditions as the fiducial solution in §3.3.1 of their work: the density parameter is $A = 3$; the initial radial velocity is parameterised by $u_0 = -1$; the nondimensional mass-to-flux ratio is $\mu_0 = 2.9$ and the initial azimuthal velocity is $v_0 = 0.73$. This core is initially rotating at a rate that would be termed fast in the previous models, however the changed magnetic braking caused by ambipolar diffusion in the azimuthal direction causes the centrifugal force to remain unimportant until x is small. The magnetic braking parameter is given by $\alpha = 0.08$, which is slightly reduced from the value $\alpha = 0.1$ used in the IMHD solutions; the azimuthal field cap remains at $\delta = 1$ for simplicity (so that the maximum value of the azimuthal field is $b_{\phi,s} = -b_z$) and the ambipolar diffusion parameter is chosen to be $\tilde{\eta}_A = 1.0$, which is slightly larger than that expected.

The outer regions of the ambipolar diffusion collapse match those from the IMHD similarity solutions, as the mass-to-flux and the mass-to-angular momentum ratios remain constant as the material falls in at supersonic speeds. The radial velocity and scale height are dominated by the self-gravity of the disc, which pulls the gas towards the equator before it then flows towards the central mass. The magnetic field gradually builds up as the matter falls inwards, and it becomes important to the dynamics at around $x \approx 2$ where the magnetic braking starts to affect the angular momentum transport and the constant ratio of the mass to the angular momentum breaks down. The azimuthal field component attains its capped value, and is important to the angular momentum transport throughout the rest of the collapse.

The mass and angular momentum tend towards their plateau values as in the previous solutions, and ambipolar diffusion becomes important to the field transport as the surface density and magnetic field build up. The gravity of the central point mass becomes important to the radial velocity — this pulls more mass and flux inwards until ambipolar diffusion causes flux freezing to break down.

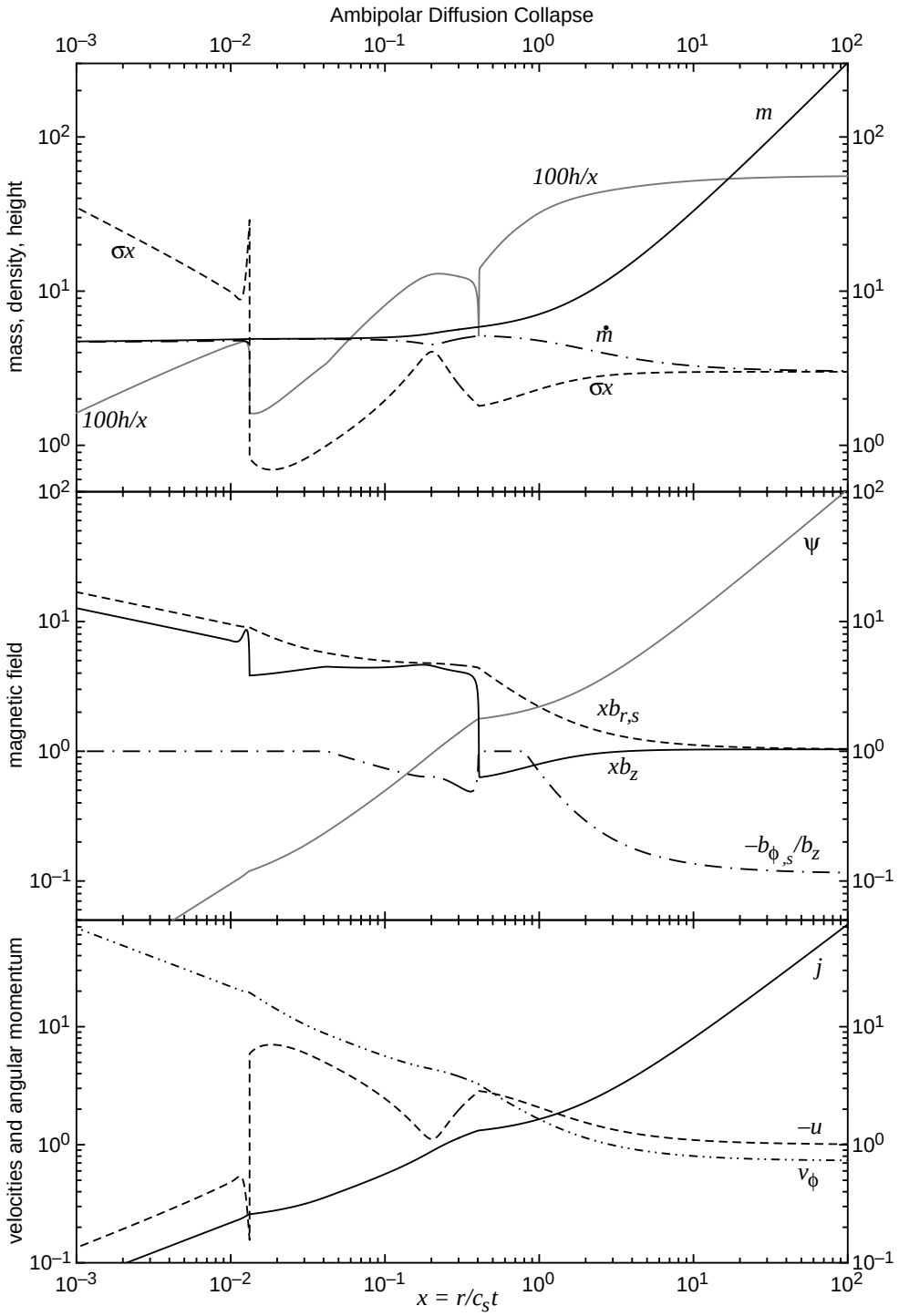

Figure 4.9: Similarity solution for the moderately rotating ambipolar diffusion collapse, with outer asymptotic boundary conditions $A = 3$, $u_0 = -1$, $\mu_0 = 2.9$ and $v_0 = 0.73$, and magnetic parameters $\alpha = 0.08$, $\delta = 1$ and $\tilde{\eta}_A = 1.0$; these match the parameters in figure 7 of Krasnopolsky and Königl (2002). The displayed variables are the same as in Figure 4.3 for the IMHD case; the nondimensional central mass is $m_c = 4.67$, and the magnetic diffusion and centrifugal shocks are located at $x_d = 0.406$ and $x_c = 1.32\times10^{-2}$ respectively.

The magnetic diffusion shock at $x_d = 0.41$ (which is much smaller than the estimated position of $x_d \approx 0.49$; see Table 4.3) takes the form of a sudden increase in the vertical field component as the field lines diffusing against the flow from the downstream ambipolar diffusion-dominated regime meet those coming inward with the IMHD collapse. The sudden increase in the field causes the gas to slow down due to the magnetic pressure terms in the radial momentum equation (4.144) and the magnetic squeezing terms come to dominate the vertical compression of the disc. The particular dip in the scale height at the shock suggests that the rapid compression of the disc causes a breakdown of the vertical hydrostatic equilibrium in the shock; in reality the magnetic squeezing at the shock should produce a smooth reduction of the disc thickness over the shocked region.

IMHD breaks down at around the position of the magnetic diffusion shock where m (and by extension ψ) have fallen to a plateau value. This value is not affected by the addition of ambipolar diffusion to the calculations, so that the amount of flux contained within x_d is roughly that trapped at the origin in the IMHD solutions. Ambipolar diffusion causes the flux to be redistributed downstream of the magnetic diffusion shock, so that no flux is contained at the origin.

The decoupling of the field from the neutral particles primarily takes place at the magnetic diffusion shock, which also changes the disc geometry. Upstream of the shock, the magnetic field is dominated by the radial component, which can be an order of magnitude larger than the vertical and azimuthal field components. During the shock and the transition region that follows downstream of it, the field lines straighten until the poloidal components at the disc surface are approximately equal; this field geometry is illustrated in Figure 4.10. Relative to the vertical component $b_{\phi,s}$ drops in the shock, however the decoupling of the field causes the magnetic braking rate to increase so that the azimuthal field component increases by a factor of 1.5 during the immediate post-shock region.

Inside the magnetic diffusion shock the poloidal field components scale with $\sim x^{-1}$ as the surface density and thickness of the disc increase and the radial velocity and accretion rate drop. The gas is slowed due a weak outward acceleration caused by the radial magnetic pressure, and this in turn causes the density to rise. Rotation is not dynamically important in this region and so the shock has a similar structure to that seen in the nonrotating similarity solution of Contopoulos et al. (1998). The gravity of the central mass eventually overcomes the magnetic pressure and the gas starts accelerating inwards once more.

As in the slowly rotating similarity solutions obtained from the IMHD and non-magnetic models, rotation remains dynamically unimportant until the vicinity of the centrifugal shock. For most of the region between the two shocks the gravity of the

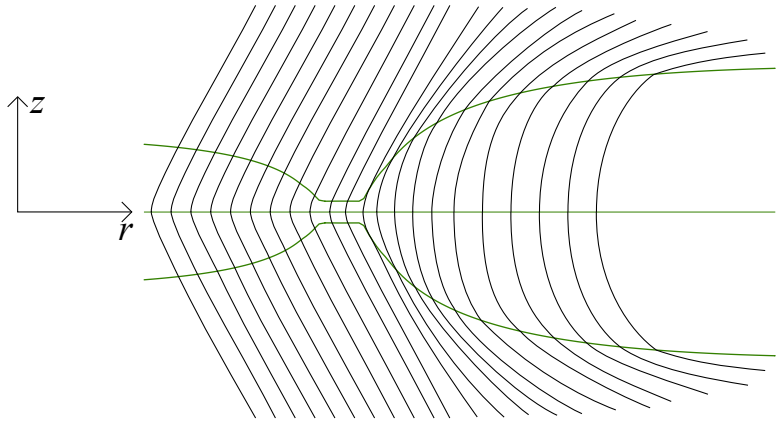

Figure 4.10: Schematic of the magnetic field behaviour in the magnetic diffusion shock. The disc (green) is compressed as the vertical field becomes large, causing the field lines at the surface to straighten from being largely radial upstream of the shock to having roughly equal values of b_z and $b_{r,s}$ downstream of the shock. (Not to scale.)

central mass dominates the radial acceleration of the gas until it is in near-free fall collapse, slowed only a little by ambipolar diffusion of the magnetic flux and the magnetic pressure. The azimuthal field component increases in this free fall region until it is again equal to the vertical component, which causes the change in the scale height behaviour at $x \sim 4.5 \times 10^{-2}$ as it contributes more to the magnetic squeezing forces in the pseudodisc. By this point the enclosed mass and the accretion rate have flattened and remain near-constant throughout the remainder of the collapse. The angular momentum has yet to reach its second plateau value (see Table 4.4) when the centrifugal force becomes large and triggers the formation of the Keplerian disc.

Eventually the centrifugal force becomes equal to the gravitational force and the centrifugal shock occurs at $x_c = 1.32 \times 10^{-2}$, which is much smaller than the estimated value $x_c \approx 3 \times 10^{-2}$ (see Table 4.4). This discrepancy is likely caused by the overlarge estimate of the magnetic diffusion shock radius used to approximate the centrifugal shock position. In this similarity solution the shock is not strong enough that it can create a region of backflow, however the gas is slowed so that the infall is now subsonic and the surface density increases by more than an order of magnitude.

The centrifugal shock is followed immediately by a very thin layer in which the azimuthal and vertical magnetic field components increase rapidly. This increase causes a decrease in the angular momentum to its asymptotic value, as the surface density and the other variables adjust with a few overshoots towards their expected rotationally-supported disc behaviour. The transition between the full model and the simplified set of equations outlined in subsection 4.3.3 occurs at $x \sim 8.6 \times 10^{-3}$, after the variables have joined onto the asymptotic inner disc described by Equations 4.152–4.162.

The Keplerian disc itself is rather small compared to that in the rapidly rotating similarity solutions without ambipolar diffusion (as $x_c = 1.32 \times 10^{-2}$ corresponds to a disc radius of $r_c \approx 53$ AU at time $t = 10^5$ years), and it has a mass $m_d = 0.23$ that is $\sim 5\%$ that of the central point mass. The nondimensional mass at the origin is $m_c = 4.67$, which corresponds to a moderate accretion rate of $\dot{M}_c = 7.6 \times 10^{-6}$ $\mathrm{M}_\odot$ yr^{-1} (so that at time $t = 10^5$ yr, the central mass is $M_c = 0.76$ $\mathrm{M}_\odot$). The surface density of the disc depends upon the ambipolar diffusion and azimuthal field cap parameters, as does the infall velocity, which is subsonic and very low. The disc is extremely thin and the vertical squeezing is dominated by the tidal and self-gravitational forces.

Within the rotationally-supported disc the angular momentum problem of star formation is solved as the disc is in Keplerian orbit, and as the flux is clearly reduced from the constant value in the IMHD solution the magnetic flux problem is seemingly resolved as well. The amount of magnetic flux in the disc scales with $x^{3/4}$, so that $\psi \to 0$ as $x \to 0$; clearly the amount of flux present in the protostar depends upon more detailed flux transport and destruction mechanisms than are included in this model, such as Ohmic diffusion (e.g. Li and McKee, 1996) and reconnection (e.g. Galli and Shu, 1993b; Lazarian, 2005).

Figure 4.11, reproduced from figure 8a of Krasnopolsky and Königl (2002), shows a slowly rotating similarity solution with the same initial conditions as Figure 4.9, save for the initial azimuthal velocity which has been reduced from $v_0 = 0.73$ to $v_0 = 0.18$. This solution is qualitatively similar to that in Figure 4.9 in the outermost region where IMHD is dominant; the values of the angular momentum and the enclosed mass plateau as the magnetic braking and ambipolar diffusion start to become important to the flux and angular momentum transport. In this region the self-gravity of the disc and the gravity of the central mass dominate the forces on the radial velocity so that it increases rapidly, and rotation is not yet important to the dynamics of collapse.

The magnetic diffusion shock occurs further from the origin in this solution at $x_d = 0.46$, which is much closer to the estimated position $x_d \approx 0.49$ than in the previous similarity solution. This occurs because the reduced rotational support allows more gas and flux to fall inwards so that the ambipolar diffusion term becomes important sooner, triggering the shock. Ambipolar diffusion comes to dominate the field transport inwards of the magnetic diffusion shock as the increase in the vertical field component at the shock is stronger in this solution than in the previous solution. The post-magnetic diffusion shock transition region is smoothed by the reduction in the initial angular momentum — the radial velocity only decreases very slightly downstream of the shock before accelerating inwards once more.

The decrease in the initial azimuthal velocity changes the width of the free fall region between the two shocks, as there is less angular momentum to trigger the

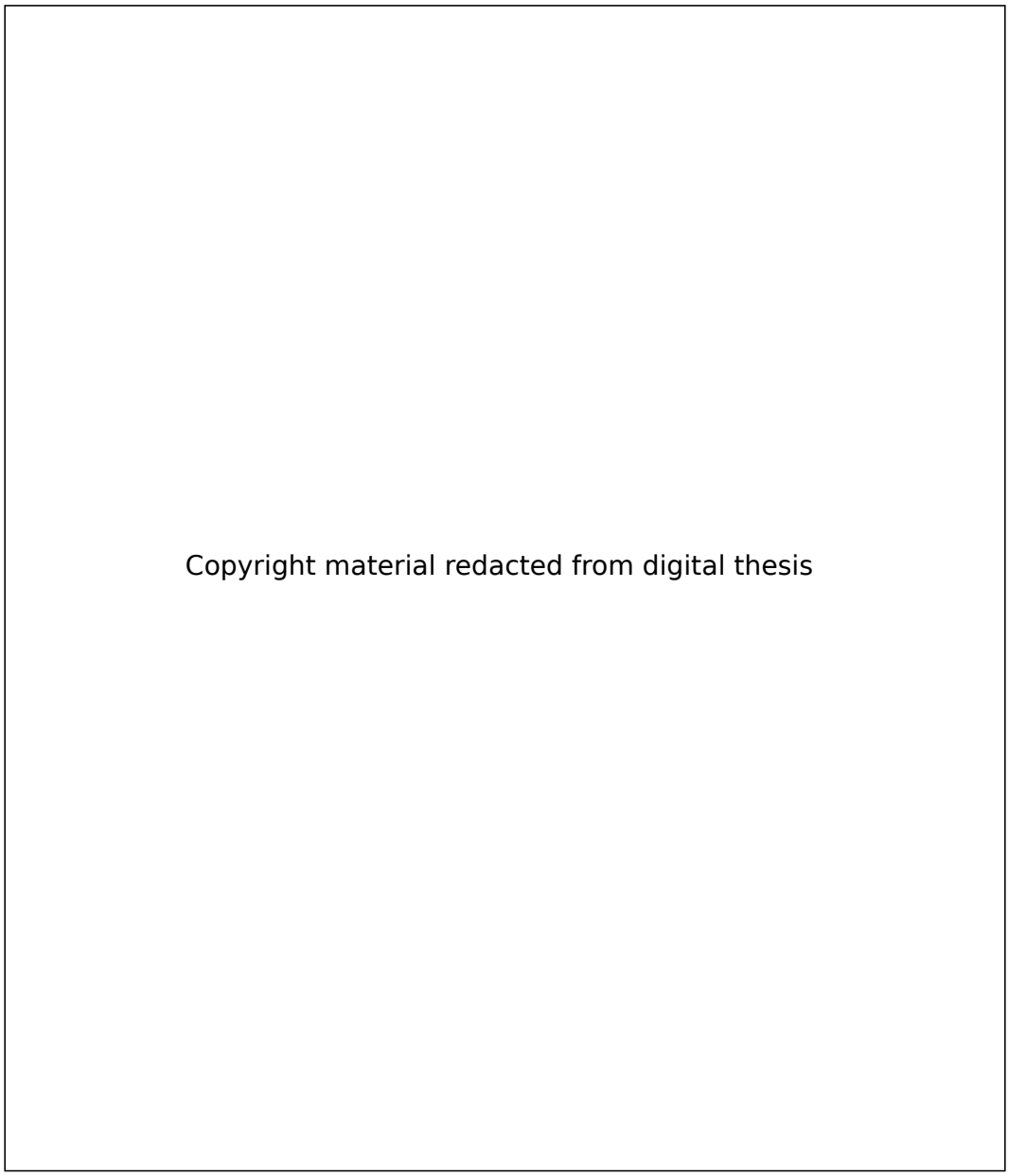

Figure 4.11: Similarity solution for the slowly rotating ambipolar diffusion collapse (figure 8a of Krasnopolsky and Königl, 2002). The initial conditions and parameters are the same as those in Figure 4.9, save that the initial azimuthal velocity is reduced to $v_0 = 0.18$. The position of the magnetic diffusion shock (labelled "AD") is increased to $x_d = 0.46$, which smooths out the post-magnetic diffusion shock region before the gas starts accelerating towards the free fall collapse. The reduction of the initial angular momentum moves the centrifugal shock inwards (as in the IMHD solutions) to $x_c = 1.7 \times 10^{-3}$, for it takes longer for the centrifugal force to balance gravity. The central mass is increased to $m_c = 6.0$. The horizontal scale covers a wider range of x than in the previous plot, and inwards of the centrifugal shock the scale has been expanded to better highlight the post-centrifugal shock transition to the asymptotic solution.

formation of the centrifugal shock. The azimuthal field component reaches its capped value at around $x \sim 6 \times 10^{-3}$ (where xb_z has its maximum turning point in Figure 4.11), so that it is better able to transport the angular momentum from the disc than in Figure 4.9. In this solution j falls to the second plateau value given by $j_{pl2} \approx 0.1$, which matches the predicted value quite well (see subsection 4.3.2 for more on the formation of this angular momentum plateau).

The centrifugal force becomes large enough to balance gravity and cause the formation of the centrifugal shock at $x_c \approx 1.75 \times 10^{-3}$, which is an order of magnitude smaller than in the moderately rotating similarity solution, and also smaller than the $v_0 = 0.1$ IMHD solution in Figure 4.3. The horizontal scale in the post-centrifugal shock region has been expanded to show that there is no overshoot and adjustment period inwards of the shock; the variables tend directly towards their asymptotic solutions. The Keplerian disc in this similarity solution is much smaller than in Figure 4.9 (corresponding to only $r_c = 7$ AU at a time $t = 10^5$ yr), and it contains a mass that is only $\sim 2\%$ of the central mass $m_c = 6.0$ (corresponding to $\dot{M}_c \approx 9.8 \times 10^{-6}$ $\mathrm{M}_\odot$ yr^{-1}; values from Krasnopolsky and Königl, 2002). The central point mass has increased compared with the more rapidly rotating similarity solution; this also occurred in the slow and fast IMHD solutions, suggesting that the reduction in the initial azimuthal velocity causes a reduction in the radial support which allows more matter to accrete in the slower similarity solutions.

The third solution, plotted in Figure 4.12 (figure 8b of Krasnopolsky and Königl, 2002) is another slowly rotating collapse, with initial conditions matching those in Figure 4.11 save that the ambipolar diffusion parameter is reduced from 1.0 to $\tilde{\eta}_A = 0.7$. Both shocks move even further inwards as predicted by the theory outlined in subsection 4.3.2, because the decrease in ambipolar diffusion causes the build up of flux necessary to trigger the magnetic diffusion shock to be a slower process. The post-magnetic diffusion shock region in which the density increases and the infall is slowed is more dynamic than in the previous slowly rotating solution, however the magnetic field does not increase downstream of the shock as in the more moderately rotating Figure 4.9.

The width of the near-free fall region in logarithmic space is again increased in comparison to the other slow similarity solution, and the degree of magnetic braking is increased, so that it takes longer for the angular momentum to reach its second plateau value of $j_{pl2} \approx 0.04$ and balance gravity. The centrifugal shock at the boundary of the Keplerian disc occurs at $x_c = 2.6 \times 10^{-4}$ (which corresponds to $r_c = 1$ AU at $t = 10^5$ yr), showing that the amount of ambipolar diffusion (as well as the initial rotation rate) determines the size and mass of the rotationally supported protostellar disc, which in this similarity solution has only 0.4% the mass of the central point mass. The mass at

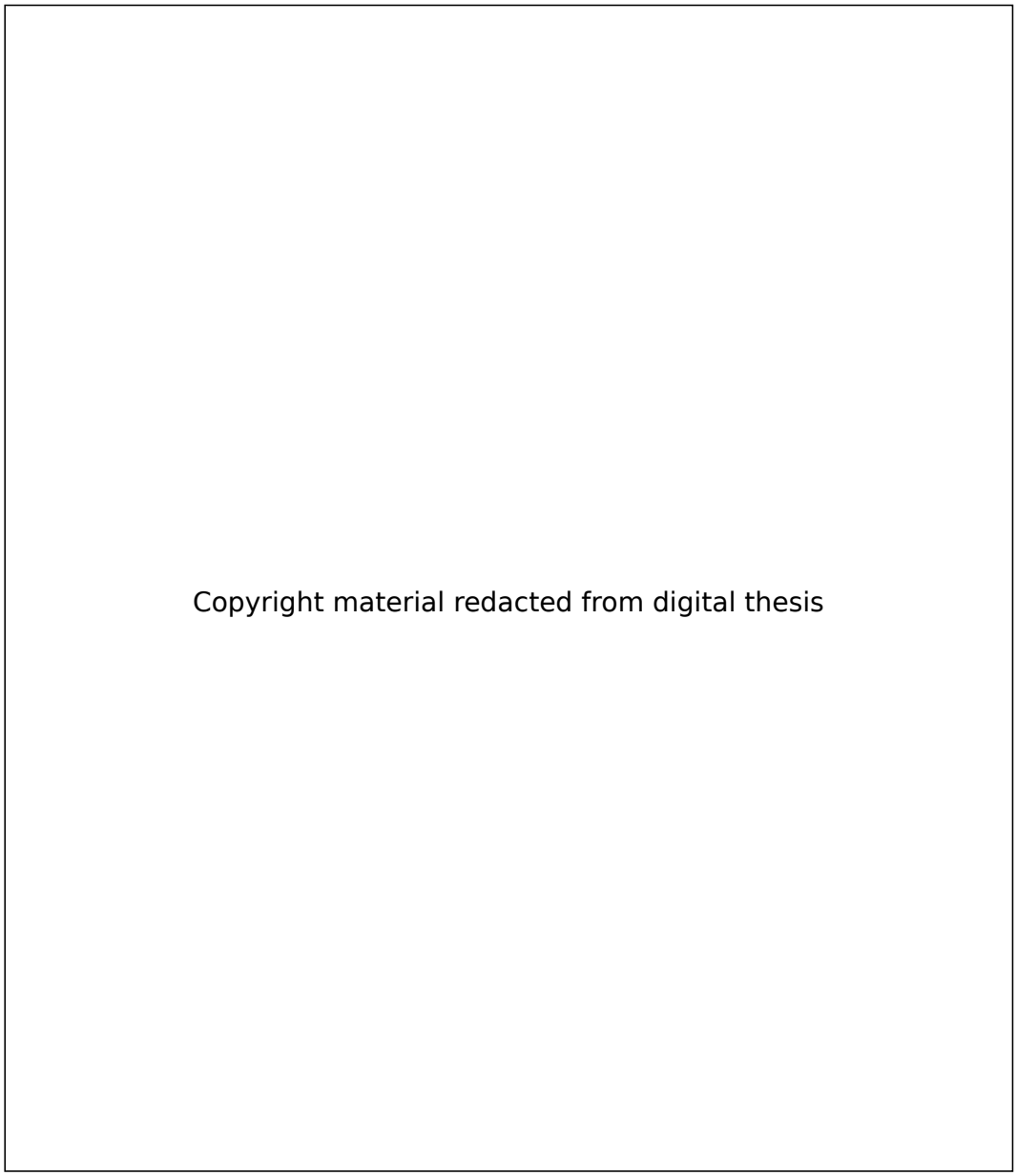

Figure 4.12: Slowly rotating reduced ambipolar diffusion collapse, reproduced from figure 8b of Krasnopolsky and Königl (2002). This similarity solution has the same parameters and initial conditions as Figure 4.11, with an initial rotational velocity of $v_0 = 0.18$ and reduced ambipolar diffusion parameter $\tilde{\eta}_A = 0.7$. The reduced ambipolar diffusion parameter causes the decoupling front to move inwards to $x_d = 0.33$, while its influence on the magnetic braking causes the secondary angular momentum plateau to be reduced further so that the centrifugal shock position is also closer to the origin at $x_c = 2.6 \times 10^{-4}$. The central point mass is $m_c = 6.0$ as in the previous solution.

the origin is unchanged by the reduction of $\tilde{\eta}_A$, remaining constant at $m_c = 6.0$; this implies that the amount of ambipolar diffusion does not affect the accretion rate onto the central star. Again, the variables match rapidly onto their asymptotic values, the surface density within the disc is decreased and the infall velocity is higher than in the other slow solution in Figure 4.11.

The final ambipolar diffusion solution in Figure 4.13 is a rapidly rotating collapse with an initial azimuthal velocity $v_0 = 1.5$ and magnetic braking parameter $\alpha = 0.1$, matching the parameters of the IMHD solution presented in Figure 4.4. The ambipolar diffusion parameter is restored to $\tilde{\eta}_A = 1.0$ so that the amount of diffusion is high, however it is not large enough to generate a magnetic diffusion shock as in the previous solutions. The infall rate in the outer regions is slow, and is already dropping towards zero when the gas encounters the centrifugal radius. As the gas is rapidly rotating, the centrifugal force becomes large early in the collapse (as in the fast IMHD solution), and the centrifugal shock causes the already slow radial velocity to become a backflow, representing a ring of material downstream of the shock forcing it outwards.

As most of the momentum of the gas is in the azimuthal direction, the radial velocity is always slow and subsonic (even in the backflow region) in this solution. Downstream of the centrifugal shock the magnetic braking reduces the angular momentum as the density and magnetic field (which are still tied by flux-freezing until around $x \sim 0.2$) increase until ambipolar diffusion becomes important and the variables settle with a number of overshoots to the asymptotic values at around $x \sim 0.03$. Note that the disc mass is much larger (by an order of magnitude) than the central point mass which has $m_c = 0.5$, and that at the inner edge of this plot the enclosed mass has yet to plateau to its asymptotic value. Although the accretion rate onto m_c is slow ($\dot{M}_c \approx 8 \times 10^{-7}$ M$_\odot$ yr^{-1}), the disc is very large in comparison, so that by a time of 10^5 years the disc has radius $r_c = 6000$ AU and is orbiting a "protostar" of mass $M \approx 8 \times 10^{-2}$ M$_\odot$, which is startlingly small. Without the requirement of axisymmetry, such a disc would experience gravitational instability and fragment, leading to the formation of a small cluster of stars (e.g. Matsumoto and Hanawa, 2003).

The addition of ambipolar diffusion to the model changes the dynamics of the gravitational collapse process by decoupling the magnetic field from the neutral particles at moderate densities so their behaviour is no longer tied by flux freezing. Because of this, less magnetic flux is carried inwards to the origin than in the IMHD model, and the magnetic flux problem of star formation is essentially resolved. The change in the field behaviour also allows more angular momentum to be transported to the external envelope by magnetic braking, which helps solve the angular momentum problem. The inner Keplerian disc is changed by the inclusion of ambipolar diffusion, which affects the radius of the disc and the surface density and infall velocity of the gas inwards of

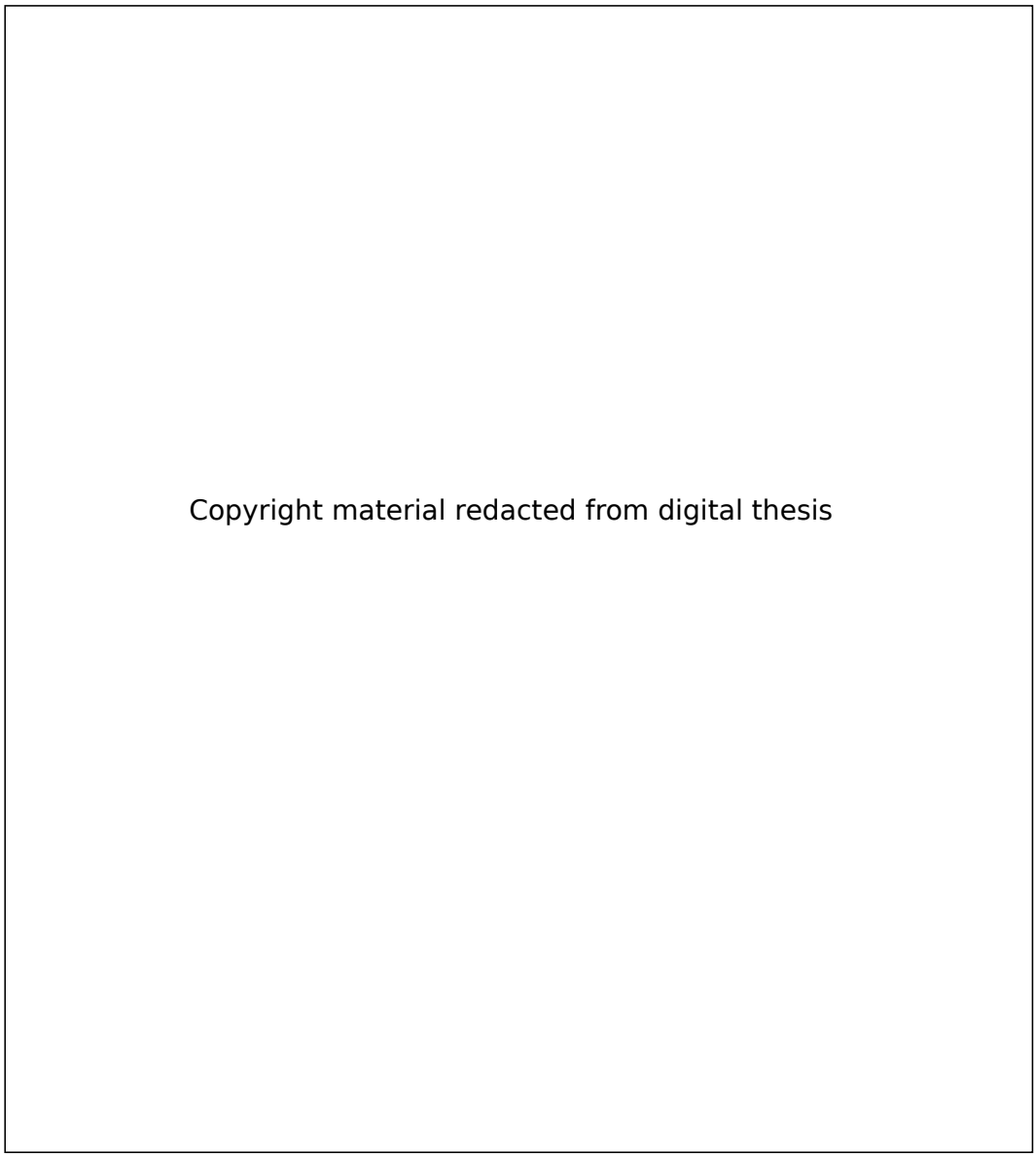

Figure 4.13: Similarity solution for the rapidly rotating ambipolar diffusion collapse, with outer asymptotic boundary conditions matching those in Figure 4.9 except for the azimuthal velocity parameter which has been increased from 0.73 to $v_0 = 1.5$, and the magnetic braking parameter α has been increased to $\alpha = 0.1$ from 0.08 (figure 9 of Krasnopolsky and Königl, 2002). These match the parameters from the fast IMHD similarity solution in Figure 4.4. The solution is similar to that in the IMHD case, with an increased centrifugal shock position $x_c = 1.5$, and reduced central mass $m_c = 0.5$. There is no magnetic diffusion shock, as the density remains too low for ambipolar diffusion to become important before the centrifugal shock occurs. After an extended region of backflow and slow infall the variables settle onto the inner asymptotic solutions.

the centrifugal shock. These are all expected to be further changed by the inclusion of Hall diffusion, which alters the magnetic behaviour of the collapsing core further from that in the simple models.

4.4 Summary

Three forms of gravitational collapse were described within this chapter: a nonmagnetic model, an ideal MHD model, and finally one with ambipolar diffusion as the dominant flux transport mechanism in the collapsing flow once the density is high enough that flux freezing breaks down. These were intermediate models constructed as part of the process of building and testing a model of rotational molecular cloud core collapse that shall demonstrate the influence of both ambipolar and Hall diffusion, which shall be described in the following chapter. The solutions here were reconstructions of those by Krasnopolsky and Königl (2002), and their results were duplicated in order to test the code calculations. Comparisons were also made to other collapse simulations in the literature, demonstrating the power of the self-similar formulation as a tool for exploring the physics of star formation over a wide range of densities and length and time scalings.

In order to ensure that the similarity solutions matched onto appropriate inner boundary conditions, the inner asymptotic power law solutions describing the collapse behaviour close to the origin had to be derived; for each of the models these took the form of rotationally-supported accretion discs. The outer boundary of these discs was marked by a shock discontinuity that occurred near the centrifugal radius, and the exact position of this shock determined the matching onto the inner asymptotic solution. The jump conditions, and an estimation of the centrifugal shock position were derived, and for the ambipolar diffusion model an estimate of the magnetic diffusion shock position was also derived.

The ambipolar diffusion model required the calculation of a simplified model for the purpose of estimating the variables at a matching point located between the two shocks, which is used as the initial guess in the shooting routine. Inside of the centrifugal shock, a second simplified model is used to perform the innermost integration and ensure convergence on the true similarity solution. The numerical procedures in each version of the model code were briefly described, along with a discussion of the numerical instabilities and complexities that limit the precision of the similarity models. Finally, similarity solutions of interest in each case were presented and the physics discussed, in order to explore the effect of the magnetic field transport, the magnetic braking and the initial rotation rate in the core on the collapse process.

The nonmagnetic model (Figures 4.1 and 4.2) has no way to brake the angular

momentum in the gas, so the angular momentum-to-mass ratio, Φ, is a constant that parameterises the similarity solutions. The pseudodisc thickness is dominated by its self-gravity, as is the radial velocity. In these solutions the fluid falls in from the outer asymptotic solution describing a rotationally-flattened core undergoing supersonic collapse just before point mass formation. The centrifugal force builds up until it is able to balance the gravitational force, triggering the formation of the centrifugal shock.

The shock represents a sudden deceleration of the infalling matter as it encounters a wall of increased density at the boundary of the inner disc, which is supported by the radial pressure and rotation. The variables quickly settle to their asymptotic disc behaviour, and as there is no way to brake the angular momentum the gas cannot fall inwards through the disc to the origin, so that no central mass is able to form. The disc has a constant (with x) azimuthal velocity v_ϕ, which depends only upon the initial ratio Φ.

The size of the inner disc depends upon the initial azimuthal velocity in the core relative to the mass. As the ratio Φ increases, the centrifugal force becomes important earlier in the collapse, resulting in a larger disc. If this initial velocity is sufficiently high then the material can be pulled along after the shock in a backflow for quite some time before the gravity of the protostar causes it to lose its outward radial momentum and settle onto the centrifugally-supported disc. This backflow appears in all of the similarity solutions discussed in this work that have a high initial rotation rate.

The ideal MHD model (Figures 4.3–4.5) saw the introduction of a magnetic field to the collapsing core. The field is frozen into the material, moving with it so that the nondimensional mass-to-flux ratio μ remains constant throughout the collapse; a magnetic braking term included in the angular momentum equation allows for the removal of angular momentum from the thin disc to the external envelope by Alfvén waves. This braking allows matter from the rotationally-supported disc to lose its angular momentum and spiral down to the origin, creating a central point mass of nondimensional mass m_c.

In the IMHD solutions the inner disc is in near-Keplerian rotation, as the magnetic pressure term in the radial momentum equation aids the centrifugal force in supporting the disc against collapse. As flux is dragged into the central point mass with the gas (creating a magnetic flux problem) the field takes on a split monopole form with the field lines strongly inclined in the radial direction. The dominance of the radial magnetic field component over the vertical component also appears in the discs of the ambipolar diffusion model, and is strong enough in both models to drive a centrifugal disc wind from the surface, although such behaviour is not explored in these models.

The amount of angular momentum in the initial core continues to affect the size of the protostellar disc, with rapidly rotating cores forming larger discs. It also affects

the central point mass so that those cores with a higher initial rotational velocity form larger discs with smaller point masses, as accretion through the disc is low and subsonic. Reducing the amount of magnetic braking further reduces the central point mass, and causes the backflow region outside of the disc, in a core that was initially rotating rapidly, to be extended so that the magnetic and rotationally-supported disc is much smaller than in those solutions with higher rates of magnetic braking.

The inclusion of ambipolar diffusion in the similarity solutions (Figures 4.9–4.13) reduces the magnetic flux problem induced in the IMHD solutions by redistributing the flux in the central protostar throughout the inner disc and the surrounding near-free fall collapse region. The boundary between the ambipolar diffusion-dominated free fall and the outermost dynamic collapse where IMHD is still dominant is marked by the magnetic diffusion shock, which is a thin (but numerically resolvable) discontinuity in the vertical magnetic field strength. The magnetic field is increased rapidly by the decoupling of the field from the infalling neutral particles; this causes a compression of the pseudodisc thickness by magnetic squeezing and an increase in the amount of magnetic braking affecting the collapsing flow. This additional shock is a feature of the ambipolar diffusion similarity solutions that is not present in the simpler models; the infalling gas is slowed as the density increases in a post-shock transition region before the gravity of the protostar comes to dominate the radial acceleration and the matter begins to infall at near-free fall speeds.

The mass of the protostar and the size of the rotationally-supported protostellar disc both depend on the amount of ambipolar diffusion in the flow, as the decoupling of the field from the neutral particles causes an increase in the magnetic force that slows the inflow and reduces the accretion rate onto the protostar. The size of the disc depends also on the amount of magnetic braking and the initial rotation of the core: reduced braking or a larger value of v_0 correspond to a larger rotationally-supported disc; stronger braking or a low initial rotation rate lead to a smaller disc, or the prevention of disc formation entirely. The density, scale height and infall velocity within the inner Keplerian disc all depend upon the ratio of the ambipolar diffusion parameter to the azimuthal field cap, which limits the amount of magnetic braking in the disc; the surface density scales with $x^{-3/2}$ as expected in protostellar accretion discs. The disc is rotationally-supported with a low infall speed, so that the angular momentum problem is effectively resolved.

A clear problem with all of the models is the cap on the azimuthal field parameter, which limits the amount of angular momentum that can be removed from the collapsing core and ensures disc formation. Although not duplicated in this work, Krasnopolsky and Königl (2002) also produced a similarity solution with $\alpha = \delta = 10$ and $\tilde{\eta}_A = 0.5$, in which the magnetic braking was so strong that all angular momentum was removed

from the gas and no rotationally-supported disc could form (see their §3.3.3 and Section 6.2 for a discussion of this similarity solution). Similarly, the numerical simulations of Mellon and Li (2008, 2009) and others have shown that magnetic braking is more than capable of suppressing disc formation, which could have serious consequences for studies of protoplanet formation. Overstrong magnetic braking may be responsible for observations of slowly rotating YSOs without discs (e.g. Stassun et al., 2001), as such stars could have formed in cores that were so strongly braked that not only were they unable to form a rotationally-supported disc but the angular momentum of the protostar itself was braked during collapse.

This magnetic braking catastrophe is unresolved at present, however, Hall diffusion has been neglected in previous simulations of star formation. Hall diffusion changes the amount of magnetic braking affecting the collapsing flow, either increasing or decreasing it depending upon the sign of the Hall parameter; this changes the dynamics of the collapse by allowing more or less matter to fall onto the central protostar, and affects the infall rate through the inner Keplerian disc by providing more or less magnetic support. This behaviour is explored in the following chapter in which Hall diffusion is introduced into the self-similar collapse model.

Chapter 5

Collapse with the Hall Effect

The introduction of Hall diffusion modifies the behaviour of the collapsing fluid, changing the size and strength of the magnetic diffusion shock, the effect of magnetic braking and the radius of the rotationally-supported disc in the central regions of the collapse. The sign of the Hall parameter, which corresponds to the orientation of the magnetic field with respect to the axis of rotation, can reduce the complexity of the similarity solutions when it is negative or add to it when the Hall parameter is positive. Additional shocks may form in the post-shock regions downstream of the magnetic diffusion and centrifugal shocks; these slow the infall and reduce the accretion onto the central protostar.

The model that is used to find the similarity solutions is a modified version of that used in Section 4.3 to calculate the solutions with only ambipolar diffusion. The full set of self-similar equations derived in Chapter 2 are integrated from a matching point across a wide range of x until they match onto the initial supersonic collapse of a molecular cloud core at the outer boundary and the Keplerian disc described in Chapter 3 at the inner boundary. Only the induction equation and the azimuthal field component are changed from their counterparts in the ambipolar diffusion model, as both of these need to account for Hall diffusion:

$$\psi - xwb_z + \tilde{\eta}_H x b_{\phi,s} b_z b h^{1/2} \sigma^{-3/2} + \tilde{\eta}_A x b_z^2 h^{1/2} \sigma^{-3/2} \left(b_{r,s} - h \frac{db_z}{dx} \right) = 0 \tag{5.1}$$

and

$$b_{\phi,s} = -\min \left[\frac{2\alpha\psi}{x^2} \left[\frac{j}{x} - \frac{\tilde{\eta}_H h^{1/2} b}{\sigma^{3/2}} \left(b_{r,s} - h \frac{db_z}{dx} \right) \right] \left[1 + \frac{2\alpha\tilde{\eta}_A h^{1/2} \psi b_z}{x^2 \sigma^{3/2}} \right]^{-1} ; \delta b_z \right] \tag{5.2}$$

(Equations 2.109 and 2.114). The other equations remain unchanged from those used in the ambipolar diffusion model; they are reproduced here from Equations 2.104–2.113

for ease of reference:

$$\frac{d\psi}{dx} = xb_z, \tag{5.3}$$

$$\frac{dm}{dx} = x\sigma, \tag{5.4}$$

$$(1-w^2)\frac{1}{\sigma}\frac{d\sigma}{dx} = g + \frac{b_z}{\sigma}\left(b_{r,s} - h\frac{db_z}{dz}\right) + \frac{j^2}{x^3} + \frac{w^2}{x}, \tag{5.5}$$

$$\frac{dj}{dx} = \frac{1}{w}\left(j - \frac{xb_z b_{\phi,s}}{\sigma}\right), \tag{5.6}$$

$$\left(\frac{\sigma m_c}{x^3} - b_{r,s}\frac{db_z}{dx}\right)h^2 + \left(b_{r,s}^2 + b_{\phi,s}^2 + \sigma^2\right)h - 2\sigma = 0, \tag{5.7}$$

$$m = xw\sigma, \tag{5.8}$$

$$\dot{m} = -xu\sigma, \tag{5.9}$$

$$g = -\frac{m}{x^2} \tag{5.10}$$

$$\text{and } b_{r,s} = \frac{\psi}{x^2}. \tag{5.11}$$

This chapter aims to show the importance of the Hall effect in gravitational collapse by outlining the construction and results of the model with Hall diffusion. The inner asymptotic solution for the Keplerian accretion disc shall be briefly recapped in Section 5.1 before the numerical procedure for finding the similarity solutions is outlined in Section 5.2. This is followed by a discussion of the behaviour of the shocks and their positions in Section 5.3, which also contains an exploration of the importance of the Hall term in determining the size of the centrifugally-supported disc and the region bounded by the magnetic diffusion shock. Finally, a series of similarity solutions are presented and discussed in Section 5.4, demonstrating how the Hall term changes the dynamics of the flow, and how the orientation of the field with respect to the axis of rotation influences the size of the accretion disc. Hall diffusion also introduces additional shocks into the flow and modifies the accretion rate onto the central protostar; these will be briefly discussed in the context of the magnetic braking catastrophe, which will be described more fully in Chapter 6.

5.1 Inner Asymptotic Solution

The inner asymptotic solutions to the collapse with both Hall and ambipolar diffusion were the focus of the derivation and discussion contained in Chapter 3. As this work is principally concerned with the influence of the Hall effect on the disc formation problem in star formation, only those similarity solutions in which a Keplerian disc forms around the protostar are calculated in this chapter. These solutions are characterised by the

existence of an accretion disc around the central mass which is described by the set of power laws with respect to x in Equations 3.18–3.28, which are reproduced here for clarity:

$$m = m_c, \tag{5.12}$$

$$\dot{m} = m_c, \tag{5.13}$$

$$\sigma = \sigma_1 \, x^{-3/2} = \frac{\sqrt{2m_c} f}{2\delta\sqrt{(2\delta/f)^2 + 1}} \, x^{-3/2}, \tag{5.14}$$

$$h = h_1 \, x^{3/2} = \left(\frac{2}{m_c[1 + (f/2\delta)^2]} \right)^{1/2} x^{3/2}, \tag{5.15}$$

$$u = -\frac{m_c}{\sigma_1} \, x^{1/2}, \tag{5.16}$$

$$v = \sqrt{\frac{m_c}{x}}, \tag{5.17}$$

$$j = \sqrt{m_c x}, \tag{5.18}$$

$$\psi = \frac{4}{3} b_z x^2, \tag{5.19}$$

$$b_z = \frac{m_c^{3/4}}{\sqrt{2\delta}} \, x^{-5/4}, \tag{5.20}$$

$$b_{r,s} = \frac{4}{3} \, b_z \tag{5.21}$$

$$\text{and } b_{\phi,s} = -\delta \, b_z. \tag{5.22}$$

The constant m_c is the nondimensional central mass infall rate, and δ is the artificial cap placed upon $b_{\phi,s}$ to prevent it from becoming the dominant field component in the innermost regions of the disc. The diffusion constant f is a function of the ambipolar and Hall diffusion parameters, and is given by the equation

$$f = \frac{4}{3} \, \tilde{\eta}_A - \delta \tilde{\eta}_H \sqrt{\frac{25}{9} + \delta^2}; \tag{5.23}$$

this definition shows how the Hall term is able to counteract the ambipolar diffusion term in determining the surface density of the disc and the accretion rate onto the central protostar when the nondimensional Hall parameter $\tilde{\eta}_H$ is positive, and add to the ambipolar diffusion if the Hall parameter is negative. The characteristic parameter of the disc, f, must be positive lest the surface density be negative; this places limits on the allowed relative sizes of the two diffusion parameters that must be satisfied in order to form a Keplerian disc.

The full physical meaning of this solution is discussed at length in Section 3.2. To summarise, the inner accretion disc is in Keplerian rotation, with the centrifugal force balancing the inwards pull of gravity. The accretion rate onto the protostar is constant

and low, and accretion through the disc is determined by the total amount of magnetic diffusion, which removes radial support by the magnetic field and allows the gas to fall inwards.

Section 3.3 described another asymptotic solution in which the magnetic braking is so strong that all angular momentum is removed from the gas which free falls onto the protostar without forming a disc. No similarity solutions matching onto this inner solution are calculated in this work, but the similarity solution with no Hall diffusion but strong magnetic braking, and its role in describing the magnetic braking catastrophe are discussed further in Chapter 6.

The Keplerian disc equations, in particular Equations 5.12 and 5.19, are the inner boundary conditions that must be evaluated to test the accuracy of any individual integration and satisfied in the true similarity solution. The method in which these are employed to ensure convergence of the shooting routine for finding the similarity solutions shall be described in the following section.

5.2 Numerical Method

The numerical procedures used to calculated the similarity solutions are relatively unchanged from those used in the ambipolar diffusion model, save for those changes that were necessary to handle the additional complications introduced with Hall diffusion. As mentioned previously, sonic points and subshocks occur downstream of the magnetic diffusion and centrifugal shocks, which may be the "viscous subshock" mentioned in Krasnopolsky and Königl (2002), although these do not appear in their published solutions. Locating and integrating through such shocks requires the introduction of new routines that monitor the integration and perform such adjustments as are necessary.

Overall the iterative routine for finding the correct similarity solution remains unchanged, using the globally convergent multidimensional Newton-Raphson root-finding routine (`newt` and its dependences, converted to double precision) from *Numerical Recipes* (Press et al., 1992). This routine performs a series of integrations (using the routine `shoot`) from the unknown initial values to the boundaries whereupon the difference between the integrated variables and the boundary conditions are evaluated. Each of the initial values is perturbed in turn, and the Jacobian of the shooting routine is calculated; `newt` then uses the inverse of the Jacobian to determine the changes to the initial values necessary to zero the discrepancies. This step is then taken and assessed (a smaller change in the variables is made if needed) and the process is repeated until the shooting routine converges on the true solution. Once the initial values are close enough to the true solution the Newton-Raphson routine will converge quadratically.

As in the ambipolar diffusion model, the problem is recast as a two-point boundary

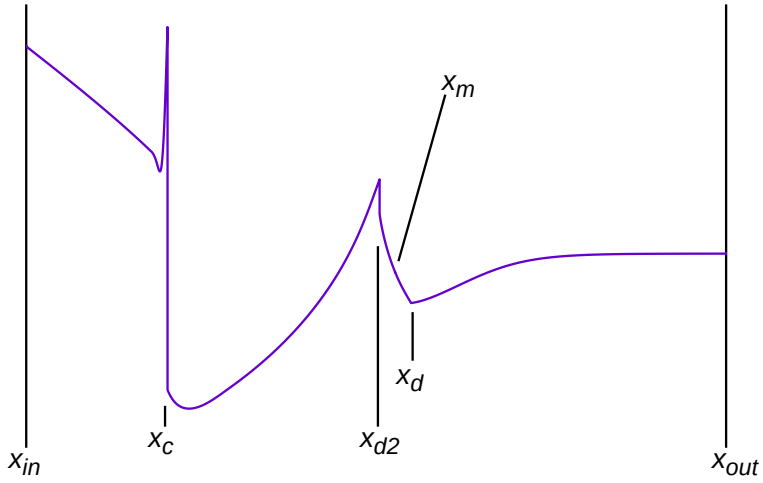

Figure 5.1: Schematic of the two-point boundary value problem, showing the integration of a variable (in this case σ) from the matching point x_m to the inner and outer boundaries. In the outwards direction the integration is slowed only by the continuous magnetic diffusion shock at x_d. Inwards of the matching point the integration encounters the centrifugal shock at x_c; it may also need to integrate through sonic points and subshocks (e.g. x_{d2}) downstream of both the magnetic diffusion and centrifugal shocks.

value problem in which the variables are integrated from a matching point x_m to both the inner and outer boundaries, as depicted in Figure 5.1. The matching point is located at a position $x_c < x_m < x_d$, and is typically chosen to lie just downstream of the magnetic diffusion shock and upstream of any subshocks that may occur. The values of the variables m, σ, j, ψ and b_z at x_m are initially unknown but may be estimated by integrating a simplified set of equations as shall be outlined in subsection 5.2.1. The initial value of the central mass parameter m_c is estimated using the plateau value defined in Section 4.1:

$$m_c \approx m_{pl} \approx 2|u_0|A. \tag{5.24}$$

The integration itself is performed using either a fifth order Runge–Kutta step (`rkqs`) or a Bulirsch–Stoer semi-implicit midpoint rule step (`stifbs`) as the equations may be stiff, requiring a different method of integration. The driver routine for both is `odeint`, which exerts an adaptive stepsize control to improve the accuracy and efficiency of the integration; all of these routines and their dependencies were taken from *Numerical Recipes* (Press et al., 1992) and have been converted to double precision.

Integration in the outwards direction is usually performed without difficulty unless a particularly poor guess of the values of the variables at x_m is employed. As the magnetic diffusion shock is continuous, both routines for stepping through the integration are able to integrate through it without pause. At the outer boundary (which is

usually located at $x_{out} = 10^4$ or 10^5) the variables are compared to the outer boundary conditions outlined in Section 2.7:

$$m = Ax_{out}, \tag{5.25}$$

$$\sigma = \frac{A}{x_{out}}, \tag{5.26}$$

$$b_z = \frac{\sigma}{\mu_0} \tag{5.27}$$

$$\text{and } v = v_0; \tag{5.28}$$

the difference between these variables and their boundary values is passed to the root-finding routine as a score that must be minimised. Both `rkqs` and `stifbs` give similar results so they may be used interchangeably; `stifbs` is typically used for the outer integration, while `rkqs` is used for the inwards path, as `stifbs` occasionally fails downstream of the centrifugal shock.

Integrating in the inwards direction is more problematic, as the calculation is very sensitive both to the initial values of the variables at x_m and the Hall diffusion parameter $\tilde{\eta}_H$. Close to the magnetic diffusion shock (downstream of x_m) there may occur a subshock in which the supersonic (but slowing due to the sudden increase in b_z at the magnetic diffusion shock) inflow is abruptly slowed to a subsonic rate. This only occurs when the Hall parameter is positive, and is likely caused by the change in the azimuthal field in the shock affecting the downstream magnetic braking. This subshock is a sharpening of the post-shock variation of the density and infall speed in the ambipolar diffusion solution in Figure 4.9, and its position and jump conditions (discussed in Section 5.3) must be calculated explicitly using the method to be described in subsection 5.2.2.

The magnetic diffusion subshock's existence is detected by performing a test integration inwards; if the variables approach a sonic point (where $w^2 = 1$) then a shock must exist before this point. Downstream of the subshock a sonic point occurs as the radial velocity becomes supersonic once more; this is integrated through using the method described in subsection 5.2.3. Past this point, the variables are integrated without any further interruption until they reach the centrifugal shock.

The centrifugal shock is located by integrating to an upper bound on the shock position and then calling the iterative routine outlined in subsection 5.2.2 which tests the initial guess of the shock position x_c and refines this guess based upon the downstream behaviour of the variables. Once x_c is known as precisely as possible, the variables are integrated to the shock position and the jump conditions (again described in subsection 5.3.3) are evaluated. Downstream of this shock, if the Hall parameter is positive, one or more subshocks may occur. As with the magnetic diffusion subshock, the centrifugal subshocks are preceded by a sonic point that must be calculated carefully and

then the subshock position is found using the same iterative process as the centrifugal shock. Inwards of these shocks the variables approach the expected asymptotic behaviour outlined in Section 5.1.

In the innermost regions of the collapse the derivatives $d\sigma/dx$ and db_z/dx become very large in comparison to the other derivatives. These can cause σ and b_z to become large, and small numerical errors in the calculation of these derivatives and their integrals can cause the appearance of a spontaneous singularity in which the variables diverge dramatically from the asymptotic similarity solutions. This behaviour is avoided by simplifying the calculation of the derivatives in this region using the expected asymptotic behaviour of the variables; the simplified equations, and the criteria used to match onto this simple model are described in subsection 5.2.4.

When the inwards integration reaches the inner boundary (typically located around $x_{in} = 10^{-4}$, depending upon the position of x_c) the variables are compared to the inner boundary conditions

$$m(x_{in}) = m_c \tag{5.29}$$

$$\text{and } \psi(x_{in}) = \frac{4m_c^{3/4}}{3\sqrt{2\delta}}\, x_{in}^{3/4}. \tag{5.30}$$

The difference between the expected boundary value and the integrated variable are passed back to the shooting routine, which modifies the initial values at x_m and begins the next iteration of the integration. The similarity solution is considered to have converged when the integrated variables match the boundary condition values to at least 0.002%. Due to the ease of convergence in the outwards direction, the outer boundary conditions match the integrated variables to a much higher degree.

Some of the earlier (low $|\tilde{\eta}_H|$) similarity solutions were calculated using a modified shooting routine that only integrated in the outwards direction. This method required the adoption of specific values of $\psi(x_m)$ and m_c, which were held constant as the root-finding routine minimised the scores at the outer boundary; only after that convergence was achieved was the inwards integration performed and the values of $\psi(x_m)$ and m_c altered. This process was repeated until the initial values were properly converged. While this method was less efficient than the full version of `shoot` that integrates in both directions, due to the complications involved in integrating inwards (especially when multiple subshocks exist in the solution) this was often a more reliable mechanism for solving to the full set of boundary conditions.

Both methods require a good initial estimate of the values of the variables at x_m and take at least a full day to compute on a desktop machine. If a particularly poor initial guess at the matching point is chosen, or if more than one sonic point occurs in the collapse, the calculation may require close monitoring to ensure that integration in

the inwards direction proceeds as expected and convergence on the true solution takes place.

5.2.1 Simplified model

The initial guess of the variables at the matching point is estimated by calculating a simplified model in which the induction equation is replaced by an algebraic expression for the vertical field component. As the derivative of b_z is a negligible term in the equations (see Section 2.5), when the fluid equations are integrated inward from the outer boundary the evaluation of db_z/dx causes the integration to become unstable. Removing this term allows the induction equation to be written as an algebraic expression for b_z as a function of the other variables. The other equations are unchanged, and using the expression for b_z it is possible to integrate these from the outer boundary to the matching point x_m. This simplified model is quite similar to the one constructed for the ambipolar diffusion collapse in Section 4.3, differing only in the inclusion of the Hall diffusion term.

With the exception of during the magnetic diffusion shock where b_z changes rapidly, the inequality $b_{r,s} \gg h(db_z/dx)$ holds true everywhere during the collapse; and as this term is always small compared to the other terms in the induction equation it may be dropped. The magnitude of the magnetic field b is always of order b_z, so that it may be approximated by $b = b_1 b_z$ where b_1 is a constant that depends on the relative sizes of $b_{r,s}$ and b_z. The induction equation may then be written as a quadratic in b_z:

$$xh^{1/2}\sigma^{-3/2}\left(\tilde{\eta}_H b_1 b_{\phi,s} + \tilde{\eta}_A b_{r,s}\right) b_z^2 - xwb_z + \psi = 0. \tag{5.31}$$

The two well-separated roots of this equation provide an acceptable approximation to the behaviour of b_z on either side of the magnetic diffusion shock, with the prescription

$$b_{z,low} \approx \frac{\psi\sigma}{m} \approx \frac{\sigma}{\mu_0} \tag{5.32}$$

(which is unchanged from that in the ambipolar diffusion model) applying in the large x regime where flux freezing still mostly holds true and the mass-to-flux ratio is given by its initial value $\mu = \mu_0$. This is equivalent to the initial condition for the vertical field component on the outer boundary derived in Section 2.7; although IMHD breaks down before the magnetic diffusion shock this remains a good approximation to the field in this region.

The larger root of the two gives the value of the vertical field component in the magnetic diffusion regime where x is small. It is approximated by dropping the constant (with respect to b_z) term in the quadratic equation (5.31) and solving for b_z to obtain

$$b_{z,high} = \frac{m}{x}\left(\frac{\sigma}{h}\right)^{1/2}\left(\tilde{\eta}_H b_1 b_{\phi,s} + \tilde{\eta}_A b_{r,s}\right)^{-1}, \tag{5.33}$$

which reduces to Equation 4.167 in the ambipolar diffusion limit.

The transition between the two approximations to b_z occurs at the magnetic diffusion shock, x_d, the position of which is estimated in Section 5.3. The matching point is usually taken to be $x_m \sim 0.3$ depending slightly upon the position of the magnetic diffusion shock and its potential subshocks, and m_c is estimated by the plateau value in Equation 5.24. Figure 4.6 showed such a simple model for the ambipolar diffusion calculations — inwards of the matching point the variables diverged from the expected values due to the poor guess of x_d used.

The values of the variables at the matching point from this simple model are often a good enough guess to the true values that the code is able to use them as the initial values for the iterative root-finding routine that solves the full set of equations. In those cases where this is not a good estimate (typically when $|\tilde{\eta}_H| \gtrsim 0.1$), the values of ψ and b_z are adjusted by hand until the shooting routine is able to integrate in both directions and match the boundary conditions to approximately 10%. Once this is achieved the root-finding routine is typically able to converge on the similarity solution.

5.2.2 Iterative routine for locating the shock position

The position of the centrifugal shock, x_c, is found by employing a simple binary search over an appropriate interval. The upper and lower bounds on this position are initially described by $x_{c0} \pm 0.2x_{c0}$ where x_{c0} is the estimated value that is derived in Section 5.3. Once the position of the shock has been found for the initial guess of the variables, a smaller pair of limits and the previous value of the shock position may be used in later integrations, as x_c does not vary greatly in its position with changing initial values of the variables at x_m. The variables are integrated down to the estimated position of x_c, where the jump conditions from subsection 5.3.3 are applied, and then integrated inwards towards the inner boundary. Unless the shock position is known very precisely, the variables will approach their asymptotic values and then veer off course.

This behaviour is most clearly seen in the surface density σ, which increases rapidly downstream of the shock if x_c is an overestimate to the true shock position, and decreases dramatically if x_c is an underestimate. The incorrect estimate is then assigned to be the new upper or lower boundary on the shock position as appropriate, and a new estimate of the shock position is chosen at the midpoint between the boundaries. As the position of the shock is more precisely known, the variables follow the expected asymptotic behaviour for longer, as can be seen in Figure 5.2.

When the shock position is known to approximately ten decimal places, it is considered to be known to the precision of the full calculation, as the precision of the integration itself (typically to around 10^{-10}) limits the accuracy of all other calcula-

tions. Note that even when the position of the shock is known "precisely" (as is the case with the solid black plot in Figure 5.2), the integrating routine is unable to complete the integration all the way to the inner boundary. As was the case in the ambipolar diffusion model, a simplified set of equations need to be integrated from a point far from the centrifugal shock, where the variables follow their asymptotic behaviour, to the inner boundary. The simplified set of equations with Hall and ambipolar diffusion and the matching criteria is outlined in subsection 5.2.4.

The potential presence of a sonic point and subshock does not particularly interfere with the initial iterative routine for finding the shock position. When there exists a sonic point downstream of the shock, if x_c is too high then σx bounces upwards at the sonic point, as seen in Figure 5.3a, while if x_c is too low then the integration fails at the sonic point as demonstrated in Figure 5.3b. The same iterative routine may then be used to find the shock position even when the shock is followed by one or more subshocks.

Downstream of any of the sonic points the iterative routine must again be employed to find the position of the associated shock front that follows. In this instance the upper boundary of the search (x_{up}) is initially chosen to be the sonic point, and the lower boundary is located at a value of $x_{down} = 0.1x_{up}$; these typically enclose the shock. The behaviour of the variables downstream of the subshock is the same as that downstream of the principal shock, so the binary search described above is able to locate the true shock position without alteration, and once x_{c2} has been found the variables typically match onto the simplified set of equations used to integrate to the inner boundary without difficulty.

5.2.3 Subshocks

Perhaps the most obvious difference between those solutions in which the Hall parameter is positive and those with no or negative Hall diffusion is the presence of subshocks downstream of either or both of the magnetic diffusion and centrifugal shocks as described in the previous subsection. To date only one magnetic diffusion subshock has been found in the similarity solutions, however many subshocks may occur downstream of the centrifugal shock. These subshocks occur after the density increase in the principal shock causes the gas to be slowed to a subsonic speed. The gas is abruptly halted as the magnetic or centrifugal forces overcome the radial gravity, causing another steep density increase.

The first of these subshocks, downstream of the magnetic diffusion shock, occurs when the post-shock density increase is so steep that the gas is slowed dramatically, eventually forming a shock front. This shock can be seen in Figure 5.4, which is a

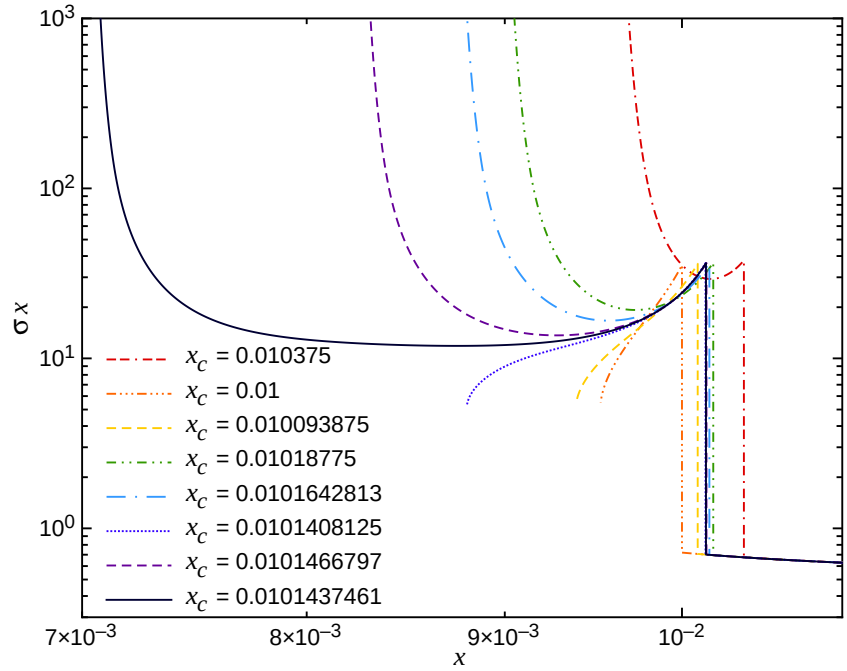

Figure 5.2: Locating the centrifugal shock position for a non-converged solution by integrating inwards and observing the behaviour of σx. When the estimated value of x_c is too high, the surface density diverges from its expected behaviour and becomes very large; when it is too low, the surface density becomes small. The more accurate the value of x_c the longer the variables follow the expected asymptotic behaviour before diverging.

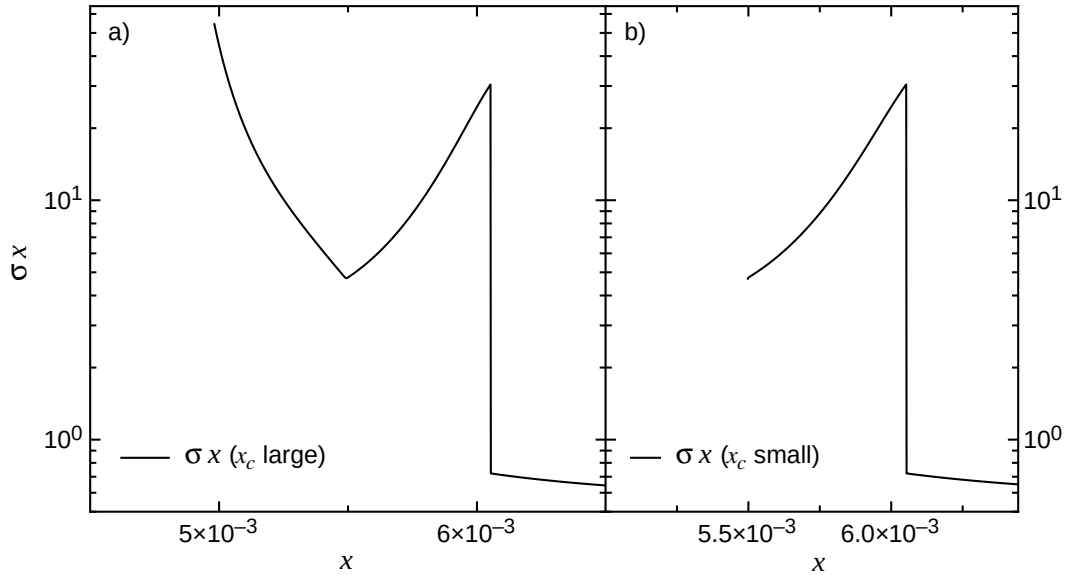

Figure 5.3: Locating the centrifugal shock in the presence of one or more subshocks. When the estimated value of x_c is too high (panel a) the surface density diverges from the expected behaviour at the sonic point and becomes very large. When the estimate of x_c is too low (panel b) the integration simply fails at the sonic point. This contrasting behaviour is used to refine the shock position.

close view of the magnetic diffusion subshock in the $\tilde{\eta}_H = 0.2$, $\tilde{\eta}_A = 1.0$ similarity solution presented in Section 5.4. At this shock the azimuthal field component is increased suddenly, and this straightening of the field at the pseudodisc surface slows the fluid. There are discontinuities in the scale height and the vertical field derivative, and the corresponding increase in $b_{\phi,s}$ also increases the amount of magnetic braking downstream of the shock.

As described in the introduction to this section, the magnetic diffusion subshock occurs when the integration tends towards a numerical sonic point downstream of the principal shock; this sonic point would see the radial inflow become subsonic gradually, while the code rapidly encounters an unphysical singularity and fails. This is clearly undesirable and the solution to this behaviour is to use the iterative routine described in the previous subsection to find the subshock position, using the magnetic diffusion shock position as the upper boundary and the sonic point position as the lower boundary. Once the subshock position is known it is possible to integrate from the magnetic diffusion shock to the subshock, and from there towards the centrifugal shock.

Downstream of the magnetic diffusion subshock the radial velocity increases gradually under the influence of gravity; it passes from subsonic to supersonic at a sonic point that must be calculated explicitly. The singularity in the radial momentum equation (5.5), occurring when $(x-u)^2 = w^2 = 1$, prevents the smooth integration through this point as $d\sigma/dx$ diverges; this behaviour is prevented by checking the value of w at each intermediate point between the magnetic diffusion subshock and the sonic point. When $|w^2 - 1| < 0.01$ then a small manual step (or series of steps) is taken by evaluating the derivatives and multiplying these by the stepsize $\Delta x < 0.001$ to give a small change to the variables. This change is added to the variables to give the value at the new position, $x - \Delta x$, which is written as

$$f(x - \Delta x) = f(x) - \Delta x f'(x) \tag{5.34}$$

for each of the variables f. If w has not passed through the sonic point this manual step is repeated as necessary until it has. Once past the sonic point the gas flow tends towards the free fall collapse behaviour as in the ambipolar diffusion solutions.

Similarly, those subshocks that occur downstream of the centrifugal shock form because the density increase in the shock is narrow, and once past the sharp peak of the shock the matter starts falling inward again at a rapid rate. This behaviour can be seen in Figure 5.5, which again is a close view of the similarity solution with $\tilde{\eta}_H = 0.2$ and $\tilde{\eta}_A = 1.0$ focussing on the centrifugal subshock; the surface density and other variables overshoot their asymptotic behaviours and the infall quickly becomes supersonic once more. The centrifugal force remains important, and once the infalling material has overcome the increased magnetic pressure caused by the increase in the

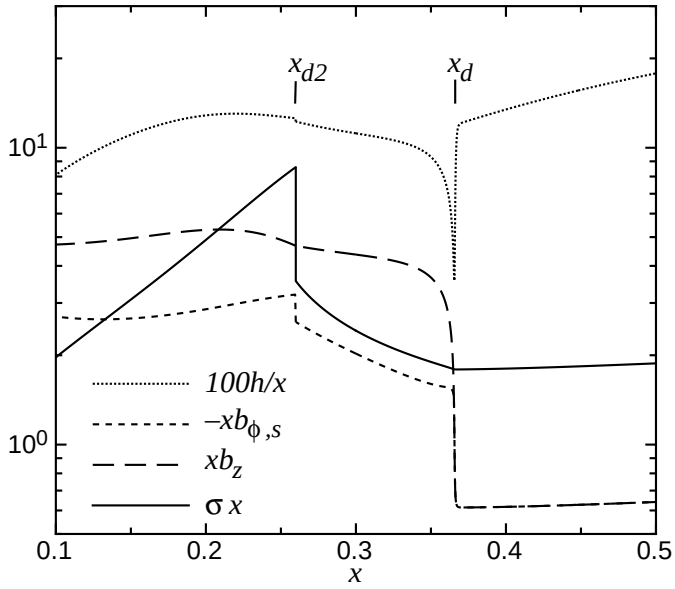

Figure 5.4: Close view of the magnetic diffusion shock at $x_d = 0.366$ and associated subshock at $x_{d2} = 0.260$ for the similarity solution with $\tilde{\eta}_H = 0.2$ and $\tilde{\eta}_A = \delta = 1.0$. The scale height h and the vertical and azimuthal field components (b_z and $b_{\phi,s}$) change at the principal shock, while it is the scale height, the azimuthal field component and the surface density σ (as well as the infall speed $-u$, not pictured here) that change values at the subshock, while the vertical field component remains constant.

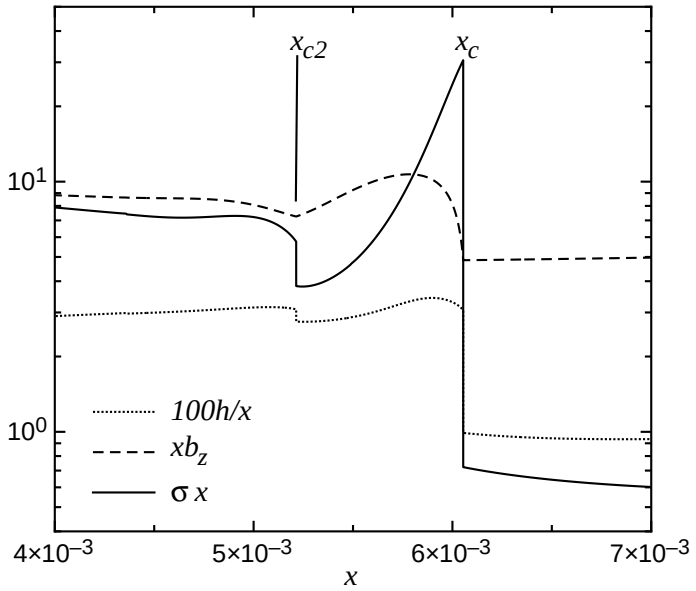

Figure 5.5: Close view of the centrifugal shock at $x_c = 6.05 \times 10^{-3}$ and associated subshock at $x_{c2} = 5.21 \times 10^{-3}$ for the similarity solution with $\tilde{\eta}_H = 0.2$ and $\tilde{\eta}_A = \delta = 1.0$. The scale height h and the surface density σ (and the infall speed $-u$, not pictured here) increase at each of the shocks, while the vertical field component b_z changes only in the post-shock region. By 4×10^{-3} the variables have matched to their asymptotic behaviour.

field downstream of the shock it starts to fall in under gravity once more, so that the centrifugal force causes the gas to be shocked once more. Multiple subshocks occur as the Hall parameter becomes large — the increasing number of subshocks make it computationally difficult for the iterative root-finding routine to converge on the true similarity solution, preventing the publication of larger positive Hall parameter solutions in this work.

The presence of the centrifugal subshock is indicated by the presence of a sonic point downstream of the principal centrifugal shock, in which the infall speed seemingly passes from being subsonic to supersonic in a smooth manner. As with the magnetic diffusion subshock, this sonic point is caused by the singularity in the radial momentum equation and is manually integrated through using Equation 5.34. The position of the subshock downstream of the sonic point is found iteratively using the routine outlined in subsection 5.2.2, using the sonic point x_{sp} as the upper bound and a position $0.6x_{sp}$ as the lower bound. If multiple subshocks exist (caused by the steep increase in the magnetic field and correspondingly the magnetic pressure) then this behaviour will be repeated, with the first subshock being followed by an additional sonic point and then a second subshock. This behaviour is repeated until the variables match onto the inner asymptotic solution and can be integrated without further intervention to the inner boundary.

The jump conditions calculated at all of the subshocks are those jump conditions used for the centrifugal shock that shall be outlined in Section 5.3. It is possible that as the positive Hall parameter becomes larger the magnetic diffusion subshock may require different jump conditions that take the twisting of the magnetic field lines due to the Hall effect into account; for the solutions presented in this work such changes were unnecessary.

Subshocks do not occur in those similarity solutions where the Hall parameter is negative, as the reduced radial magnetic field diffusion causes the post-shock regions to be smoothed and less dynamic. The variables match onto the expected behaviour downstream from the shocks with smaller overshoots, and the shocks themselves are weaker. Making the Hall parameter increasingly negative (while keeping the ambipolar diffusion parameter constant) reduces the severity of the magnetic diffusion shock (much as reducing $\tilde{\eta}_A$ does). Furthermore, tweaking $\tilde{\eta}_H$ changes the amount of magnetic braking affecting the disc, as larger negative values of $\tilde{\eta}_H$ lead to $b_{\phi,s}$ attaining its capped value faster; the reduced flux in the inner regions of the pseudodisc slows the rate of magnetic braking so that the centrifugal shock occurs sooner in the collapse process.

5.2.4 Simplified inner integration

As can be seen in Figure 5.2, the shooting routine is sometimes unable to integrate the equations all the way to the inner boundary, even when the position of the centrifugal shock is known as accurately as possible. The divergence from the true similarity solution occurs because the derivatives db_z/dx and $d\sigma/dx$ become very large downstream of the centrifugal shock and associated subshocks; the accumulation of small numerical errors and the contributions of small terms in the equations leads to a situation in which the integrated variables veer away from the expected asymptotic solutions.

In order to avert this behaviour and integrate to the inner boundary, the method used in the ambipolar diffusion model (described in Section 4.3) is reproduced here for the full model with both Hall and ambipolar diffusion. This simplification sees the MHD equations replaced by a simplified set that can be integrated all the way to the inner boundary. In this calculation the problematic derivatives that become large are replaced by approximations that are derived from the expected inner asymptotic solution that was outlined in Section 5.1, that is,

$$\frac{db_z}{dx} = -\frac{5m_c^{3/4}}{4\sqrt{2\delta}}\, x^{-9/4} \tag{5.35}$$

$$\text{and } \frac{d\sigma}{dx} = -\frac{3}{2}\,\frac{\sqrt{2m_c}f}{2\delta\sqrt{(2\delta/f)^2+1}}\, x^{-5/2}. \tag{5.36}$$

These are then substituted into the appropriate MHD equations so that σ, b_z, $b_{\phi,s}$ and h are then found by solving Equations 5.1, 5.2, 5.5 and 5.7 simultaneously, leaving only Equations 5.3, 5.4 and 5.6 to be integrated.

Switching between the full and simplified models takes place after the minimum turning point in the surface density when the variables have joined the inner asymptotic solutions, but before they diverge from the expected behaviour. Typically this switch occurs when the old and new values of σ match to within $0.01/x$ (which is $\sim 0.1\%$ of the value from the full set of equations) and $d\sigma/dx$ calculated using both methods matches less well to around $200/x$ ($\sim 7\%$). As in the ambipolar diffusion model this means that, in general, the transition between equation sets is visually seamless; the required precision of the match is raised from those stated here when the transition is visible and the change in the derivatives is apparent — such a slope change would clearly influence the accuracy of the calculations. When the precision of the match is as high as possible the change between the two equation sets is smooth.

The simplified set of equations is not subject to the same numerical instabilities as the full set unless the initial values of the variables at the matching point are a particularly poor guess of the true values. Should such a guess be adopted then the routine is unable to match onto the simplified model, and the failure of the inwards

integration is used to refine the values at the matching point. Using a simplified set of equations to integrate to the inner boundary is not expected to introduce significant errors into the calculation.

The shooting routine can then continue the integration to the inner boundary where the difference between the integrated variables and the boundary conditions are evaluated and the values of the variables at the matching point are adjusted.

5.3 Shocks

The inclusion of Hall diffusion in the collapse changes the position and behaviour of the magnetic diffusion and centrifugal shocks, and can cause there to be subshocks associated with these. As mentioned previously, when the Hall diffusion parameter $\tilde{\eta}_H$ is positive the increased magnetic forces and braking may cause the formation of subshocks, while the strength of the shocks is reduced and the dynamics of the post-shock regions smoothed when the Hall parameter is negative.

An analytic estimate of the shock positions is necessary for the calculation of the simple model described in subsection 5.2.1 and as an initial guess for the iterative routine in subsection 5.2.2; these are derived in subsections 5.3.1 and 5.3.2 for the magnetic diffusion and centrifugal shocks respectively. The shock positions depend upon the Hall parameter, as the outwards diffusion of the field leads to the formation of the magnetic diffusion shock, and the magnetic braking determines the position of the centrifugal shock, and Hall diffusion is important to both of these processes. For simplicity, the subshocks shall not be examined analytically at this point, as they were adequately described in the preceding sections, and their positions are usually well-estimated by those of the principal shock they follow. The Hall diffusion parameter does not affect the jump conditions applied at the shocks (described in subsection 5.3.3), although its influence on the shock position and the values of the density and magnetic field at this point does change the intensity of the shock.

5.3.1 Magnetic diffusion shock position

The first shock encountered by the collapsing flow is the decoupling front in which flux freezing breaks down and the magnetic field behaviour comes to be dominated by Hall and ambipolar diffusion. Similarly to the calculation of the magnetic diffusion shock position in the ambipolar diffusion model in Section 4.3, x_d is estimated by examining the vertical magnetic field behaviour on both sides of the shock. In the outermost regions of the core the material is collapsing inward at a near-free fall rate, ideal magnetohydrodynamics holds true, and the vertical field component is given by

$b_{z,low}$ defined in Equation 5.32. Inwards of the magnetic diffusion shock, the magnetic diffusion terms are important to the field transport and the drift of the magnetic field depends on the coupling between field lines and charged species; in this region the vertical field component may be approximated by $b_{z,high}$, which was given in Equation 5.33.

When calculating the position of the magnetic diffusion shock for the ambipolar diffusion model, it was noted that downstream of the shock the thickness of the disc was controlled by magnetic squeezing. The scale height of the disc may then be approximated by the relation

$$h \approx \frac{2\sigma}{b_{r,s}^2}; \tag{5.37}$$

this is then substituted into Equation 5.33 to give

$$b_{z,high} \approx \frac{m}{\sqrt{2}x}\left(\tilde{\eta}_H b_1 \frac{b_{\phi,s}}{b_{r,s}} + \tilde{\eta}_A\right)^{-1}, \tag{5.38}$$

where b_1 is the coefficient of b such that $b = b_1 b_z$. If the field components are approximately equal interior to the magnetic diffusion shock as expected then $b_{r,s} \approx b_{z,high}$ and $b_{\phi,s} \approx -\delta b_{z,high}$, and the magnitude of the total field strength (in terms of b_z) is then

$$b_1 \approx \sqrt{2+\delta^2}. \tag{5.39}$$

These relationships are then substituted into Equation 5.38, which becomes

$$\frac{\psi}{x^2} \approx \frac{m}{\sqrt{2}x}\left(\tilde{\eta}_A - \delta\tilde{\eta}_H\sqrt{2+\delta^2}\right)^{-1}. \tag{5.40}$$

Assuming that the mass-to-flux ratio is still constant in this regime and close to its initial value (this is not strictly true, as flux freezing does break down upstream of the magnetic diffusion shock), it is possible to solve this equation and obtain an estimate of the position of the magnetic diffusion shock:

$$x_d \approx \frac{\sqrt{2}}{\mu_0}\left(\tilde{\eta}_A - \delta\tilde{\eta}_H\sqrt{2+\delta^2}\right), \tag{5.41}$$

which reduces to Equation 4.171 in the ambipolar diffusion limit.

It was shown in subsection 4.3.2 that this equation was a poor match to the similarity solution in which $\tilde{\eta}_A = 1.0$, $\tilde{\eta}_H = 0$ and $v_0 = 0.73$ (Figure 4.9), although it did provide an adequate approximation to the shock position when the initial azimuthal velocity is lower. It is also a poor match for those similarity solutions with both ambipolar and Hall diffusion calculated in this work: although the magnetic diffusion shock positions plotted against the nondimensional Hall diffusion parameter in Figure 5.6 show that the relationship between the two is near-linear, the dashed plot of

estimated parameter	fitted parameter
$c = -0.845$	$c = -0.278$
$d = 0.488$	$d = 0.411$

Table 5.1: As shown in Figure 5.6, the position of the magnetic diffusion shock, x_d, does not follow the linear relationship described in Equation 5.41. Fitting a straight line of the form $x_d = c\tilde{\eta}_H + d$ to the data from the similarity solutions gives the parameters to the fit outlined above (with $\chi^2 = 0.26 \times 10^{-3}$), which are clearly very different to those estimated by Equation 5.41.

Equation 5.41 is clearly a very poor match to the data, as is the dot-dashed plot which shows the result of deriving Equation 5.41 under the assumption that $b_1 = 1$ rather than the value given by Equation 5.39. The solid line is the best linear fit to the data (using an equation of the form $x_d = c\tilde{\eta}_H + d$); the parameters of this fit are given in Table 5.1.

Clearly the linear estimation to the magnetic diffusion shock position given by Equation 5.41 is a poor match to the data from the similarity solutions (with a typical error of $\Delta x_d \approx 20\%$); even the simplified form of this equation with $b = b_z$ is unable to fit the data. A more accurate estimation of the shock position is therefore required, and the largest source of error in this calculation is the approximation to $b_{\phi,s}$ used in $b_{z,high}$ (that $b_{\phi,s} = -\delta b_z$).

On the upstream side of the magnetic diffusion shock $b_{\phi,s} \approx -\delta b_{z,low}$ (as can be seen in the solutions as Section 5.4), however downstream of the shock the azimuthal field component is not equal to $-\delta b_{z,high}$ as was assumed. The magnetic field lines are compressed in the shock resulting in an increase in the vertical field and the azimuthal field as the field lines are twisted up by the slowing of the compressed gas. Conservation of flux ensures that the radial field component does not change in the shock.

The magnetic diffusion shock represents a continuous increase in the magnetic field strength, and though the matter is slowed in the post-shock region, w is near-constant and $w > 1$ throughout the magnetic diffusion shock itself. While the vertical field component increases from $b_{z,low}$ to $b_{z,high}$, the azimuthal component downstream of the shock is given by

$$b_{\phi,sd} \approx w b_{\phi,su} \approx -w\delta b_{z,low}, \tag{5.42}$$

using the subscripts u and d to indicate the upstream and downstream sides of the shock. Equation 5.32 is then substituted into this equation, and this is solved for $b_{\phi,s}$ downstream of the shock:

$$b_{\phi,s} \approx -x_d \delta b_{r,s}. \tag{5.43}$$

As $x_d < 1$ in all of the similarity solutions, $b_{\phi,s} < b_{r,s}$ in this region and there is no

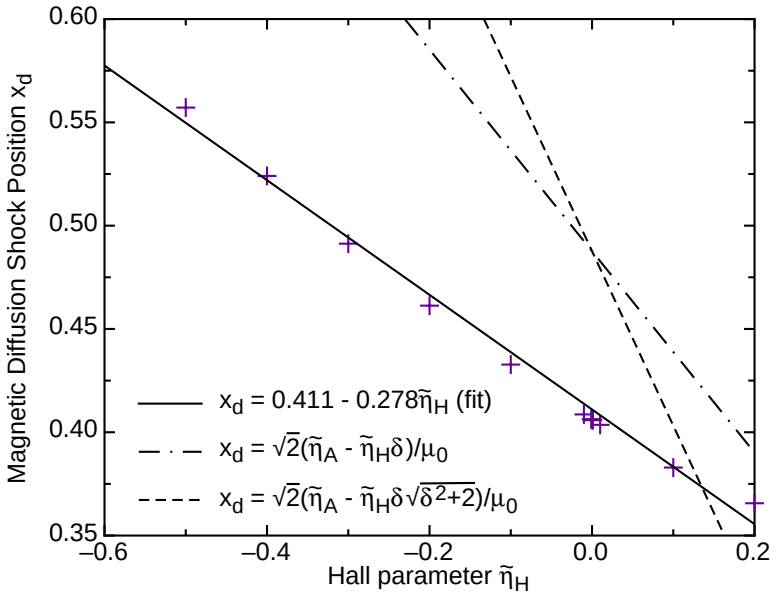

Figure 5.6: The position of the magnetic diffusion shock x_d depends in a seemingly near-linear manner on the nondimensional Hall parameter $\tilde{\eta}_H$; crosses denote the values of the shock position for the solutions tabulated in Table B.2, where $\tilde{\eta}_A = \delta = 1$. The solid line is the best linear fit to this data; the dashed line is that given by Equation 5.41 for these parameters; and the dot-dashed line is a simplified theoretical approximation in which $b_1 = 1$.

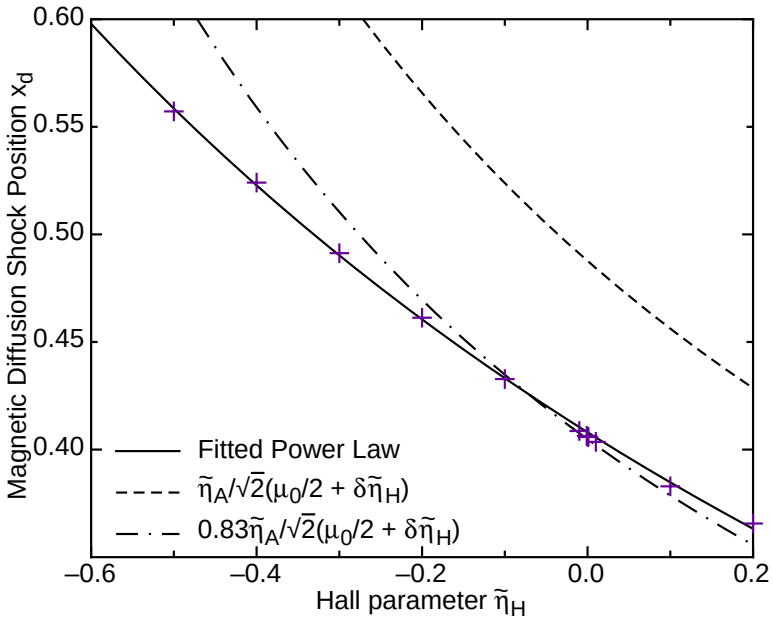

Figure 5.7: As in Figure 5.6 the position of the magnetic diffusion shock x_d from the similarity solutions is plotted as a series of crosses against the nondimensional Hall parameter $\tilde{\eta}_H$ for solutions in which $\tilde{\eta}_A = \delta = 1$. The dashed curve is the estimate to the shock position given by Equation 5.46 for these parameters, while the dot-dashed curve is Equation 5.46 multiplied by the constant 0.83. The solid curve is the best fit of a curve defined by Equation 5.47 to the data, using the parameters in Table 5.2.

estimated parameter	fitted parameter
$c = 0.707$	$c = 0.742$
$d = 1.450$	$d = 1.821$

Table 5.2: As shown in Figure 5.7, a power law of the form described by Equation 5.47 may be fit to the position of the magnetic diffusion shock. The estimated parameters are those for Equation 5.46 for the similarity solutions with $\tilde{\eta}_A = \delta = 1$. The value of $\chi^2 = 6.7 \times 10^{-5}$ suggests that this is a good fit to the data.

need to include the azimuthal field component in the magnetic squeezing; downstream of the shock the disc scale height may still be approximated by Equation 5.37 and the magnitude of the magnetic field (in terms of b_z) is

$$b_1 \approx \sqrt{2}. \tag{5.44}$$

These are then substituted into Equation 5.38 for the downstream vertical field component

$$b_{z,high} \approx \frac{m}{x}\left(\sqrt{2}\tilde{\eta}_A - 2\delta x_d \tilde{\eta}_H\right)^{-1}. \tag{5.45}$$

It is then possible (using the approximation that $b_{z,high} = b_{r,s}$) to rearrange this into a new estimation of the magnetic diffusion shock position

$$x_d \approx \frac{\tilde{\eta}_A}{\sqrt{2}}\left(\frac{\mu_0}{2} + \delta\tilde{\eta}_H\right)^{-1}, \tag{5.46}$$

which again reduces to Equation 4.171 in the ambipolar diffusion limit.

The dashed curve in Figure 5.7 illustrates Equation 5.46; this is a much better fit to the shape of the data from the similarity solutions although it is still an overestimation of the actual magnetic diffusion shock positions which are represented by crosses. Multiplying Equation 5.46 by a constant 0.83 gives an approximation to the magnetic diffusion shock position (shown as the dot-dashed curve in the figure) that is good enough that it may be used in the simple model for calculating the initial value of the variables at x_m; this constant may be assumed to replace some missing physics in this approximation. Table 5.2 compares the derived equation to the parameters for the solid curve of best fit in Figure 5.7, which takes the form

$$x_d \approx c(d + \tilde{\eta}_H)^{-1} \tag{5.47}$$

where c and d are constants; these parameters are similar to their equivalents from the derived estimation to the magnetic diffusion shock position, with the largest different arising in the calculation of the constant c as expected.

The curved approximation to x_d (when multiplied by the constant 0.83) is accurate to within 10% of the true value for all of the data in Figure 5.7, and to within 5%

for $-0.3 \leq \tilde{\eta}_H \leq 0.2$. Even Equation 5.46 without the constant is accurate to within 20% of the true values, which is much better than the linear analytic estimate given by Equation 5.41. It is the nonlinear estimate of x_d (using the factor of 0.83) that is used in the simple model, and in calculating the initial estimate of the centrifugal shock position x_c.

5.3.2 Centrifugal shock position

The presence of Hall diffusion in the model complicates the calculation of the centrifugal shock position as its dependence on the prescription for $b_{\phi,s}$ (Equation 5.2) makes it much more difficult to solve the angular momentum equation (5.6) explicitly, to the point where the method used to estimate x_c in the ambipolar diffusion model is not duplicated in this chapter. Instead, the approximation to the centrifugal shock position from the ambipolar diffusion model is taken and modified to include Hall diffusion in a simplistic manner.

In order to find the centrifugal shock position, the iterative routine requires an estimate of x_c that is accurate to around 20%, as the routine described in subsection 5.2.2 is very flexible and able to cope with most poor initial guesses of this shock position. Starting then with Equation 4.180 for the centrifugal shock in the limit where $\tilde{\eta}_H = 0$,

$$x_c \approx \frac{v_0^2}{A^2} m_c \exp\left[-\sqrt{\frac{2^{3/2} m_c}{\mu_0 \tilde{\eta}_A^3}}\right], \tag{5.48}$$

the nondimensional ambipolar diffusion parameter is replaced by a term $(\tilde{\eta}_A - \delta\tilde{\eta}_H)$ that includes both Hall and ambipolar diffusion, as well as the magnetic braking parameter:

$$x_c \approx \frac{v_0^2}{A^2} m_c \exp\left[-\sqrt{\frac{2^{3/2} m_c}{\mu_0 (\tilde{\eta}_A - \delta\tilde{\eta}_H)^3}}\right]. \tag{5.49}$$

This equation, depicted as the dashed line in Figure 5.8, is a poor match to the shock position data from the similarity solutions (listed in Table B.2).

Although Equation 5.49 gives a position that is typically close enough to the true value that the routine will succeed in finding x_c, a better match to the behaviour of x_c is sought as finding the position of x_c is one of the slower parts of the model to compute. Equation 5.49 can be somewhat improved by multiplying the magnetic diffusion term by the constant 0.83 that was used to improve the determination of x_d; this then gives the equation

$$x_c \approx \frac{v_0^2}{A^2} m_c \exp\left[-\sqrt{\frac{2^{3/2} m_c}{\mu_0 [0.83(\tilde{\eta}_A - \delta\tilde{\eta}_H)]^3}}\right], \tag{5.50}$$

which is shown as the dot-dashed line in Figure 5.8. As can be seen from the plot, this approximation to x_c is only close enough to be used as a first guess in the shock-finding routine when $\tilde{\eta}_H \gtrsim -0.1$.

The remainder of the Hall parameter space is mapped by the linear relation plotted as the dotted line in Figure 5.8, which has the equation

$$x_c \approx -0.156\tilde{\eta}_H + 0.01\tilde{\eta}_A - 0.0025; \tag{5.51}$$

while this approach is simplistic, and required the calculation of a number of similarity solutions before it could be adopted, it provides an acceptable guess of the centrifugal shock position to the iterative routine described in 5.2.2 for solutions with $\tilde{\eta}_H \lesssim -0.1$ (and $\tilde{\eta}_A \approx 1$). This linear relationship is a more refined form of the linear extrapolation (from the two closest solutions in $\tilde{\eta}_H$-space) that was used to estimate the shock position before an analytic estimate was available.

All of the shocks that require explicit calculation of the jump conditions share the same set of jump conditions, which are outlined in the following subsection.

5.3.3 Jump conditions

As in the first ambipolar diffusion solution of Chapter 4, the magnetic diffusion shock in these similarity solutions is smooth and continuous, and does not require any explicit calculation of shock conditions. The shock itself is a transition between the two approximations to the vertical field component, $b_{z,low}$ and $b_{z,high}$, and in the shock front only b_z, $b_{\phi,s}$ and h are changed, with $b_{\phi,s}$ downstream of the shock given by $b_{\phi,s} \approx -wx_d\delta b_{z,low}$ (see Figure 5.4 and subsection 5.3.1). At the shock h is dramatically compressed, suggesting that a breakdown of the vertical hydrostatic equilibrium occurs at this point. In reality, the enhanced magnetic squeezing during the shock front is unable to reduce the disc thickness so dramatically over the fluid transit time through the shock, and the magnetic pressure far exceeds the gas pressure so that any breakdown of isothermality would not greatly affect the collapse.

On the other hand, the jump conditions at the centrifugal shock must be explicitly calculated at the position found using the iterative routine described in subsection 5.2.2. The shock conditions at x_c are those derived in Section 4.1 for the nonmagnetic solutions; these were found by integrating the conservation of mass and radial momentum equations (5.4 and 5.5) at the shock position to give the relations

$$\sigma w = \text{constant} \tag{5.52}$$

$$\text{and } \sigma\left(w^2+1\right) = \text{constant}. \tag{5.53}$$

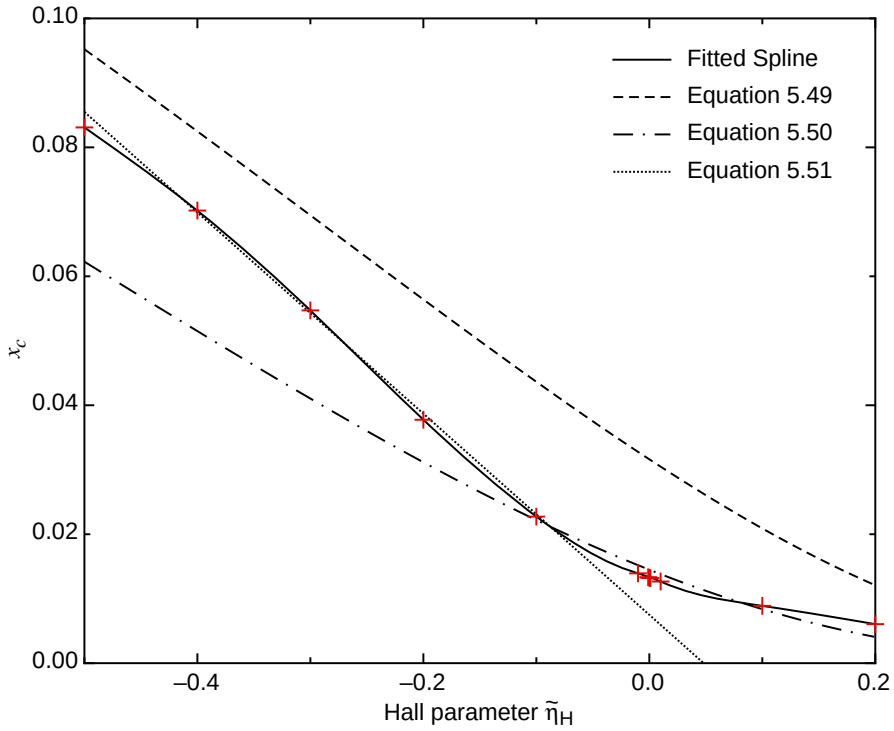

Figure 5.8: The positions of the centrifugal shock position x_c are plotted against the nondimensional Hall parameter $\tilde{\eta}_H$ for similarity solutions in which $\tilde{\eta}_A = \delta = 1$. The dashed curve is the estimate to the shock position given by Equation 5.49 for these parameters, while the dot-dashed curve is Equation 5.50 and the dotted line is the linear relation given in Equation 5.51.

These equations are then solved simultaneously to give the non-trivial solution to the jump conditions

$$w_d = \frac{1}{w_u} \tag{5.54}$$

$$\text{and } \sigma_d = \sigma_u w_u^2, \tag{5.55}$$

where u and d denote the upstream and downstream sides of the shock.

The magnetic field strength does not change at the centrifugal shock front itself, as the magnetic pressure and tension terms are not large enough during the shock transition to change the field behaviour, however it typically increases in the regions immediately interior to the shock as the other variables settle to their asymptotic values. The centrifugal shock is the boundary of the rotationally-supported disc and as the position of this shock depends on the Hall diffusion parameter so too does the strength of the shock, with stronger shocks occurring with increasing Hall parameter. The increased magnetic diffusion can also cause the formation of subshocks — rings of sharply-enhanced density in the post-centrifugal shock region — as the outward-

boundary condition	value	parameter	value
μ_0	2.9	$\tilde{\eta}_A$	1.0
v_0	0.73	δ	1.0
u_0	-1	α	0.08
A	3		

Table 5.3: Boundary conditions and parameters for all the Hall similarity solutions presented in this chapter, and those in Appendix C.

moving flux causes the infalling gas to be slowed.

The jump conditions defined in Equations 5.54 and 5.55 are also used for any subshocks that may be encountered downstream of the principal shocks. Although the magnetically-squeezed jump conditions defined in Section 4.2 could be applied at the magnetic diffusion subshock, they produce numerically similar results to the jump conditions defined above and so no benefit was seen to adding this complexity to the code. The second set of jump conditions derived in Section 4.2 only apply when IMHD holds true and could not be used for any of the subshocks encountered in this model, as magnetic diffusion is always active near to the shock fronts.

Having summarised the behaviour, jump conditions and the ways in which both the principal and subshocks affect the numerical routines that integrate the ordinary differential equations that define the self-similar collapse problem, it is now possible to calculate the similarity solutions.

5.4 Hall Solutions

Superficially, the similarity solutions within this section appear to be similar to those of the ambipolar diffusion model in Section 4.3. They all have the same parameters and boundary conditions, outlined in Table 5.3, which match those in Figure 4.9 and figure 7 of Krasnopolsky and Königl (2002). The nondimensional ambipolar diffusion parameter is held constant at $\tilde{\eta}_A = 1.0$, as is the cap on the magnetic braking $\delta = 1.0$ and the magnetic braking parameter $\alpha = 0.08$, so that the only changes between the similarity solutions presented here and the ambipolar diffusion-only solution in Figure 4.9 are those wrought by the addition of Hall diffusion. The values of the variables at the matching point x_m for a selection of similarity solutions are given in Table B.3; interpolating between these it is possible to obtain a good initial guess of the variables for the calculation of a similarity solution with any value of the Hall parameter $\tilde{\eta}_H \in [-0.5, 0.2]$.

The first of these similarity solutions is that presented in Figure 5.9 for the self-similar collapse of a molecular cloud with $\tilde{\eta}_H = -0.2$. Those similarity solutions that

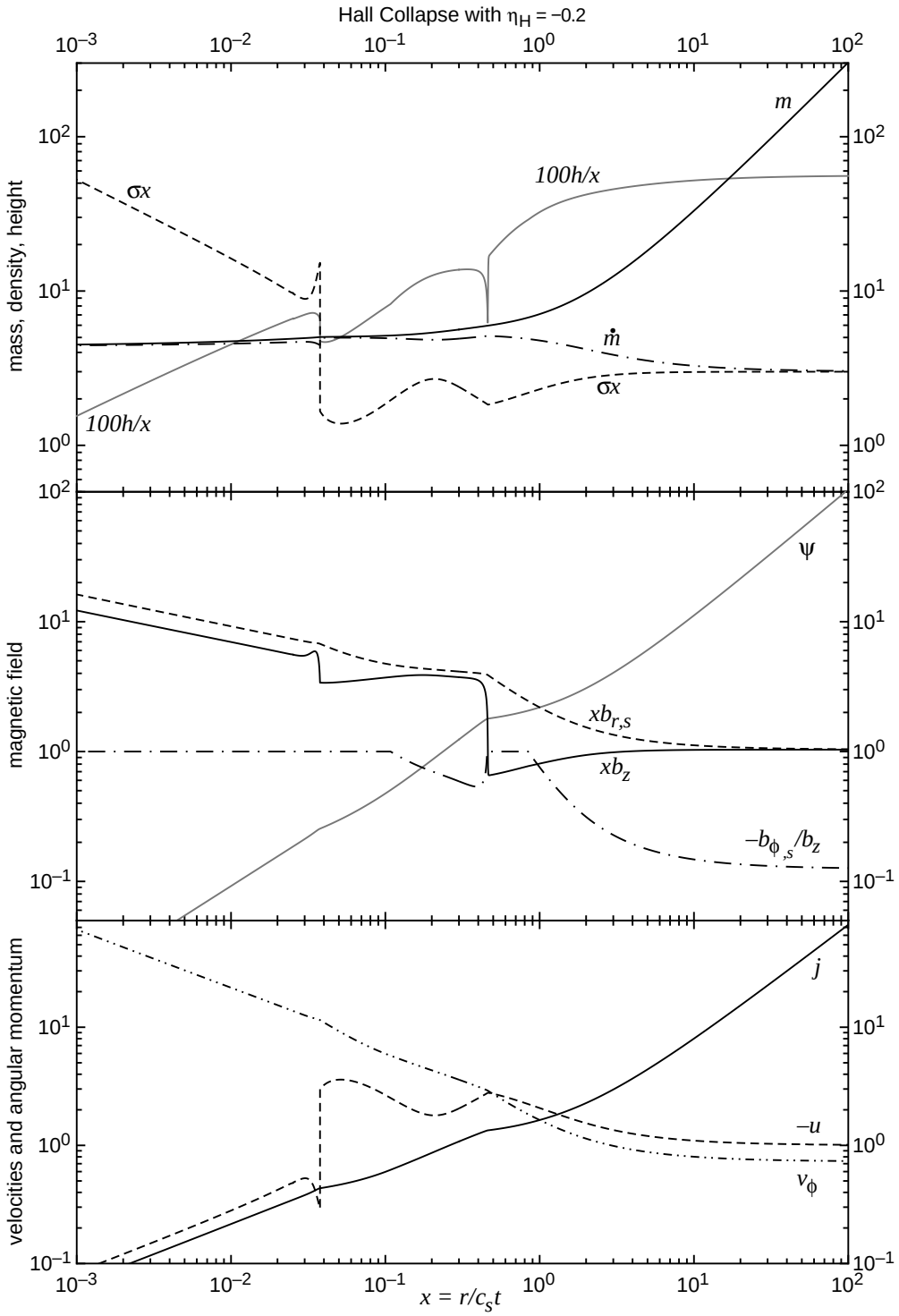

Figure 5.9: Similarity solution for Hall collapse with $\tilde{\eta}_H = -0.2$. The displayed variables are the same as those in Figure 4.9; the parameters and boundary conditions are given in Table 5.3. The nondimensional central mass is $m_c = 4.23$; the magnetic diffusion and centrifugal shocks are located at $x_d = 0.461$ and $x_c = 3.78 \times 10^{-2}$ respectively; both of these have increased from the non-Hall positions, and the post-shock regions have been smoothed by the presence of Hall diffusion.

possess a negative Hall parameter have more radial diffusion of the magnetic field against the neutral fluid and the charged grains (see the induction equation, 5.1), so that the magnetic pressure builds up much earlier in the collapse process, triggering the formation of the magnetic diffusion shock. The negative Hall parameter also increases the initial rate of magnetic braking (by increasing the first term in the brackets of Equation 5.2) so that $b_{\phi,s}$ attains its capped value much earlier in the collapse, and the magnetic braking is then determined by the strength of the vertical field component (see the right term in the brackets of Equation 5.2).

As in the previous solutions, at the outer edge of the collapse the matter is falling in supersonically under IMHD, bringing the magnetic field with it. As the surface density builds up the field does so too, causing the magnetic pressure terms to become important, while the magnetic braking transports angular momentum from the infalling gas to the external envelope by twisting the magnetic field lines. The angular momentum and enclosed mass start to plateau as the dominant force on the radial velocity changes between the self-gravity of the disc and the gravity of the central mass, which in turn causes the accretion rate to taper off. The formation of the magnetic diffusion shock at $x_d = 0.461$ (*cf.* $x_d = 0.406$ in the ambipolar diffusion similarity solution with the same parameters) is caused by the decoupling of the field from the neutral particles.

The magnetic diffusion shock in this solution is weaker than that in Figure 4.9 as most of the neutral particles and the grains have already been decoupled from the magnetic field, so that the vertical field component increases by only 4.5 times (as opposed to 6.2 times in Figure 4.9). The scale height is less compressed by the field, producing a thinner shock, while $b_{\phi,s}$ does not grow rapidly under the build up of flux and braking in the shock. Within the shock the field is further decoupled from the neutral particles and charged grains, allowing Hall and ambipolar diffusion to become more important downstream of the shock and throughout the remainder of the solution. The field lines straighten as in Figure 4.10; although the radial field component is still dominant, the vertical component increases in the shock until it is just smaller than $b_{r,s}$.

Downstream of the magnetic diffusion shock the surface density gradually increases as the infall velocity is slowed by the increased magnetic support. This post-shock region is smoother than that without Hall diffusion, presenting a gentler transition to the free fall collapse that occurs outside of the rotationally-supported disc. The vertical field scales with x^{-1} during the post-magnetic diffusion shock region as the increased radial magnetic diffusion means that there are fewer field lines in total moving against the flow of the neutral particles. In this region the disc scale height is dominated by the magnetic squeezing; the gravity of the central mass becomes the most important radial force on the gas at the end of the post-shock region (the peak in the surface

density) and the matter is accelerated inwards until it is in near-free fall collapse. The magnetic braking decreases the angular momentum rapidly until $b_{\phi,s}$ attains its capped value and j begins to plateau once more.

The centrifugal force builds up as the matter falls inwards until it exceeds the gravitational force, triggering the formation of the centrifugal shock at $x_c = 3.78 \times 10^{-2}$ (*cf.* $x_c = 1.32 \times 10^{-2}$ in Figure 4.9). This shock is a discontinuity in the surface density and the radial velocity, which is again less strong than that in the solution without Hall diffusion, and inwards of this the vertical and azimuthal field components increase steeply throughout the post-shock reaction of the field (although $b_{\phi,s}$ remains capped at $-\delta b_z$). Downstream of the centrifugal shock the variables tend (with overshoots in b_z) towards their asymptotic values.

The inner disc is in Keplerian rotation and satisfies Equations 5.12–5.23 for the given parameters. The central mass is given by $m_c = 4.42$, which is decreased from the non-Hall solution (*cf.* $m_c = 4.67$) and corresponds to an accretion rate onto the central star of $\dot{M}_c = 7.21 \times 10^{-6}$ $\mathrm{M}_\odot$ yr^{-1}. The scalings with respect to x of the other variables are the same as in Figure 4.9 (see Section 5.1), however the surface density is increased by the changed magnetic diffusion parameter $f = 1.72$ (compared to $f(\tilde{\eta}_H = 0) = 1.\dot{3}$) and the increased radial magnetic diffusion causes the strength of the magnetic field threading the disc to be decreased from that in the ambipolar diffusion-only solution. This in turn means that less matter can lose its angular momentum by magnetic braking and fall onto the central mass, so that the gas is at a higher surface density in this larger Keplerian disc.

The next similarity solution, presented in Figure 5.10, shows the results of a calculation with $\tilde{\eta}_H = -0.5$ on the same scale and with the same parameters as Figure 5.9. The total radial magnetic diffusion is further increased in this solution so that many of the neutral particles have decoupled from the field before the diffusion shock; this causes the intensity of the magnetic diffusion shock at $x_d = 0.557$ to drop further so that the increase in the vertical field strength is only 4 times its original value. There is less of a magnetic wall at this point as less of the field needs to be decoupled from the neutrals within the shock itself.

As in the previous solution with a negative Hall parameter the post-magnetic diffusion shock region is smoothed, with even less change occurring to the surface density and radial infall. The gas is still somewhat slowed by the magnetic diffusion shock, but the gravity of the central mass quickly overcomes this and pulls the fluid inwards. The radial velocity downstream of the post-shock region is accelerated as the fluid nears the protostar, however it remains below the free fall velocity at all times. The mass and angular momentum both plateau in this region before the increasing centrifugal force causes the formation of the centrifugal shock.

The centrifugal shock occurs earlier in this similarity solution at $x_c = 8.31 \times 10^{-2}$, which is a large increase over that in the $\tilde{\eta}_H = -0.2$ similarity solution. This change is brought about by the decreased values of b_z and $b_{\phi,s}$ in the free fall region, which reduce the amount of magnetic braking that takes place and cause the centrifugal force to become important earlier in the collapse. Inwards of this shock is a much wider post-shock region of adjustment in which the variables tend towards the inner disc solution.

The Keplerian disc in this similarity solution is substantially larger than that in the previous solution, containing $\sim 38\%$ of the mass of the central protostar. The surface density of this disc has also increased as the magnetic diffusion parameter $f = 2.31$, while the lowered central mass $m_c = 3.77$ corresponds to an accretion rate of $\dot{M}_c = 6.15 \times 10^{-6}$ $\mathrm{M}_\odot$ yr^{-1} onto the central star. Again, the larger disc corresponds to a lower accretion rate, as the reduced magnetic braking makes it more difficult for the fluid to lose rotational support and fall inwards.

The final similarity solution presented in this chapter is that with $\tilde{\eta}_H = +0.2$ in Figure 5.11, which is the most dynamically different solution from the ambipolar diffusion solutions in Chapter 4. Although the initial conditions and parameters remain the same as in the previous solutions, the change in the sign of the Hall parameter, which corresponds to a reversal of the orientation of the initial magnetic field with respect to the direction of rotation, introduces many changes to the collapse dynamics.

These begin at the magnetic diffusion shock, which is located inwards of the position for the $\tilde{\eta}_H = 0$ solution in Figure 4.9 at $x_d = 0.366$. This shock is of increased intensity due to the reduced radial magnetic diffusion prior to the passage of the shock, which causes a larger increase in b_z in the shock front. The magnetic braking downstream of the shock is increased by the presence of a stronger field and the sign of the Hall term in the expression for $b_{\phi,s}$ (5.2). The disc is more sharply compressed as the field lines straighten at the shock front, and the fluid is so slowed by the increase in the magnetic pressure that a second shock front forms at $x_{d2} = 0.260$.

In the magnetic diffusion subshock, which was shown at higher resolution in Figure 5.4 and described in subsection 5.2.3, the fluid is abruptly slowed until the radial velocity is low and subsonic. The surface density increases under the jump conditions given in Section 5.3.3; this ring of matter contains approximately 18% of the mass in the central protostar. The azimuthal field component and the disc scale height also increase in the subshock, while the derivative db_z/dx decreases steeply. The infall region downstream of the subshock is much wider in logarithmic similarity space than in the previous solutions, with the increased magnetic braking reducing the angular momentum more rapidly as the radial velocity increases under the gravitational pull of the central mass. The surface density drops as the fluid rapidly falls in and magnetic

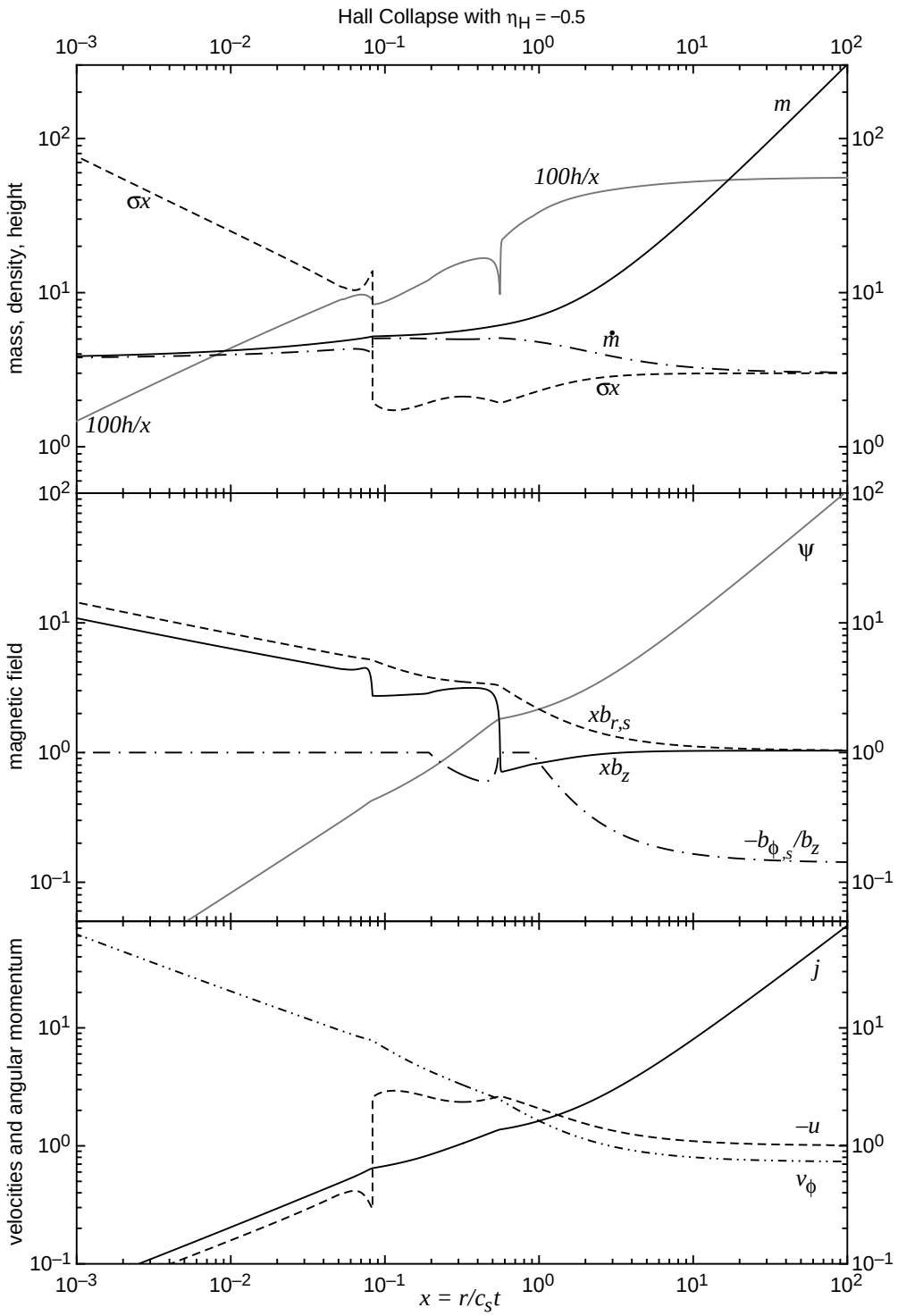

Figure 5.10: Similarity solution for Hall collapse with larger negative Hall parameter $\tilde{\eta}_H = -0.5$. The boundary conditions and parameters match those in Figure 5.9 (see Table 5.3). In this similarity solution the nondimensional central mass is reduced to $m_c = 3.77$; the magnetic diffusion and centrifugal shocks have moved outwards to $x_d = 0.557$ and $x_c = 8.31 \times 10^{-2}$ respectively; and the increased radial magnetic diffusion has smoothed the post-shock regions and increased the size of the inner Keplerian disc.

squeezing dominates the vertical compression until the gravity of the central mass takes over near to the centrifugal shock.

The centrifugal shock occurs at $x_c = 6.05 \times 10^{-3}$, half that of the $\tilde{\eta}_H = 0$ solution, dramatically decreasing the size of the rotationally-supported disc. This change is brought about by the increased magnetic braking caused by the positive Hall term, which reduces the angular momentum so that the centrifugal force cannot become dynamically important until the gas is very close to the protostar. The centrifugal shock is followed by another subshock at $x_{c2} = 5.21 \times 10^{-3}$, which was shown in more detail in Figure 5.5 and also described in subsection 5.2.3. Upstream of this shock the fluid is rapidly accelerated inward as the magnetic field increases in the very thin region between the two shocks, forcing further magnetic braking and a rapid drop in the centrifugal force. The surface density drops as the radial velocity becomes supersonic once more, and as the fluid nears the protostar the centrifugal force becomes important once more — triggering the formation of the subshock. At the subshock discontinuity the matter is slowed until the infall rate is low and subsonic once more.

Downstream of the subshock, the variables settle with overshoots to the asymptotic disc behaviour. The central mass is given by $m_c = 4.63$, which corresponds to an accretion rate onto the central star of $\dot{M}_c = 7.53 \times 10^{-6}$ $\mathrm{M}_\odot$ yr^{-1}, and the small Keplerian disc contains only 1.6% the mass of the central disc. The magnetic diffusion parameter in this disc is $f = 0.945$, decreasing the surface density in the disc as the strength of the magnetic field is increased.

The magnetic diffusion and centrifugal subshocks both occur only in those solutions in which $\tilde{\eta}_H$ is positive, where the increased magnetic pressures and braking caused by the increase in the magnetic field falling inwards force the gas to rapidly change in radial velocity and density. The number of subshocks downstream of the principal centrifugal shock increases with increasing $\tilde{\eta}_H$ — three subshocks have been observed in one similarity solution that was not properly converged at the time of publication. The restriction that $f > 0$ (see Chapter 3) also limits the range of positive $\tilde{\eta}_H$ that can be explored; as $\tilde{\eta}_H$ increases, the size and surface density of the rotationally-supported disc decrease, and the rings of gas formed by the subshocks are likely to be gravitationally unstable.

The inclusion of Hall diffusion into the calculations causes many changes to the dynamics of gravitational collapse, with the sign of $\tilde{\eta}_H$ introducing or suppressing the formation of subshocks downstream of the principal shocks. The intensity and position of these shocks change with the Hall parameter, as does the mass of the central protostar. Additional similarity solutions with $\tilde{\eta}_H \in [-0.5, 0.2]$ that demonstrate these trends in more detail are presented in Appendix C.

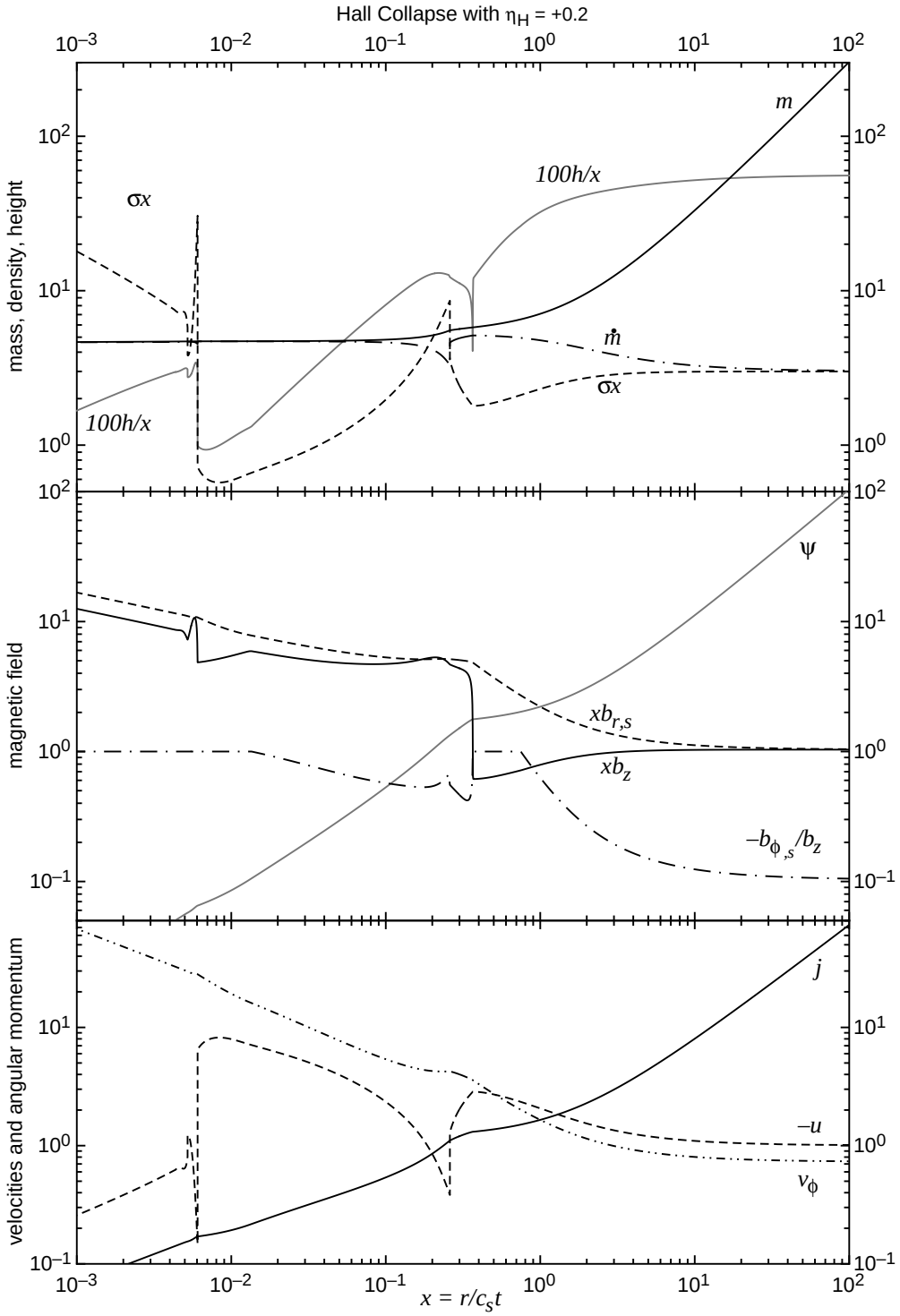

Figure 5.11: Similarity solution for gravitational collapse with positive Hall parameter $\tilde{\eta}_H = +0.2$. The boundary conditions and parameters otherwise match those in Figure 5.9 and Table 5.3; the nondimensional central mass is $m_c = 4.63$. The positive Hall term causes the formation of subshocks downstream of the principal shocks: the magnetic diffusion shocks are located at $x_d = 0.365$ and $x_{d2} = 0.260$; the centrifugal shocks at $x_c = 6.05 \times 10^{-3}$ and $x_{c2} = 5.21 \times 10^{-3}$.

5.5 Summary

Building on the work of the previous chapter, this chapter oversaw the calculation of similarity solutions to the MHD equations for gravitational collapse including Hall and ambipolar diffusion. Hall diffusion introduces new subshocks and sonic points downstream of the shocks (where the radial speed changes between being sub- and supersonic), as seen in Figure 5.12, requiring a more complicated approach to finding the similarity solutions. A simplified model for calculating the initial guess of the values of the variables at the matching point and the model used for performing the innermost integration were presented, as were the analytic expressions for the initial guesses of the magnetic diffusion and centrifugal shock positions. Finally a number of similarity solutions with initial conditions identical to those of the first ambipolar diffusion-only similarity solution were discussed, showing the importance of Hall diffusion to the collapse dynamics.

The presented similarity solutions showed that Hall diffusion has a profound effect on the complexity of the solution, depending on the orientation of the magnetic field with respect to the rotational axis. When the Hall parameter $\tilde{\eta}_H$ was negative, Hall diffusion smoothed the post-shock regions, and the solutions matched onto the inner disc solution with fewer overshoots. The magnetic diffusion in the radial direction was increased, so that the magnetic diffusion shock formed much earlier in the collapse; this shock was less strong than in the solution without Hall diffusion with smaller changes to b_z and h, and the post-shock slowing of the radial velocity was also weakened. Similarly, the reduced magnetic braking caused $b_{\phi,s}$ to attain its capped value much earlier in the collapse, causing the centrifugal force to become dynamically important sooner and triggering the formation of a larger rotationally-supported disc, as shown in Figure 5.12 which demonstrates the relationship between the shock positions and $\tilde{\eta}_H$. As accretion through the Keplerian disc is slow, larger discs tend to correlate with lower accretion rates onto the protostar.

On the other hand, when the Hall parameter was positive the similarity solutions were complicated by the introduction of subshocks driven by the addition of Hall diffusion. The increased magnetic pressure caused by the reduced radial magnetic diffusion enhanced the strength of the principal shocks and caused them to occur much later than in the non-Hall similarity solutions. The azimuthal magnetic field component $b_{\phi,s}$ reached its capped value much later in the collapse process, changing the behaviour of the angular momentum so that the size of the innermost Keplerian disc was much reduced from that in the similarity solution with no Hall diffusion. The smaller rotationally-supported disc surrounded a larger protostar, as the increased magnetic braking allowed more gas to lose its angular momentum and fall onto the

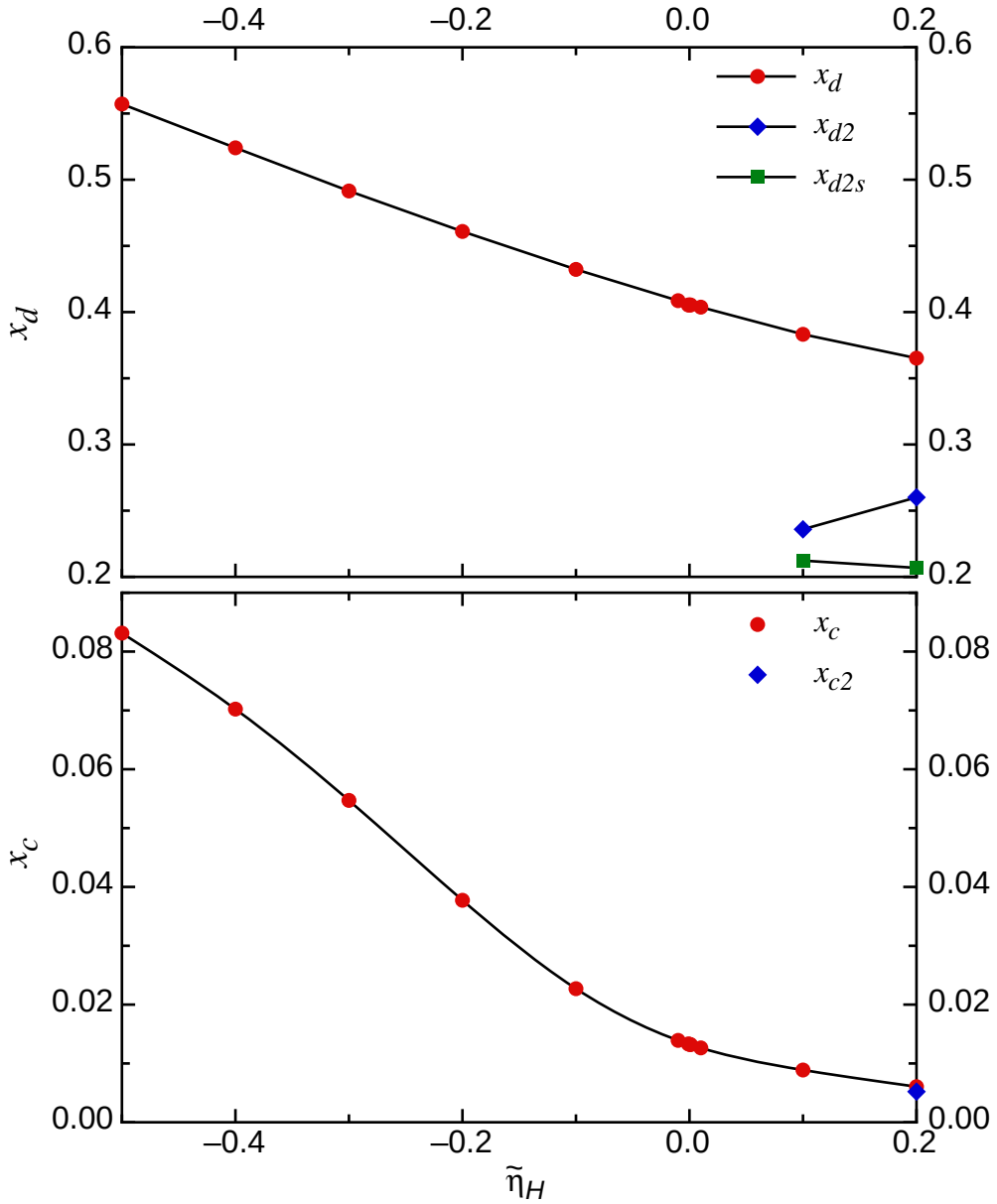

Figure 5.12: The relationship between the shock positions and the nondimensional Hall parameter $\tilde{\eta}_H$. The top panel shows the position of the magnetic diffusion shock x_d, which decreases as $\tilde{\eta}_H$ becomes more positive, as well as the position of the subshock x_{d2} and its associated sonic point x_{d2s}. The lower panel shows the position of the centrifugal shock x_c, which also decreases with increasing $\tilde{\eta}_H$, and the position of the subshock at x_{c2} for the similarity solution with $\tilde{\eta}_H = +0.2$, which is the only solution that possesses a subshock to the centrifugal shock. The sonic point between the centrifugal shock and subshock is not plotted due to the resolution of this graph. All of the similarity solutions have initial conditions matching those in Table 5.3, values of the variables at x_m and shock positions as described in Appendix B, and are plotted individually in Appendix C.

protostar.

The accretion rate and the size of the rotationally-supported disc both depend upon the Hall parameter; this relationship shall be discussed further in the following chapter. The importance of the sign of the Hall term with respect to the axis of rotation shall be analysed in the context of the magnetic braking catastrophe and potential future observations of young stellar objects.

Chapter 6

Discussion and Conclusions

The similarity solutions have shown clearly that Hall diffusion changes the structure and dynamics of the collapse of molecular cloud cores into protostars and protostellar discs. The size of the rotationally-supported disc and the accretion rate onto the protostar are determined by the ratio of the Hall and ambipolar diffusivities, which influences the amount of magnetic braking affecting the rotation of the collapsing core. It is also clear that Hall diffusion can inhibit disc formation by enhancing the magnetic braking, or by counteracting ambipolar diffusion to the point that the field starts to infall faster than the fluid, increasing the magnetic pressure. These behaviours depend both upon the size of the Hall parameter and its sign (which represents the orientation of the field with respect to the direction of rotation and that of the Hall current).

This final chapter explores the trends that exist between the similarity solutions in Chapters 4 and 5, and those in Appendix C, and contrasts these results with simulations from the literature in Section 6.1. The results show that there is a preferred handedness to the combination of the magnetic field alignment, the sign of the Hall diffusivity and the axis of rotation in disc formation calculations, which could be observed using new instruments such as ALMA. The role of Hall diffusion in resolving the magnetic braking catastrophe is expounded in Section 6.2, and the Hall effect is shown to induce rotation in initially nonrotating collapsing cores.

Options for future work will be outlined in Section 6.3 — these include improving upon the limitations and assumptions of the self-similar model; adopting alternative scalings of the Hall diffusivity η_H as functions of the similarity variable x; and further explorations of the influence of Hall diffusion on the rotation of the collapsing gas. Large regions of parameter space remain unexplored, as the similarity solutions in this work differed only in the magnitude of the Hall parameter, while keeping the initial angular momentum, density and ambipolar diffusion parameters constant. Several directions for further explorations of parameter space are considered, as well as

$\tilde{\eta}_H$	Σ (g cm^{-2})	B_z (G)	M_c (M$_\odot$)	M_{disc} (M$_\odot$)	R_c (AU)
-0.2	$1,920$	0.289	7.21×10^{-2}	9.99×10^{-3}	15.10
0	$1,250$	0.299	7.62×10^{-2}	3.75×10^{-3}	5.31
0.2	620	0.304	7.54×10^{-2}	1.24×10^{-3}	2.43

Table 6.1: Values of the surface density and vertical field component in the Keplerian disc at $r = 1$ AU and $t = 10^4$ years, as well as the mass of the central object and the size and mass of the rotationally-supported disc at the same time, for the similarity solutions depicted in Figure 6.1. The masses and the centrifugal shock radius all increase linearly with time, while the surface density $\Sigma \propto t^{1/2}$ and the vertical magnetic field is $B_z \propto t^{1/4}$.

alternate methods for modelling the vertical angular momentum transport, which was here limited by the cap on the azimuthal field. Finally, a summary of the results and their astrophysical implications are discussed in Section 6.4.

6.1 Star Formation and the Hall Effect

The dependence of the similarity solutions upon the orientation of the magnetic field and the sign of the Hall diffusion parameter $\tilde{\eta}_H$ (more specifically upon the sign of $\tilde{\eta}_H(\mathbf{B}\cdot\Omega)$, although in this work only the sign of the Hall diffusion parameter is altered) gives rise to two different patterns of collapse behaviours. Three similarity solutions, with $\tilde{\eta}_H = 0, \pm 0.2$ (originally plotted in nondimensional form in Figures 4.9, 5.11 and 5.9 respectively) are converted to dimensional form and plotted against the radius r (at a time $t = 10^4$ years) in Figure 6.1, with the surface density Σ plotted in the upper panel and the vertical magnetic field strength plotted as rB_z in the lower. The three curves in each panel have the same outer boundary conditions and parameters (listed in Table 5.3), and the surface density and vertical field strength (at $r = 1$ AU), as well as the central mass, and the mass and size of the inner disc (all at $t = 10^4$ years) of the solutions are listed in Table 6.1. The outer regions of the collapse are near-identical, as the collapse is dominated by IMHD (so that diffusion is not important) and it is only near the magnetic diffusion shock at $r \approx 100$ AU that the changes brought on by Hall diffusion become apparent.

The dotted blue lines in Figure 6.1, corresponding to the negative Hall solution in Figure 5.9, show the formation of a large rotationally-supported disc that has a radius $R_c \approx 12$ AU at $t = 10^4$ years, and the highest inner Keplerian disc surface density of all the solutions. The dashed black lines are the $\tilde{\eta}_H = 0$ ambipolar diffusion-only solution from Figure 4.9, which possesses a disc half the size of the negative Hall solution. The surface density of the Keplerian disc in this solution is decreased from that in the

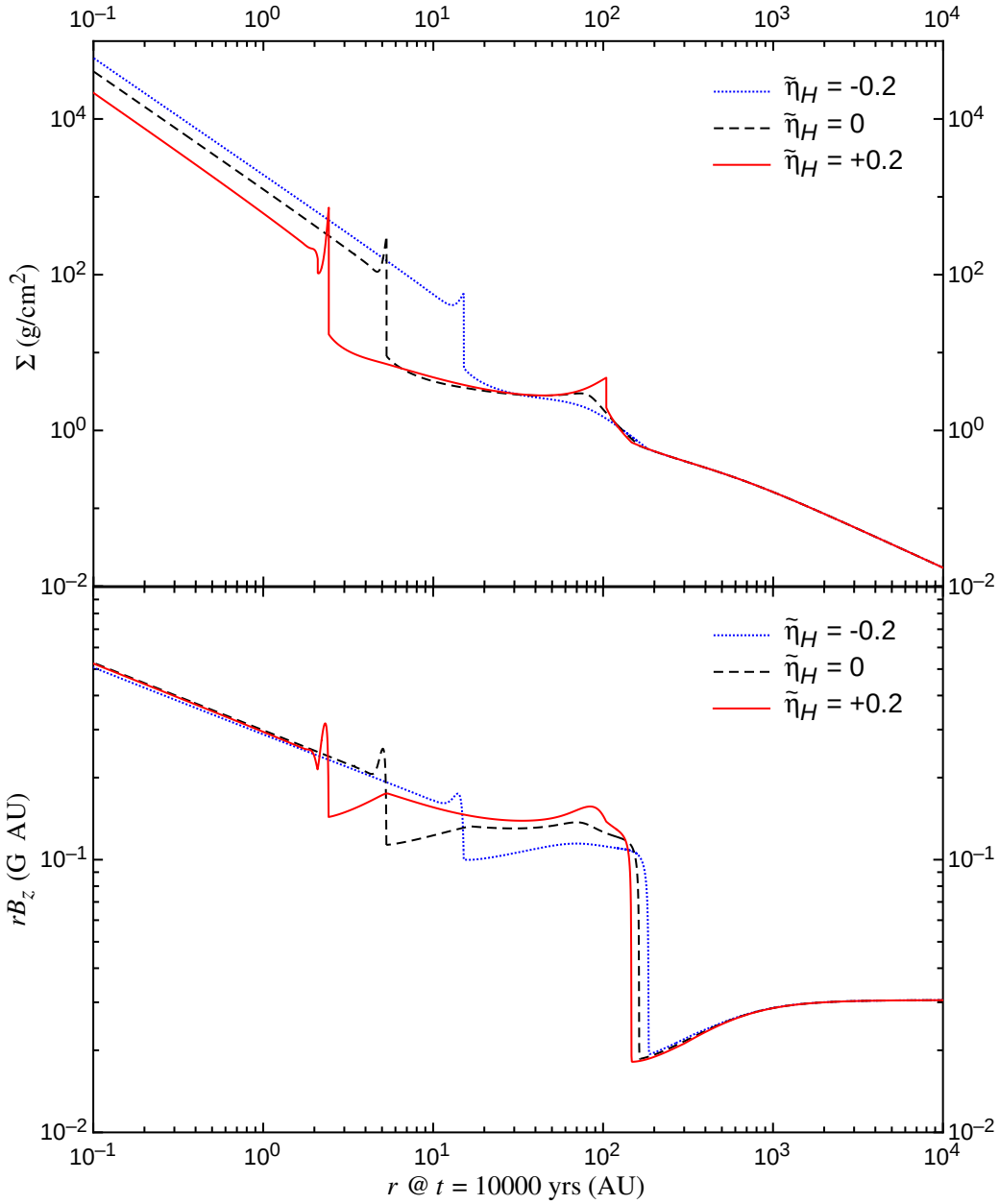

Figure 6.1: The surface density Σ and the vertical magnetic field component B_z (more specifically rB_z) plotted against radius at $t = 10^4$ yr for the similarity solutions with $\tilde{\eta}_A = 1.0$ and $\tilde{\eta}_H = -0.2$ (dotted blue line), 0 (black dashed line) and +0.2 (solid red line). These solutions were plotted individually in nondimensional form against x in Figures 5.9, 4.9 and 5.11 respectively.

negative Hall solution by a constant factor as the accretion rate increases (this change in $\dot{M}_c$ is discussed below). Finally, the solid red curves characterise the similarity solution with a positive Hall parameter $\tilde{\eta}_H = 0.2$ (illustrated in Figure 5.11) which has a Keplerian disc that is almost an order of magnitude smaller than that in the equivalent negative Hall case. This disc is bounded by a thin ring of enhanced density, which rapidly drops off as the magnetic field peaks; the material is then shocked again and comes to match onto the inner solution. The density in this smaller disc is much lower than in the previous solutions, and the disc grows at a much slower rate.

The similarity solutions span many orders of magnitude in both radius and density, and the inclusion of a Hall parameter that is only 20% that of the ambipolar diffusion parameter has a large effect on the behaviour of the magnetic field. In the radial direction, the drift of the field lines with respect to the fluid takes place with velocity

$$V_{Br} = \frac{1}{H}\left[\frac{\eta_H}{B}\,B_{\phi,s} + \frac{\eta_P}{B^2}\left(B_{r,s} - H\frac{\partial B_z}{\partial r}\right)B_z\right]. \tag{6.1}$$

In the intermediate region between the magnetic diffusion shock (at $R_d \approx 100$ AU in Figure 6.1) and the centrifugal shock ($R_c \approx 1 - 10$ AU), when $\tilde{\eta}_H$ is negative, the azimuthal field tension causes the Hall drift to enhance the radial diffusion of the field lines. This torque creates a radial force on the infalling neutral particles that slows the infall speed. The magnetic diffusion shock occurs earlier in the collapse and is less dynamic, that is, there is less of an increase in B_z than in the other solutions, as much of the field has already been decoupled from the fluid.

However, when $\tilde{\eta}_H$ is positive then Hall diffusion acts to reduce the net radial diffusion, resulting in magnetic walls and subshocks that disrupt the flow. The magnetic field carried in towards the protostar increases, and the magnetic pressure and tension terms remain important throughout the collapse. Any twist in the field lines causes an increase in the magnetic pressure gradient, so that the net amount of radial diffusion drops off as the magnetic braking slows the rotation by twisting the field above the pseudodisc.

There is a similar duality to the azimuthal field drift, which occurs with a drift velocity as defined in Equation 2.83:

$$V_{B\phi} = -\frac{1}{H}\left[\frac{\eta_H}{B}\left(B_{r,s} - H\frac{\partial B_z}{\partial r}\right) - \frac{\eta_P}{B^2}\,B_z B_{\phi,s}\right]. \tag{6.2}$$

Again looking at the intermediate regions between the two shocks, when $\tilde{\eta}_H$ is negative the bracketed terms, which are proportional to the vertically integrated component of the current density, cause the Hall drift in the azimuthal direction, which twists up the field lines in the pseudodisc and creates a leading torque on the neutral rotation. The reduced value of B_z in this region causes the azimuthal field component to reach

its capped value $B_{\phi,s} = -\delta B_z$ sooner in the collapse, and the magnetic braking, which depends upon $B_z B_{\phi,s}$, is also reduced. Because of this, less angular momentum is removed from the pseudodisc, causing the centrifugal force to become dynamically important earlier and a larger rotationally-supported disc to form.

In the other orientation, that is, when $\tilde{\eta}_H$ is positive, Hall and ambipolar diffusion act together to untwist the field lines in the pseudodisc. In these similarity solutions B_z is larger, and so while it takes longer for $B_{\phi,s}$ to achieve its capped value there is more total magnetic braking and the angular momentum is further reduced. A smaller Keplerian disc forms due to the reduced centrifugal force, and both shocks have subshocks where the magnetic forces alter the radial velocity of the fluid. Downstream of the magnetic diffusion shock the radial magnetic pressure gradient causes the fluid to be slowed in the radial and azimuthal directions, while downstream of the centrifugal shock the gas is accelerated inward as the increase in B_z causes a burst of magnetic braking that disrupts the disc and causes the formation of a subshock.

While the angular momentum behaviour between the magnetic diffusion and centrifugal shocks is changed by the inclusion of Hall diffusion, the cap on $B_{\phi,s}$ acts to ensure that the angular momentum in the inner disc is that expected for a Keplerian disc. The cap, while physically motivated, replaces unspecified disc physics such as reconnection, a disc wind, or turbulence, which would act to prevent the azimuthal field component from greatly exceeding the vertical component; the magnitude at which it ought to act to limit $B_{\phi,s}$ is uncertain. It is also unclear if such limiting of the azimuthal field component happens in real collapsing cores, and the numerical simulations illustrating disc formation that are discussed in the next section do demonstrate tightly-wound magnetic fields (e.g. Machida et al., 2008a). The azimuthal field cap limits the similarity solution set explored in the previous chapter to those in which discs form, however despite this Hall diffusion has been shown to restrict disc formation if the Hall diffusion is too strong in comparison to ambipolar diffusion and $\tilde{\eta}_H$ has the "wrong" sign.

It is in the region between the magnetic diffusion and centrifugal shocks that the influence of Hall diffusion on the field behaviour becomes more obvious in this comparison. In the negative Hall solution this region is characterised by a steady increase in B_z with decreasing r, while the surface density gradually varies, decreasing near both shocks where the radial velocity is high. In the ambipolar diffusion-only solution the peak in Σ interior to the magnetic diffusion shock is sharpened, and causes a subtle change in the slope of B_z. The positive Hall solution sees the peak in the surface density become so strong that a subshock forms interior to the magnetic diffusion shock. This subshock is a sharp increase in the surface density and a marked change in the gradient of the magnetic field. The region between the two shocks is extended as the

gas is slowed by the subshock, and the rate of magnetic braking in this solution has been increased by the Hall diffusion, which acts to increase B_z.

As shown in Figure 6.1, there exists a clear relationship between the Hall diffusion parameter and the radius of the centrifugal shock. This is further demonstrated in Figure 6.2, which plots the shock position for similarity solutions with initial parameters equal to those in Table 5.3 (at a time $t = 10^4$ years) against the ratio of the Hall to ambipolar diffusion parameters. The centrifugal shock marks the edge of the Keplerian disc, and it clearly decreases in radius as the ratio of diffusion parameters increases; this behaviour was noted in the analytic estimation of the shock position derived in Section 5.3. While both directions of Hall drift contribute to the change in the size of the disc, the radial drift of B_z, which increases when the Hall parameter is negative (see Equation 6.1), has a greater effect on the radius of the centrifugal shock than the torque caused by the azimuthal Hall drift.

The constant velocity of the shocks in Figure 6.1 is given by $V_s = x_s c_s$, where the nondimensional shock positions x_s are those listed in Table B.2 for these values of $\tilde{\eta}_H$, and $c_s = 0.19$ km s^{-1} is the isothermal sound speed. All of the solutions form a protostar of around 0.7 solar masses and a protostellar disc of radius $R_c \sim$10–150 AU and mass $M_d \sim 10^{-2}$–10^{-1} M$_\odot$ in $t = 10^5$ years; these are the same order of magnitude expected from observations of Class I YSOs (e.g. Jørgensen et al., 2007).

The solutions compared in Figure 6.1, and those in Appendix C, have surface densities $\Sigma \propto r^{-3/2}$ and $\Sigma \propto t^{1/2}$ in the inner Keplerian disc, with a value $\Sigma(r = 1$ AU$, t = 10^4$ years$) \sim 10^3$ g cm^{-2}; the exact value of Σ at this point for each of these solutions are given in Table 6.1. These values of the surface density are consistent with what is thought to have occurred in the solar nebula (e.g. the minimum mass solar nebula has $\Sigma = 1700$ g cm^{-2} at $r = 1$ AU; Weidenschilling, 1977). Although the scaling of the surface density with radius appears to be imposed upon the disc by the simple model used to integrate to the inner boundary (see Section 5.2), the surface density tends asymptotically towards this behaviour before the simple model is activated. The parameter space explored was chosen to correspond to such disc-forming similarity solutions; variations in the model parameters (particularly the cap on the azimuthal field δ) could cause the disc surface density to behave differently, however no other disc-forming asymptotic solutions to the collapse equations were found in Chapter 3.

With increasing $\tilde{\eta}_H$ the increasing number of subshocks force the calculations to become so unstable that they cannot converge on the true similarity solution, which makes it difficult to speak of trends within the solution space. However, for the other polarity (where $\tilde{\eta}_H$ is negative) the solutions tend towards the behaviour exhibited in the slow IMHD collapse solutions discussed in Section 4.2; this trend can be seen across the similarity solutions in Appendix C. The region between the magnetic diffusion

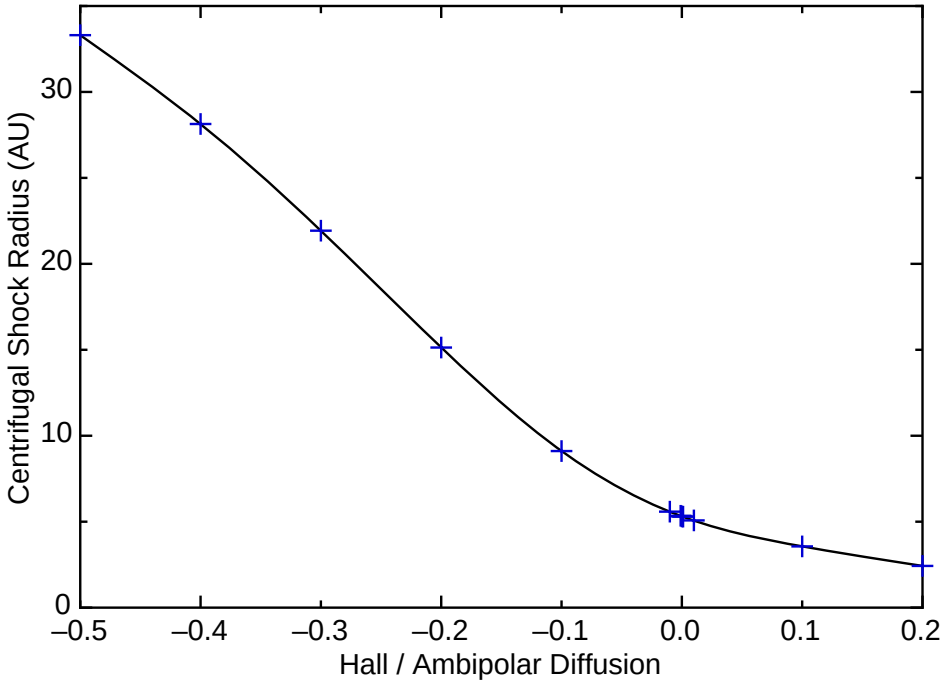

Figure 6.2: The dependence of the centrifugal shock radius (in AU at 10^4 years) on the ratio of the nondimensional Hall to ambipolar diffusion parameters for the calculated similarity solutions. The shock positions are tabulated in Appendix B.

and centrifugal shocks becomes smaller as the magnetic pressure gradient becomes less important to the infall rate. As $\tilde{\eta}_H$ becomes increasingly large and negative, Hall diffusion continues to be important to the azimuthal field diffusion and the magnetic braking, controlling the amount of angular momentum in the inner regions of the collapse and determining the size of the Keplerian disc.

The value of Σ in the Keplerian disc depends quite sensitively on the Hall parameter $\tilde{\eta}_H$, even though the vertical field component B_z increases only very slightly with increasing $\tilde{\eta}_H$. As the magnetic field is decoupled from the fluid there is a corresponding increase in the magnetic force, which slows down the inflow and reduces the inflow rate (see Equation 3.45). The inflow rate decreases with decreasing $\tilde{\eta}_H$ and $\tilde{\eta}_A$, and the decrease in radial velocity corresponds to an increase in the disc surface density. The amount of radial field diffusion determines the accretion rate $\dot{M}_c$, as well as the disc surface density; this behaviour was noted by Contopoulos et al. (1998) for their ambipolar diffusion solutions without rotation.

The vertical magnetic field behaves the same (and has very similar magnitudes) in all three similarity solutions in Figure 6.1 on the inner Keplerian disc; this is merely an artefact of the choice of illustrated solutions, as the additional Hall similarity solutions in Appendix C show that the vertical field in the disc drops off with increasingly large

negative Hall parameter. The accretion onto the central protostar depends upon the magnetic tension so that $\dot{M}$ and B_z are tied with $\dot{M} \sim \delta B_z^2/J$, and as Table 6.1 shows, there is little change in either of B_z or M_c across these three solutions. Similarly, in the outer regions of the disc where there is very little magnetic field diffusion and IMHD generally holds true, the vertical field magnitude is the same across all three solutions.

There also exists a correlation between the accretion rate onto the central protostar and the ratio of the Hall to ambipolar diffusion parameters, as can be seen in Figure 6.3. The behaviour of the accretion rate depends upon the disc radius, with larger discs corresponding to lower accretion rates and vice versa; this behaviour was also noted by Allen et al. (2003a). The infall rate through the Keplerian disc depends upon the radial diffusion of field lines (see Section 3.2), with larger negative Hall parameters causing an increased drag on the neutrals and a reduction of the radial velocity of the neutral fluid. The disc radius (and by extension the accretion rate) depends also upon the initial rotational velocity of the molecular cloud core, as the centrifugal force becomes important sooner and a larger disc forms when there is more initial angular momentum; this relationship was demonstrated in Chapter 4 for the similarity solutions without Hall diffusion.

The accretion rate onto the central protostar appears to turn over at around $\dot{M}_c = 7.6 \times 10^{-6}$ M$_\odot$ yr^{-1} once the ratio of the nondimensional Hall to ambipolar diffusion parameters becomes positive and greater than 0.05. This is likely due to the introduction of the subshocks in the solutions with $\tilde{\eta}_H$ positive. In the subshocks the density is enhanced, as is $dm/dx = \sigma x$, and so the accretion rate drops and less matter can be accreted onto the central mass. As the positive Hall parameter is increased, further subshocks are introduced into the solutions, which cause there to be an even lower inflow rate; and as $\tilde{\eta}_H$ tends towards the value that would see the diffusion parameter

$$f = \frac{4}{3}\tilde{\eta}_A - \delta\tilde{\eta}_H\sqrt{\frac{25}{9} + \delta^2} \tag{6.3}$$

become 0, Σ in the disc also tends towards 0 (see Section 3.2). The surface density and the accretion rate through the disc depend upon f because the accretion is regulated by the magnetic diffusion and associated torques, and this parameter places constraints on the possible values of Σ that exist in rotationally supported discs.

Clearly, the diffusion parameter of the disc, f, cannot be negative or equal to zero, as this implies that the field moves inward faster than the neutral particles; this causes an increase in the magnetic forces that would inhibit further collapse and disc formation. Disc formation is also inhibited when δ is too large and $\tilde{\eta}_H$ is positive, as again f would tend towards 0, constraining the azimuthal field twisting in a rotationally-supported disc. Similar constraints on the launching of disc winds were found by Salmeron et al. (2011), who showed that self-consistent disc wind solutions only exist

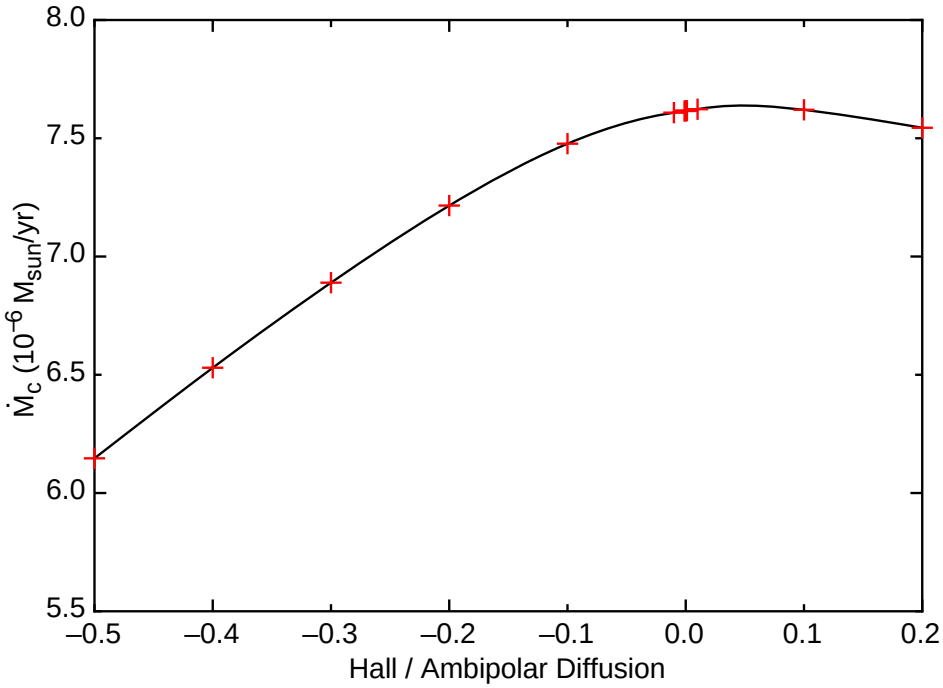

Figure 6.3: The dependence of the accretion rate onto the central star (in 10^{-6} $M_\odot$/yr) on the ratio of the nondimensional Hall to ambipolar diffusion parameters. The values of $\dot{M}_c$ are calculated using the converged self-similar accretion rates m_c tabulated in Appendix B.

for particular combinations of the field polarity and the ratio of the Hall to ambipolar diffusion parameters.

It has recently been argued that there exists a handedness to observations of transverse gradients in the Faraday rotation measure across the base of jets associated with active galactic nuclei (AGN; Contopoulos et al., 2009). The majority of sources in which it was possible to determine the transverse gradients were found to have clockwise gradients, which imply that the outflow has a helical magnetic field with a preferred positive magnetic polarity (i.e. that B_z is parallel to the rotation vector). One explanation of this behaviour is that the Hall effect is important in the inner accretion disc, acting to cause the formation of a jet when the field has a positive magnetic polarity, and to suppress jet formation when the polarity is negative (Königl, 2010). This explanation fits the limited available data well, although it can only be confirmed by future observations at higher resolutions and sensitivities, which will illuminate the properties of the dense molecular gas in the accretion discs of AGNs and show whether the Hall current is important to the jet formation.

Similarly, it may be possible to show observationally the importance of the sign of the Hall parameter in determining the properties of protostars and their discs. Measuring the polarisation of the magnetic field with respect to the axis of rotation

using Zeeman observations of newly-forming stars and their discs would provide a means of testing whether Hall diffusion plays an important role in star formation — should larger discs and lower accretion rates be correlated in observations with a particular field orientation then the Hall effect will have been shown to be important to the collapse process. ALMA (among other next-generation instruments) shall be capable of imaging nearby dense prestellar cores and their envelopes in both dust and molecular line emission, and also use polarised dust emission to map the magnetic field configuration in such cores (ESO, 2001). Such observations could be sensitive enough to observe if there is any difference in the field alignment between protostellar discs and their envelopes, and whether there is any correlation between disc size and the direction of rotation in the disc.

None of the solutions calculated in this work explored the effects of very weak magnetic diffusion and strong magnetic braking on the core, where the angular momentum of the collapsing flow is expected to be so reduced that near to the protostar the fluid is nonrotating (or rotating very slowly). This behaviour, and its predictions for star and protostellar disc formation are discussed in the following section.

6.2 The Magnetic Braking Catastrophe

In gravitational collapse models with magnetic fields two problems arise. The first occurs in nonrotating collapse simulations where the mass-to-flux ratio is constant and there is no mechanism for preventing the magnetic field from falling in, so that as the mass of the protostar builds up so too does its field. This results in the formation of a star with a very large (by many orders of magnitude in comparison to observations) magnetic field, and is referred to as the classical "magnetic flux problem" of star formation, which was described by Chandrasekhar and Fermi (1953) and outlined in Section 1.5. This is resolved by the inclusion of magnetic diffusion, which allows the field to drift against the flow of the infalling fluid.

However, there also exists a secondary problem tying the magnetic flux problem and the angular momentum problem (described in Section 1.4) together, in which strong magnetic braking removes all of the angular momentum from the collapse, preventing the formation of a rotationally-supported disc. This behaviour, dubbed the "magnetic braking catastrophe", affects many recent numerical collapse simulations (see e.g. Allen et al., 2003a; Mellon and Li, 2008, 2009; Hennebelle and Ciardi, 2009), whereas observations of young stars show that protostellar discs are common (e.g. Jørgensen et al., 2007).

The cap placed upon the magnitude of $B_{\phi,s}$ restricted the amount of magnetic braking in the solutions presented in the previous chapters and is perhaps the greatest

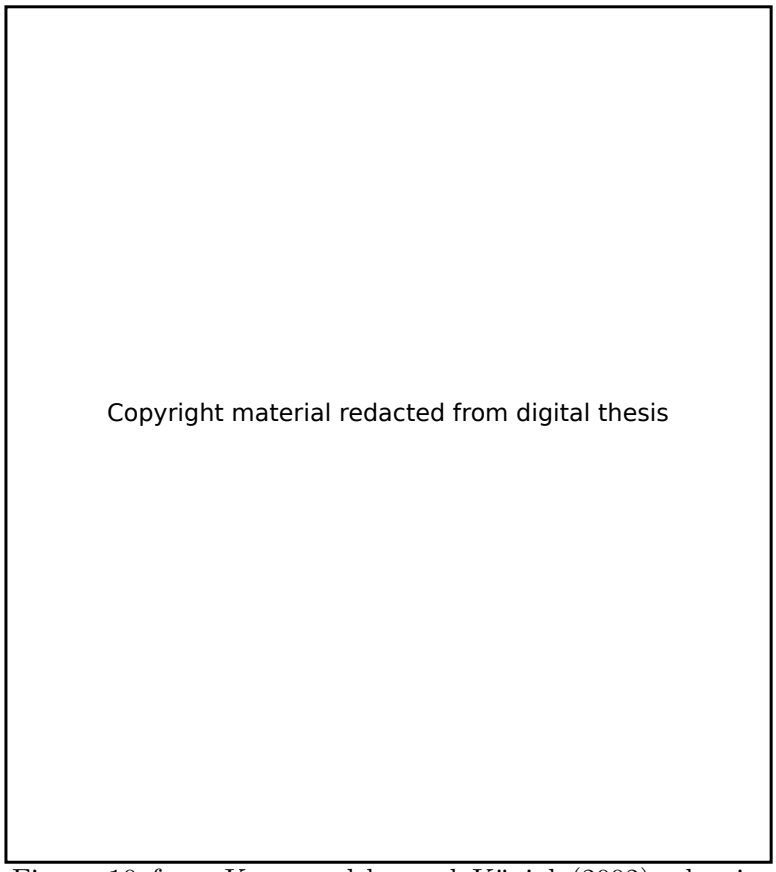

Figure 6.4: Figure 10 from Krasnopolsky and Königl (2002), showing a similarity solution with very strong magnetic braking. The model parameters are $\tilde{\eta}_A = 0.5$, $v_0 = 1.0$, $\alpha = 10$ and $\delta = 10$, with the remainder as in Table 5.3. The magnetic diffusion shock (labelled "AD Shock") is located at $x_d = 0.24$, and the central mass is $m_c = 5.9$.

limitation of the semianalytic model constructed in this work. While it is reasonable to assume that physical processes other than those included in the self-similar equations will restrict the growth of the azimuthal field, the fact that $B_{\phi,s}$ is capped for almost all of the solutions interior to the magnetic diffusion shock suggests that the results are sensitive to this prescription. Were the cap to be lifted, stronger magnetic braking could remove all of the angular momentum from the infalling gas, preventing disc formation.

In their semianalytic solutions to gravitational collapse with ambipolar diffusion Krasnopolsky and Königl (2002) found solutions in which disc formation was inhibited by the magnetic braking. These "strong braking" solutions were found by raising the azimuthal field cap, δ, and the magnetic braking parameter, α (where α is the ratio of the sound speed c_s to the external Alfvén speed $V_{A,ext}$, defined in Equation 2.84), so that the magnetic braking reduces the centrifugal force until it is incapable of supporting the gas against collapse. The high value of the azimuthal field cap ($\delta = 10$)

allows the magnetic field to become tightly wrapped around the rotational axis (this has also been seen in numerical simulations such as Machida et al., 2008a), however this wrapping may not be possible in real cores.

This behaviour was illustrated in figure 10 of Krasnopolsky and Königl (2002), reproduced here in Figure 6.4, which is characterised by $\delta = \alpha = 10$, $\tilde{\eta}_A = 0.5$ and $v_0 = 1.0$, with the rest of the parameters as listed in Table 5.3. In the outer region of the core the collapse follows that for the similarity solutions with capped braking in Figure 4.9, as IMHD is dominant. However, as the field is decoupled from the neutrals the magnetic braking rapidly starts to reduce the angular momentum. The magnetic diffusion shock at $x_d = 0.24$ sees an increase in the vertical magnetic field component that accelerates the magnetic braking further, and the angular momentum of the infalling material drops to a small nonzero value $j_{pl} \approx 2 \times 10^{-5}$ which depends upon the ambipolar diffusion parameter and the initial rotation rate. In this ambipolar diffusion solution the neutral component must be rotating relative to the charged component of the fluid in order to feel the magnetic braking torque; this causes the formation of a plateau from which the angular momentum cannot be reduced further. As there is no rotational support the fluid falls in with a radial velocity u close to the free fall velocity, and no disc forms.

Such "strong braking" solutions were not duplicated in this work, however it is clear that if the magnetic braking parameter and the azimuthal field cap are raised then the similarity solutions with Hall diffusion will display similar behaviour to that in Figure 6.4. The inner asymptotic behaviour of the solutions would follow that outlined by Equations 3.64–3.73 in Section 3.3 for the supersonic magnetically-diluted free fall onto the central protostar. No rotationally-supported disc would form, clearly demonstrating the magnetic braking catastrophe.

The contrast in behaviour between the ambipolar diffusion solutions of Krasnopolsky and Königl (2002) demonstrating disc formation and those of Mellon and Li (2009) illustrating the magnetic braking catastrophe is discussed in the following subsection.

6.2.1 Case study: ambipolar diffusion collapse

The similarity solution calculated in Chapter 4 for the ambipolar diffusion-only collapse (reproducing the fiducial result of Krasnopolsky and Königl, 2002) used a cap on the azimuthal field component to limit the magnetic braking and ensure disc formation. This is in direct contrast with the numerical simulations of Mellon and Li (2009), who were unable to observe disc formation in their simulations of collapsing cores with ambipolar diffusion unless the cosmic ray ionisation rate was unreasonably low or the magnetic field was particularly weak. To explore the discrepancy in disc forming

Figure 6.5: Radial and rotational velocities from the standard model of Mellon and Li (2009, figure 3) in units of the sound speed at a time $t = 5.85 \times 10^{11}$ s. The rotational velocity decreases with decreasing radius, indicating that there is strong magnetic braking, particularly in the deceleration region (which has been shaded). The thick lines are the velocities of the neutral particles, and the thin lines those of the ions.

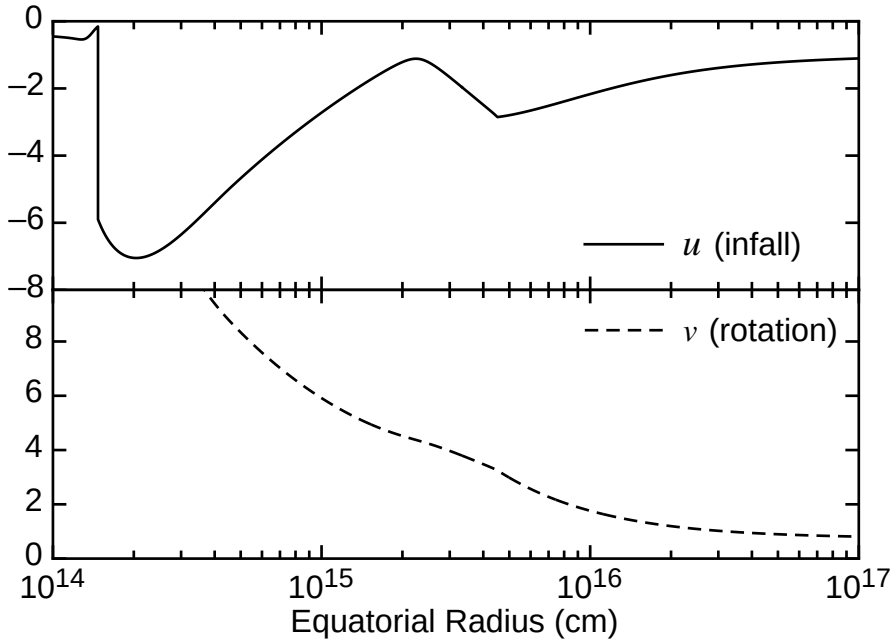

Figure 6.6: Rotational and radial velocity profiles in units of the sound speed at a time $t = 5.85 \times 10^{11}$ s from the fiducial solution of Krasnopolsky and Königl (2002) (which was presented in Figure 4.9 of Chapter 4). In this solution the rotational velocity increases as the increased ambipolar diffusion reduces the magnetic braking so that a centrifugal disc forms at $r \approx 10^{14}$ cm.

behaviour between the two models, the velocity profiles of both the standard solution of Mellon and Li (2009, figure 3) and the fiducial solution of Krasnopolsky and Königl (2002) at a time $t = 5.85 \times 10^{11}$ s (1.85×10^4 years) are shown in Figures 6.5 and 6.6 respectively.

The sharp decrease in the infall velocity in Figure 6.6 at $r \sim 10^{14}$ cm marks the boundary of the Keplerian disc in the similarity solution, interior to which the rotational velocity increases further. No such deceleration of the infall velocity occurs in Figure 6.5, where the uncapped magnetic braking prevents disc formation on this scale by removing all rotational support from the collapsing core. Both plots demonstrate similar infall velocity behaviour in the region of the magnetic diffusion shock at $r \sim 4 \times 10^{15}$ cm, while the rotation velocity is always quite different between the two solutions. Near the inner boundary of Figure 6.5 the rotation velocity does start to increase, however this is sufficiently far from the Keplerian value that any disc would have to form inside the inner boundary of the calculations. While it is most likely the cap on the magnetic braking in the similarity solution of Figure 6.6 that is responsible for the difference in disc-forming behaviour, there are other discrepancies between the two models that explain why one is able to form discs and the other cannot.

The simulations of Mellon and Li (2009) were an extension of their previous work on the collapse of molecular cloud cores under IMHD (Mellon and Li, 2008), which was modified to include ambipolar diffusion of the magnetic field. A spherical coordinate system under the assumption of axisymmetry was adopted, and the computational grid extended from 10^{14} to 10^{17} cm in r, and from 0 to π in ϕ. The resolution of the solution was characterised by 120 grid points in the radial direction and 60 angular points; these grid points were logarithmically spaced in radius. The collapse solutions were not fully isothermal; a broken power law equation of state was used to describe the behaviour of the fluid so that the gas was isothermal below $\rho = 10^{-13}$ g cm^{-3} and adiabatic with $\gamma = 7/5$ above.

The outer boundary of the collapse simulations of Mellon and Li (2009) was taken to be the standard "outflow" condition that was implemented as a feature of the ZeusMP MHD code in Hayes et al. (2006). The inner boundary was a modified outflow condition, with the mass accreted across the boundary added to the central point mass and a torque-free condition imposed upon the magnetic field (that $B_\phi = 0$). The initial conditions of the core were idealised as a rotating self-similar isothermal toroid supported against gravity partially by thermal pressure and partially by the magnetic field at the moment of point mass formation. These initial conditions are compared in Table 6.2 to those used for the fiducial solution of Krasnopolsky and Königl (2002) (reproduced in Section 4.3 as Figure 4.9).

There are two major discrepancies between the initial conditions and collapse pa-

Parameter	Mellon and Li (2009) Figure 6.5	Krasnopolsky and Königl (2002) Figure 6.6
v_0	0.5	0.73
u_0	0	-1.0
μ_0	4	2.9
A	2.8	3
m_c	4.5	4.7
$\tilde{\eta}_A$	0.087	1
c_s (km s^{-1})	0.3	0.19
ξ (s^{-1})	10^{-17}	10^{-17}

Table 6.2: Comparison of initial conditions and collapse parameters between the models illustrated in Figures 6.5 and 6.6. All of these are given in the nondimensional form used in this work (see Section 2.7 for details).

rameters between the two models: the first is the infall rate at the outer boundary $V_r = c_s u_0$, and the second is the nondimensional ambipolar diffusion parameter $\tilde{\eta}_A$, which changes by more than an order of magnitude between the models. The initial velocity at the outer boundary was found to have no qualitative effect on the simulations of collapse with IMHD by Mellon and Li (2008); this is used to justify their choice of no initial infall rate as the outer boundary condition in this model. However, the ambipolar diffusion parameter is key to the disc formation behaviour of the two models and this large variation between the two models, in addition to the capped magnetic braking, is more than enough to explain the differences between them.

Although both models cite the same cosmic ray ionisation rate (see Table 6.2), there is an order of magnitude difference between the ambipolar diffusion parameters adopted by each model. This occurs because Krasnopolsky and Königl (2002) chose an anomalously large value of $\tilde{\eta}_A = 1$ to use in their fiducial solution. In exploring the applicability of the assumption that $\tilde{\eta}_A$ is a constant in their model, Krasnopolsky and Königl (2002) stated that $\tilde{\eta}_A \approx 0.2\xi_{-17}^{-1/2}$ in the outer regions of the collapse where the density is typically between $\sim 10^4$ and $\lesssim 10^7$ cm^{-3}, and $\tilde{\eta}_A \approx 0.07$ in the inner regions where the density lies between 10^7 and 10^{12} cm^{-3}. These values are clearly much closer to the value used by Mellon and Li (2009) in their standard model, and indeed when Mellon and Li (2009) dropped their ionisation rate to $\xi = 10^{-18}$ s^{-1} (corresponding to $\tilde{\eta}_A = 0.87$) their collapse model was able to form a centrifugal disc around the protostar.

In Section 4.3, it was shown that the position of the centrifugal shock depends quite clearly upon the ambipolar diffusion parameter. Substituting the fiducial model parameters of Mellon and Li (2009) into Equation 4.180 gives an estimate of the shock

position at the time $t = 5.85 \times 10^{11}$ s that is many orders of magnitude smaller than the inner boundary of the collapse (due to the exponential in the equation). Although it is a poor approximation to the shock position in this region of parameter space, Equation 4.180 suggests that no rotationally-supported disc larger than the inner boundary of Figure 6.5 ($R = 10^{14}$ cm) will form unless $\tilde{\eta}_A > 0.68$. Earlier in this section it was demonstrated that a large decrease in the ambipolar diffusion parameter such as that between the two solutions, coupled with the corresponding increase in the rate of magnetic braking, prevented disc formation in the similarity solutions of Krasnopolsky and Königl (2002), as the magnetic braking catastrophe also inhibited disc formation in their similarity solution with $\tilde{\eta}_A = 0.5$ (shown in Figure 6.4).

The fiducial similarity solution of Krasnopolsky and Königl (2002) in Figure 6.6 also possessed a higher initial rotation velocity than the simulation of Mellon and Li (2009) in Figure 6.5, and it was shown in Chapter 4 that the value of v_0 directly affects the size of the rotationally-supported disc, with larger discs corresponding to larger initial rotational velocities. Contrasting the two simulations, as well as the strong braking solutions of Krasnopolsky and Königl (2002) in Figure 6.4, shows that the cap on $B_{\phi,s}$ is most likely responsible for the differences in the magnetic braking behaviour.

Further exploration of parameter space, particularly in matching the parameters used in numerical and self-similar models, is needed to explore whether adopting realistic values and scalings of the ambipolar and Hall diffusion parameters will resolve the magnetic braking problem. In the following subsection several mechanisms for reducing the magnetic braking in the collapsing flow and their expected results shall be discussed.

6.2.2 Proposed Solutions

Keplerian discs form in those simulations in which there is enough angular momentum that the centrifugal force is able to support the fluid against collapse. The magnetic braking catastrophe occurs because the twisting of the field lines caused by the rotation of the fluid in the disc transports angular momentum from the core to the envelope, slowing the rotation and inhibiting disc formation. This can be seen in the results of Sections 4.1 and 4.2, where the introduction of ideal MHD to the previously nonmagnetic collapse saw magnetic braking reduce the size of the rotationally-supported disc, and prevents disc formation entirely in both the IMHD strong braking similarity solution in figure 6 of Krasnopolsky and Königl (2002) and many numerical simulations (see e.g. Allen et al., 2003a; Galli et al., 2006; Mellon and Li, 2008)

Various approaches to solving the magnetic braking catastrophe have been adopted with different degrees of success. It is possible to reduce the magnetic braking by

changing the alignment of the magnetic field with respect to the rotational axis, limiting the twisting of the field within the core or the amount of angular momentum that can be accepted by the envelope and employing magnetic diffusion to change the coupling between the magnetic field and the fluid. Magnetic diffusion reduces the amount of braking by allowing the field lines at the midplane to slip against the neutrals rather than rotating with them around the core.

The amount of magnetic braking affecting the core depends upon the product $B_z B_{\phi,s}$, and so any change in the alignment of the field with respect to the axis of rotation shall influence the magnetic braking behaviour. Mouschovias and Paleologou (1980) showed that the magnetic braking affecting a disc of fixed height was more efficient when the magnetic field and the axis of rotation were perpendicular. The rotational waves in their discussion propagated perpendicular to the axis of rotation, affecting matter in the external medium with increasing moments of inertia as the moment of inertia of the core itself decreased, and this lead to a higher magnetic braking efficiency.

Hennebelle and Ciardi (2009) found that the opposite was true. In their three-dimensional simulations including IMHD the height of the pseudodisc and inner Keplerian disc increases with the angle of alignment between the field and the rotational axis as the magnetic field lines are twisted about an axis parallel to the plane of the pseudodisc. The rotation of the core itself also impedes contraction along the magnetic field lines, further increasing the scale height of the core. This increase in scale height causes a reduction in the magnetic braking as the braking time is shorter, so that larger Keplerian discs form when the angle between the rotation and magnetic field axes is 90°.

This conclusion was supported by the results of Ciardi and Hennebelle (2010), which showed that the angle between the rotation and magnetic field axes also influences the formation of outflows and jets, and can suppress these when the axes are perpendicular. Any misalignment causes the jets to precess, which further reduces the efficiency of the magnetic torque in removing angular momentum from the pseudodisc and allows a larger Keplerian disc to form when the angle is perpendicular.

Other mechanisms for limiting the magnetic braking in the collapsing core and enabling disc formation include capping the azimuthal field and insisting that the core possess a finite boundary, as disc formation is clearly enabled by limiting the degree of magnetic braking in the collapsing core. In Krasnopolsky and Königl (2002) and this thesis it was assumed that the external envelope of the core was effectively infinite and that the magnetic field lines were anchored into this external medium. This meant that the magnetic braking could transfer as much angular momentum from the core as the cap on $B_{\phi,s}$ allowed, which (as shown in Figure 6.4) could inhibit disc formation

when the braking was sufficiently strong. However, this limitation is unrealistic, as the forming protostar is expected to accrete or dissipate the envelope, and the cap on $B_{\phi,s}$ is itself merely a way of representing unknown disc physics that needs to be better understood, which should be replaced in future work on the subject (discussed further in Section 6.3).

Simulations of the collapse of a core in a finite host cloud under IMHD (Galli et al., 2006) and resistive MHD (Machida et al., 2007, 2011) were able to form Keplerian discs, as the magnetic braking became less effective as the core envelope was depleted. In these simulations the early phase of collapse was characterised by slow circumstellar disc growth regulated by magnetic braking; in the later stages the envelope is depleted by accretion onto the pseudodisc, so that magnetic braking is no longer effective and a large disc is able to form. Limiting the amount of material that can accept the angular momentum from the core clearly allows a rotationally-supported disc to form, and so the boundary conditions of numerical simulations must be carefully considered in light of the magnetic braking catastrophe.

Magnetic field diffusion is also important to resolving the magnetic braking catastrophe, as less magnetic braking occurs in a pseudodisc that has less magnetic flux. In calculations where the Ohmic resistivity is taken to be spatially-constant, such as those by Shu et al. (2006) and Krasnopolsky et al. (2010), the Ohmic diffusivity required to allow disc formation must be anomalously large. Krasnopolsky et al. (2010) in particular required an Ohmic resistivity three orders of magnitude larger than that expected in molecular cloud cores and many numerical reconnection events in order to form a rotationally-supported disc that was ~ 100 AU during the Class 0 stage of star formation. In reality the importance of Ohmic dissipation is expected to vary with density (see Figure 1.3) in the inner regions of the core; by taking it to be spatially-constant across the collapsing core a higher value is required in order to avoid the magnetic braking catastrophe.

When the Ohmic diffusivity is not spatially-constant, and instead varies with the density of the neutrals, it is able to prevent the removal of all the angular momentum from the core. Machida et al. (2011) found that their simulations with Ohmic dissipation formed rotationally-supported discs with radii ~ 100 AU at $t_c = 10^5$ yr (where t_c is the time after disc formation) as the decoupling of the field from the charged particles in the innermost regions of the collapse halted the magnetic braking in these regions. Dapp and Basu (2010), following on from Machida et al. (2007), demonstrated that a canonical amount of Ohmic dissipation was able to reduce the amount of braking in the first (adiabatic) core so that a centrifugal disc formed in their axisymmetric numerical calculations. The Ohmic resistivity adopted in their calculations (and in those of Machida et al., 2011) depended upon the density in the core and never greatly

exceeded that expected from ionisation calculations such as those by Wardle and Ng (1999).

Reducing the inner field strength by ambipolar diffusion allows larger discs to form than in IMHD simulations with equivalent initial conditions and parameters (demonstrated in Section 4.3), however, this required the use of a cap on $B_{\phi,s}$. Without this cap, ambipolar diffusion is unable to completely resolve the magnetic braking catastrophe (e.g. Figure 6.4; Krasnopolsky and Königl, 2002; Mellon and Li, 2009). The simulations of Mellon and Li (2009) demonstrating the magnetic braking catastrophe were discussed in detail in the previous subsection, however these showed a possible resolution of the catastrophe by reducing the cosmic ray ionisation rate (increasing the ambipolar diffusion parameter) in the core. (Kunz and Mouschovias (2010) were able to form disc-like structures in their simulations in which the field was decoupled from all species by ambipolar diffusion before Ohmic dissipation became important, however their solutions were nonrotating and so no Keplerian disc could form.)

The results of the semianalytic model presented in this work showed that the Hall effect also plays a critical role in determining the amount of magnetic braking that affects the collapsing flow. It is difficult to include Hall diffusion in numerical simulations, due to the small time steps required to trace it accurately, however some work is being done in this area (see Krasnopolsky et al., 2011). The size of the rotationally-supported disc that formed in the solutions presented in the previous chapter depends upon the direction of the magnetic field, and varied by almost an order of magnitude between the solutions with $\tilde{\eta}_H = -0.2$ and $\tilde{\eta}_H = +0.2$. As will be discussed further in subsection 6.2.3, Hall diffusion can increase the magnetic braking affecting the core or instead act in the opposite direction to increase the amount of rotation in the disc, despite the cap that has been placed upon $B_{\phi,s}$.

Although much of the focus of this thesis has been on the magnetic braking caused by Hall and ambipolar diffusion, it is also the case that in weakly ionised cores with no initial rotation the Hall effect can induce rotation via *magnetic acceleration*. Some preliminary work has been performed to calculate such similarity solutions; in subsection 6.2.3 it shall be shown that Hall diffusion could induce disc formation in an initially nonrotating core.

6.2.3 Hall-driven spin-up of collapsing cores

In Wardle and Ng (1999) it was suggested that the Hall current in a collapsing molecular cloud core would cause B_ϕ to grow and force the fluid to pick up a toroidal component of momentum, which could contribute to the gravitational support of the core. Krasnopolsky et al. (2011) have recently published the results of a three-dimensional

simulation of the collapse of an initially nonrotating core under the influence of Hall diffusion, showing that the Hall effect causes the collapsing material to spin-up. They demonstrated that azimuthal torques powered by the Hall effect twist the ions and by extension the neutral particles (as the magnetic field is anchored in the external medium) as expected; conservation of momentum implies then that the gas and envelope will both spin-up in opposite directions, which was observed in their simulation.

The full model code from Chapter 5 has been employed here to similarly demonstrate such Hall spin-up of an initially nonrotating molecular cloud core. This model has yet to converge on the true similarity solution, as the shock-finding routine outlined in Section 5.2 does not converge properly in these calculations without modification. The variables in the outer regions and those downstream of the magnetic diffusion shock before the gravity of the central mass dominates the radial velocity of the fluid are quite trustworthy, while the inner regions of the calculations are unreliable representations of the core behaviour.

Figure 6.7 shows this non-converged solution to the outer boundary conditions, which (as in Figure 4.6) fails on the inward integration interior to the magnetic diffusion shock. This calculation has nondimensional Hall parameter $\tilde{\eta}_H = -0.1$ and ambipolar diffusion parameter $\tilde{\eta}_A = 1.0$ (matching those in Figure C.5), which were chosen to demonstrate the spin-up behaviour caused by the Hall effect, even when $\tilde{\eta}_H$ is small, is enough that a rotationally-supported disc could form in the fully converged solution. The solution satisfies the outer boundary conditions for the parameters listed in Table 5.3, save for the initial rotational velocity which is taken to be $v_0 = 0$ in the initially nonrotating core. The central mass is estimated by the plateau value $m_c \approx m_{pl} = 6$ defined in Equation 4.42.

In the outermost regions of Figure 6.7 the material undergoes near-ideal MHD collapse; the small divergences from flux-freezing cause the angular momentum of the gas to rapidly increase from zero at the outer boundary $x_{out} = 10^4$ (which is outside the domain of the figure) to a plateau value determined by the Hall diffusion parameter. The value of this plateau is estimated from the conservation of angular momentum equation (2.107), in the limit where j is constant and given by the plateau values $j = j_{pl}$:

$$\frac{dj}{dx} = \frac{j_{pl}}{w} - \frac{x^2 b_z b_{\phi,s}}{m} = 0. \tag{6.4}$$

In the large x limit the infall velocity is small compared to x so that $w = x$, and the other variables are given by the outer asymptotic power law relations defined in Section 2.7. These relations are substituted into Equation 6.4, which is rearranged to give the expression

$$j_{pl} = \frac{x b_{\phi,s}}{\mu_0}\,. \tag{6.5}$$

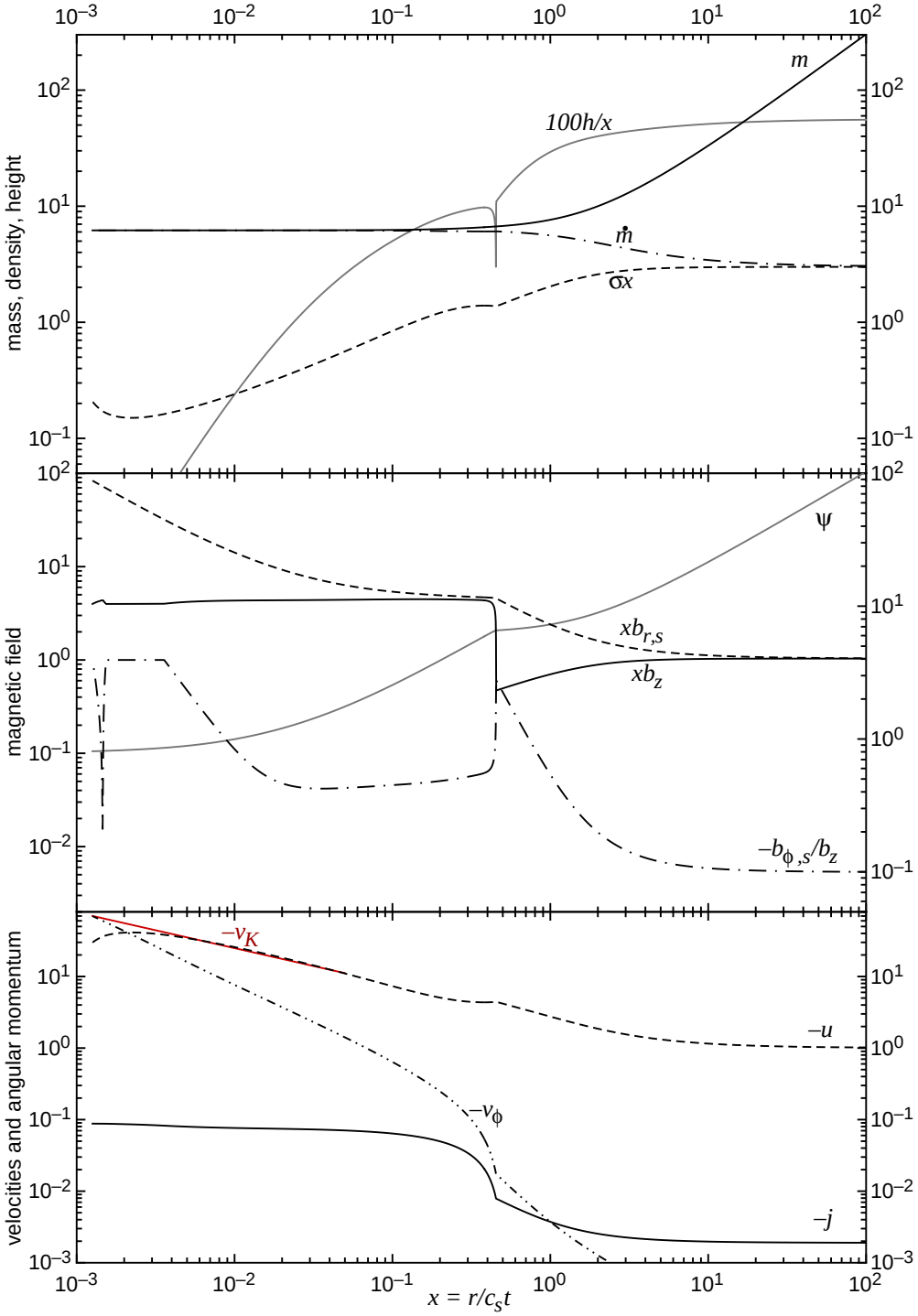

Figure 6.7: Non-converged similarity solution with $\tilde{\eta}_H = -0.1$ and initial rotational velocity $v_0 = 0$. The other initial conditions and parameters are those in Table 5.3. The model code used to calculate the similarity solutions in Chapter 5 was unable to locate the inner centrifugal shock position and converge on the true solution; however, the angular momentum has increased downstream of the magnetic diffusion shock until it is comparable to that for the similarity solutions with nonzero v_0. The solid red line in the lower panel is the nondimensional Keplerian velocity $v_K = \sqrt{m_c/x}$.

The azimuthal field component $b_{\phi,s}$ in this region is determined by both the Hall diffusion and the vertical compression of the disc, which in turn depend upon the self-gravity of the pseudo disc and the magnetic squeezing caused by $b_{r,s}$. The vertical hydrostatic equilibrium equation (2.108) is

$$\left(\frac{\sigma m_c}{x^3} - b_{r,s}\frac{db_z}{dx}\right) h^2 + \left(b_{r,s}^2 + b_{\phi,s}^2 + \sigma^2\right) h - 2\sigma = 0; \tag{6.6}$$

in the limit of large x, both db_z/dx and $b_{r,s}$ are inversely proportional to x and as such their product may be dropped from the equation. Similarly the azimuthal field component is small in comparison to the poloidal components, so that Equation 6.6 may be simplified into

$$\left(b_{r,s}^2 + \sigma^2\right) h = 2\sigma, \tag{6.7}$$

which becomes

$$h = \frac{2}{\sigma(1+\mu_0^{-2})} \tag{6.8}$$

upon substitution of the outer boundary flux-freezing condition for the radial field component. Physically, in the outermost regions of the core the scale height is dominated by tidal compression and magnetic squeezing associated with the radial field component $b_{r,s}$.

As the azimuthal field component and angular momentum are small when x is large, Equation 2.114 may then be written as

$$b_{\phi,s} = \frac{2\alpha\tilde{\eta}_H \psi b b_{r,s} h^{1/2}}{x^2\sigma^{3/2}} \left[1 + \frac{2\alpha\tilde{\eta}_A \psi b_z h^{1/2}}{x^2\sigma^{3/2}}\right]^{-1}. \tag{6.9}$$

The total field magnitude may be approximated by $b = \sqrt{2}b_z$ as the azimuthal component is small. The outer asymptotic relations (Equations 2.128–2.130) are then substituted into Equation 6.9, so that $b_{\phi,s}$ may then be approximated by

$$b_{\phi,s} = \frac{4\alpha A\tilde{\eta}_H}{x\mu_0} \left[\mu_0^2\sqrt{1+\mu_0^{-2}} + 2\sqrt{2}\alpha\tilde{\eta}_A\right]^{-1}. \tag{6.10}$$

This is then substituted into Equation 6.5 to give an estimate of the angular momentum plateau,

$$j_{pl} = \frac{4\alpha A\tilde{\eta}_H}{\mu_0^2} \left[\mu_0^2\sqrt{1+\mu_0^{-2}} + 2\sqrt{2}\alpha\tilde{\eta}_A\right]^{-1}. \tag{6.11}$$

The value of the angular momentum plateau and the near-constant ratio of the azimuthal to vertical field components in the plateau region for the non-converged similarity solution in Figure 6.7 and a second calculation in which $\tilde{\eta}_H = -0.6$ (which is also matched to the outer boundary only) are compared to the theoretical estimations

$\tilde{\eta}_A$	$\tilde{\eta}_H$	$j_{pl,est}$	$j_{pl,sol}$	$(-b_{\phi,s}/b_z)_{est}$	$(-b_{\phi,s}/b_z)_{sol}$
1.0	-0.6	-7.508×10^{-3}	-7.506×10^{-3}	0.02105	0.02146
1.0	-0.1	-1.251×10^{-3}	-1.251×10^{-3}	3.508×10^{-3}	3.577×10^{-3}

Table 6.3: Calculated and actual values of the angular momentum plateau and the relation $-b_{\phi,s}/b_z$ in the non-converged (though matching on the outer boundary) solution for an initially nonrotating core. The values from the solutions are taken at $x = 100$; and the parameters used in the estimations are those for the similarity solutions presented in Chapters 4 and 5 ($\alpha = 0.08$, $A = 3$ and $\mu_0 = 2.9$).

from Equations 6.10–6.11 in Table 6.3. The estimated values match the calculated ones very well, with j_{pl} matching to $\sim 0.1\%$ and $b_{\phi,s}/b_z$ to $\sim 2\%$, demonstrating that the physics of the region is well accounted for by the approximations. All of the angular momentum in the core, and the twisting of the field lines is caused by the Hall effect, as the radial component of the magnetic pressure gradient causes azimuthal drift of the field lines, which in turn creates the torque that spins up the ions and neutrals. The value of the specific angular momentum plateaus once the induced rotation is rapid enough that the magnetic torque is balanced by the rotational torque. As the density of the gas is quite limited in the outer regions, the Hall spin-up of the disc is limited until the variables start to diverge from their asymptotic behaviour and IMHD breaks down.

The behaviour of the fluid downstream of the magnetic diffusion shock at $x_d = 0.453$ (which is close to the value $x_d = 0.435$ estimated by multiplying Equation 5.46 by the factor 0.83; see Section 5.3) is less clear, as the solution has not yet converged and the position of the centrifugal shock is only approximately known. As in the initially rotating solutions in Chapter 5, the fluid is slowed at the shock, until the gravity of the central mass starts to dominate the radial velocity and the fluid is accelerated inwards once more. Hall diffusion quickly spins up the gas in the post-shock region, until again it reaches a plateau which is similar in value to that experienced in the rotating solution in Figure C.5. Near the region where the centrifugal force becomes important, the azimuthal component of the magnetic field $b_{\phi,s}$ reaches its capped value, and the angular velocity is quite close to that expected from Keplerian rotation (depicted as the solid red line in the lower panel of Figure 6.7).

Much remains to be done on this model to ensure that the similarity solution converges to the true solution and matches the expected asymptotic behaviour on both boundaries of the collapse. The spin-up behaviour can clearly only exist when there is Hall diffusion of the magnetic field, as when $\tilde{\eta}_H = 0$ there is no mechanism for inducing rotation in an initially nonrotating core and neither the angular momentum or the azimuthal field component can acquire a nonzero value. Although disc formation

has yet to be observed, the solution in Figure 6.7 shows that the rotational velocity of the collapsing material reaches the rotationally-supported value of $v = v_K$ near the point where the code breaks down, suggesting that disc formation may be enabled by the Hall effect in the collapsing gas, supporting the numerical results of Krasnopolsky et al. (2011).

The direction of rotation within the collapsing flow is determined by the sign of $\tilde{\eta}_H$. The spin in the outer regions of the core, given by Equation 6.11, shows this; and as the field increases the magnetic acceleration causes the gas to spin-up further in this direction. While this solution is clearly a special case, such spin-up behaviour caused by the Hall effect could in fact resolve the magnetic braking catastrophe. Hall diffusion causes a rotational torque on the gas that can enhance or reduce the magnetic braking that removes angular momentum from the disc and it does not stop acting once all of the angular momentum reaches zero — indeed, it could act at this point to start spinning the fluid back up in the opposite direction to the initial rotation of the core. This may produce enough angular momentum to form a Keplerian disc, in complete defiance of the expected behaviour from non-Hall solutions in which there is no way to increase the rotational energy of the flow.

The magnetic braking catastrophe prevents the formation of rotationally-supported discs around protostars by the removal of angular momentum from the collapsing flow, in contrast with observations that show protostellar discs are common. This causes the collapse downstream of the magnetic diffusion shock to occur in near-free fall, limited only by the magnetic pressure, which is insufficient to prevent collapse, particularly when the field is allowed to diffuse outward against the fluid. Various approaches have been adopted to solve this problem, including limiting the magnetic braking by placing a cap upon $B_{\phi,s}$ and introducing Ohmic diffusion, which decouples the field from the fluid and limits the effectiveness of magnetic braking in the inner regions.

Hall diffusion is capable of inducing spin in an initially nonrotating core, and could resolve the magnetic braking catastrophe by further inducing spin in the opposite direction once magnetic braking has removed the initial angular momentum from the core. Further work must be done to study the role of the Hall effect on the magnetic field diffusion in star formation, particularly using the semianalytic model constructed in this thesis, and possible directions for further study of Hall diffusion in collapse are discussed in the following section.

6.3 Future Work

Much still needs to be done both with the self-similar model of gravitational collapse as presented in this thesis and with the model modified by improved assumptions about

such physics as the vertical angular momentum transport and the way in which the Hall diffusion parameter scales with the density in the collapsing flow. This section shall explore some of the work that is already underway and the directions yet to be examined in future studies of magnetized gravitational collapse.

6.3.1 Limitations and assumptions

The self-similar model is quite limited in that it is effectively only two dimensional with much of the physics simplified so as to produce a self-similar semianalytic solution of infinite resolution to the equations of gravitational collapse, with azimuthal and vertical effects in the disc sacrificed for ease of calculation. Numerical solutions can trace the behaviour of the collapse until the density of the inner regions becomes so high compared to the resolution in space, and the time step required to trace the fluid so short as to make further integration possible (although the application of a sink particle at the centre of the collapse can allow some further calculation). It is also the case that some numerical models do not possess the resolution necessary to see the formation of rotationally-supported discs of equivalent size to those that form within the self-similar model at a given system age. However, numerical simulations are able to include nonaxisymmetric and vertical effects, which allow them to better explore the magnetic braking catastrophe and outflows.

The assumptions of isothermality, axisymmetry and that the magnetic field and axis of rotation are aligned are all required to ensure the self-similarity of collapse, and cannot be lifted. Isothermality keeps the sound speed in the fluid constant, and although it breaks down in the late stages of collapse when $n = 10^{10}$ cm^{-3} (Gaustad, 1963) this only occurs in the innermost regions of the rotationally-supported disc in the similarity solutions. The only other place in the solutions where isothermality is likely to break down is in the magnetic diffusion shock, however the magnetic pressure is more than an order of magnitude larger than the gas pressure in the shock front and this is not likely to greatly affect the nature of the collapse. Axisymmetry, which reduces the dimensionality of the problem, causes the suppression of disc physics such as turbulence and gravitational instabilities; these could potentially be included in the model using a scaled prescription, but it is not clear that any such prescription would add meaningfully to the physics in the core. Hennebelle and Ciardi (2009) showed that varying the angle between the magnetic field and the axis of rotation affected the efficiency of disc formation, however such behaviour is fully three-dimensional and could never be included in self-similar collapse models.

The assumptions that $b_{r,s}$ and g_r can be approximated by monopoles is another that could be improved upon with more careful calculation. Adding an additional cycle

of computation to the convergence routine that would find these terms more precisely (as in Contopoulos et al., 1998) would slow the calculation of similarity solutions down further; however, this could be offset by some parallelization of the full code which is made possible by recent increases in the computing power and number of processors on individual CPUs. Such calculations would improve the accuracy of the determination of the radial gravitational and magnetic field components, although it is not clear that these approximations need to be replaced.

The thin disc assumption made it possible to adopt linear scalings of the radial and azimuthal field components with height in the disc and average the other parameters with respect to the disc scale height to produce a set of equations that depended only upon r and t. This averaging prevents the examination of any behaviours that occur within the thin disc, such as the MRI and other turbulent effects, that may be important to the angular momentum transport. The α-viscosity of Shakura and Sunyaev (1973) provides an axisymmetric average of turbulence within the disc, which can be scaled with the self-similar variables and could in future be included in the model. The thin disc assumption also allows terms of order H/r to be dropped from the equation set, on the grounds that they are usually small. Reintroducing these terms would allow the structure of the collapsing flow to be refined without adding very much to the computation costs. It is not clear what changes (if any) these small terms would bring to the self-similar model of collapse.

The transportation of angular momentum in the vertical direction is perhaps the most limiting of the simplifications adopted in the model. Several mechanisms for better calculating the behaviour of the azimuthal field and the angular momentum transport are outlined in the following subsection.

6.3.2 Vertical angular momentum transport

The azimuthal field in this model was limited by an artificial cap that was specifically designed to replace physics missing from the rest of the model. Based on the assumption that B_z is the dominant component of the field, it is unclear what the magnitude and applicability of this cap ought to be. For the purpose of properly solving the magnetic braking catastrophe, different ways of replacing or calculating this cap need to be determined.

The assumption of axisymmetry precludes the addition of magnetohydrodynamic instabilities such as internal kinks and turbulence to the self-similar model; such behaviour would prevent $B_{\phi,s}$ from greatly exceeding the poloidal field components. These effects could potentially be parameterised according to the way in which they scale with the field strength, the density and other variables in numerical solutions,

and then included into the self-similar model as a mechanism for constraining $B_{\phi,s}$.

In the inner Keplerian disc $B_{r,s}/B_z > 1/\sqrt{3}$, which is the launching condition for a cold, centrifugally-driven wind, and the radial scaling of the magnetic field components is identical to that of the radially-self-similar wind solution of Blandford and Payne (1982). Such a disc wind, which was described in appendix C of Krasnopolsky and Königl (2002), would be the dominant mechanism for the transfer of angular momentum from the disc to the envelope. A disc wind must be included in future self-similar collapse simulations in order to explore the influence a wind may have on the angular momentum transport, the magnetic braking catastrophe and furthermore to simply improve the accuracy of the models, as disc winds and jets are known to occur in numerical simulations (e.g Tomisaka, 2002; Machida et al., 2007; Mellon and Li, 2009; Ciardi and Hennebelle, 2010) of collapsing protostellar discs.

6.3.3 Scaling the magnetic diffusivities

For an idealised fluid with no grains, the Hall and ambipolar diffusivities are given in dimensional form by

$$\eta_H = \frac{cB}{4\pi e n_e} \tag{6.12}$$

$$\text{and } \eta_A = \frac{D^2 B^2}{4\pi \rho_i \nu_{in}}, \tag{6.13}$$

where $D \equiv \rho_n/\rho$ is the neutral density fraction (which tends towards 1 in weakly ionised fluids such as are found in molecular clouds cores; Cowling, 1957; Wardle, 1999; Pandey and Wardle, 2008). In their numerical solutions Krasnopolsky et al. (2011) used a spatially constant coefficient $Q = \eta_H/B$ for the Hall diffusivity, so that the behaviour of the Hall effect was not directly dependent upon the density of the disc. The Hall term spins up the inner part of the collapsing flow to Keplerian speeds, with the direction of the field determining the direction of the Hall-induced magnetic torque, and rotationally-supported disc formation was found to be possible in their calculations only when $Q \gtrsim 3 \times 10^{20}$ cm^2 s^{-1} G^{-1}.

The self-similarised Hall diffusivity $\eta'_H = (c_s^2 t)^{-1}\eta_H$ from the full set of fluid equations solved in this work was taken to scale with the surface density and scale height of the disc as

$$\frac{\eta'_H}{b} = \tilde{\eta}_H b \left(\frac{h}{\sigma}\right)^{3/2}, \tag{6.14}$$

where $\tilde{\eta}_H$ was a constant. The decision to employ this scaling was a pragmatic one, as the Hall diffusion then becomes important with the ambipolar diffusion (which also scaled as

$$\frac{\eta'_A}{b^2} = \tilde{\eta}_A \left(\frac{h}{\sigma}\right)^{3/2} \tag{6.15}$$

in self-similar space), and the drift of both grains and ions are important to the collapse. The ratio of the diffusion parameters was then critical to all discussions of the similarity solutions, and by keeping the ambipolar diffusion coefficient constant it was possible to explore the individual influence of the Hall term. In general though, both diffusion parameters could scale as any function of the similarity variable x and the fluid variables without breaking self-similarity.

For example, a second choice for scaling the Hall parameter that could be adopted in future is

$$\frac{\eta_H'}{b} = \tilde{\eta}_H \sqrt{\frac{h}{\sigma}}\,, \tag{6.16}$$

which would be the behaviour expected if

$$\eta_H \sim \frac{B}{n_i}, \tag{6.17}$$

that is, if the only important particles in the collapsing core are neutrals and ions, without grains. This change would see the Hall diffusion become important earlier in the collapse, as the density increases and would also change the degree of magnetic braking. Such a formulation would also change the behaviour in the inner Keplerian disc, and a new set of asymptotic inner boundary conditions describing this disc behaviour would need to be derived.

There is considerable scope for examining similarity solutions where the relationship between the two diffusivities changes with x, so that each may become important at different points in the collapse process. This is the case in reality; Figure 1.3 showed that Hall diffusion is expected to become important when the density and the magnetic field are both of intermediate strength, while ambipolar diffusion is dominant where the density is low and the field strength high, and these could be better reflected in the collapse solutions. The diffusivities may be made to scale with any function of the self-similar variables and x, in order to mimic the behaviour expected from ionisation equilibrium calculations, and these scalings could include changing the sign as well as the magnitude of the Hall diffusivity with increasing density.

6.3.4 Exploring parameter space

The Hall similarity solutions presented in Chapter 5 explored only a very narrow region of parameter space where the outer boundary conditions and the magnetic parameters were held constant as the Hall diffusion parameter was varied in both directions. The similarity solutions without Hall diffusion from Chapter 4 and Section 6.2 showed that reducing the initial rotational velocity of the core altered the size of the Keplerian disc; that raising the azimuthal field cap and the magnetic braking parameter caused all of the angular momentum to be removed from the core so that no disc formed; and

that reducing the ambipolar diffusion parameter caused the size of the rotationally-supported disc and the accretion rate onto the protostar to be reduced further. Future work on the Hall similarity solutions must reproduce this diversity of parameter space, in order to better understand the importance of Hall diffusion on the collapse process.

Perhaps the most interesting region of parameter space to explore is that in which Hall diffusion is the dominant form of flux transport. Without changing the magnetic braking parameter and the cap on $b_{\phi,s}$, it is only possible to find similarity solutions in which rotationally-supported discs form when the Hall diffusion parameter is negative and large (see Section 6.1 and Equation 6.3). If Hall diffusion were dominant, it would further change the overall structure of the collapse, as it appears in the equations for determining both the rotational velocity of the collapsing gas as well as the magnetic support in the flow. In reality Hall diffusion is not necessarily expected to exceed ambipolar diffusion except in the innermost regions of the collapse (Wardle, 2004a, 2007), but this presents an interesting goal for theoretical calculations as such similarity solutions would further demonstrate the importance of the Hall effect on the collapse.

Further to this, it would be of interest to calculate solutions without ambipolar diffusion at all, in which all of the magnetic field diffusion is performed by the Hall diffusion term, as in Krasnopolsky et al. (2011). Hall diffusion would change the nature of the collapse, as all of the field diffusion would then depend upon the $\mathbf{J} \times \mathbf{B}$ terms, so the radial field diffusion depends on the azimuthal field component (which may be capped) as opposed to the whole of the field, and the azimuthal diffusion depends upon the radial component. Such similarity solutions would again be not strictly realistic, however in the regions of the collapse interior to the magnetic diffusion shock (which would likely occur later in the collapse due to the absence of ambipolar diffusion) the density and field strength are both of intermediate value and Hall diffusion could already be more important than ambipolar diffusion (see Section 1.2).

As mentioned in the previous section, more needs to be done to explore the importance of the magnetic braking parameter α and the cap on the azimuthal field component δ. Should these be increased it seems likely that the increased magnetic braking will remove all angular momentum from the collapse and the solutions will tend towards the asymptotic free fall collapse described in Section 3.3. In that inner asymptotic solution Hall diffusion changes the field strength in the disc, while the surface density and radial velocity depend only upon the central mass. Such similarity solutions would provide further insight into the magnetic braking catastrophe and should be determined in future work on this topic.

In Chapter 4 it was shown that the initial rotational velocity plays an important role in determining the size of the Keplerian disc in those solutions without Hall diffusion. Further work should be done to confirm that larger discs form if the core is initially

rapidly-rotating in the similarity solutions with Hall diffusion. Although the Hall effect does change the behaviour of the magnetic braking in the disc, it is not expected to make any dramatic changes to the collapse behaviour otherwise as the initial angular momentum is varied. The orientation of the field, and in consequence the strength of the magnetic braking, could influence the effect of the initial rotational velocity of the molecular cloud core on the centrifugal shock position; obviously work must be done to properly explore this concept.

6.4 Conclusions

This thesis described a semianalytic self-similar model of the gravitational collapse of rotating magnetic molecular cloud cores with both Hall and ambipolar diffusion, presenting similarity solutions that showed that the Hall effect has a profound influence on the dynamics of collapse. The solutions satisfied the vertically-averaged self-similar equations for MHD collapse under the assumptions of axisymmetry and isothermality, matching onto the self-similar power law relations describing an isothermal core at the moment of point mass formation on the outer boundary and a Keplerian disc on the inner boundary.

Two power law similarity solutions were derived that satisfy the collapse equations on the inner boundary. The first of these represents a Keplerian disc in which accretion through the disc depends upon the magnetic diffusion; with an appropriate value of the nondimensional Hall diffusion parameter $\tilde{\eta}_H$ a stable rotationally-supported disc forms in which the surface density Σ scales as $r^{-3/2}$ and vertical field strength $B_z \propto r^{-5/4}$. These are the scalings expected from other simulations of protostellar discs to which the solutions calculated in this work compare favourably. No disc may form when the Hall parameter is large (in comparison to the ambipolar diffusion parameter) and has the wrong sign (which indicates the orientation of the magnetic field with respect to the axis of rotation), as the diffusion in these solutions is too strong and causes disruptive torques that form subshocks in the full similarity solutions. This seemingly-odd behaviour occurs because the response of the fluid to Hall diffusion is not invariant under a global reversal of the magnetic field.

The second power law similarity solution describes the behaviour of the infall when the magnetic braking is efficient at removing angular momentum from the flow and no rotationally-supported disc forms. The matter falls rapidly onto the central protostar and what little angular momentum remains is that induced by the Hall effect; the direction of rotation depends upon the sign of the Hall parameter. This behaviour is indicative of the "magnetic braking catastrophe" that occurs in many magnetic collapse simulations.

The size of the rotationally-supported disc in the full similarity solutions was shown to vary with the amount of Hall and ambipolar diffusion affecting the pseudodisc through their effect on the magnetic braking in the fluid. By creating an additional torque on the disc, Hall diffusion can either increase or decrease the angular momentum and rotational support in the infalling fluid, leading to an order of magnitude change in the Keplerian disc radius between the similarity solutions at the extremes of $-0.5 \leq \tilde{\eta}_H/\tilde{\eta}_A \leq 0.2$ (where the ambipolar diffusion parameter, $\tilde{\eta}_A = 1$). A small amount of Hall diffusion was shown have a large effect on the solution because the dynamic range of collapse is itself many orders of magnitude in space and time. Hall diffusion causes there to be a preferred handedness to the field alignment and the direction of rotation in forming a large Keplerian disc that could be observed using next-generation instruments such as ALMA.

The accretion rate onto the central point mass is similarly influenced by the inclusion of Hall diffusion. This is a smaller effect than that on the disc radius, as between $\tilde{\eta}_H = \pm 0.1\tilde{\eta}_A$ (again with $\tilde{\eta}_A = 1$) the accretion rate onto the protostar only changes by 6%, or 0.2×10^{-6} $\mathrm{M}_\odot$ yr^{-1}. There exists a clear trend in which the accretion rate drops off with increasingly negative Hall parameters, as the reduced magnetic braking in these solutions causes a larger Keplerian disc to form through which accretion onto the protostar is slow.

It has also been shown that Hall diffusion can induce rotation in an initially non-rotating molecular cloud core, as the azimuthal torques twist the field lines, spinning up the core and envelope in opposite directions. The direction of spin in the core is determined by the sign of the Hall parameter; changing the sign of $\tilde{\eta}_H$ reverses the direction of rotation and shall also affect the size of the disc as in the solutions where the initial rotation is nonzero. As the density and flux rise the field decouples from the neutrals, and the azimuthal Hall diffusion causes the angular momentum to increase to the point where the centrifugal force roughly matches the gravitational force, suggesting that it is possible to form a centrifugal disc around the protostar.

The magnetic braking catastrophe could be resolved by the inclusion of Hall diffusion in numerical solutions, as with one sign of $\tilde{\eta}_H$ the Hall effect acts to reduce the total amount of braking affecting the core, preventing it from removing too much angular momentum from the collapse. However, with the other sign of $\tilde{\eta}_H$ the magnetic braking is increased so that more angular momentum is transported to the envelope. As magnetic braking due to Hall diffusion does not stop acting once no angular momentum remains (as ambipolar diffusion does) it could also then spin-up the collapsing fluid back up in the opposite direction to the initial rotation. This acceleration is only possible with Hall diffusion, and it has the potential to completely resolve the magnetic braking catastrophe.

Because of its tendency to pull the gas in unusual directions Hall diffusion is usually overlooked in simulations of gravitational collapse and star formation. It has been shown that the Hall effect is important to the dynamics of the collapse, particularly the magnetic braking behaviour which determines the existence and size of the rotationally-supported protostellar disc. The handedness of the response of the collapse to the inclusion of the Hall effect has obvious dynamical and potentially observable consequences for the gravitational collapse of molecular cloud cores, which must be studied more closely if the dynamics of the star formation process and the variations observed across YSOs and their discs are to be properly understood.

References

F. C. Adams and F. H. Shu. Ambipolar Diffusion in Molecular Cloud Cores and the Gravomagneto Catastrophe. *ApJ*, 671:497–517, 2007.

A. Allen, Z.-Y. Li, and F. H. Shu. Collapse of Magnetized Singular Isothermal Toroids: II. Rotation and Magnetic Braking. *ApJ*, 599:363–379, 2003a.

A. Allen, F. H. Shu, and Z.-Y. Li. Collapse of Magnetized Singular Isothermal Toroids: I. Non-Rotating Case. *ApJ*, 599:351–362, 2003b.

P. André, D. Ward-Thompson, and M. Barsony. From Prestellar Cores to Protostars: the Initial Conditions of Star Formation. In V. Mannings, A. P. Boss, and S. S. Russell, editors, *Protostars and Planets IV*. University of Arizona Press, 2000.

P. André, S. Basu, and S. Inutsuka. The Formation and Evolution of Prestellar Cores. In Chabrier, G., editor, *Structure Formation in Astrophysics*. Cambridge University Press, 2009.

S. M. Andrews and J. P. Williams. High-Resolution Submillimeter Constraints on Circumstellar Disk Structure. *ApJ*, 659:705–728, 2007.

M. Attard, M. Houde, G. Novak, H. Li, J. E. Vaillancourt, C. D. Dowell, J. Davidson, and H. Shinnaga. Magnetic Fields and Infall Motions in NGC 1333 IRAS 4. *ApJ*, 702:1584–1592, 2009.

S. A. Balbus and J. F. Hawley. Instability, Turbulence, and Enhanced Transport in Accretion Disks. *Reviews of Modern Physics*, 70:1–53, 1998.

J. Ballesteros-Paredes, R. S. Klessen, M.-M. Mac Low, and E. Vázquez-Semadeni. Molecular Cloud Turbulence and Star Formation. In B. Reipurth, D. Jewitt, and K. Keil, editors, *Protostars and Planets V*. University of Arizona Press, 2007.

S. Basu. A Semianalytic Model for Supercritical Core Collapse: Self-Similar Evolution and the Approach to Protostar Formation. *ApJ*, 485:240–253, 1997.

S. Basu. Constraints on the Formation and Evolution of Circumstellar Disks in Rotating Magnetized Cloud Cores. *ApJ*, 509:229–237, 1998.

S. Basu and G. E. Ciolek. Formation and Collapse of Nonaxisymmetric Protostellar Cores in Planar Magnetic Molecular Clouds. *ApJ*, 607:L39–L42, 2004.

S. Basu and T. Ch. Mouschovias. Magnetic Braking, Ambipolar Diffusion, and the Formation of Cloud Cores and Protostars. I: Axisymmetric Solutions. *ApJ*, 432: 720–741, 1994.

S. Basu and T. Ch. Mouschovias. Magnetic Braking, Ambipolar Diffusion, and the Formation of Cloud Cores and Protostars. II: A Parameter Study. *ApJ*, 452:386–400, 1995a.

S. Basu and T. Ch. Mouschovias. Magnetic Braking, Ambipolar Diffusion, and the Formation of Cloud Cores and Protostars. III: Effect of the Initial Mass-to-Flux Ratio. *ApJ*, 453:271–283, 1995b.

M. R. Bate. Collapse of a Molecular Cloud Core to Stellar Densities: the Radiative Impact of Stellar Core Formation on the Circumstellar Disc. *MNRAS*, 404:L79–L83, 2010.

M. R. Bate and I. A. Bonnell. The Origin of the Initial Mass Function and its Dependence on the Mean Jeans Mass in Molecular Clouds. *MNRAS*, 356:1201–1221, 2005.

E. A. Bergin and W. D. Langer. Chemical Evolution in Preprotostellar and Protostellar Cores. *ApJ*, 486:316–328, 1997.

F. Bertoldi and C. F. McKee. Pressure-confined Clumps in Magnetized Molecular Clouds. *ApJ*, 395:140–157, 1992.

R. D. Blandford and D. G. Payne. Hydrodynamic Flows from Accretion Discs and the Production of Radio Jets. *MNRAS*, 199:883–903, 1982.

J. Blum and G. Wurm. The Growth Mechanisms of Macroscopic Bodies in Protoplanetary Disks. *Ann. Rev. Astron. Astrophys.*, 46:21–56, 2008.

P. Bodenheimer. Angular Momentum Evolution of Young Stars and Disks. *Ann. Rev. Astron. Astrophys.*, 33:199–238, 1995.

I. A. Bonnell, M. A. Bate, C. J. Clarke, and J. E. Pringle. Accretion and the Stellar Mass Spectrum in Small Clusters. *MNRAS*, 285:201–208, 1997.

A. P. Boss. Collapse and Fragmentation of Molecular Cloud Cores. X: Magnetic Braking of Prolate and Oblate Cores. *ApJ*, 697:1940–1945, 2009.

A. G. W. Cameron and M. R. Pine. Numerical Models of the Primitive Solar Nebula. *Icarus*, 18:377–406, 1973.

G. Chabrier, I. Baraffe, F. Selsis, T. S. Barman, P. Hennebelle, and Y. Alibert. Gaseous Planets, Protostars and Young Brown Dwarfs: Birth and Fate. In B. Reipurth, D. Jewitt, and K. Keil, editors, *Protostars and Planets V*. University of Arizona Press, 2007.

S. Chandrasekhar and E. Fermi. Problems of Gravitational Stability in the Presence of a Magnetic Field. *ApJ*, 118:116–141, 1953.

A. Ciardi and P. Hennebelle. Outflows and Mass Accretion in Collapsing Dense Cores with Misaligned Rotation Axis and Magnetic Field. *MNRAS*, 409:L39–L43, 2010.

G. E. Ciolek and A. Königl. Dynamical Collapse of Nonrotating Magnetic Molecular Cloud Cores: Evolution Through Point-Mass Formation. *ApJ*, 504:257–279, 1998.

G. E. Ciolek and T. Ch. Mouschovias. Ambipolar Diffusion, Interstellar Dust, and the Formation of Cloud Cores and Protostars. I: Basic Physics and Formulation of the Problem. *ApJ*, 418:774–493, 1993.

G. E. Ciolek and T. Ch. Mouschovias. Ambipolar Diffusion, Interstellar Dust, and the Formation of Cloud Cores and Protostars. III: Typical Axisymmetric Solutions. *ApJ*, 425:142–160, 1994.

G. E. Ciolek and T. Ch. Mouschovias. Ambipolar Diffusion, Interstellar Dust, and the Formation of Cloud Cores and Protostars. IV: Effect of Ultraviolet Ionization and Magnetically Controlled Infall Rate. *ApJ*, 454:194–216, 1995.

G. E. Ciolek and T. Ch. Mouschovias. Effect of Ambipolar Diffusion on Ion Abundances in Contracting Protostellar Cores. *ApJ*, 504:280–289, 1998.

P. C. Clark and I. A. Bonnell. Star Formation in Transient Molecular Clouds. *MNRAS*, 347:L36–L40, 2004.

P. C. Clark and I. A. Bonnell. Clumpy Shocks and the Clump Mass Function. *MNRAS*, 368:1787–1795, 2006.

I. Contopoulos, G. E. Ciolek, and A. Königl. Self-Similar Collapse of Nonrotating Magnetic Molecular Cloud Cores. *ApJ*, 504:247–256, 1998.

I. Contopoulos, D. M. Christodoulou, D. Kazanas, and D. C. Gabuzda. The Invariant Twist of Magnetic Fields in the Relativistic Jets of Active Galactic Nuclei. *ApJL*, 702:L148–L152, 2009.

P. Cortes and R. M. Crutcher. Interferometric Mapping of Magnetic Fields: G30.79 FIR 10. *ApJ*, 639:965–968, 2006.

T. G. Cowling. *Magnetohydrodynamics*. Interscience, New York, 1957.

R. M. Crutcher. Magnetic Fields in Molecular Clouds: Observations Confront Theory. *ApJ*, 520:706–713, 1999.

R. M. Crutcher and T. H. Troland. Magnetic Fields and Star Formation — New Observational Results. In B. G. Elmegreen and J. Palous, editors, *Proceedings IAU Symposium No. 237: Triggered Star Formation in a Turbulent ISM*. Cambridge University Press, 2007.

R. M. Crutcher, N. Hakobian, and T. H. Troland. Testing Magnetic Star Formation Theory. *ApJ*, 692:844–855, 2009.

P. D'Alessio, J. Canto, N. Calvet, and S. Lizano. Accretion Disks Around Young Objects. I: The Detailed Vertical Structure. *ApJ*, 500:411–427, 1998.

W. B. Dapp and S. Basu. Averting the Magnetic Braking Catastrophe on Small Scales: Disk Formation due to Ohmic Dissipation. *A&A*, 521:L56–L59, 2010.

S. J. Desch and T. Ch. Mouschovias. The Magnetic Decoupling Stage of Star Formation. *ApJ*, 550:314–333, 2001.

J. di Francesco, P. C. Myers, D. J. Wilner, N. Ohashi, and D. Mardones. Infall, Outflow, Rotation, and Turbulent Motions of Dense Gas within NGC 1333 IRAS 4. *ApJ*, 562:770–789, 2001.

J. di Francesco, N. J. Evans, II, P. Caselli, P. C. Myers, Y. Shirley, Y. Aikawa, and M. Tafalla. An Observational Perspective of Low-Mass Dense Cores I: Internal Physical and Chemical Properties. In B. Reipurth, D. Jewitt, and K. Keil, editors, *Protostars and Planets V*. University of Arizona Press, 2007.

C. L. Dobbs. GMC formation by agglomeration and self-gravity. *MNRAS*, 391:844–858, 2008.

C. L. Dobbs, A. Burkert, and J. E. Pringle. Why Are Most Molecular Clouds Not Gravitationally Bound? *MNRAS*, 413:2935–2942, 2011.

B. T. Draine and C. F. McKee. Theory of Interstellar Shocks. *Ann. Rev. Astron. Astrophys.*, 31:373–433, 1993.

B. T. Draine, W. G. Roberge, and A. Dalgarno. Magnetohydrodynamic Shock Waves in Molecular Clouds. *ApJ*, 264:485–507, 1983.

C. P. Dullemond and J. D. Monnier. The Inner Regions of Protoplanetary Disks. *Ann. Rev. Astron. Astrophys.*, 48:205–239, 2010.

B. G. Elmegreen. Magnetic Diffusion and Ionization Fractions in Dense Molecular Clouds — the Role of Charged Grains. *ApJ*, 232:729–739, 1979.

B. G. Elmegreen. Formation of Interstellar Clouds and Structure. In E. H. Levy and J. I. Lunine, editors, *Protostars and Planets III*. University of Arizona Press, 1993.

B. G. Elmegreen. On the Rapid Collapse and Evolution of Molecular Clouds. *ApJ*, 668:1064–1082, 2007.

ESO. Science With ALMA, 2001. URL `www.eso.org/sci/facilities/alma/science/papers/alma-science.pdf`.

N. J. Evans, II. Physical Conditions in Regions of Star Formation. *Ann. Rev. Astron. Astrophys.*, 37:311–362, 1999.

M. Fatuzzo, F. C. Adams, and P. C. Myers. Generalized Collapse Solutions with Nonzero Initial Velocities for Star Formation in Molecular Cloud Cores. *ApJ*, 615: 813–831, 2004.

C. Federrath, R. Banerjee, P. C. Clark, and R. S. Klessen. Modeling Collapse and Accretion in Turbulent Gas Clouds: Implementation and Comparison of Sink Particles in AMR and SPH. *ApJ*, 713:269–290, 2010.

R. A. Fiedler and T. Ch. Mouschovias. Ambipolar Diffusion and Star Formation: Formation and Contraction of Axisymmetric Cloud Cores. I: Formulation of the Problem and Method of Solution. *ApJ*, 391:199–219, 1992.

R. A. Fiedler and T. Ch. Mouschovias. Ambipolar Diffusion and Star Formation: Formation and Contraction of Axisymmetric Cloud Cores. II: Results. *ApJ*, 415: 680–700, 1993.

G. B. Field. Conditions in Collapsing Clouds. In T. Gehrels, editor, *Protostars and Planets*. University of Arizona Press, 1978.

K. Freeman and J. Bland-Hawthorn. The New Galaxy: Signatures of Its Formation. *Ann. Rev. Astron. Astrophys.*, 40:487–537, 2002.

D. Galli and F. H. Shu. Collapse of Magnetized Molecular Cloud Cores. I: Semianalytical Solution. *ApJ*, 417:220–242, 1993a.

D. Galli and F. H. Shu. Collapse of Magnetized Molecular Cloud Cores. II: Numerical Results. *ApJ*, 417:243–258, 1993b.

D. Galli, S. Lizano, F. H. Shu, and A. Allen. Gravitational Collapse of Magnetized Clouds. I: Ideal Magnetohydrodynamic Accretion Flow. *ApJ*, 647:374–381, 2006.

D. Galli, M. Cai, S. Lizano, and F. H. Shu. Magnetic Braking and Field Dissipation in the Protostellar Accretion Phase. In A. Esquivel, J. Franco, G. García-Segura, E. M. de Gouveia Dal Pino, A. Lazarian, and A. Raga, editors, *Magnetic Fields in the Universe II*. Revista Mexicana de Astronomía y Astrofísica (Serie de Conferencias), 2009.

J. E. Gaustad. The Opacity of Diffuse Cosmic Matter and the Early Stages of Star Formation. *ApJ*, 138:1050–1073, 1963.

P. Ghosh and F. K. Lamb. Accretion by Rotating Magnetic Neutron Stars. II: Radial and Vertical Structure of the Transition Zone in Disk Accretion. *ApJ*, 232:259–276, 1979a.

P. Ghosh and F. K. Lamb. Accretion by Rotating Magnetic Neutron Stars. III: Accretion Torques and Period Changes in Pulsating X-Ray Sources. *ApJ*, 234:296–316, 1979b.

P. Ghosh, C. J. Pethick, and F. K. Lamb. Accretion by Rotating Magnetic Neutron Stars. I: Flow of Matter Inside the Magnetosphere and its Implications for Spin-up and Spin-down of the Star. *ApJ*, 217:578–596, 1977.

D. L. Gilden. Thermal Instability in Molecular Clouds. *ApJ*, 282:679–686, 1984.

J. M. Girart, R. Rao, and D. P. Marrone. Magnetic Fields in the Formation of Sun-Like Stars. *Science*, 313:812–814, 2006.

A. E. Glassgold, P. S. Krstić, and D. R. Schultz. H^++H Scattering and Ambipolar Diffusion Heating. *ApJ*, 621:808–816, 2005.

J. Gonçalves, D. Galli, and J. M. Girart. Modeling the Magnetic Field in the Protostellar Source NGC 1333 IRAS 4A. *A&A*, 490:L39–L42, 2008.

A. A. Goodman, P. J. Benson, G. A. Fuller, and P. C. Myers. Dense Cores in Dark Clouds. VIII: Velocity Gradients. *ApJ*, 406:528–547, 1993.

A. A. Goodman, J. A. Barranco, D. J. Wilner, and M. H. Heyer. Coherence in Dense Cores. II: The Transition to Coherence. *ApJ*, 504:223–246, 1998.

S. P. Goodwin, D. Ward-Thompson, and A. P. Whitworth. Why Do Starless Cores Appear More Flattened than Protostellar Cores? *MNRAS*, 330:769–771, 2002.

T. Greene. Protostars. *American Scientist*, 89(4):316, 2001.

C. Hayashi. Structure of the Solar Nebula, Growth and Decay of Magnetic Fields and Effects of Magnetic and Turbulent Viscosities on the Nebula. *Progress of Theoretical Physics Supplement*, 70:35–53, 1981.

C. Hayashi and T. Nakano. Thermal and Dynamical Properties of a Protostar and its Contraction to the Stage of Quasi-Static Equilibrium. *Progress of Theoretical Physics*, 34:754–775, 1965.

C. Hayashi, S. Narita, and S. M. Miyama. Analytic Solutions for Equilibrium of Rotating Isothermal Clouds — One-Parameter Family of Axisymmetric and Conformal Configurations. *Progress of Theoretical Physics*, 68:1949–1966, 1982.

J. C. Hayes, M. L. Norman, R. A. Fiedler, J. O. Bordner, P. S. Li, S. E. Clark, A. ud-Doula, and M. Mac Low. Simulating Radiating and Magnetized Flows in Multiple Dimensions with ZEUS-MP. *ApJS*, 165:188–228, 2006.

P. Hennebelle and A. Ciardi. Disk Formation During Collapse of Magnetized Protostellar Cores. *A&A*, 506:L29–L32, 2009.

F. Hoyle. The Synthesis of the Elements from Hydrogen. *MNRAS*, 106:343–383, 1946.

W. M. Irvine. The Composition of Interstellar Molecular Clouds. *Space Science Reviews*, 90:203–218, 1999.

J. H. Jeans. *Astronomy and Cosmogony*. Cambridge University Press, 1928.

C. E. Jones and S. Basu. The Intrinsic Shapes of Molecular Cloud Fragments over a Range of Length Scales. *ApJ*, 569:280–287, 2002.

C. E. Jones, S. Basu, and J. Dubinski. Intrinsic Shapes of Molecular Cloud Cores. *ApJ*, 551:387–393, 2001.

J. K. Jørgensen, T. L. Bourke, P. C. Myers, J. Di Francesco, E. F. van Dishoeck, C. Lee, N. Ohashi, F. L. Schöier, S. Takakuwa, D. J. Wilner, and Q. Zhang. PROSAC: A Submillimeter Array Survey of Low-Mass Protostars. I. Overview of Program: Envelopes, Disks, Outflows, and Hot Cores. *ApJ*, 659:479–498, 2007.

H. Kamaya and R. Nishi. Frozen Condition for the Charged Particles in Molecular Clouds. *ApJ*, 543:257–270, 2000.

B. D. Kane and D. P. Clemens. Rotation of Starless Bok Globules. *AJ*, 113:1799–1814, 1997.

Y. Kitamura, M. Momose, S. Yokogawa, R. Kawabe, M. Tamura, and S. Ida. Investigation of the Physical Properties of Protoplanetary Disks around T Tauri Stars by a 1 Arcsecond Imaging Survey: Evolution and Diversity of the Disks in Their Accretion Stage. *ApJ*, 581:357–380, 2002.

R. S. Klessen, M. R. Krumholz, and F. Heitsch. Numerical Star-Formation Studies — A Status Report. *Advanced Science Letters*, 4(2):258–285, 2011.

A. Königl. Disk accretion onto magnetic T Tauri stars. *ApJL*, 370:L39–L43, 1991.

A. Königl. On the Interpretation of the Apparent Existence of a Preferred Magnetic Polarity in Extragalactic Jet Sources. *MNRAS*, 407:L79–L83, 2010.

A. Königl and R. Salmeron. The Effects of Large-Scale Magnetic Fields on Disk Formation and Evolution. In P. J. V. Garcia, editor, *Physical Processes in Circumstellar Disks around Young Stars*. University of Chicago Press, 2011.

R. Krasnopolsky and A. Königl. Self-Similar Collapse of Rotating Magnetic Molecular Cloud Cores. *ApJ*, 580:987–1012, 2002.

R. Krasnopolsky, Z. Li, and H. Shang. Disk Formation Enabled by Enhanced Resistivity. *ApJ*, 716:1541–1550, 2010.

R. Krasnopolsky, Z. Li, and H. Shang. Disk Formation in Magnetized Clouds Enabled by the Hall Effect. *ApJ*, 733:54–59, 2011.

M. R. Krumholz. Star Formation with Adaptive Mesh Refinement Radiation Hydrodynamics. In Alves, J and Elmegreen, B. G. and Girart, J. M. and Trimble, V., editor, *Proceedings IAU Symposium 270: Computational Star Formation*. Cambridge University Press, 2011.

M. R. Krumholz and C. F. McKee. A Minimum Column Density of 1 g cm^{-2} for Massive Star Formation. *Nature*, 451:1082–1084, 2008.

T. Kudoh, S. Basu, Y. Ogata, and T. Yabe. Three-Dimensional Simulations of Molecular Cloud Fragmentation Regulated by Magnetic Fields and Ambipolar Diffusion. *MNRAS*, 380:499–505, 2007.

T. B. H. Kuiper, W. D. Langer, and T. Velusamy. Evolutionary Status of the Preprotostellar Core L1498. *ApJ*, 468:761–773, 1996.

M. W. Kunz and T. C. Mouschovias. The Non-Isothermal Stage of Magnetic Star Formation. II: Results. *MNRAS*, 408:322–341, 2010.

M. W. Kunz and T. Ch. Mouschovias. The Nonisothermal Stage of Magnetic Star Formation. I: Formulation of the Problem and Method of Solution. *ApJ*, 693:1895–1911, 2009.

C. J. Lada, E. A. Bergin, J. F. Alves, and T. L. Huard. The Dynamical State of Barnard 68: A Thermally Supported, Pulsating Dark Cloud. *ApJ*, 586:286–295, 2003.

W. D. Langer, E. F. van Dishoek, E. A. Bergin, G. A. Blake, A. G. G. M. Tielens, T. Velusamy, and D. C. B. Whittet. Chemical Evolution of Protostellar Matter. In V. Mannings, A. P. Boss, and S. S. Russell, editors, *Protostars and Planets IV*. University of Arizona Press, 2000.

R. B. Larson. Numerical Calculations of the Dynamics of a Collapsing Proto-Star. *MNRAS*, 145:271–295, 1969.

R. B. Larson. Cloud Fragmentation and Stellar Masses. *MNRAS*, 214:379–393, 1985.

R. B. Larson. The Physics of Star Formation. *Reports on Progress in Physics*, 66: 1651–1697, 2003.

R. B. Larson. Insights from Simulations of Star Formation. *Reports on Progress in Physics*, 70:337–356, 2007.

A. Lazarian. Astrophysical Implications of Turbulent Reconnection: From Cosmic Rays to Star Formation. In E. M. de Gouveia dal Pino, G. Lugones, & A. Lazarian, editor, *Magnetic Fields in the Universe: From Laboratory and Stars to Primordial Structures.*, volume 784 of *American Institute of Physics Conference Series*, pages 42–53, 2005.

C. Lee, P. T. P. Ho, and S. M. White. Molecular Line Observations of IRAM 04191+1522. *ApJ*, 619:948–958, 2005.

C. W. Lee, P. C. Myers, and M. Tafalla. A Survey for Infall Motions toward Starless Cores. II: CS (2–1) and N_2H^+ (1–0) Mapping Observations. *ApJS*, 136:703–734, 2001.

Z. Li. Magnetohydrodynamic Disk-Wind Connection: Magnetocentrifugal Winds from Ambipolar Diffusion-Dominated Accretion Disks. *ApJ*, 465:855–868, 1996.

Z.-Y. Li. Self-Similar Collapse of Magnetized Molecular Cloud Cores with Ambipolar Diffusion and the "Magnetic Flux Problem" in Star Formation. *ApJ*, 497:850–858, Apr. 1998.

Z.-Y. Li and C. F. McKee. Hydromagnetic Accretion Shocks Around Low-Mass Protostars. *ApJ*, 464:373–386, 1996.

Z.-Y. Li and F. Nakamura. Magnetically Regulated Star Formation in Turbulent Clouds. *ApJL*, 609:L83–L86, 2004.

Z.-Y. Li and F. H. Shu. Self-Similar Collapse of an Isopedic Isothermal Disk. *ApJ*, 457:237–250, 1997.

R. V. E. Lovelace, M. M. Romanova, and W. I. Newman. Implosive Accretion and Outbursts of Active Galactic Nuclei. *ApJ*, 437:136–143, 1994.

M.-M. Mac Low and R. S. Klessen. Control of Star Formation by Supersonic Turbulence. *Reviews of Modern Physics*, 76:125–194, 2004.

M. N. Machida. Recent Developments in Simulations of Low-Mass Star Formation. In Alves, J and Elmegreen, B. G. and Girart, J. M. and Trimble, V., editor, *Proceedings IAU Symposium 270: Computational Star Formation*. Cambridge University Press, 2011.

M. N. Machida, S. Inutsuka, and T. Matsumoto. Second Core Formation and High-Speed Jets: Resistive Magnetohydrodynamic Nested Grid Simulations. *ApJL*, 647: L151–L154, 2006.

M. N. Machida, S. Inutsuka, and T. Matsumoto. Magnetic Fields and Rotations of Protostars. *ApJ*, 670:1198–1213, 2007.

M. N. Machida, S. Inutsuka, and T. Matsumoto. High- and Low-Velocity Magnetized Outflows in the Star Formation Process in a Gravitationally Collapsing Cloud. *ApJ*, 676:1088–1108, 2008a.

M. N. Machida, T. Matsumoto, and S. Inutsuka. Magnetohydrodynamics of Population III Star Formation. *ApJ*, 685:690–704, 2008b.

M. N. Machida, S. Inutsuka, and T. Matsumoto. Effect of Magnetic Braking on the Circumstellar Disk Formation in a Strongly Magnetized Cloud. *PASJ*, 63:555–573, 2011.

L. Magnani, J. Caillault, A. Buchalter, and C. A. Beichman. A Search for T Tauri Stars in High-Latitude Molecular Clouds. II: The IRAS Faint Source Survey Catalog. *ApJS*, 96:159–173, 1995.

H. Masunaga and S. Inutsuka. A Radiation Hydrodynamic Model for Protostellar Collapse. II: The Second Collapse and the Birth of a Protostar. *ApJ*, 531:350–365, 2000.

T. Matsumoto and T. Hanawa. Fragmentation of a Molecular Cloud Core versus Fragmentation of the Massive Protoplanetary Disk in the Main Accretion Phase. *ApJ*, 595:913–934, 2003.

T. Matsumoto, T. Hanawa, and F. Nakamura. Gravitational Contraction of Rotating Clouds: Formation of Self-Similarly Collapsing Disks. *ApJ*, 478:569–584, 1997.

S. Matt and R. E. Pudritz. Accretion-Powered Stellar Winds. III: Spin-Equilibrium Solutions. *ApJ*, 681:391–399, 2008.

C. F. McKee and E. C. Ostriker. Theory of Star Formation. *Ann. Rev. Astron. Astrophys.*, 45:565–687, 2007.

C. F. McKee, J. W. V. Storey, D. M. Watson, and S. Green. Far-Infrared Rotational Emission by Carbon Monoxide. *ApJ*, 259:647–656, 1982.

C. F. McKee, E. G. Zweibel, A. A. Goodman, and C. Heiles. Magnetic Fields in Star-Forming Regions — Theory. In E. H. Levy and J. I. Lunine, editors, *Protostars and Planets III*. University of Arizona Press, 1993.

R. R. Mellon and Z.-Y. Li. Magnetic Braking and Protostar Formation: The Ideal MHD Limit. *ApJ*, 681:1356–1376, 2008.

R. R. Mellon and Z.-Y. Li. Magnetic Braking and Protostar Formation: Ambipolar Diffusion. *ApJ*, 698:922–927, 2009.

L. Mestel and L. Spitzer, Jr. Star Formation in Magnetic Dust Clouds. *MNRAS*, 116: 503–514, 1956.

S. A. Morton, T. Ch. Mouschovias, and G. E. Ciolek. Ambipolar Diffusion, Interstellar Dust, and the Formation of Cloud Cores and Protostars. II: Numerical Method of solution. *ApJ*, 421:561–569, 1994.

T. Ch. Mouschovias. Magnetic Braking, Ambipolar Diffusion, Cloud Cores, and Star Formation: Natural Length Scales and Protostellar Masses. *ApJ*, 373:169–186, 1991.

T. Ch. Mouschovias and E. V. Paleologou. The Angular Momentum Problem and Magnetic Braking: An Exact, Time-dependent Solution. *ApJ*, 230:204–222, 1979.

T. Ch. Mouschovias and E. V. Paleologou. Magnetic Braking of an Aligned Rotator During Star Formation: An Exact, Time-dependent Solution. *ApJ*, 237:877–899, 1980.

T. Ch. Mouschovias and L. Spitzer, Jr. Note on the Collapse of Magnetic Interstellar Clouds. *ApJ*, 210:326–327, 1976.

T. Ch. Mouschovias and K. Tassis. Testing Molecular-Cloud Fragmentation Theories: Self-Consistent Analysis of OH Zeeman Observations. *MNRAS*, 400:L15–L19, 2009.

P. C. Myers. Initial Conditions and Motions in Star-Forming Dense Cores. In V. Ossenkopf, J. Stutzki, and G. Winnewisser, editors, *The Physics and Chemistry of the Interstellar Medium, Proceedings of the 3rd Cologne-Zermatt Symposium*. GCA-Verlag, 1999.

T. Nakano. Nonconservation of Magnetic Flux in Star Formation. *PASJ*, 35:87–90, 1983.

T. Nakano and T. Nakamura. Gravitational Instability of Magnetized Gaseous Disks. *PASJ*, 30:671–679, 1978.

T. Nakano and T. Umebayashi. Dissipation of Magnetic Fields in Very Dense Interstellar Clouds. I: Formulation and Conditions for Efficient Dissipation. *MNRAS*, 218:663–684, 1986a.

T. Nakano and T. Umebayashi. Dissipation of Magnetic Fields in Very Dense Interstellar Clouds. II: Final Phases of Star Formation and the Magnetic Flux of a Newborn Star. *MNRAS*, 231:319–338, 1986b.

T. Nakano, R. Nishi, and T. Umebayashi. Mechanism of Magnetic Flux Loss in Molecular Clouds. *ApJ*, 573:199–214, 2002.

D. A. Neufeld and D. J. Hollenbach. Dense Molecular Shocks and Accretion onto Protostellar Disks. *ApJ*, 428:170–185, 1994.

I. Newton. *Philosophiae naturalis principia mathematica, Vol. 1–4*. 1760.

R. Nishi, T. Nakano, and T. Umebayashi. Magnetic Flux Loss from Interstellar Clouds with Various Grain-Size Distributions. *ApJ*, 368:181–194, 1991.

C. Norman and J. Heyvaerts. Anomalous Magnetic Field Diffusion During Star Formation. *A&A*, 147:247–256, 1985.

C. Norman and J. Silk. Clumpy Molecular Clouds — A Dynamic Model Self-Consistently Regulated by T Tauri Star Formation. *ApJ*, 238:158–174, 1980.

M. Ohishi and N. Kaifu. Chemical and Physical Evolution of Dark Clouds. Molecular Spectral Line Survey Toward TMC-1. In *Chemistry and Physics of Molecules and Grains in Space*, Faraday Discussions No. 109, pages 205–216. The Faraday Division of the Royal Society of Chemistry, London, 1998.

B. P. Pandey and M. Wardle. Hall Magnetohydrodynamics of Partially Ionized Plasmas. *MNRAS*, 385:2269–2278, 2008.

M. V. Penston. Dynamics of Self-Gravitating Gaseous Spheres. III: Analytical Results in the Free-Fall of Isothermal Cases. *MNRAS*, 144:425–448, 1969.

L. Pirogov, I. Zinchenko, P. Caselli, L. E. B. Johansson, and P. C. Myers. $N_2H^+(1-0)$ Survey of Massive Molecular Cloud Cores. *A&A*, 405:639–654, 2003.

G. W. Pneuman and T. P. Mitchell. Evolution of the Solar Magnetic Field. *Icarus*, 4: 494–505, 1965.

W. H. Press, S. A. Teukolsky, W. T. Vetterling, and B. P. Flannery. *Numerical Recipes in Fortran 77*. Cambridge University Press, second edition, 1992.

D. J. Price and M. R. Bate. The Impact of Magnetic Fields on Single and Binary Star Formation. *MNRAS*, 377:77–90, 2007.

D. J. Price and M. R. Bate. Inefficient Star Formation: the Combined Effects of Magnetic Fields and Radiative Feedback. *MNRAS*, 398:33–46, 2009.

D. J. Price, M. R. Bate, and C. L. Dobbs. Magnetic Fields in Star Formation: From Galaxies to Stars. In A. Esquivel, J. Franco, G. García-Segura, E. M. de Gouveia Dal Pino, A. Lazarian, and A. Raga, editors, *Magnetic Fields in the Universe II*. Revista Mexicana de Astronomía y Astrofísica (Serie de Conferencias), 2008.

R. E. Pudritz, R. Ouyed, C. Fendt, and A. Brandenburg. Disk Winds, Jets, and Outflows: Theoretical and Computational Foundations. In B. Reipurth, D. Jewitt, and K. Keil, editors, *Protostars and Planets V*. University of Arizona Press, 2007.

B. S. Ryden. The Shapes of Dense Cores and Bok Globules. *ApJ*, 471:822–831, 1996.

V. S. Safronov. The Protoplanetary Cloud and Its Evolution. *Soviet Astronomy*, 10: 650–658, 1967.

K. Saigo and T. Hanawa. Similarity Solution for Formation of a Circumstellar Disk Through the Collapse of a Flattened Rotating Cloud. *ApJ*, 493:342–350, 1998.

R. Salmeron. The Role of Magnetic Fields in Star Formation. In W. Short and I. Cairns, editors, *Australian Space Science Conference Series: 8th Conference Proceedings NSSA Full Referreed Proceedings CD*. National Space Society of Australia Ltd, 2009.

R. Salmeron and M. Wardle. Magnetorotational Instability in Stratified, Weakly Ionized Accretion Discs. *MNRAS*, 345:992–1008, 2003.

R. Salmeron and M. Wardle. Magnetorotational Instability in Weakly Ionised, Stratified Accretion Discs. *Ap&SS*, 292:451–456, 2004.

R. Salmeron and M. Wardle. Magnetorotational Instability in Protoplanetary Discs. *MNRAS*, 361:45–69, 2005.

R. Salmeron, A. Königl, and M. Wardle. Angular Momentum Transport in Protostellar Discs. *MNRAS*, 375:177–183, 2007a.

R. Salmeron, A. Königl, and M. Wardle. Radial and Vertical Angular Momentum Transport in Protostellar Discs. *Ap&SS*, 311:81–85, 2007b.

R. Salmeron, A. Königl, and M. Wardle. Wind-Driving Protostellar Accretion Discs. II. Numerical Method and Illustrative Solutions. *MNRAS*, 412:1162–1180, 2011.

T. Sano and J. M. Stone. The Effect of the Hall Term on the Nonlinear Evolution of the Magnetorotational Instability. I: Local Axisymmetric Simulations. *ApJ*, 570: 314–328, 2002a.

T. Sano and J. M. Stone. The Effect of the Hall Term on the Nonlinear Evolution of the Magnetorotational Instability. II: Saturation Level and Critical Magnetic Reynolds Number. *ApJ*, 577:534–553, 2002b.

R. Santos-Lima, A. Lazarian, E. M. de Gouveia Dal Pino, and J. Cho. Diffusion of Magnetic Field and Removal of Magnetic Flux from Clouds via Turbulent Reconnection. *ApJ*, 714:442–461, 2010.

N. I. Shakura and R. A. Sunyaev. Black holes in binary systems. Observational appearance. *A&A*, 24:337–355, 1973.

F. H. Shu. Self-Similar Collapse of Isothermal Spheres and Star Formation. *ApJ*, 214: 488–497, 1977.

F. H. Shu and Z.-Y. Li. Magnetic Forces in an Isopedic Disk. *ApJ*, 457:251–259, 1997.

F. H. Shu, F. C. Adams, and S. Lizano. Star Formation in Molecular Clouds: Observation and Theory. *Ann. Rev. Astron. Astrophys.*, 25:23–81, 1987.

F. H. Shu, D. Galli, S. Lizano, and M. Cai. Gravitational Collapse of Magnetized Clouds. II: The Role of Ohmic Dissipation. *ApJ*, 647:382–389, 2006.

L. Spitzer. *Physical Processes in the Interstellar Medium.* New York: Wiley-Interscience, 1978.

H. C. Spruit, R. Stehle, and J. C. B. Papaloizou. Interchange Instability in an Accretion Disc with a Poloidal Magnetic Field. *MNRAS*, 275:1223–1231, 1995.

S. W. Stahler and F. Palla. *The Formation of Stars.* Wiley-VCH, 2004.

S. W. Stahler, D. G. Korycansky, M. J. Brothers, and J. Touma. The Early Evolution of Protostellar Disks. *ApJ*, 431:341–358, 1994.

A. A. Stark and Y. Lee. Giant Molecular Clouds are More Concentrated toward Spiral Arms than Smaller Clouds. *ApJL*, 641:L113–L116, 2006.

K. G. Stassun, R. D. Mathieu, T. Mazeh, and F. J. Vrba. The Rotation Period Distribution of Pre-Main-Sequence Stars in and around the Orion Nebula. *AJ*, 117: 2941–2979, 1999.

K. G. Stassun, R. D. Mathieu, F. J. Vrba, T. Mazeh, and A. Henden. A 10 Micron Search for Truncated Disks Among Pre-Main-Sequence Stars with Photometric Rotation Periods. *AJ*, 121:1003–1012, 2001.

P. A. Strittmatter. Gravitational Collapse in the Presence of a Magnetic Field. *MNRAS*, 132:359–378, 1966.

E. J. Tasker and J. C. Tan. Star Formation in Disk Galaxies. I: Formation and Evolution of Giant Molecular Clouds via Gravitational Instability and Cloud Collisions. *ApJ*, 700:358–375, 2009.

K. Tassis and T. Ch. Mouschovias. Magnetically Controlled Spasmodic Accretion During Star Formation. I: Formulation of the Problem and Method of Solution. *ApJ*, 618:769–782, 2005a.

K. Tassis and T. Ch. Mouschovias. Magnetically Controlled Spasmodic Accretion During Star Formation. II: Results. *ApJ*, 618:783–794, 2005b.

K. Tassis and T. Ch. Mouschovias. Protostar Formation in Magnetic Molecular Clouds Beyond Ion Detachment. I: Formulation of the Problem and Method of Solution. *ApJ*, 660:370–387, 2007a.

K. Tassis and T. Ch. Mouschovias. Protostar Formation in Magnetic Molecular Clouds Beyond Ion Detachment. II: Typical Axisymmetric Solution. *ApJ*, 660:388–401, 2007b.

K. Tassis and T. Ch. Mouschovias. Protostar Formation in Magnetic Molecular Clouds Beyond Ion Detachment. III: A Parameter Study. *ApJ*, 660:402–417, 2007c.

S. Terebey, F. H. Shu, and P. Cassen. The Collapse of the Cores of Slowly Rotating Isothermal Clouds. *ApJ*, 286:529–551, 1984.

A. G. G. M. Tielens. *The Physics and Chemistry of the Interstellar Medium*. Cambridge University Press, 2005.

K. Tomisaka. Collapse of Rotating Magnetized Molecular Cloud Cores and Mass Outflows. *ApJ*, 575:306–326, 2002.

K. Tomisaka, S. Ikeuchi, and T. Nakamura. The Equilibria and Evolutions of Magnetized, Rotating, Isothermal Clouds. I: Basic Equations and Numerical Methods. *ApJ*, 326:208–222, 1988a.

K. Tomisaka, S. Ikeuchi, and T. Nakamura. The Equilibria and Evolutions of Magnetized, Rotating, Isothermal Clouds. II: The Extreme Case: Nonrotating Clouds. *ApJ*, 335:239–262, 1988b.

A. Toomre. Some Flattened Isothermal Models of Galaxies. *ApJ*, 259:535–543, 1982.

W. M. Tscharnuter, J. Schönke, H. Gail, M. Trieloff, and E. Lüttjohann. Protostellar Collapse: Rotation and Disk Formation. *A&A*, 504:109–113, 2009.

T. Tsuribe and S. Inutsuka. Criteria for Fragmentation of Rotating Isothermal Clouds Revisited. *ApJL*, 523:L155–L158, 1999a.

T. Tsuribe and S. Inutsuka. Criteria for Fragmentation of Rotating Isothermal Clouds. I: Semianalytic Approach. *ApJ*, 526:307–313, 1999b.

T. Umebayashi and T. Nakano. Magnetic Flux Loss From Interstellar Clouds. *MNRAS*, 243:103–113, 1990.

J. S. Vink, J. E. Drew, T. J. Harries, R. D. Oudmaijer, and Y. Unruh. Probing the Circumstellar Structures of T Tauri Stars and their Relationship to those of Herbig Stars. *MNRAS*, 359:1049–1064, 2005.

D. Ward-Thompson. Isolated Star Formation: From Cloud Formation to Core Collapse. *Science*, 295:76–81, 2002.

D. Ward-Thompson, P. André, R. Crutcher, D. Johnston, T. Onishi, and C. Wilson. An Observational Perspective of Low Mass Dense Cores II: Evolution towards the Initial Mass Function. In B. Reipurth, D. Jewitt, and K. Keil, editors, *Protostars and Planets V*. University of Arizona Press, 2007.

M. Wardle. The Stability of Magnetohydrodynamic Shock Waves in Molecular Clouds. *MNRAS*, 246:98–109, Sept. 1990.

M. Wardle. Magnetically-Driven Winds from Protostellar Disks. In Wickramasinghe, D. T. and Bicknell, G. V. and Ferrario, L., editor, *Proceedings IAU Colloquium 163: Accretion Phenomena and Related Outflows*, volume 121 of *Astronomical Society of the Pacific Conference Series*, 1997.

M. Wardle. The Balbus–Hawley Instability in Weakly Ionized Discs. *MNRAS*, 307: 849–856, 1999.

M. Wardle. Star Formation and the Hall Effect. *Ap&SS*, 292:317–323, 2004a.

M. Wardle. Early Disk Evolution. In M. Burton, R. Jayawardhana, and T. Bourke, editors, *Proceedings IAU Symposium No. 221: Star Formation at High Angular Resolution*. Cambridge University Press, 2004b.

M. Wardle. Magnetic Fields in Protoplanetary Disks. *Ap&SS*, 311:35–45, 2007.

M. Wardle. Magnetic Activity in Protoplanetary Discs. In *Planetessimal Formation Workshop, Isaac Newton Institute for Mathematical Sciences, University of Cambridge*, available online at http://www.newton.ac.uk/programmes/DDP/seminars/093009001.html, 2009.

M. Wardle and A. Königl. The Structure of Protostellar Accretion Disks and the Origin of Bipolar Flows. *ApJ*, 410:218–238, 1993.

M. Wardle and C. Ng. The Conductivity of Dense Molecular Gas. *MNRAS*, 303: 239–246, 1999.

S. J. Weidenschilling. The Distribution of Mass in the Planetary System and Solar Nebula. *Ap&SS*, 51:153–158, 1977.

A. Whitworth and D. Summers. Self-Similar Condensation of Spherically Symmetric Self-gravitating Isothermal Gas Clouds. *MNRAS*, 214:1–25, 1985.

J. P. Williams, L. Blitz, and A. A. Stark. The Density Structure in the Rosette Molecular Cloud: Signposts of Evolution. *ApJ*, 451:252–274, 1995.

J. P. Williams, L. Blitz, and C. F. McKee. The Structure and Evolution of Molecular Clouds: From Clumps to Cores to the IMF. In V. Mannings, A. P. Boss, and S. S. Russell, editors, *Protostars and Planets IV*. University of Arizona Press, 2000.

K. Winkler and M. J. Newman. Formation of Solar-type Stars in Spherical Symmetry. I: The Key Role of the Accretion Shock. *ApJ*, 236:201–211, 1980.

M. C. Wyatt. Evolution of Debris Disks. *Ann. Rev. Astron. Astrophys.*, 46:339–383, 2008.

B. Zuckerman and P. Palmer. Radio Radiation from Interstellar Molecules. *Ann. Rev. Astron. Astrophys.*, 12:279–312, 1974.

Appendix A

Deriving the Inner Solutions

In this appendix the derivation of the inner asymptotic solutions discussed in Chapter 3 is presented as part of the exploration of pq-space that was proposed in Section 3.1. Only the derivation of physical solutions is presented here; while solutions in which the scale height tends to zero or the surface density is negative may satisfy the collapse equations they are unphysical and not pursued in this work. To briefly recap the early stages of the derivation from 3: the inner asymptotic similarity solutions are assumed to take the form of power laws in x, specifically

$$\sigma = \sigma_1 \, x^{-p}, \tag{A.1}$$

$$b_z = b_{z1} \, x^{-q}, \tag{A.2}$$

$$\text{and } j = j_1 \, x^{-r}, \tag{A.3}$$

where p, q and r are real numbers, and σ_1, b_{z1} and j_1 are constants. By substituting these power laws into the fluid equations and taking the limit as $x \to 0$ it is possible to solve for all of the fluid variables. The enclosed mass and flux may be written as

$$m = m_c + \frac{\sigma_1}{2-p} x^{2-p} \tag{A.4}$$

$$\text{and } \psi = \frac{b_{z1}}{2-q} \, x^{2-q}, \tag{A.5}$$

and the radial field component is

$$b_{r,s} = \frac{b_{z1}}{(2-q)} \, x^{-q}, \tag{A.6}$$

which clearly scales with the vertical field component.

Due to the cap on $b_{\phi,s}$, its precise value is not easily determined. However, as $|b_{\phi,s}| \leq \delta b_z$, the azimuthal field component is taken to be its largest possible value, scaling with $b_z \sim x^{-q}$, until it is possible to make refine this calculation.

The scale height is written as the solution to the quadratic equation (2.108):

$$h = \frac{\hat{\sigma} x^3}{2\hat{m}_c}\left[-1 + \sqrt{1 + \frac{8\hat{m}_c}{\hat{\sigma}^2 x^3}}\right], \tag{A.7}$$

where

$$\hat{m}_c = m_c - x^3 b_{r,s}\frac{db_z}{dx} \tag{A.8}$$

and

$$\hat{\sigma} = \sigma + \frac{b_{r,s}^2 + b_{\phi,s}^2}{\sigma}; \tag{A.9}$$

for any combination of p and q the behaviour of h can be determined. Figure 3.1, reproduced here as A.1, shows the different regions of pq-space in which $\hat{\sigma}$ and $\hat{m}_c$ take on the following forms:

A. $\hat{m}_c = m_c$ $(p > 2q - 2)$ (A.10)

B. $\hat{m}_c = -\frac{x^3 b_{r,s}}{\sigma}\left(\frac{db_z}{dx}\right)$ $(p < 2q - 2)$ (A.11)

C. $\hat{\sigma} = \sigma$ $(p > q)$ (A.12)

D. $\hat{\sigma} = \frac{(b_{r,s}^2 + b_{\phi,s}^2)}{\sigma}$ $(p < q)$ (A.13)

As explained in Section 3.1, only those solutions where

$$\frac{8\hat{m}_c}{\hat{\sigma}^2 x^3} \geq 1 \tag{A.14}$$

are sought, so that

$$h \sim \sqrt{\frac{2x^3}{\hat{m}_c}}. \tag{A.15}$$

Any similarity solutions that do not satisfy this criteria, while mathematically valid, are unphysical and so those regions of parameter space are not explored in this work. Each of the four regions of the pq-plane must be examined in order to find those physically possible similarity solutions.

A.1 Region AC

This section of the pq-plane is characterised by the following inequalities:

$$p > 2q - 2, \tag{A.16}$$

$$\text{and } p > q; \tag{A.17}$$

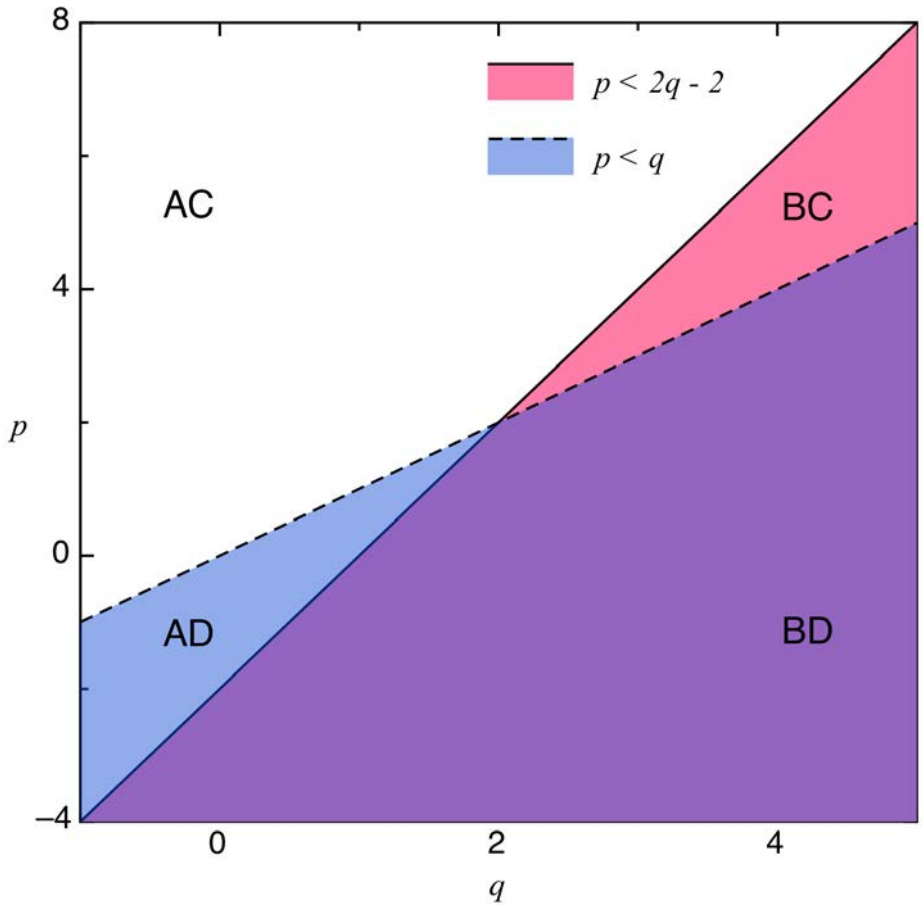

Figure A.1: The pq-plane used to describe how the components of h behave with respect to the exponents of σ and b_z. The different regions have been colour coded, for example, the white area in the upper left section of the plane represents the region AC where the inequalities $p > 2q - 2$ and $p > q$ are satisfied.

and is represented by the white area in the upper left of Figure A.1. In this region $8\hat{m}_c/\hat{\sigma}^2 x^3$ scales as

$$\frac{8\hat{m}_c}{\hat{\sigma}^2 x^3} \sim \frac{m_c}{\sigma^2 x^3} \sim x^{2p-3}, \tag{A.18}$$

so that h is given by

$$h = \frac{\sigma_1}{2m_c} x^{3-p} \left[-1 + \sqrt{1 + \frac{8m_c}{\sigma_1^2} x^{2p-3}} \right]. \tag{A.19}$$

The desired behaviour of h (denoted "case b" in Section 3.1) occurs when

$$2p - 3 < 0 \quad \Rightarrow \quad p, q < 3/2. \tag{A.20}$$

As these limits are well within the boundaries of region AC, the boundary case where $2p-3 = 0$ ($p = 3/2$) should also be examined. All of these restrictions on the exponents

imply that $2 - p \geq 1/2$, which means that as $x \to 0$

$$m = m_c, \tag{A.21}$$

while $h \sim x^{3/2}$ and $b_{\phi,s} \lesssim x^{-q}$.

Substituting these power law expressions into the angular momentum equation (2.107) shows that its terms scale as

$$\begin{aligned} \frac{dj}{dx} &\sim x^{-r-1}, \\ \frac{j}{w} &\sim x^{1-r-p}, \\ \text{and } \frac{x^2 b_z b_{\phi,s}}{m} &\lesssim x^{2-2q}. \end{aligned} \tag{A.22}$$

It is not possible to directly compare the exponents of these terms at this point, however it is clear that there are two possible solutions to this equation, the first of which is

$$\frac{dj}{dx} = \frac{j}{w}. \tag{A.23}$$

For this equation to be satisfied the exponents of the two terms must be equal, which implies that

$$-r - 1 = 1 - r - p \quad \Rightarrow \quad p = 2; \tag{A.24}$$

but as $p \leq 3/2$ this is a contradiction and there can be no solution to Equation A.23 satisfying the requirement that h has a positive and physically possible value.

The second possible solution to the angular momentum equation must then be adopted, which takes the form

$$\frac{dj}{dx} = -\frac{x^2 b_z b_{\phi,s}}{m}; \tag{A.25}$$

this equation cannot be solved fully until the scaling of $b_{\phi,s}$ is properly known, however examination of the exponents allows for a limit on r to be derived, as

$$-r - 1 \leq 2 - 2q \tag{A.26}$$

$$\therefore r \geq 2q - 3. \tag{A.27}$$

This also implies that $1 - r - p > 2 - 2q$, which can be used with the inequalities in A.16–A.17 to show that $r < 1$.

Examining the scaling of the pair of terms $b_{r,s} - h(db_z/dx)$ that occur in many of the equations shows that they scale with x as

$$\begin{aligned} b_{r,s} &\sim x^{-q} \\ \text{and } h\frac{db_z}{dz} &\sim x^{1/2-q}; \end{aligned} \tag{A.28}$$

the second exponent is clearly larger than the first, implying that this term is the smaller as the limit $x \to 0$ is taken, and can be discarded wherever it appears in the equations.

The other terms of the radial momentum equation (2.106) then scale with x as

$$\begin{aligned} \frac{1}{\sigma}\frac{d\sigma}{dx} &\sim x^{-1}, \\ \frac{w^2}{\sigma}\frac{d\sigma}{dx} &\sim x^{2p-3}, \\ \frac{m}{x^2} &\sim x^{-2}, \\ \frac{b_z b_{r,s}}{\sigma} &\sim x^{p-2q}, \\ \frac{j^2}{x^3} &\sim x^{-2r-3}, \\ \text{and } \frac{w^2}{x} &\sim x^{2p-3}. \end{aligned} \tag{A.29}$$

It is clear from comparing the exponents that the first term is smaller than the third and can be disregarded as small. The inequality A.16 gives $p - 2q > -2$, which means that the fourth term may also be disregarded, leaving a simplified radial momentum equation,

$$-w^2\left(\frac{1}{x} + \frac{1}{\sigma}\frac{d\sigma}{dx}\right) = -\frac{m}{x^2} + \frac{j^2}{x^3}, \tag{A.30}$$

that cannot be easily solved.

Without knowing the values of p and r, there are multiple simplified solutions to this equation:

$$\frac{m}{x^2} = \frac{j^2}{x^3} \qquad w^2\left(\frac{1}{x} + \frac{1}{\sigma}\frac{d\sigma}{dx}\right) = \frac{m}{x^2} \qquad -w^2\left(\frac{1}{x} + \frac{1}{\sigma}\frac{d\sigma}{dx}\right) = \frac{j^2}{x^3}. \tag{A.31}$$

The third of these requires that $2p - 3 < -2$, which is satisfied whenever $p < 1/2$. However, for j to be a real number the left hand side of the equation must be positive, which is only possible when $p > 1$. This contradiction means that there can be no physical solution to this equation.

The second of the equations in A.31 has the solution $p = 1/2$ and is satisfied when the inequality $p < -r$ holds true. This can be substituted into A.27 to show that $p < 2q - 3$, which is a contradiction of the inequality A.16 that defines this region of pq-space. Therefore this also cannot be a valid solution to the radial momentum equation.

The only solution to the radial momentum equation is then the first equation in A.31, which is solved to give

$$j = \sqrt{m_c x} \tag{A.32}$$

so that the exponent

$$r = -\frac{1}{2}. \tag{A.33}$$

This exponent is then substituted into the inequality A.27 to show that $q \leq 5/4$.

The scaling of $b_{\phi,s}$ can now be determined by examining the scaling with x of its component terms. The non-constant term in the denominator of the fraction on the left hand side of Equation 2.114 scales as

$$\frac{2\alpha\tilde{\eta}_A h^{1/2}\psi b_z}{x^2\sigma^{3/2}} \sim x^{3/4+3p/2-2q}; \tag{A.34}$$

as $p > q$, it is clear that $3p/2 - 2q > -q/2$, and that

$$3/4 + 3p/2 - 2q > 3/4 - q/2. \tag{A.35}$$

Finally, as $q \leq 3/2$, the inequality in A.35 becomes

$$3/4 + 3p/2 - 2q > 0; \tag{A.36}$$

this means that the non-constant term in the denominator of this fraction becomes smaller than the constant term as $x \to 0$ and may be dropped from the equation.

The $h(db_z/dx)$ term has already been dropped from the equation for $b_{\phi,s}$ (2.114), and the remaining terms in the numerator scale as

$$\frac{j}{x} \sim x^{-1/2}$$
$$\text{and } \frac{\tilde{\eta}_H b b_{r,s} h^{1/2}}{\sigma^{3/2}} \sim x^{3/4+3p/2-2q}. \tag{A.37}$$

The inequality in A.36 shows that j/x is therefore the dominant term in the numerator of this fraction, so that the Hall term is not important and the left hand side of the equation for $b_{\phi,s}$ scales with x as

$$\frac{2\alpha\psi j}{x^3} \sim x^{5/2-q-3} = x^{-q-1/2}. \tag{A.38}$$

This is a larger term than that on the right hand side of the equation for $b_{\phi,s}$, and so the right hand side is the minimum of these two sides, giving

$$b_{\phi,s} = -\delta b_z. \tag{A.39}$$

This solution illuminates the flaws in the way that $b_{\phi,s}$ was defined and the method adopted for describing the vertical angular momentum transport. It is not realistic for the azimuthal field to dominate the vertical field in the disc, and limiting the value of $b_{\phi,s}$ so that it scales as b_z is a reasonable simplification to keep it from becoming too large in this inner region. However, a better prescription for $b_{\phi,s}$ is needed in order to

properly understand and model the actual behaviour of the field as $x \to 0$, as discussed in Section 6.3.

To find the value of b_z, Equations A.21, A.32 and A.39 are substituted into the simplified angular momentum equation (A.25) to obtain the equation

$$\frac{1}{2}\sqrt{\frac{m_c}{x}} = \frac{x^2 \delta {b_z}^2}{m_c}, \tag{A.40}$$

which is rearranged and solved for b_z,

$$b_z = \frac{m_c^{3/4}}{\sqrt{2\delta}}\, x^{-5/4}, \tag{A.41}$$

and the exponent

$$q = \frac{5}{4}. \tag{A.42}$$

Curiously, b_z does not depend upon the diffusion coefficients, although they do influence the value of m_c in the solutions presented in Chapters 4 and 5, as discussed in Section 6.1. The flux and the other field components are then described by the power laws:

$$\psi = \frac{4}{3}\frac{m_c^{3/4}}{\sqrt{2\delta}}\, x^{3/4}, \tag{A.43}$$

$$b_{r,s} = \frac{4}{3} b_z = \frac{4}{3}\frac{m_c^{3/4}}{\sqrt{2\delta}}\, x^{-5/4}, \tag{A.44}$$

$$b_{\phi,s} = -\delta b_z = -\sqrt{\frac{\delta}{2}}\, m_c^{3/4} x^{-5/4} \tag{A.45}$$

$$\text{and } b = b_z \sqrt{\frac{25}{9} + \delta^2}. \tag{A.46}$$

Finally the induction equation (2.109) is examined, and as with the other equations the $h(db_z/dx)$ term is small and may be disregarded as $x \to 0$. The remaining terms in the equation scale with x as

$$\begin{aligned} \psi &\sim x^{3/4}, \\ x w b_z &\sim x^{p-5/4}, \\ \tilde{\eta}_H x b_{\phi,s} b_z b h^{1/2} \sigma^{-3/2} &\sim x^{3p/2-2}, \\ \text{and } \tilde{\eta}_A x b_{r,s} b_z^2 h^{1/2} \sigma^{-3/2} &\sim x^{3p/2-2}; \end{aligned} \tag{A.47}$$

as $3p/2 - 2 \leq 1/4$, then ψ is small compared to the other terms and is dropped from the induction equation. The induction equation is then simplified to

$$-x w b_z + \tilde{\eta}_H x b_{\phi,s} b_z b h^{1/2} \sigma^{-3/2} + \tilde{\eta}_A x b_{r,s} b_z^2 h^{1/2} \sigma^{-3/2} = 0; \tag{A.48}$$

which upon substitution of the scalings in A.21, A.32, A.41 and A.43–A.46 becomes

$$-\frac{m_c}{x\sigma}+\left(-\tilde{\eta}_H\delta\sqrt{\frac{25}{9}+\delta^2}+\frac{4}{3}\tilde{\eta}_A\right)b_z^2h^{1/2}\sigma^{-3/2}=0, \tag{A.49}$$

which is tidied to give

$$\frac{m_c\sigma^{1/2}}{x}=\left(\frac{4}{3}\tilde{\eta}_A-\tilde{\eta}_H\delta\sqrt{\frac{25}{9}+\delta^2}\right)b_z^2h^{1/2}. \tag{A.50}$$

The equation is then rearranged so that h is the subject:

$$h^{1/2}=\frac{2\delta}{f}\sqrt{\frac{\sigma_1}{m_c}}\,x^{3/2-p/2}; \tag{A.51}$$

the magnetic diffusion and azimuthal field cap parameters have been combined into a single parameter, f, defined as

$$f=\frac{4}{3}\tilde{\eta}_A-\tilde{\eta}_H\delta\sqrt{\frac{25}{9}+\delta^2}. \tag{A.52}$$

As it is known that $h\sim x^{3/2}$, equating the exponents of x in Equation A.51 gives

$$p=\frac{3}{2}. \tag{A.53}$$

This straddles the boundaries between cases a and b for the behaviour of h defined in Section 3.1, and so all of the terms in the equation for h (A.19) must be kept.

Squaring equation A.51 and equating it with Equation A.19 gives

$$\left(\frac{2\delta}{f}\right)^2\frac{\sigma_1}{m_c}=\frac{\sigma_1}{2m_c}\left(-1+\sqrt{1+\frac{8m_c}{\sigma_1^2}}\right), \tag{A.54}$$

where σ_1 is the coefficient of σ. This is rearranged into

$$2\left(\frac{2\delta}{f}\right)^2+1=\sqrt{1+\frac{8m_c}{\sigma_1^2}}, \tag{A.55}$$

and both sides are squared so that this equation becomes

$$4\left(\frac{2\delta}{f}\right)^4+4\left(\frac{2\delta}{f}\right)^2+1=1+\frac{8m_c}{\sigma_1^2}. \tag{A.56}$$

Equation A.56 may then be solved for the coefficient of σ:

$$\sigma_1^2=\frac{2m_c(f/2\delta)^2}{(2\delta/f)^2+1}; \tag{A.57}$$

so that the surface density is given by the equation

$$\sigma = \frac{\sqrt{2m_c}f}{2\delta\sqrt{(2\delta/f)^2+1}}\, x^{-3/2} \tag{A.58}$$

and the scale height of the disc is

$$h = \left(\frac{2}{m_c[1+(f/2\delta)^2]}\right)^{1/2} x^{3/2}. \tag{A.59}$$

The magnetic diffusion terms play an important role in these equations as σ cannot be negative; this requires that f must always be greater than zero. This in turn places limits on the size of the Hall diffusion parameter with respect to the ambipolar diffusion parameter in order to ensure that disc formation may take place.

This solution to the disc equations represents the slowly-accreting Keplerian disc that was discussed in detail in Section 3.2.

A.2 Region AD

Region AD is the blue area in the lower left of Figure A.1, where p and q satisfy the inequalities

$$p > 2q - 2, \tag{A.60}$$

$$\text{and } p < p, \tag{A.61}$$

which together imply that

$$p, q < 2. \tag{A.62}$$

In this region, $\hat{m}_c = m_c$ and $\hat{\sigma} = (b_{r,s}^2 + b_{\phi,s}^2)/\sigma$, so that the scaling of $8\hat{m}_c/\hat{\sigma}^2x^3$ goes as

$$\frac{8\hat{m}_c}{\hat{\sigma}^2x^3} \sim \frac{m_c}{x^3(x^{p-2q})^2} \sim x^{4q-2p-3}. \tag{A.63}$$

In this region of the pq-plane, the desired case (b) for the behaviour of the scaling of h is defined by the inequality

$$0 > 4q - 2p - 3 \tag{A.64}$$

which can be rearranged into

$$p - 2q > -3/2. \tag{A.65}$$

The boundary case when $p - 2q = -3/2$ must also be examined, as this inequality is satisfied whenever both p and $q < 3/2$ in this region.

As in region AC this means that $h \sim x^{3/2}$, and as in the previous solution $b_{r,s} \sim x^{-q}$ and $h(db_z/dx) \sim x^{1/2-q}$, so that once more the latter term is the smaller of the two

and can be disregarded when compared with $b_{r,s}$ in the induction equation, the radial momentum equation and the equation for the azimuthal component of the magnetic field.

The remaining terms in the induction equation (2.109) scale with x as

$$\begin{aligned} \psi &\sim x^{2-q}, \\ xwb_z &\sim x^{p-q}, \\ \tilde{\eta}_H x b_{\phi,s} b_z b h^{1/2} \sigma^{-3/2} &\lesssim x^{7/4+3p/2-3q}, \\ \text{and } \tilde{\eta}_A x b_{r,s} b_z^2 h^{1/2} \sigma^{-3/2} &\sim x^{7/4+3p/2-3q}; \end{aligned} \tag{A.66}$$

and as $p < 2$, then $x^{2-q} < x^{p-q}$ in the small x limit. Therefore ψ can be dropped from the induction equation as in region AC, and the equation becomes

$$-w + \tilde{\eta}_H b_{\phi,s} b h^{1/2} \sigma^{-3/2} + \tilde{\eta}_A b_{r,s} b_z h^{1/2} \sigma^{-3/2} = 0. \tag{A.67}$$

Equating the exponents of these remaining terms gives the exponent

$$q = \frac{p}{4} + \frac{7}{8}, \tag{A.68}$$

which can be substituted into the inequalities in A.60–A.61 and A.64 to place further limits on p:

$$1/2 \leq p \leq 3/2. \tag{A.69}$$

The rest of this solution depends critically upon the value of $b_{\phi,s}$, so it must be the next focus of the derivation. The scaling with x of the variable term in the denominator of the fraction on the left hand side of the equation for $b_{\phi,s}$, 2.114, is

$$\frac{2\alpha\tilde{\eta}_A \psi b_z h^{1/2}}{\sigma^{3/2} x^2} \sim x^{3/4+3p/2-2q} = x^{p-1}, \tag{A.70}$$

which cannot easily be compared with the constant as in the AC case. The situations in which each of the terms in the denominator is dominant must be examined separately, in order to properly survey pq-space.

A.2.1 p < 1

The first case is the situation where $p < 1$ and the equation for $b_{\phi,s}$ becomes

$$b_{\phi,s} = -\min\left[\frac{\sigma^{3/2}}{\tilde{\eta}_A b_z h^{1/2}}\left(\frac{j}{x} - \frac{\tilde{\eta}_H b b_{r,s} h^{1/2}}{\sigma^{3/2}}\right); \delta b_z\right]; \tag{A.71}$$

and the terms on the left hand side scale as

$$\begin{aligned} \frac{\sigma^{3/2}}{\tilde{\eta}_A b_z h^{1/2}} &\sim x^{-5p/4+1/8}, \\ \frac{j}{x} &\sim x^{-r-1} \\ \text{and } \frac{\tilde{\eta}_H b b_{r,s} h^{1/2}}{\sigma^{3/2}} &\sim x^{p-1}. \end{aligned} \tag{A.72}$$

If $-r < p$ then the left hand side of Equation A.71 scales as $x^{-5p/4-7/8-r}$ and is larger than the term on the right hand side (which scales as $x^{-q=-p/4-7/8}$), and so the cap is applicable and $b_{\phi,s} = -\delta b_z$. Alternatively, if $-r > p$ then both sides of Equation A.71 scale as b_z and the coefficient of $b_{\phi,s}$ cannot be determined until the coefficients of the other variables are known. In both situations then $b_{\phi,s} \sim x^{-q}$.

Adopting this scaling of $b_{\phi,s}$ with x and looking at the angular momentum equation (2.107) shows that its terms scale with x as

$$\begin{aligned} \frac{dj}{dx} &\sim x^{-r-1}, \\ \frac{j}{w} &\sim x^{1-r-p} \\ \text{and } \frac{x b_z b_{\phi,s}}{w\sigma} &\sim x^{1/4-p/2}. \end{aligned} \tag{A.73}$$

As $p < 1$, it is clear that $1 - r - p > -r - 1$ so that the angular momentum equation may be simplified into

$$\frac{dj}{dx} = \frac{x b_z b_{\phi,s}}{w\sigma} \tag{A.74}$$

and solved for the exponent of j,

$$r = \frac{p}{2} - \frac{5}{4}. \tag{A.75}$$

Again, the constant coefficient of j cannot be determined until the coefficient of $b_{\phi,s}$ is known.

Turning finally to the radial momentum equation (2.106), it can be shown that the terms scale as

$$\begin{aligned} \frac{1}{\sigma}\frac{d\sigma}{dx} &\sim x^{-1}, \\ -\frac{w^2}{\sigma}\frac{d\sigma}{dx} &\sim x^{2p-3}, \\ -\frac{m}{x^2} &\sim x^{-2}, \\ \frac{b_z b_{r,s}}{\sigma} &\sim x^{p-2q} = x^{p/2-7/4}, \\ \frac{j^2}{x^3} &\sim x^{-2r-3} = x^{-p-1/2}, \end{aligned}$$

$$\text{and } \frac{w^2}{x} \sim x^{2p-3}; \tag{A.76}$$

clearly $x^{-1} < x^{-2}$ in the small x limit, and as $p < 1$ it is trivial to show that $-p - 1/2 > -3/2$. The lower limit on p (see A.69) is then manipulated to show that $-3/2 < p/2 - 7/4$, so that the angular momentum contribution to the radial support may also be dropped. The radial momentum equation is then simplified into the form

$$\frac{m}{x^2} = w^2 \left(\frac{1}{x} + \frac{1}{\sigma} \frac{d\sigma}{dx} \right). \tag{A.77}$$

From this equation the exponents of the power law relations can then be equated to give

$$p = \frac{1}{2}, \tag{A.78}$$

which can be substituted into Equations A.68 and A.75 to solve for the other exponents

$$r = -1 \tag{A.79}$$

$$\text{and } q = 1. \tag{A.80}$$

This is the only solution to the power law expansion of σ, j and b_z in this region of the pq-plane that also satisfies $p < 1$. The coefficients of the variables and the conditions under which they satisfy the fluid equations are derived below in subsection A.2.3.

A.2.2 p > 1

The other behaviour of the denominator of the left hand side of $b_{\phi,s}$ occurs when $p > 1$, and so $b_{\phi,s}$ is given by

$$b_{\phi,s} = -\min \left[\frac{2\alpha\psi}{x^2} \left(\frac{j}{x} - \frac{\tilde{\eta}_H b b_{r,s} h^{1/2}}{\sigma^{3/2}} \right); \delta b_z \right]. \tag{A.81}$$

The bracketed terms on the left hand side scale as

$$\frac{j}{x} \sim x^{-r-1}$$

$$\text{and } \frac{\tilde{\eta}_H h^{1/2} b}{\sigma^{3/2}} b_{r,s} \sim x^{3/4+3p/2-2q} \sim x^{p-1}, \tag{A.82}$$

and as the relationship between p and r has yet to be determined the dominant term cannot be decided. As before, both possibilities must be considered.

When $-r < p$, the left hand side of Equation A.81 scales as $x^{-r-p/4-15/8}$, and if $-r < 1$ then this side is the larger of the two and $b_{\phi,s}$ takes on the value of the right hand side. The rest of the derivation then follows that outlined in subsection A.2.1, giving the solution $p = 1/2$, which is a contradiction of the requirement that $p > 1$.

However, if $1 < -r < p$, then $b_{\phi,s}$ will then scale with x as $x^{-r-p/4-15/8}$, and the terms of the angular momentum equation will scale as

$$\begin{aligned} \frac{dj}{dx} &\sim x^{-r-1}, \\ \frac{j}{w} &\sim x^{1-r-p}, \\ \text{and } \frac{xb_{\phi,s}b_z}{w\sigma} &\sim x^{-r-p/2-3/4}. \end{aligned} \tag{A.83}$$

Rearranging the limits on both p and r then allows for the derivation of limits on the exponents of the scaling terms:

$$0 < -r - 1, \tag{A.84}$$

$$\frac{1}{2} < 1 - r - p < 1 \tag{A.85}$$

$$\text{and } -r - \frac{p}{2} - \frac{3}{4} < 0; \tag{A.86}$$

only one of these terms is less than 0, and as there are not two large terms that can be equated there is no way to solve this equation. Therefore there is no solution to the fluid equations when $-r < p$ in the region AD of the pq-plane.

Finally, there is the case where $1 < p < -r$. In this circumstance the left hand side of Equation A.81 scales as $x^{3p/4-15/8}$. As $p > 1$,

$$\frac{3p}{4} - \frac{15}{8} > -\frac{9}{8} \tag{A.87}$$

$$\text{and } -\frac{p}{4} - \frac{7}{8} < -\frac{9}{8} \tag{A.88}$$

so that $b_{\phi,s} \sim x^{3p/4-15/8}$. The scalings of the terms in the angular momentum equation remain as in A.83, save for the last term which is now

$$\frac{xb_{\phi,s}b_z}{w\sigma} \sim x^{p/2-3/4}. \tag{A.89}$$

As above, the first two terms both have exponents that are greater than zero, while the final term has the exponent $p/2 - 3/4 < 0$; again there is no solution to this equation in the small x limit when $p > 1$. The only valid solution to the power law behaviour of the variables in the disc equations in this region of the pq-plane is then that outlined in Equations A.78–A.80.

A.2.3 Coefficients of the solution

Having explored the entirety of Region AD, the only solution to the fluid equations with a nontrivial value of the scale height of the pseudodisc is that described by the

series of power laws with exponents $p = 1/2$, $q = 1$ and $r = -1$. Substituting these into the radial momentum equation gives

$$w^2 \left(\frac{1}{x} + \frac{1}{\sigma} \frac{d\sigma}{dx} \right) = \frac{m}{x^2}, \tag{A.90}$$

which is rearranged into the form

$$\left(\frac{1}{x} - \frac{1}{2x} \right) = \frac{\sigma^2}{m} \tag{A.91}$$

and then solved for the surface density,

$$\sigma = \sqrt{\frac{m_c}{2x}}. \tag{A.92}$$

The flux is given by Equation 3.5 to be

$$\psi = b_z x^2 \tag{A.93}$$

and the radial field component from Equation 3.6 is

$$b_{r,s} = b_z; \tag{A.94}$$

the azimuthal field component is critical to the determination of the coefficients of the other variables, and Equation A.71 is simplified to give

$$b_{\phi,s} = -\min \left[-\frac{\tilde{\eta}_H b b_{r,s}}{\tilde{\eta}_A b_z} \, ; \delta b_z \right]. \tag{A.95}$$

As mentioned previously, both sides of $b_{\phi,s}$ scale with x in the same manner, and the precise value chosen depends entirely upon the constants that describe the magnetic diffusion and the cap placed upon $b_{\phi,s}$. It is also clear from Equation A.95 that changing the sign of $\tilde{\eta}_H$ changes the sign of $b_{\phi,s}$, however, changing the sign of $b_{\phi,s}$ leads to a change in the signs of both j and b_z, so that the similarity solution is effectively upside down but otherwise unchanged. Taking the absolute value of $\tilde{\eta}_H$ allows for the sign of $b_{\phi,s}$ to be kept negative, so that the final value of the azimuthal field component is given by

$$b_{\phi,s} = -\min \left[\frac{|\tilde{\eta}_H|}{\tilde{\eta}_A} \, b \, ; \delta b_z \right]. \tag{A.96}$$

Before exploring the two different values that $b_{\phi,s}$ can take (with coefficients $b_{\phi 1}$ and $b_{\phi 2}$) in great detail, more generalised solutions to the magnetic field components and scale height may then be written down:

$$b_{\phi,s} = -b_{\phi 1,2} \, x^{-1}, \tag{A.97}$$

$$b_z = b_{z1,2} \, x^{-1}, \tag{A.98}$$

$$b_{r,s} = b_{z1,2} \, x^{-1}, \tag{A.99}$$

$$b = \sqrt{2b_z^2 + b_{\phi,s}^2} = \sqrt{2b_{z1,2}^2 + b_{\phi 1,2}^2} \, x^{-1}, \tag{A.100}$$

and

$$h = h_{1,2}\, x^{3/2} = \frac{(b_{z1,2}^2 + b_{\phi 1,2}^2)}{\sqrt{2m_c^3}} \left[-1 + \sqrt{1 + \frac{4m_c^2}{(b_{z1,2}^2 + b_{\phi 1,2}^2)^2}} \right] x^{3/2}; \tag{A.101}$$

the induction equation (A.67) then becomes

$$\left(\tilde{\eta}_A b_{z1,2}^2 + \tilde{\eta}_H b_{\phi 1,2} \sqrt{2b_{z1,2}^2 + b_{\phi 1,2}^2} \right) h_{1,2}^{1/2} = 2^{-1/4} m_c^{5/4}. \tag{A.102}$$

The first of the two solutions is defined by $b_{\phi,s} = -b_{\phi 1}\, x^{-1} = -|\tilde{\eta}_H| b / \tilde{\eta}_A$ which is solved to give

$$b_{\phi,s} = -|\tilde{\eta}_H| b_z \sqrt{\frac{2}{\tilde{\eta}_A^2 - \tilde{\eta}_H^2}}\,. \tag{A.103}$$

In this case

$$b = b_{z1}\, x^{-1} \sqrt{\frac{2\tilde{\eta}_A^2}{\tilde{\eta}_A^2 - \tilde{\eta}_H^2}}\,; \tag{A.104}$$

the coefficient of h is given by

$$h_1 = \frac{f_1 b_{z1}^2}{\sqrt{2m_c^3}} \left[-1 + \sqrt{1 + \frac{4m_c^2}{f_1^2 b_{z1}^4}} \right], \tag{A.105}$$

where the diffusion parameter f_1 is defined as

$$f_1 = \frac{\tilde{\eta}_A^2 + \tilde{\eta}_H^2}{\tilde{\eta}_A^2 - \tilde{\eta}_H^2}; \tag{A.106}$$

the angular momentum coefficient, j_1, is determined by

$$j_1 = \frac{b_{z1}}{m_c} \sqrt{\frac{2\tilde{\eta}_H^2}{\tilde{\eta}_A^2 - \tilde{\eta}_H^2}}; \tag{A.107}$$

and b_{z1} is obtained by substituting these into Equation A.102 and finding the single positive real root of the polynomial

$$b_{z1}^8 - \frac{m_c^2}{2\tilde{\eta}_A^2 f_1}\, b_{z1}^6 - \frac{m_c^6}{4\tilde{\eta}_A^4 f_1^4} = 0. \tag{A.108}$$

This similarity solution applies when the inequality

$$\sqrt{\frac{2\tilde{\eta}_H^2}{\tilde{\eta}_A^2 - \tilde{\eta}_H^2}} < \delta \tag{A.109}$$

is satisfied, and corresponds to the asymptotic inner solution for the strong braking case presented by Krasnopolsky and Königl (2002) in the limit of pure ambipolar diffusion. In their solution $\tilde{\eta}_H = b_{\phi,s} = 0$ and there is effectively no angular momentum,

although as can be seen in Figure 6.4, the angular momentum j actually settles to a small asymptotic plateau value. This particular solution applies in their calculations when the magnetic braking parameter α is large, although the parameter itself does not appear in any of the coefficients describing the asymptotic power law solution.

The second solution exists when the other value of $b_{\phi,s}$ is chosen, that is, when

$$b_{\phi,s} = -b_{\phi 2}\, x^{-1} = -\delta\, b_z. \tag{A.110}$$

In this case the coefficient of h is determined by the equation

$$h_2 = \frac{(1+\delta^2) b_{z2}^2}{\sqrt{2 m_c^3}} \left[-1 + \sqrt{1 + \frac{4 m_c^2}{(1+\delta^2)^2 b_{z2}^4}} \right]; \tag{A.111}$$

the coefficient j_2 is simply

$$j_2 = \frac{\delta b_{z2}^2}{m_c}; \tag{A.112}$$

and b_{z2} is the single positive real root of the equation

$$b_{z2}^8 - \frac{m_c^2 (1+\delta^2)}{2 f_2^2}\, b_{z2}^6 - \frac{m_c^6}{4 f_2^4} = 0 \tag{A.113}$$

where f_2 is given by

$$f_2 = \tilde{\eta}_A - \tilde{\eta}_H \delta \sqrt{2+\delta^2}. \tag{A.114}$$

This particular similarity solution has no corresponding solution in the results of Krasnopolsky and Königl (2002) and is unique to this work. Both similarity solutions represent a flow of matter onto the protostar at near-free fall rates with little rotational momentum; these solutions are representative of the magnetic braking catastrophe in star formation, and are discussed in more detail in Section 3.3.

A.3 Region BC

This section of the pq-plane is painted pink in the upper right of Figure A.1 and defined mathematically by the inequalities

$$p < 2q - 2, \tag{A.115}$$

$$p > q, \tag{A.116}$$

$$\text{and } p, q > 2. \tag{A.117}$$

In this region $\hat{m}_c = -x^3 b_{r,s} (db_z/dx)/\sigma$ and $\hat{\sigma} = \sigma$, so that the term that determines the scaling of h is given by

$$\frac{8\hat{m}_c}{\hat{\sigma}^2 x^3} \sim \frac{x^{2+p-2q}}{x^{3-2p}} \sim x^{3p-2q-1}. \tag{A.118}$$

In this region of the plane, case b (restricting h to only physical solutions) is defined by the inequality

$$3p - 2q - 1 < 0, \tag{A.119}$$

however, using the inequalities in A.115–A.117 it can be seen that

$$p - q > 0, \tag{A.120}$$

so that

$$3p - 2q > q, \tag{A.121}$$

and

$$3p - 2q - 1 > q - 1 > 1, \tag{A.122}$$

which is a clear contradiction of A.119. In this region then the only similarity solutions that may exist are those in which h very small and may be unphysical. The boundary case where $3p - 2q - 1 = 0$ is also unsatisfied in this region, and so there can be no physical similarity solutions to the disc equations in region BC of the pq-plane.

A.4 Region BD

The large purple region at the lower right of Figure A.1 is region BD, which is characterised by the inequalities

$$p < 2q - 2 \tag{A.123}$$

$$\text{and } p < q, \tag{A.124}$$

and has $\hat{m}_c = -x^3 b_{r,s}(db_z/dx)/\sigma$ and $\hat{\sigma} = (b_{r,s}^2 + b_{\phi,s}^2)/\sigma$. The term that determines the scaling of h with x goes as

$$\frac{8\hat{m}_c}{\hat{\sigma}^2 x^3} \sim \frac{x^{2+p-2q}}{x^3 (x^{p-2q})^2} \sim x^{2q-p-1}, \tag{A.125}$$

so that in this region the desired case b for the scaling of h applies when the inequality

$$2q - p - 1 \leq 0 \tag{A.126}$$

is satisfied. However, as in region BC, the inequalities that define the region (Equations A.123–A.124) can be rearranged to show

$$0 < 2q - p - 2. \tag{A.127}$$

This implies that

$$1 < 2q - p - 1, \tag{A.128}$$

which is a contradiction of A.126, and so case b, and the boundary case between cases a and b, cannot exist in this region. Therefore there is no physical similarity solution to the fluid equations in region BD of the pq-plane.

Appendix B

Parameters and Shock Positions

In order to assist any future researchers in this area who wish to duplicate the results of this work, the shock positions and values of the variables at the matching point are listed in this appendix for all of the similarity solutions illustrated in Chapters 4 and 5 and Appendix C. The centrifugal shock position and the nondimensional central mass for the nonmagnetic and ideal MHD similarity solutions that were calculated in Sections 4.1 and 4.2 (which were simply integrated inwards from the outer boundary) are given in Table B.1.

The positions of the centrifugal and magnetic diffusion shocks, as well as the location of any subshocks that occur downstream of these, for the Hall similarity solutions with nondimensional Hall parameter $\tilde{\eta}_H \in [-0.2, 0.5]$ are presented in Table B.2. The converged (or near-converged) values of the variables at the matching point x_m, and the nondimensional central mass m_c, of the same solutions are listed in Table B.3.

Unless otherwise indicated, all of the similarity solutions with both Hall and ambipolar diffusion listed in Table B.2 have boundary conditions and parameters matching those in Table 5.3. The parameters for the nonmagnetic and ideal MHD solutions are listed in the captions of their plots, which are referenced in Table B.1.

Figure	v_0	μ_0	α	x_c	m_c
4.1	0.1	N/A	N/A	$7.65603527 \times 10^{-3}$	0
4.2	1.0	N/A	N/A	$6.31438364 \times 10^{-1}$	0
4.3	0.1	2.9	0.1	$4.93181873 \times 10^{-3}$	6.150
4.4	1.5	2.9	0.1	1.40017396	0.625
4.5	1.5	2.9	0.01	1.59239598	0.050

Table B.1: Positions of the centrifugal shock and the central mass in the nonmagnetic and IMHD similarity solutions presented in Sections 4.1 and 4.2.

$\tilde{\eta}_H$	x_d	x_{d2}	x_c	x_{c2}
-0.5	0.5571562272	–	0.08313609521	–
-0.4	0.5240689226	–	0.07022194425	–
-0.3	0.4914751233	–	0.05470475621	–
-0.2	0.4609084538	–	0.03772972380	–
-0.1	0.4322428394	–	0.02270585875	–
-0.01	0.4086267555	–	0.01391928200	–
-0.001	0.4053600464	–	0.01331861020	–
0	0.4053600464	–	0.01325501322	–
0.001	0.4053600464	–	0.01319153733	–
0.01	0.4037364982	–	0.01264383282	–
0.1	0.3832127348	0.2359118494	0.008883741072	–
0.2	0.3651949666	0.2600572227	0.006052121453	0.005212123123
-0.105*	0.4499425849	–	0.03155084518	–

Table B.2: Positions of the magnetic diffusion and centrifugal shocks, and any subshocks that may occur downstream of these in the set of converged similarity solutions with parameters and initial conditions equal to those given in Table 5.3. Those solutions that were not discussed in Chapter 5 are illustrated without comment in Appendix C.

*The similarity solution with $\tilde{\eta}_H = -0.105$ has the nondimensional ambipolar diffusion parameter $\tilde{\eta}_A = 1.05$, to explore the dependence of x_c and x_d upon the ratio of the magnetic diffusion parameters as discussed in Section 6.3. The other parameters remain unchanged.

$\tilde{\eta}_H$	x_m	$m(x_m)$	$\sigma(x_m)$	$j(x_m)$	$\psi(x_m)$	$b_z(x_m)$	m_c
-0.5*	0.32	5.662680151	6.618598505	1.050574060	1.124110348	9.826278713	3.769000000
-0.4	0.3	5.621615058	7.353687835	1.035288751	1.116077330	11.11475226	4.003813245
-0.3	0.3	5.623968680	7.669114095	1.055246418	1.175236751	11.78779585	4.224377980
-0.2	0.3	5.627639776	7.969005835	1.079020941	1.239078304	12.45420198	4.424377980
-0.1	0.3	5.632885457	8.204312082	1.106920520	1.308610399	13.09647510	4.584727813
-0.01	0.3	5.638815298	8.301889633	1.135502323	1.375848755	13.63201678	4.665173497
-0.001	0.3	5.639438769	8.303864989	1.138496344	1.382679558	13.68253865	4.669442792
0	0.3	5.639508465	8.303988767	1.138830374	1.383440138	13.68812340	4.669966724
0.001	0.3	5.639576935	8.304102170	1.139163663	1.384195474	13.69365766	4.670171632
0.01	0.3	5.640201745	8.304254061	1.142177131	1.391024425	13.74343547	4.674097803
0.1	0.3	5.645909658	8.235961519	1.172119218	1.456191209	14.19615046	4.672541054
0.2	0.3	5.650117515	8.073367472	1.202126470	1.516319914	14.56296008	4.625991391
-0.105**	0.3	5.630104509	8.102443350	1.104424953	1.271312260	12.51898858	4.480831780

Table B.3: Values of the variables at the matching point x_m, and the central mass m_c to which the code converged in the calculations for similarity solutions with $\tilde{\eta}_H \in [-0.5, 0.2]$ and $\tilde{\eta}_A = 1.0$.

*The similarity solution with $\tilde{\eta}_H = -0.5$ has a changed matching point $x_m = 0.32$, as $x = 0.3$ was too close to the local maximum in σ to allow convergence on the boundary conditions.

**The similarity solution with $\tilde{\eta}_H = -0.105$ has $\tilde{\eta}_A = 1.05$. All the other parameters are unchanged.

Appendix C

Additional Similarity Solutions

More similarity solutions were calculated in this project than could be presented in the thesis proper. This appendix contains plots of those similarity solutions listed in Tables B.2 and B.3, for the purpose of highlighting trends such as the increasing disc size with decreasing Hall parameter and the appearance of subshocks.

As in Appendix B, all of the similarity solutions match the outer boundary conditions and collapse parameters that were listed in Table 5.3 unless otherwise noted.

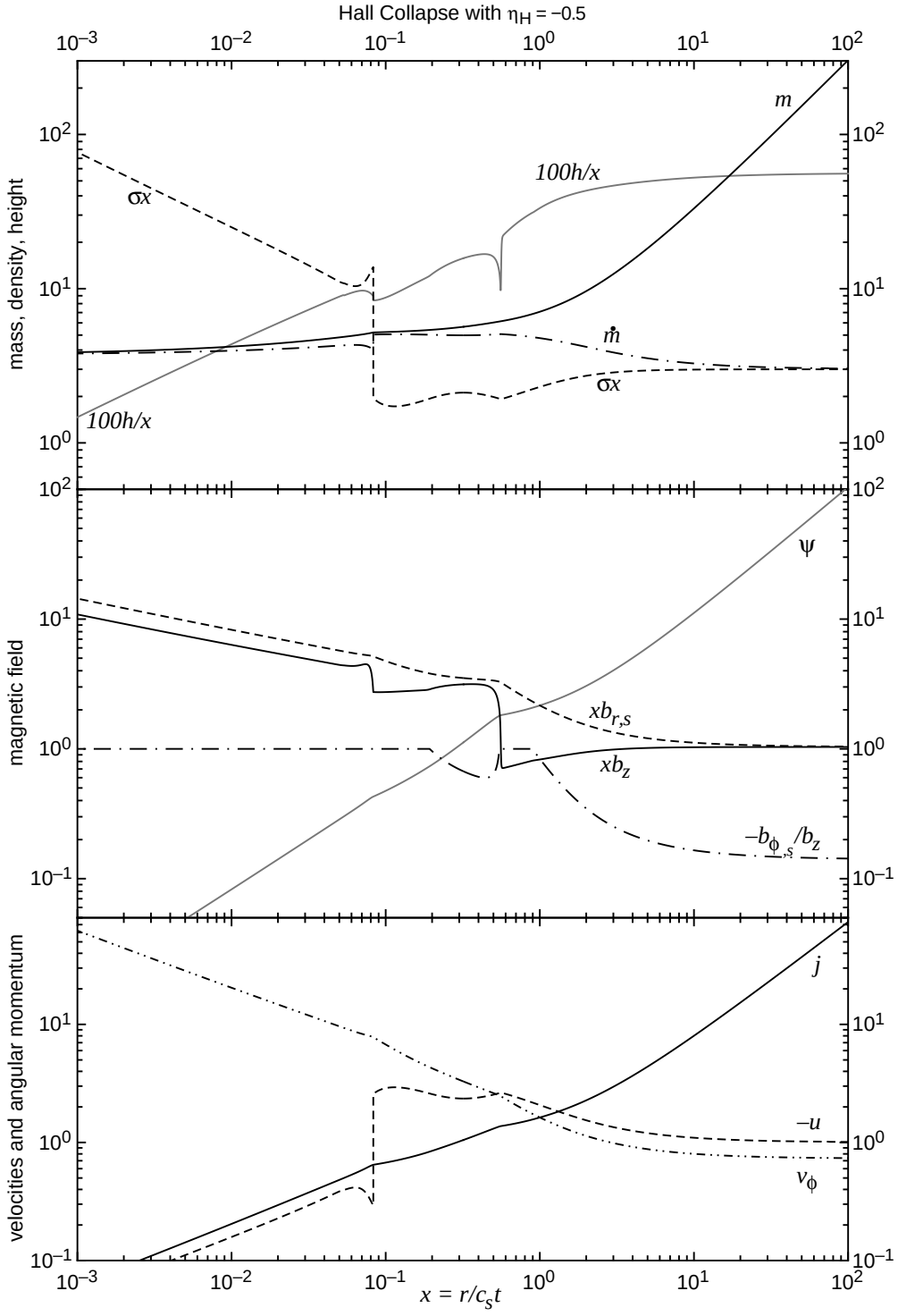

Figure C.1: Similarity solution for Hall collapse with $\tilde{\eta}_H = -0.5$. The shock positions and central mass are as listed in Appendix B.

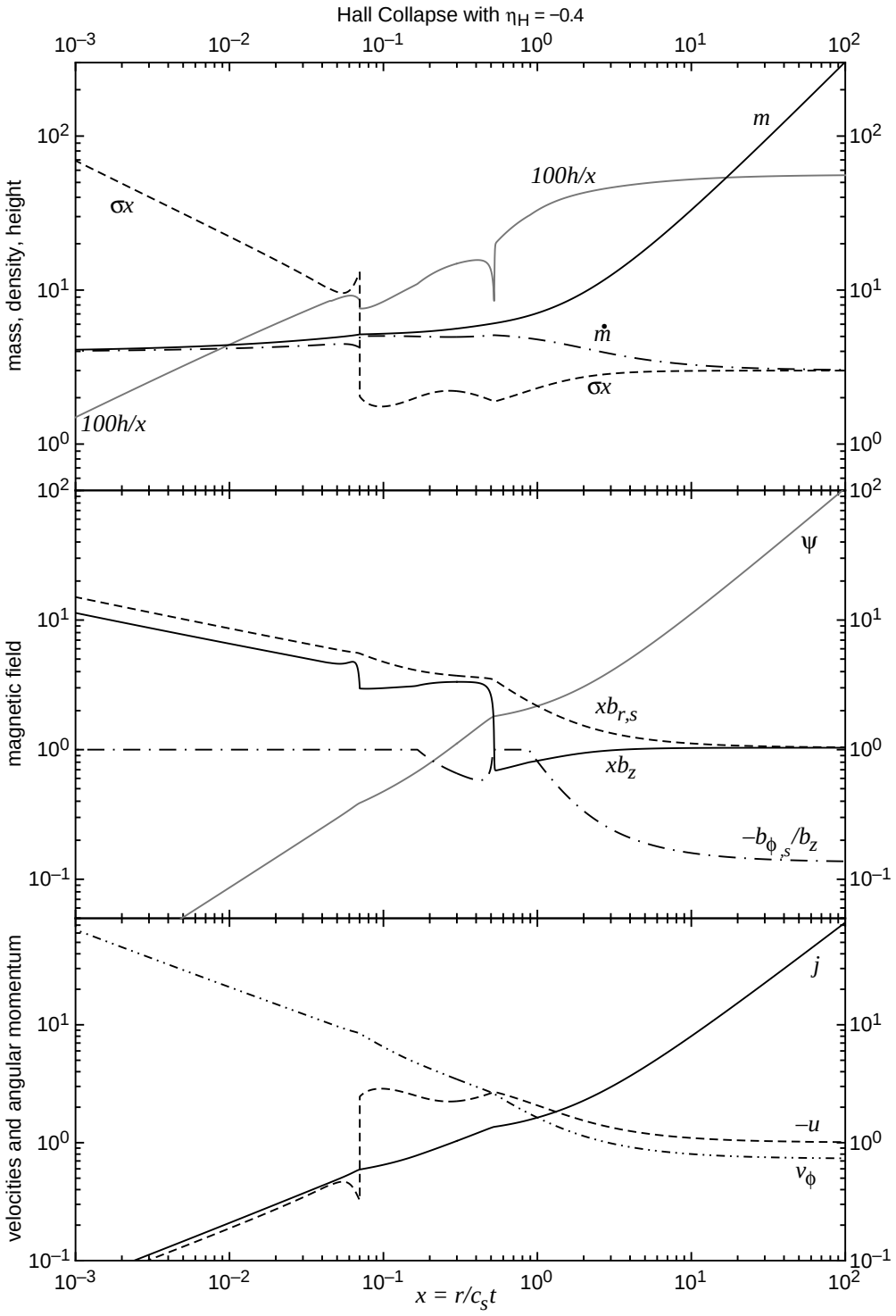

Figure C.2: Similarity solution for Hall collapse with $\tilde{\eta}_H = -0.4$. The shock positions and central mass are as listed in Appendix B.

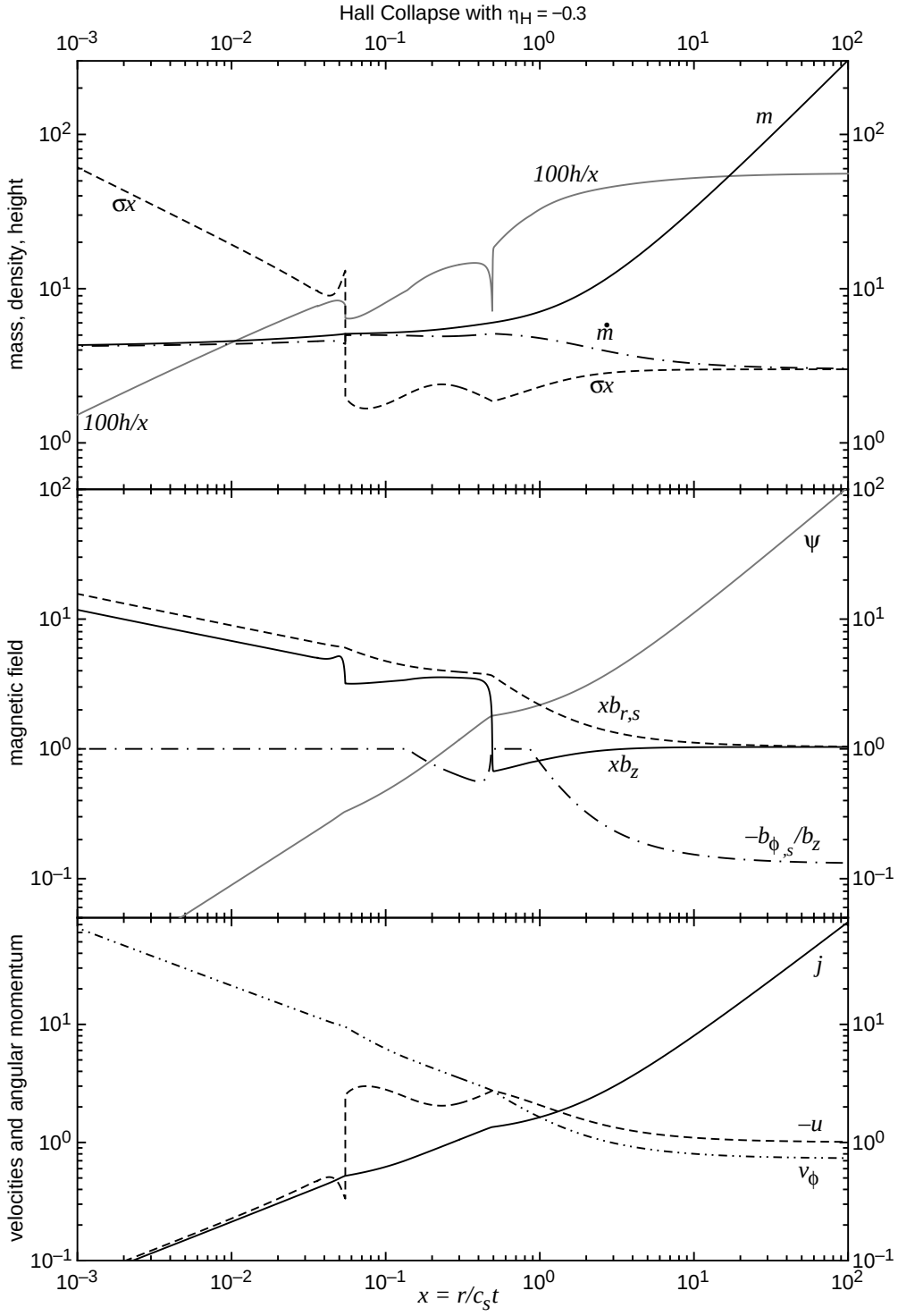

Figure C.3: Similarity solution for Hall collapse with $\tilde{\eta}_H = -0.3$. The shock positions and central mass are as listed in Appendix B.

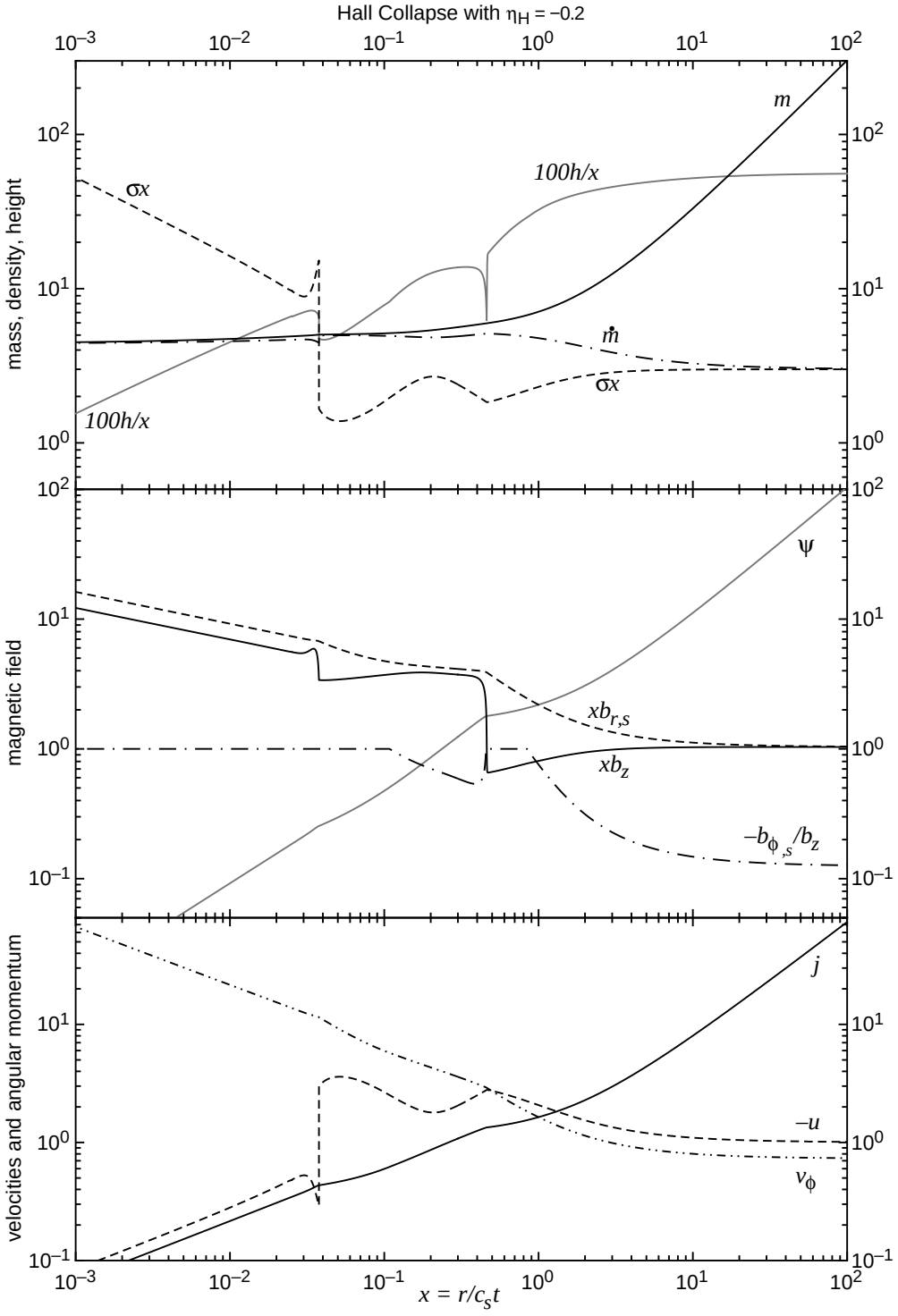

Figure C.4: Similarity solution for Hall collapse with $\tilde{\eta}_H = -0.2$. The shock positions and central mass are as listed in Appendix B.

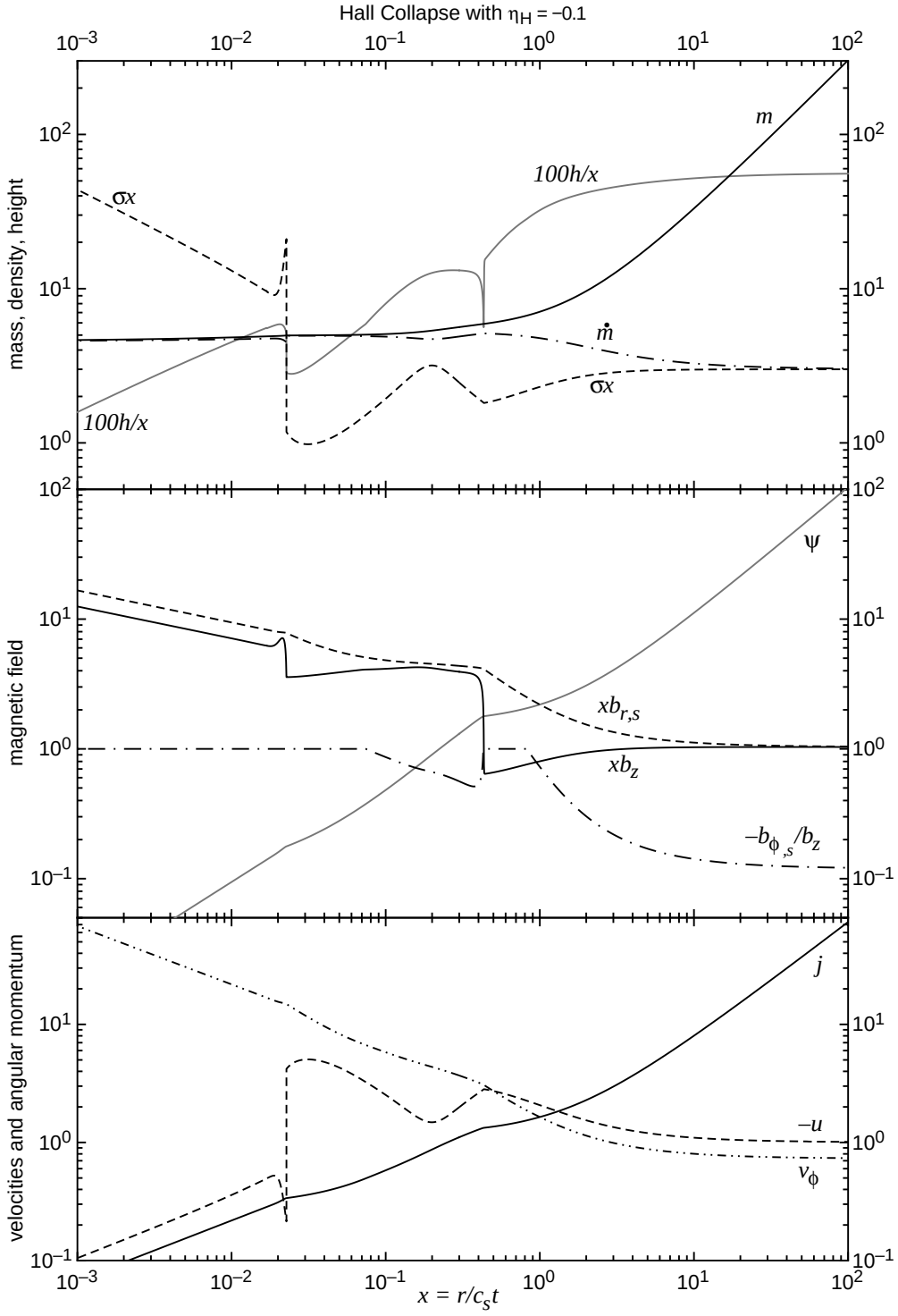

Figure C.5: Similarity solution for Hall collapse with $\tilde{\eta}_H = -0.1$. The shock positions and central mass are as listed in Appendix B.

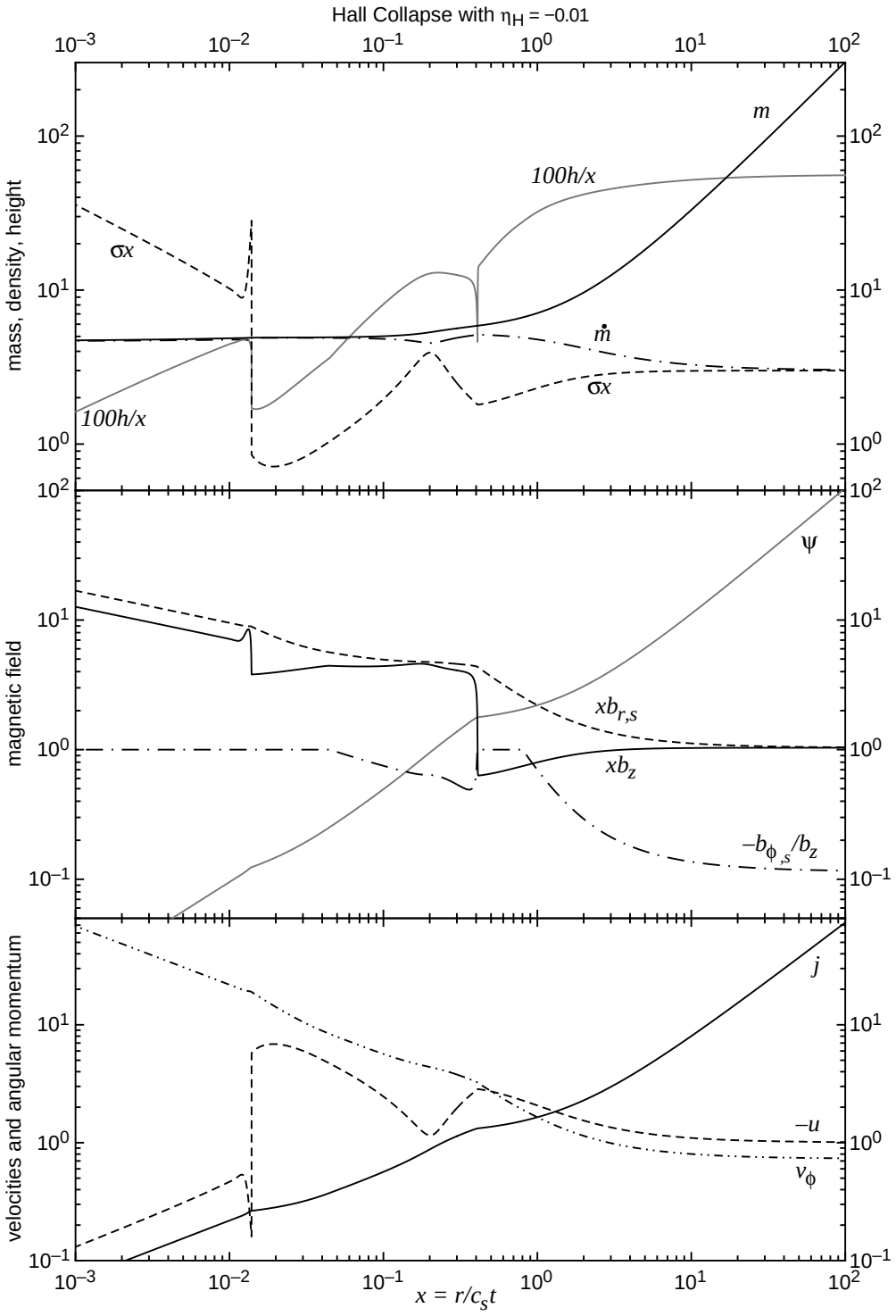

Figure C.6: Similarity solution for Hall collapse with $\tilde{\eta}_H = -0.01$. The shock positions and central mass are as listed in Appendix B.

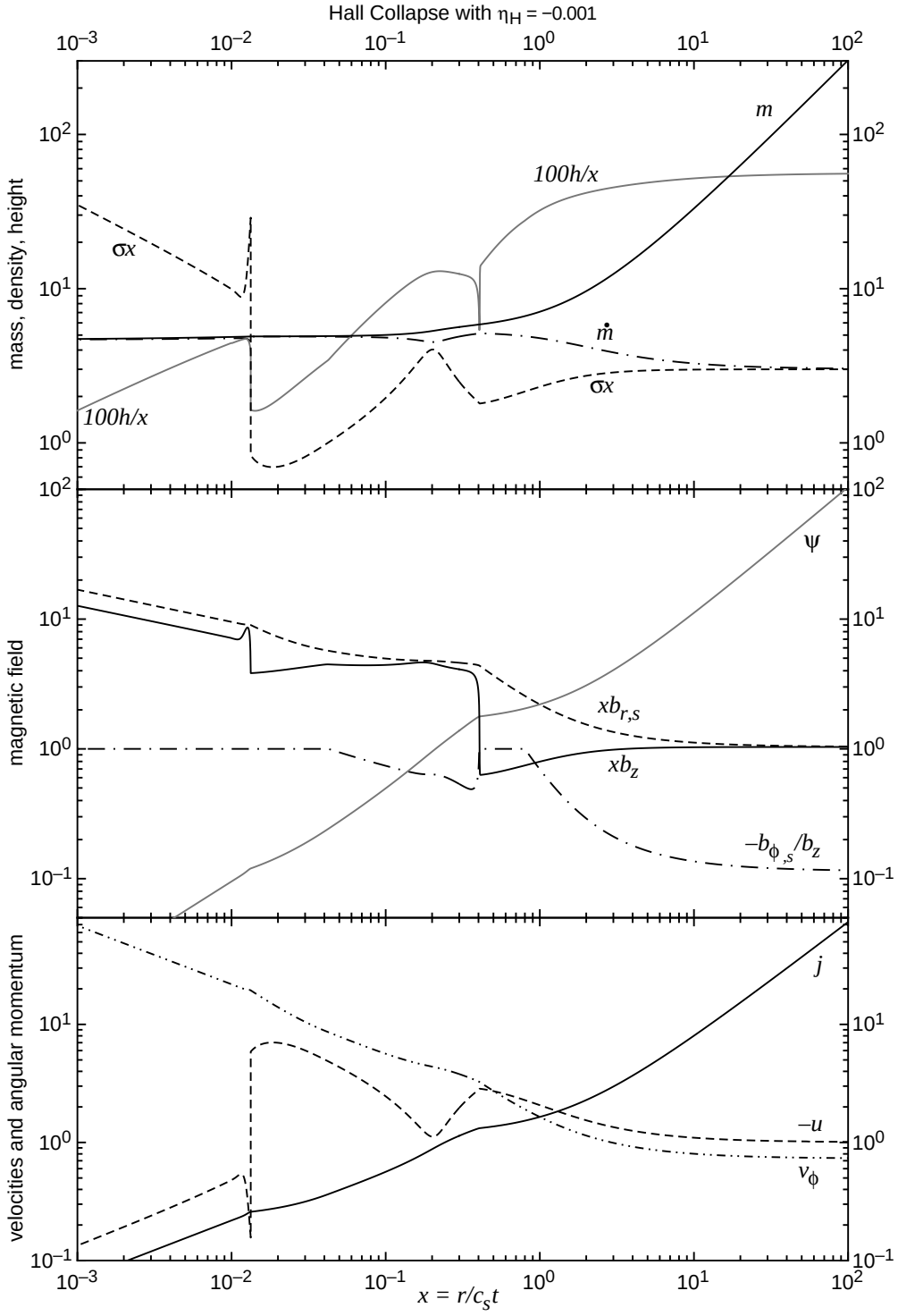

Figure C.7: Similarity solution for Hall collapse with $\tilde{\eta}_H = -0.001$. The shock positions and central mass are as listed in Appendix B.

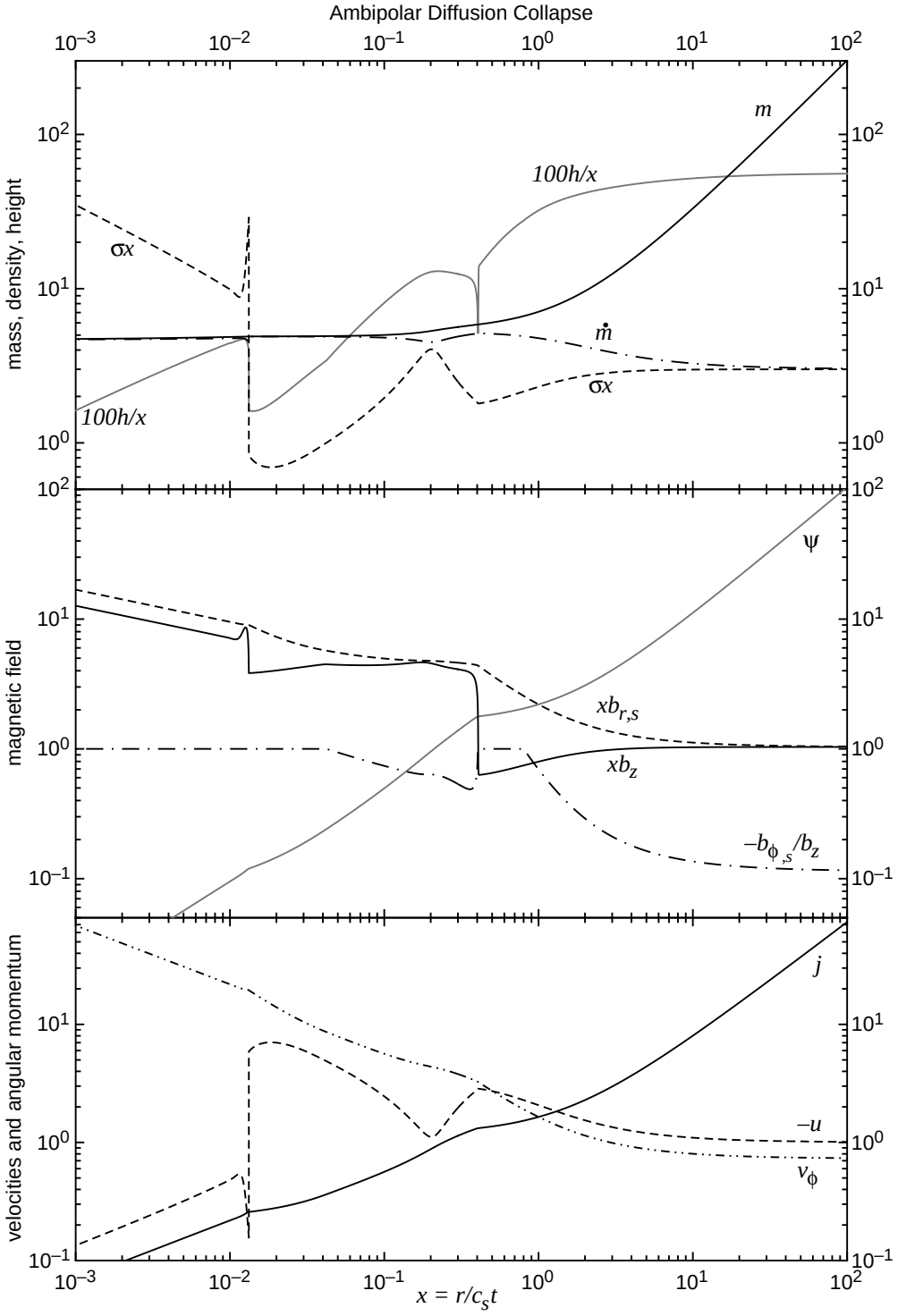

Figure C.8: Similarity solution for ambipolar diffusion-only collapse with $\tilde{\eta}_H = 0$. The shock positions and central mass are as listed in Appendix B.

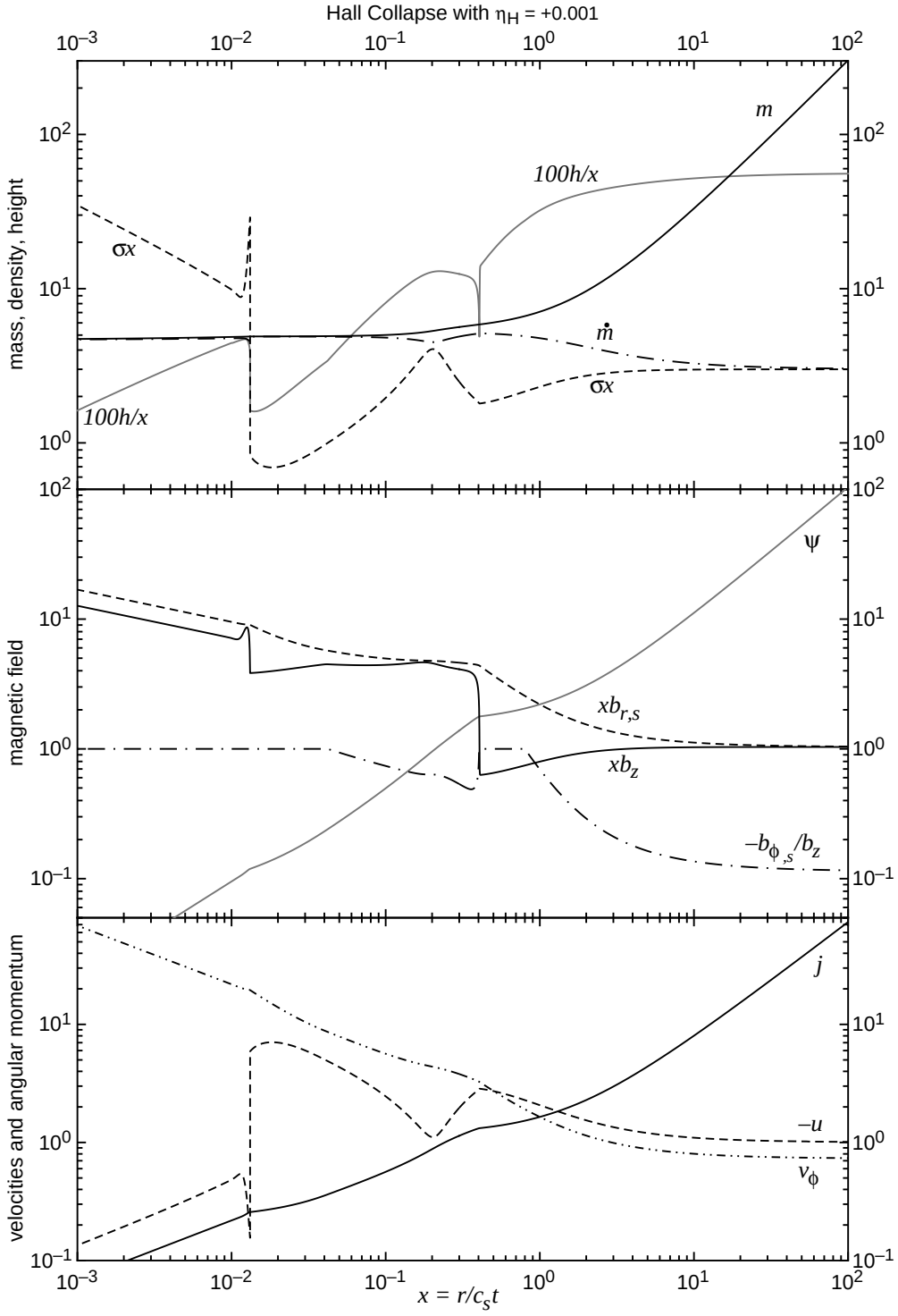

Figure C.9: Similarity solution for Hall collapse with $\tilde{\eta}_H = 0.001$. The shock positions and central mass are as listed in Appendix B.

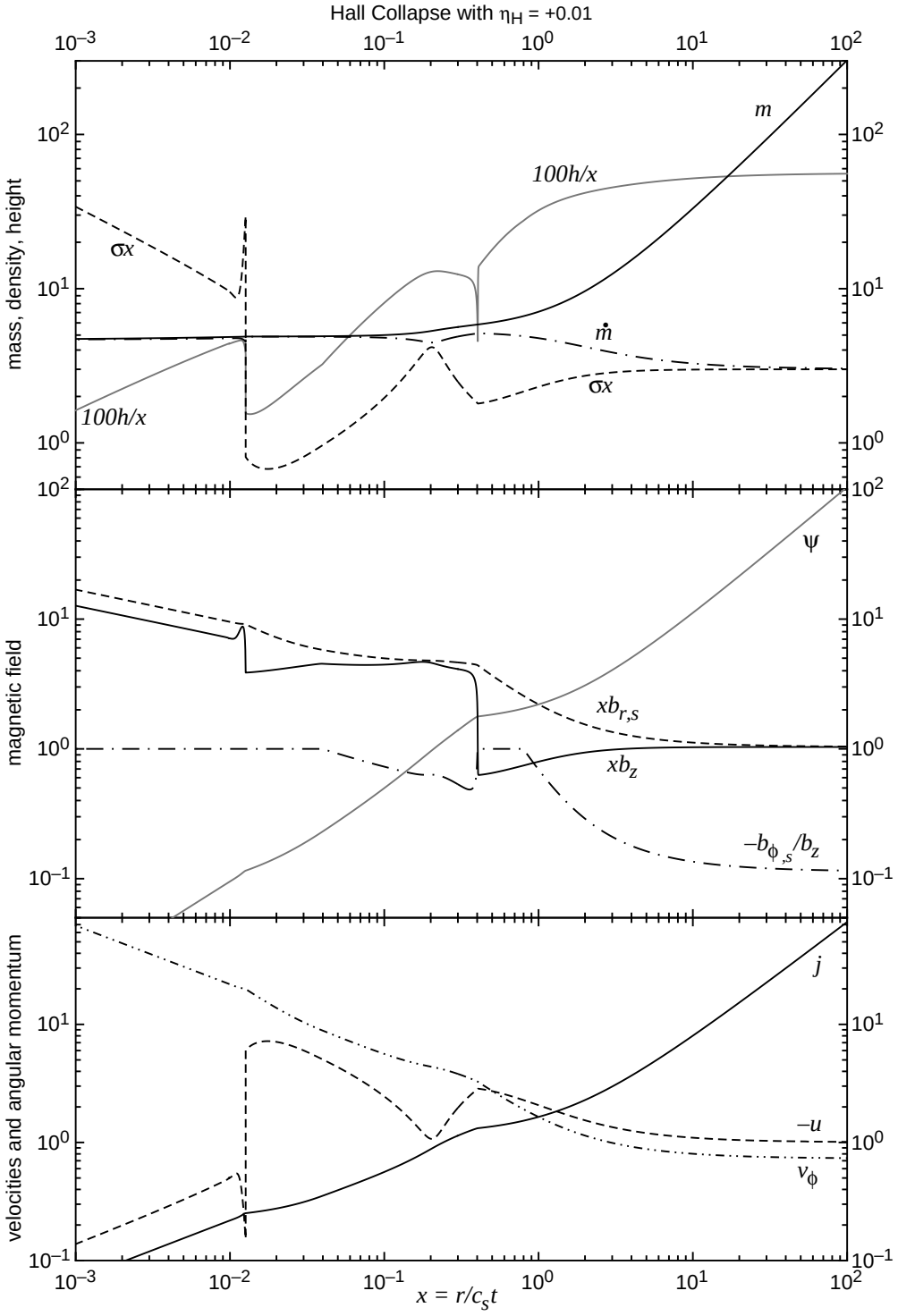

Figure C.10: Similarity solution for Hall collapse with $\tilde{\eta}_H = 0.01$. The shock positions and central mass are as listed in Appendix B.

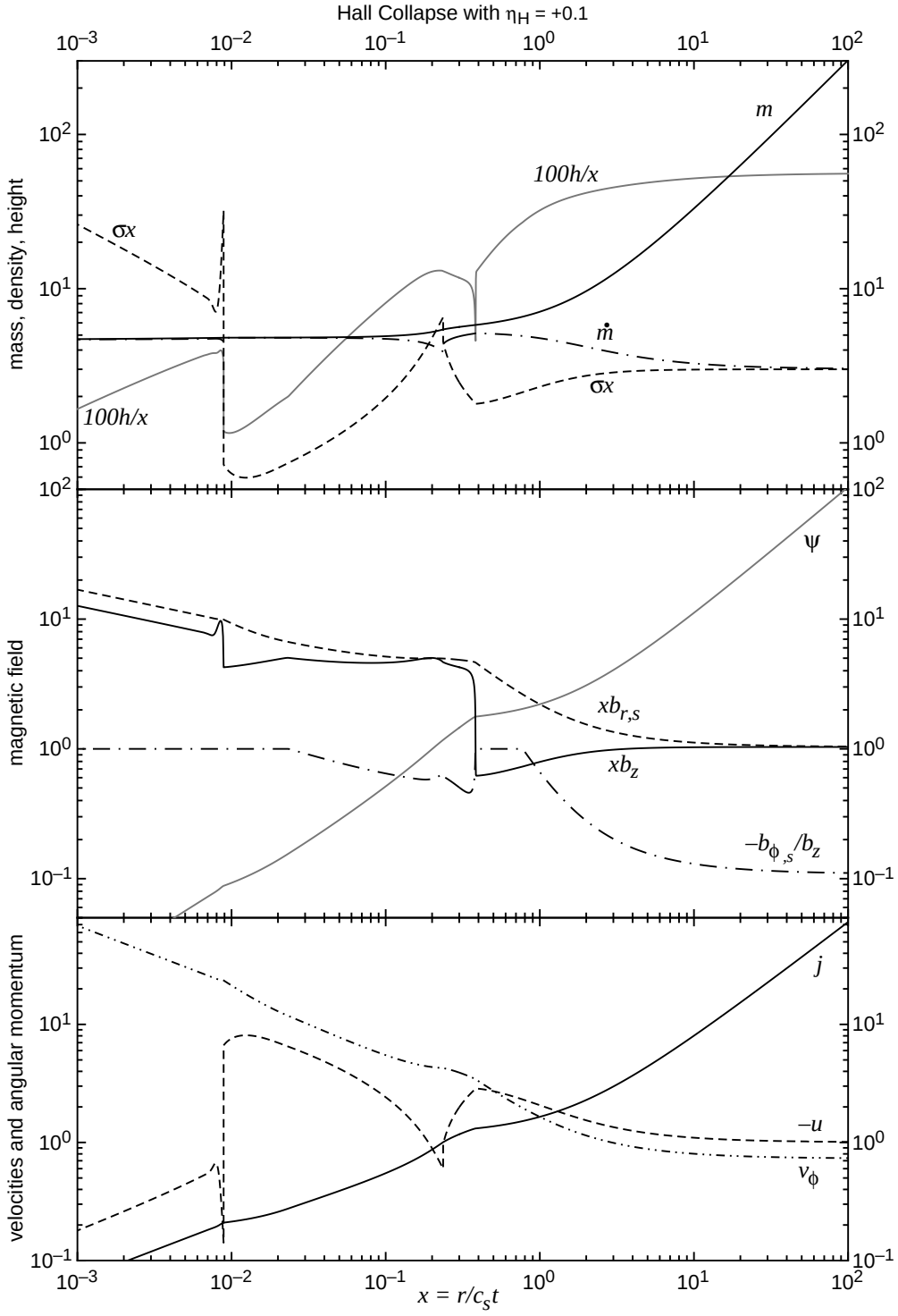

Figure C.11: Similarity solution for Hall collapse with $\tilde{\eta}_H = 0.1$. The shock positions and central mass are as listed in Appendix B.

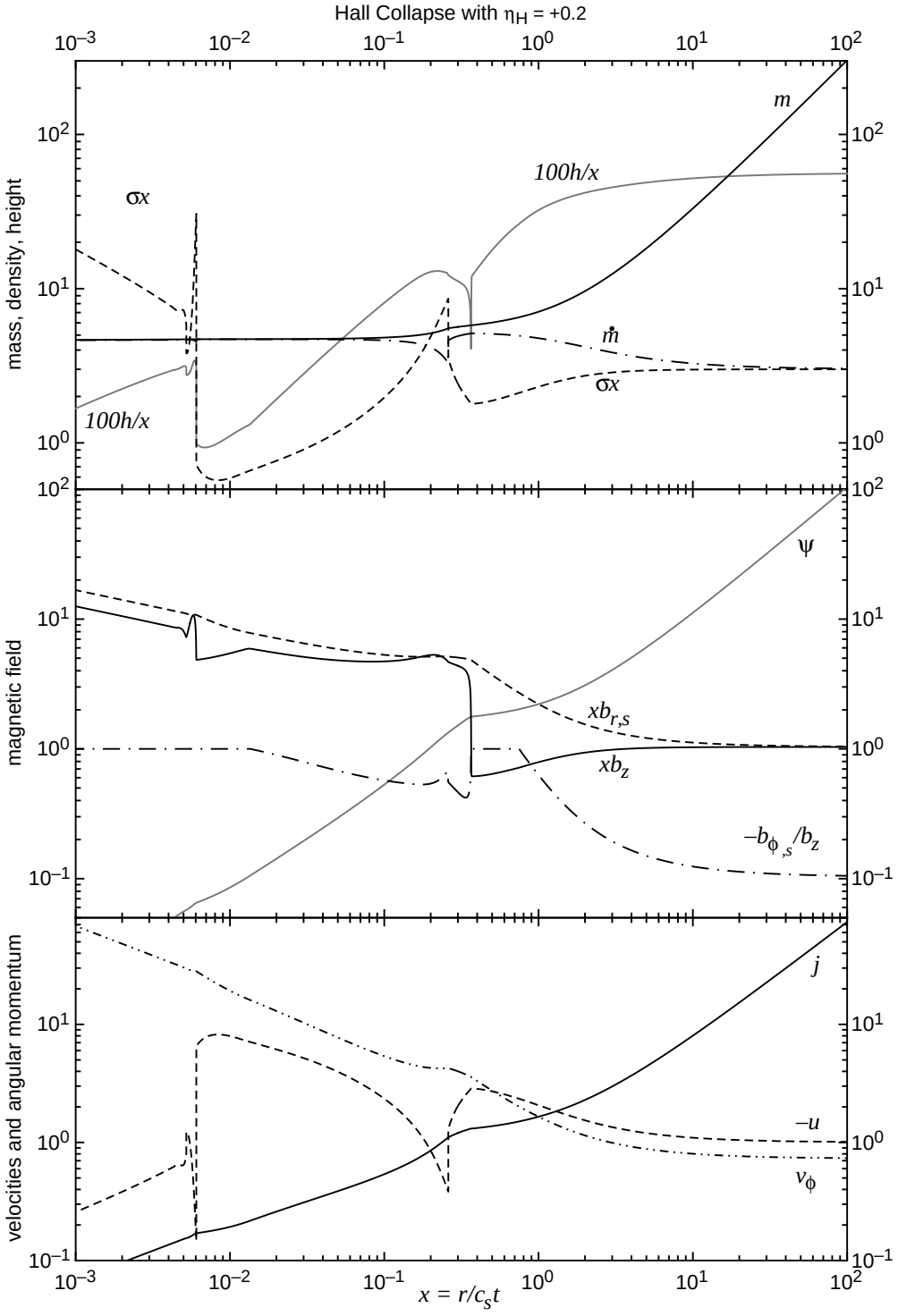

Figure C.12: Similarity solution for Hall collapse with $\tilde{\eta}_H = 0.2$. The shock positions and central mass are as listed in Appendix B.